Towards a room temperature solid state quantum processor — The nitrogen-vacancy center in diamond

Contents

List of Figures

List of Tables

List of Abbreviations

Å	angstrom
AOM	acousto-optic modulator
APD	single photon counting avalanche photodiode
arb. units	arbitrary units
BS	beam splitter
cps	counts per second
CVD	chemical vapor deposition
cw	continuous wave
DEER	double electron-electron resonance
DPSSL	diode pumped solid-state laser
DJT	Dynamic Jahn-Teller (effect)
DNP	dynamic nuclear spin polarization
ELDOR	electron-electron double resonance
ENDOR	electron-nuclear double resonance
EPR	electron paramagnetic resonance
ESEEM	electron spin echo envelope modulation
eZ	electron Zeeman energy
fcc	face-centered cubic
FID	free induction decay
FLIM	fluorescence lifetime imaging
FRET	fluorescence resonance energy transfer
fs	femtosecond
GSD	ground state depletion (microscopy)
hf	hyperfine (interaction)
HMM	Hidden Markov Model
hpht	high pressure high temperature
I_{PL}	photoluminescence/fluorescence intensity
ISC	intersystem crossing
LAC	level anti-crossing (gsLAC and esLAC for ground and excited state LAC)
Mcps	megacounts per second
mm	millimeter
ms	millisecond
mw	microwave
µm	micrometer
µs	microsecond

NV	nitrogen-vacancy (center)
nm	nanometer
NMR	nuclear magnetic resonance
ns	nanosecond
nZ	nuclear Zeeman energy
ODMR	optically detected magnetic resonance
PCB	printed circuit board
PG	pulse generator
ppm	parts per million
ps	picosecond
PSF	pointspread function
pT	picotesla
Q	quadrupole interaction
QEC	quantum error correction
QIP	quantum information processing
QND	quantum nondemolition
qubit	quantum bit
rf	radiofrequency
SNR	signal to noise ratio
SRIM	Stopping and Range of Ions in Matter, freeware program [193]
STED	stimulated emission depletion (microscopy)
T_1	longitudinal spin relaxation time
T_2	transverse spin relaxation time
T_2^*	inverse inhomogeneous broadening; decay constant of FID
ZFS	zerofield splitting
ZPL	zero-phonon line

Summary

Quantum mechanics The theory of quantum physics and its implications and applications have changed the world in the past hundred years. In the beginning it could provide solutions to some puzzling issues that classical mechanics and the theory of electromagnetism were not able to give or that they brought up in the first place. Later on, although quantum mechanics was far from being intuitive at that time it could be used to explain the foundation of almost every process at the microscopic level leading to modern atomic, nuclear or solid state physics for example. In addition it paved the way for many of nowadays used technical devices where the laser is certainly one of the most popular examples. However, until today it remains a challenge to calculate and therefore to understand the behavior of a complex quantum system because its complexity grows exponentially with the number of constituents of such a system. The reason for the latter issue is the insufficient capability of nowadays conventional computers or to put it in the words of David Deutsch "... What computers can or cannot compute is determined by the laws of physics alone ..." that govern the computational processes. Thus, the idea came up to use the laws of quantum physics exploiting the complexity of a well characterized and controllable quantum system to perform computational tasks [1]. This was the birth of quantum computation at least as a theory. Soon it was realized that quantum computers are not only capable of simulating quantum mechanics but also for special information processing tasks where their classical counterparts perform extremely slow [2, 3, 4, 5]. Additionally, the consequences of quantum theory provide the basis for quantum communication where for instance secure data transmission is assured by fundamental laws of physics [6]. As a first small quantum processor ensembles of nuclear spins were found to be ideal candidates to demonstrate first algorithms on such a quantum computer [7, 8]. In this approach a large ensemble of identical molecules containing several unequal nuclear spins is used in a liquid environment. Via standard nuclear magnetic resonance (NMR) techniques the nuclear spins are addressed and used as quantum bits (qubits). It turns out that nuclear spins preserve their quantum features (e.g. the superposition of energy eigenstates) long enough to be observed and exploited because of their weak interaction with the environment. However, this is also the reason why large ensembles have to be used in order to detect quantum phenomena. Later doubts were raised whether such a system is scalable to higher number of constituents necessary for more demanding calculations [9]. Scalable versions of a quantum computer should be rather made of single quantum systems rather than of ensembles.

Single quantum systems The search for single quantum systems that can be deliberately fabricated and controlled while retaining their quantum features is not only motivated by quantum computation and communication. While the miniaturization constantly decreases the size of electronic or electro-optic devices the limit of single quantum building blocks might be reached soon. The operation of such devices does not need to exploit the full complexity of single quantum systems like a quantum computer would need to. But still single quantum systems need to be addressed and manipulated individually. In addition, in fields like material research or in life sciences instruments for high spatial resolution measurements are needed where the actual sensor might very well be of the size of one atom or a small molecule. In that case, however, indeed the sensitivity of quantum coherence to the local environment can be exploited for measurement purposes. Major challenges for all approaches towards single quantum system control are the individual addressing, the measurement of the quantum state and the protection of especially quantum coherences from decoherence due to the environment.

Today, there is a variety of systems that allow a control on the single quantum level. First of all there are single photons which can be manipulated by linear optics elements [10, 11]. In addition, single ions [12] or atoms [13] can be trapped, controlled and addressed individually usually in vacuum. The control of single molecules in the solid state has been demonstrated [14] and single spins in semiconductors can also be controlled coherently [15]. Eventually, there are rather mesoscopic systems that nevertheless exhibit mesoscopic quantum states which behave like single quantum systems. Some examples are superconducting devices [16], nano-mechanical oscillators [17] or surface plasmon polaritons that carry a single quantum of excitation [18].

The NV center The single quantum system studied in this work is the nitrogen-vacancy (NV) center in diamond. It consists of a substitutional nitrogen atom next to a carbon vacancy in the diamond lattice [19]. Single NV centers can be addressed optically because of their high fluorescence yield upon optical excitation [20]. This makes the NV center extremely interesting for the application as a room temperature single photon source [21, 22, 23, 24]. In addition the electronic ground state is a spin triplet with exceptional coherence properties. Intersystem crossing (ISC) enables optically detected magnetic resonance (ODMR) of the electron spin state of a single NV center [20]. More precisely, the electron spin can be initialized into its $m_S = 0$ projection to a very high degree by optical pumping and the fluorescence intensity depends on the spin state even under ambient conditions. At cryogenic temperatures in addition spin selective optical excitations are allowed [25].

These promising features of the NV center in diamond inspired many interesting experiments regarding its applicability for quantum information processing (QIP). At first it could be shown that its electron spin and associated nuclear spins can be controlled in a coherent fashion [26, 27]. In addition to nuclear spins also neighboring electron spins like the one associated with nitrogen impurity atoms in the diamond lattice can

be coupled to the NV center spin in an incoherent [28] or coherent [29, 30] fashion. A deeper analysis of the coupling between electron and nuclear spins at the NV center [31, 32, 33] enabled the storage and retrieval of quantum information in and from a ^{13}C nuclear spin. Last but not least single NV centers can be deliberately created by ion implantation [34, 35].

The present work starts with the above mentioned prerequisites and analyzes how proximal spins around an NV center can be used for QIP. Therefore, naturally occurring as well as artificially created NV centers served the purpose of this work. In addition, especially the diamond host was tailored to our needs by state of the art technology which allowed studying the NV as much decoupled from its environment as possible.

Apart from the storage of quantum information it is demonstrated that a quantum register comprised of the NV electron spin and two neighboring ^{13}C nuclear spins can be used as a small quantum processor. We showed that the full Hilbert space of this three qubit system is accessible which is mandatory for quantum computation. Therefore, we created up to three-partite entangled states with high fidelity [36]. Furthermore, we could show that for quantum states containing mainly nuclear spin coherence the quantum state lifetime is limited by the electron spin flip rate whereas those states which also contain electron spin coherences decay according to the transverse relaxation of the electron spin. This quantum register was used as a test bed for first quantum algorithms in a solid state at room temperature such as super-dense coding or the Deutsch algorithm [37]. Theoretical considerations about the usage of several nuclear spin qubits associated with the NV center are given in [38].

In other solid state qubit systems such as GaAs quantum dots nuclear spins pose a tremendous thread for quantum coherences [39]. In diamond, however, the nuclear spin concentration associated with ^{13}C is comparably low (1.1%) such that other defects like nitrogen cause more decoherence [40, 41]. With the advances in artificial diamond production the concentration of nitrogen and other defects could be reduced such that again the nuclear spins cause the main part of the decoherence. We demonstrated this dependence by investigating isotopically tailored artificial diamond samples [42]. Indeed, the electron spin coherence properties of the NV center improved upon reduction of ^{13}C concentration. In addition we could show that even slightly higher than normal ^{13}C concentration still allow working quantum registers. Therefore, controlled quantum gates in a system of three ^{13}C and one ^{14}N nuclear spin plus the NV electron spin could be achieved with moderate coherence times [42].

With the availability of isotopically enriched ^{12}C diamond samples with reduced nuclear spin density and the accompanied increased coherence properties of the NV center even farther apart spins can be coupled coherently. This way it was possible to create a pair of coupled NV centers [43]. Therefore, arrays of multiple NV centers were created by ion implantation. As this is a probabilistic rather than a deterministic approach we had to search for appropriate NV center pairs. We have located a suitable pair by non-linear

optical imaging techniques [44, 45]. Among the spins of this pair we demonstrated high fidelity two qubit gates which enabled high resolution relative position measurement. In the viewpoint of spin sensing we could achieve a position accuracy of less than one unit cell of the diamond lattice. Although the measured distance of $\approx 10\,\mathrm{nm}$ would be more than enough to entangle the two spins under usual circumstances we could only achieve classical correlations. The reason for this is the extremely short coherence time of one of the two centers. We attribute this to damage of the diamond lattice from the implantation process.

Usually, the NV center spin is manipulated in the electronic ground state because of the much longer lifetime. However, by performing excited state electron paramagnetic resonance (EPR) we observed a peculiarity of the NV center [46]. From low temperature experiments it is known that the excited state comprises of a wealth of levels of different orbital and spin states with energy levels that differ drastically from one NV to another [25, 47]. Surprisingly, at room temperature the orbital structure vanishes and the inhomogeneity is also strongly reduced. Consequently, the excited state spin levels resemble those of the ground state. Particularly, they behave like a single electron spin triplet with a g-factor of a bare electron spin. In addition, the crystal field of the diamond lattice which influences the spin levels is different in ground and excited state. These results were observed in parallel by [48] and in [49] it was argued that the Dynamic Jahn-Teller (DJT) effect is responsible for this behavior.

The exact knowledge about the excited state spin level structure at room temperature was the basis for some new and exciting experiments with proximal nuclear spins. Many experiments with the NV center spins are performed in a setting where electron and nuclear spin levels are far detuned and the nuclear spins hardly affect electron spin states. In that case electron and nuclear spin single qubit and controlled multi-qubit gates can be conducted conveniently. While maintaining this setting for the ground state it is possible to create an electron spin state level anti-crossing in the excited state by proper magnetic field settings. Hence, electron and nuclear spin energies become similar and the hyperfine interaction takes over control of the spin dynamics in the excited state. By optical excitation we can switch between these two regimes. We could show that this allows to efficiently polarize proximal ^{13}C nuclear spins and the nitrogen nuclear spin of the NV center by pumping entropy out of the spin system using the electron spin polarization mechanism [50]. Whereas this polarization mechanism requires only optical pumping we could show that additional controlled quantum gates on the nuclear spins can be employed to enhance the readout efficiency of the electron spin state [51]. Similar work has been reported in [52].

Although spin states of nuclei close to the NV center are usually randomized by prolonged laser illumination [27, 33] it was shown that some part of information survives a few excitation cycles [53]. However, the precise knowledge and control about the spin system in both ground and excited state which was gained in this work led to another interesting observation. It was found that the main mechanism behind laser induced nuclear spin state destruction is hyperfine interaction induced flip-flop between electron

and nuclear spins [54]. To demonstrate the suppression of this effect we chose the nitrogen nuclear spin with its particular hyperfine tensor. Furthermore, electron and nuclear spin levels have been far detuned by a strong magnetic field. Consequently, the nitrogen nuclear spin was well isolated from both the NV center and the environment such that the nuclear spin population could survive many thousands of excitation cycles. This allowed us to perform projective quantum nondemolition (QND) measurements of a single nuclear spin at room temperature. An implication is the visibility of the quantum jumps associated with sudden nuclear spin state changes [54]. We could show that the timescale of these jumps is still limited by hyperfine interaction with the far detuned electron spin of the NV center. In addition it was demonstrated in [55] that not only the population but also quantum coherence survives optical excitation to some degree. Eventually, it is the first time that an NV spin state could be determined in a single shot yielding a binary result for spin up or spin down. This is in contrast to conventional readout where an analog signal needed to be related to an essentially unknown average spin state range. As a result more quantitative spin state measurements can be performed now.

The QND measurement of the nuclear spin has applications such as protection of quantum information or quantum error correction using active feed-forward. In addition, it can be readily applied for drastically enhanced electron spin readout (compare [53]) together with the readout enhancement mentioned above. This has some tremendous impact for example on magnetic field sensing as in [56]. We showed that our quantum register could increase the magnetic field sensitivity up to $\approx 40\,\mathrm{pT\,Hz^{-1/2}}$ for a single sensing electron spin which is an improvement by a factor of 20 (i.e. a 400 times increased measurement speed).

Outlook Up to now it has been demonstrated that single NV centers together with proximal nuclear spins are very versatile small quantum registers allowing to perform small algorithms and to protect quantum information. Further improvement especially regarding the protection of quantum information can be achieved using special ^{13}C nuclear spins that lie on the NV center symmetry axis or ^{13}C dimers [57]. Both species should protect quantum information to a very high degree. In addition a scaling of the quantum register seems to be feasible using arrays of coupled NV centers.

Eventually, it is a challenge to fabricate these registers more or less deterministically. This requires exceptionally pure diamond host crystals and advanced NV creation techniques with nanometer positioning accuracy [58, 59, 60, 61]. Furthermore, it would be of advantage to produce spatially varying magnetic and electric fields on the same length scale for convenient and switchable spin selectivity [60, 62]. For selective readout and initialization optical super-resolution techniques need to be adopted [44, 45, 63, 64].

With the progress of the above mentioned diamond and NV production techniques the storage time of quantum information especially on nuclear spins should exceed seconds whereas controlled quantum gates among an array of NV spins are achievable on

timescales of 10 µs. This ratio of coherence times vs. quantum gate times is very favorable for potential quantum computers.

As the application of the NV center as nano-scale magnetic field sensor is already feasible [65, 66, 67] the first use of an NV quantum register is certainly the improvement of such or similar metrology devices. The proposed use of the NV center for quantum repeater networks [68] also requires a small quantum register that facilitates quantum error correction. In a proof of principle experiment the entanglement of the NV electron spin with an emitted photon has recently been demonstrated [69].

Apart from purely NV diamond based quantum registers also hybrid approaches are currently being discussed. In such quantum processor schemes the advantages of several systems should be combined in a beneficial way. For example NV centers and the associated spins can be coupled to superconducting resonators and qubits [70, 71]. In addition ideas like the coupling of spins by nanomechanical oscillators are discussed [72].

Although this work is concerned with single NV centers the part of this work exploiting the ^{14}N nuclear spin can also be employed in ensemble experiments as almost every NV has its ^{14}N nucleus. For example any bulk magnetometer application would greatly benefit from the readout enhancement enabled by nitrogen nuclear spins [73, 74, 67].

Thesis outline In chapter 1 some basics about quantum computation are briefly introduced before we start with the introduction of the system under study, namely the diamond lattice and the nitrogen-vacancy defect center, and the underlying experimental techniques in chapter 2. Chapter 3 demonstrates the usage of nuclear spins as qubits. Therefore, first of all the coupling to several different nuclei is presented and a method for spin state initialization is introduced. In addition the effect of the nuclear spin bath on the electron spin coherence properties is analyzed. Finally multi-partite entanglement in a spin system comprised of the NV electron spin and two ^{13}C nuclear spins is generated. The next two chapters of this thesis rely on novel knowledge about the excited state spin level structure of the NV center at room temperature which is presented in chapter 4. It enables the effective initialization of proximal nuclear spins around the NV center by optical pumping. The same effect can be utilized to enhance the readout of the electron spin. Eventually, it allows performing QND measurements on a single nuclear spin. The latter three topics are summarized in chapter 5. Finally, in chapter 6 a pair of two proximal NV centers is examined. Their distance is small enough for their magnetic dipolar coupling to prevail over decoherence.

Some conventions used in this thesis along with important physical constants and useful information about diamond and defects in it are shortly summarized in appendix A. The appendix B contains more detailed information about the experimental setup and applied measurement techniques. Especially NV spin related facts are given in appendix C and the Hidden Markov Model used in section 5.3 is explained in appendix D.

Zusammenfassung

Quantenmechanik Die physikalische Theorie der Quantenmechanik führte zu Konsequenzen und Anwendungen, welche die Welt in den letzten hundert Jahren entscheidend beeinflusst haben. Am Anfang standen einige Ungereimtheiten und Paradoxa, welche durch die bis dahin uneingeschränkt gültigen Theorien der klassischen Mechanik sowie des Elektromagnetismus zwar aufgeworfen wurden aber von ihnen nicht erklärt werden konnten, für welche die Quantenmechanik jedoch bestechend einfache Erklärungen hatte. Obwohl die neue Theorie nicht immer intuitiv war, gelang es mit ihr im Laufe der Zeit die Ursachen für viele Prozesse im Mikrokosmos zu finden, was am Ende zu den modernen Theorien zum Beispiele der Atom-, Kern- oder Festkörperphysik führte. Gleichzeitig bereitete die Quantenmechanik den Weg für viele technische Errungenschaften, von denen einige für uns heute alltäglich sind. Sicherlich ist der Laser hierfür ein Paradebeispiel. Bei aller Euphorie ist es uns jedoch bis heute fast unmöglich, die volle Komplexität jedes größeren Quantensystems zu simulieren und daher auch zu verstehen, weil die Komplexität exponentiell mit der Anzahl der Bausteine des Systems wächst. Der Grund für dieses Unvermögen liegt an den begrenzten Möglichkeiten von heutigen konventionellen Computern. David Deutsch drückte dies sinngemäß so aus, dass allein die physikalischen Gesetze, die einem Rechenprozess zugrunde liegen, bestimmen, was dieser Computer berechnen kann und was nicht. Daher kam die Idee auf, die Gesetze der Quantenmechanik zu gebrauchen, um quantenmechanische Systeme selbst zu simulieren, was gelingen könnte, würde man die Komplexität eines gut charakterisierten und kontrollierbaren Quantensystems ausnutzen [1]. Das war die Geburtsstunde des Quantencomputers als theoretisch mögliche Rechenmaschine.

Schnell stellte man fest, dass ein Quantencomputer neben der Simulation von Quantensystemen auch einige andere Rechenaufgaben wesentlich schneller lösen könnte als seine klassischen Gegenspieler [2, 3, 4, 5]. Zusätzlich zur Quanteninformationsverarbeitung in einem Quantencomputer hält die Quantentheorie weitere fundamentale Gesetze bereit, die im Prinzip eine sichere Datenübertragung garantieren können [6].

Der erste kleine Quantenprozessor bestand aus einem großen Ensemble von identischen Molekülen in einer Flüssigkeit, die viele nicht identische Kernspins enthalten, welche die Quantenbits darstellen. In diesem System konnten mithilfe konventioneller Kernspinresonanzverfahren erste Quantenalgorithmen experimentell realisiert werden [7, 8]. Hierfür eignen sich Kernspins deshalb so gut, weil sie sehr schwach mit ihrer Umgebung wechselwirken und deshalb in ihnen gespeicherte Quanteninformation lang genug erhalten bleiben, um Quantenalgorithmen zu demonstrieren. Die schwache Wechselwirkung ist allerdings auch der Grund, warum ein Ensemble benutzt werden muss, um die schwa-

chen Signale überhaupt detektieren zu können. Nach diesen ersten Experimenten kamen allerdings Zweifel auf, ob Ensembles von Kernspins einen skalierbaren Weg bieten um einen größeren Quantencomputer zu implementieren [9]. Heute sieht man die Zukunft des Quantencomputers in einzelnen gut kontrollierbaren Quantensystemen als seine Bausteine.

Einzelne Quantensysteme Die Erforschung von einzelnen gut kontrollierbaren Quantensystemen wird nicht nur im Hinblick auf Anwendungen im Quantencomputing oder der Quantenkommunikation betrieben. Selbst herkömmliche elektronische und optoelektronische Bauteile werden bei fortschreitender Miniaturisierung in die Größenordnung kleiner einzelner Quantensysteme vorstoßen. Auch wenn hier nicht die vollen Quanteneigenschaften benötigt werden wie bei einem Quantencomputer, so wird es doch unumgänglich sein, einzelne Quantensysteme zu adressieren und zu manipulieren. Am Ende können solche kontrollierbaren Quantensysteme die Größe einzelner Atome oder Moleküle haben, was sie besonders interessant für Material- und Biowissenschaften macht, wo sie als einzelne Sensoren mit hoher Ortsauflösung benutzt werden. Hier könnte die Empfindlichkeit des Sensors allerdings schon von der Beeinflussung der Quantenkohärenz des Systems durch die Probe gegeben sein. Die größten Herausforderungen für die Benutzung einzelner Quantensysteme sind zum einen die individuelle Adressierung und die Messung des Quantenzustandes und zum anderen der Schutz der Quantenkohärenz vor unerwünschten Einflüssen aus der Umgebung. Zusätzlich müssen für ein funktionierendes Quantenregister verschiedene Quantensysteme geeignet in Wechselwirkung gebracht werden, ebenfalls ohne dabei Quantenkohärenzen zu beeinträchtigen.

Heute gibt es viele verschiedenartige Systeme, die es erlauben einzelne Quantenzustände von einzelnen Bausteinen zu kontrollieren. Zuerst sind hier einzelne Photonen zu nennen, welche man zum Beispiel durch lineare optische Elemente hinreichend beeinflussen kann [10, 11]. Weiterhin kann man auch einzelne Ionen [12] und Atome [13] heutzutage routiniert fangen, einzeln adressieren und manipulieren. Dies geschieht normalerweise in Vakuum. Auch die Kontrolle von einzelnen Molekülen im Festkörper [14] und die kohärente Manipulation von Spins in Halbleitermaterialien [15] wurden demonstriert. Zusätzlich wird auch an eher mesoskopischen Systemen geforscht, die sich dennoch wie einzelne Quantensysteme verhalten. Zu nennen sind hier supraleitende Bauteile [16], nanomechanische Oszillatoren [17] oder Oberflächenplasmon Polaritonen [18].

Das NV Zentrum Das einzelne Quantensystem, welches in dieser Arbeit studiert wird, ist das so genannte Stickstoff-Fehlstellenzentrum (englisch: NV center) in Diamant. Es besteht aus einem substitutionellen Stickstoffatom (englisch: **n**itrogen) und einer benachbarten Kohlenstofffehlstelle (englisch: **v**acancy) im Diamantgitter [19]. Solch ein einzelnes Defektzentrum kann optisch adressiert werden wegen seiner hohen Fluoreszenzausbeute bei optischer Anregung [20]. Zum einen macht dies das NV Zentrum sehr interessant für die Anwendung als Einzelphotonenquelle bei Raumtemperatur in einem

Festkörper [21, 22, 23, 24], zum anderen besitzt es einen Spintriplet-Grundzustand mit hervorragenden Kohärenzeigenschaften, die sich sehr gut nutzen lassen. So erlaubt die spinabhängige Interkombination (englisch: intersystem crossing (ISC)) die optisch detektierte Spinresonanz am Elektronenspin des NV Zentrums [20]. Genauer gesagt, führt optisches Pumpen des NV Zentrums zur Polarisation des Spins in seinen $m_S = 0$ Zustand und gleichzeitig hängt die Intensität des Fluoreszenzlichts vom Spinzustand ab. Bei tiefen Temperaturen ist es zusätzlich möglich verschiedene Spinzustände in Grund- und Anregungszustand selektiv zu adressieren, was eine zusätzliche Kontrollmöglichkeit bietet [25].

Diese vielversprechenden Eigenschaften des NV Zentrums haben zahlreiche Experimente inspiriert im Hinblick auf eine Anwendung in der Quanteninformationsverarbeitung. Zum einen wurde gezeigt das sowohl der Elektronen- als auch ein Kernspin des NV Zentrums kohärent manipuliert werden können [26, 27], zum anderen können auch Elektronenspins von entfernteren Defektzentren inkohärent [28] oder kohärent [29, 30] in ein potentielles Quantenregister integriert werden. Tiefergehende Analysen der Wechselwirkung des NV Elektronenspins mit nahe gelegenen Kernspins [31, 32, 33] führten zur Demonstration eines kernspinbasierten Quantenspeichers. Zu guter Letzt ist es wichtig, dass man einzelne NV Zentren gezielt durch Ionenimplantation in Diamant herstellen kann [34, 35].

Diese Arbeit beginnt bei den zuvor genannten Grundlagen über NV Spinsysteme und untersucht wie diese für die Quanteninformationsverarbeitung genutzt werden können. Dafür benutzten wir sowohl natürlich vorkommende als auch künstlich hergestellte NV Zentren. Besonderes Augenmerk wurde auf den Diamantkristall als Gastsystem für die NV Zentren gelegt. Die Diamantproben wurden für unsere Zwecke maßgeschneidert, was vor allem für ihre Reinheit in Bezug auf Stickstoff und ^{13}C Kernspins gilt. Somit konnten wir NV Zentren untersuchen, die so gut wie möglich von ihrer Umgebung entkoppelt sind.

Neben der bereits demonstrierten Speicherung von Quantenzuständen in Kernspins haben wir die Anwendbarkeit eines Systems aus dem NV Elektronenspin und zwei zusätzlichen ^{13}C Kernspins als kleinen Quantenprozessor untersucht. Wir haben gezeigt, dass wir den gesamten Hilbert-Raum dieses 3-Quantenbit-Systems ausnutzen können, was notwendig für Quantencomputing ist. Dafür haben wir in diesem System aus drei Spins hochverschränkte Zustände erstellt [36]. Weiterhin konnten wir zeigen, dass Quantenkohärenzen der verschränkten Zustände, welche hauptsächlich Kernspinanteil haben, sehr langlebig sind und am Ende nur durch die Umklapprate des Elektronenspins beschränkt sind. Quantenkohärenzen mit Elektronenspinanteil sind in ihrer Lebensdauer hauptsächlich durch die Kohärenzlebensdauer des einzelnen Elektronenspins begrenzt. Dieses Quantenregister wurde zudem als Testsystem für die ersten einfachen Quantenalgorithmen in einem Festkörpersystem bei Raumtemperatur benutzt. So wurden zum Beispiel der „super-dense coding“ und der Deutsch-Algorithmus implementiert [37]. Ei-

ne theoretische Analyse zur Verwendung mehrerer ^{13}C Kernspins in der Nähe des NV Zentrums ist in [38] gegeben.

In anderen Festkörpersystemen wie zum Beispiel GaAs haben Kernspins einen sehr großen Einfluss auf die Kohärenzzeiten von Elektronenspins [39]. In Diamant hingegen ist die Konzentration der Kernspins allein durch die ^{13}C Kerne gegeben, welche eine viel geringere Konzentration (1,1 %) aufweisen, sodass die Elektronenspins anderer Defekte wie Stickstoff im Diamant einen stärkeren Einfluss haben [40, 41]. Durch Fortschritte in der Diamantherstellung konnte der Einfluss von Defekten so reduziert werden, dass die Kernspins den Haupteinfluss auf die Dekohärenz des NV Spins haben. Die Untersuchung von künstlichen Diamantproben mit unterschiedlichen Isotopenzusammensetzungen konnte dieses Verhalten bestätigen [42]. So haben sich tatsächlich die Kohärenzeigenschaften des NV Elektronenspins verbessert für herabgesetzte ^{13}C Konzentrationen. Zusätzlich konnten wir zeigen, dass sogar etwas höher als normale ^{13}C Konzentrationen immer noch zu nutzbaren Quantenregistern führen können. Dafür wurden kontrollierte Quantenoperationen in einem Register aus vier Kernspins und einem Elektronenspin demonstriert bei moderaten Kohärenzzeiten [42].

Die Verfügbarkeit von künstlichen Diamantproben mit reduziertem Kernspingehalt und der damit verbundenen verbesserten Elektronenspinkohärenzzeit erlaubt es, Spins miteinander zu koppeln, die weiter als sonst voneinander entfernt sind. Auf diesem Wege war es möglich, ein Paar aus magnetisch gekoppelten NV Zentren zu finden und zu untersuchen [43]. Dazu wurde eine künstlich hergestellte und sehr reine Diamantprobe mit Stickstoffionen implantiert. Es gab ein quadratisches Muster aus Implantationsstellen mit jeweils einigen Stickstoffionen. Das ist nötig, da die Herstellung eines NV Paares heute noch sehr zufällig ist und wir deshalb nach dem „richtigen“ NV Paar erst suchen mussten. Dazu wurden nichtlineare super-auflösende optische Techniken verwendet [44, 45]. Zwischen den Elektronenspins des NV Paares konnten wir kontrollierte Quantengatter mit hoher Genauigkeit durchführen. Diese konnten verwendet werden, um die relative Position der beiden NV Zentren zueinander genau auszumessen. Im Hinblick auf bildgebende Anwendungen mit dem NV Zentrum konnten wir bei einem Abstand der Zentren von circa 10 nm eine Positionsgenauigkeit von unter einer Einheitszelle des Diamantgitters erreichen. Obwohl die Wechselwirkung dieser beiden NV Zentren grundsätzlich für deren Verschränkung ausreichen sollte, wenn man die Kohärenzeigenschaften in diesen Diamantproben zugrunde legt, war das bei diesem Paar nicht möglich. Es konnten nur klassische Korrelationen hergestellt werden. Der Grund dafür liegt in den sehr kurzen Kohärenzzeiten eines der NV Zentren. Die Ursache hierfür vermuten wir in Gitterdefekten, welche während der Implantation generiert wurden.

In dieser Arbeit wird der Elektronenspin hauptsächlich im Grundzustand des NV Zentrums manipuliert, was hauptsächlich an der längeren Lebensdauer des Grundzustandes liegt. Wenn man dennoch Elektronenspinresonanz-Experimente im angeregten Zustand des NV Zentrums durchführt, stößt man auf eine Besonderheit [46]. Von Experimenten bei tiefen Temperaturen weiß man, dass der angeregte Zustand aus vielen Unterniveaus besteht, die sich zum einen aus dem Spinmoment- und zum anderen aus dem Bahnmo-

mentfreiheitsgrad ergeben und deren Energie drastisch von NV zu NV schwankt [25, 47]. Überraschenderweise verschwindet die Struktur durch das Bahnmoment bei Raumtemperatur, verbunden mit einer drastischen Verringerung der Inhomogenität. Das führt zu einem Spinresonanzspektrum, welches dem des Grundzustandes ähnelt. Im speziellen weisen beide Spektren einen g-Faktor des freien Elektronenspins auf und beide werden durch das Kristallfeld in gleicher Weise aber verschiedener Stärke beeinflusst. Die gleichen Ergebnisse wurden zur selben Zeit von anderen Forschern demonstriert [48]. Zusätzlich wurde gezeigt, dass der dynamische Jahn-Teller-Effekt (DJT) sehr wahrscheinlich der Grund für das unterschiedliche Spinverhalten bei tiefen und normalen Temperaturen ist [49].

Die neuen Ergebnisse über die Spinzustände des angeregten NV Zentrums bei Raumtemperatur führten zu vielen faszinierenden neuen Experimenten mit benachbarten Kernspins. Viele Experimente werden in einem Regime durchgeführt in dem Elektronen- und Kernspinübergänge weit voneinander entfernt liegen und die Elektronenspinzustände somit kaum von den Kernspins beeinflusst werden. In diesem Regime wurden die in dieser Arbeit vorgestellten Quantengatter problemlos durchgeführt. Während wir dieses Regime im Grundzustand durch ein geeignetes Magnetfeld realisierten, konnten wir gleichzeitig im angeregten Zustand dafür sorgen, dass Elektronen- und Kernspinniveaus einander kreuzen oder abstoßen. Die Abstoßung wird hier durch die Hyperfeinwechselwirkung realisiert, welche hier der vorherrschende Energiebeitrag ist und somit die Spindynamik diktiert. Durch optische Anregung konnten wir nun zwischen diesen beiden Regimen wechseln. Optisches Pumpen an diesem Arbeitspunkt erlaubte es uns, nahegelegene Kernspins (^{14}N ,^{15}N und ^{13}C) zu polarisieren, indem wir mithilfe des Elektronenspins Entropie aus dem Spinsystem gepumpt haben [50]. Während diese Spininitialisierungsmethode allein durch optische Anregung funktioniert, konnten wir weiterhin zeigen, dass durch zusätzliche Anwendung von geeigneten Quantengattern auch die Auslesegenauigkeit des Elektronenspins verbessert werden kann [51]. Ähnliche Experimente wurden in [52] vorgestellt.

Obwohl die Zustände nahegelegener Kernspins sich normalerweise komplett zufällig einstellen nach längerer optischer Anregung des NV Zentrums [27, 33], konnte gezeigt werden, dass unter gewissen Umständen ein kleiner Teil an Information erhalten bleiben kann [53]. Im Gegensatz dazu konnten wir mit dem neuen Wissen über Grund- und Anregungszustand sowie durch präzise Kontrolle der Spinzustände ganz andere Beobachtungen machen. Wir konnten experimentell nachweisen, dass der Prozess hinter der Zerstörung der Kernspinzustände in konventionellen Experimenten die Hyperfeinwechselwirkung zwischen Elektronen- und Kernspin ist, welche Spin-Flip-Flops induziert [54]. Für die Demonstration benutzten wir den Stickstoffkernspin am NV Zentrum mit seinem besonderen Hyperfeintensor. Zusätzlich haben wir ein großes Magnetfeld angelegt, um Elektronen- und Kernspin voneinander zu entkoppeln. Letztendlich war der Stickstoff so gut von seiner Umgebung isoliert, dass die Bevölkerung seiner Zustände viele tausend Anregungszyklen des NV Zentrums überleben konnte. Das erlaubte uns, projektive rückwirkungsfreie quantenmechanische Messungen (englisch: quantum non-

demolition measurement (QND)) des Spinzustandes eines einzelnen Stickstoffkerns bei Raumtemperatur zu machen. Das impliziert die Sichtbarkeit von Quantensprüngen, welche mit der plötzlichen Änderung des Quantenzustandes verbunden sind [54]. Wir konnten nachweisen, dass die Zeitskala auf der diese Sprünge auftreten immer noch durch die Hyperfeinwechselwirkung zwischen den weit verstimmten Elektronen- und Kernspinübergängen bestimmt wird. Zusätzlich konnte gezeigt werden, dass nicht nur die Bevölkerung der Quantenzustände sondern auch Quantenkohärenzen die optische Anregung teilweise überleben [55]. Am Ende, erlaubt diese neue Messmethode zum ersten Mal den NV Spin in einem einzelnen Schuss auszulesen, was binäre Messergebnisse liefert (Spin hoch oder Spin runter) anstatt gemittelte analoge Daten. Das steht im Gegensatz zur herkömmlichen Messmethode, bei der analoge, gemittelte Messergebnisse mit im Prinzip unbekannten gemittelten Spinzuständen korreliert werden mussten. Als Resultat können nun viel quantitativere Messungen des Spinzustandes vorgenommen werden.

Die QND Messung des Kernspins hat unter anderem Anwendungen im Schutz von Quanteninformation vor Zerfall oder bei der Quantenfehlerkorrektur bei der der gemessene Zustand in folgenden Schritten wiederverwendet werden kann. Außerdem kann diese Messmethode ohne weiteres für eine drastische Verbesserung der Elektronenspinzustandsmessung benutzt werden (vgl. [53]), wie auch die Methode die weiter oben bereits genannt wurde. Das hat einen gewaltigen Einfluss zum Beispiel auf solche Magnetfeldmessungen mit dem NV Zentrum, wie sie in [56] gezeigt sind. Wir können zeigen, dass unser Quantenregister bestehend aus einem NV Elektronenspin und dem Stickstoffkernspin in der Lage ist eine Magnetfeldsensitivität von bis zu $\approx 40\,\mathrm{pT\,Hz^{-1/2}}$ zu erreichen. Das entspricht einer Verbesserung um einen Faktor 20 oder einer Verkürzung der Messzeit um den Faktor 400.

Ausblick Bisher konnte gezeigt werden, dass einzelne NV Zentren mit ihren benachbarten Kernspins vielseitige kleine Quantenregister sind, die für erste Quantenalgorithmen und zum Schutz von Quanteninformation benutzt werden können. Weitere Verbesserungen solcher Register können spezielle ^{13}C Atome oder ^{13}C-Dimere [57] beitragen. Spezielle ^{13}C Spins sind solche, die sich entlang der NV Symmetrieachse befinden und daher zu bevorzugende axiale Hyperfeintensoren aufweisen (wie der Stickstoffkernspin). Beide Spezies versprechen besonders in Hinblick auf den Schutz von Quanteninformation enorme Verbesserungen. Zusätzlich zu weiteren Kernspins scheint eine Skalierung des Quantenregisters durch viele magnetisch gekoppelte NV Zentren vielversprechend.

Letztendlich ist es eine Herausforderung solche Register gezielt herzustellen. Das erfordert zum einen Diamanten von sehr hoher Qualität und zum anderen Techniken zum Herstellen von NV Zentren mit hoher Erfolgswahrscheinlichkeit und hoher räumlicher Auflösung [58, 59, 60, 61]. Weiterhin wäre es von Vorteil Elektroden-, Leiterbahnen und Magnetfeldstrukturen in der Nähe der NV Zentren und mit ähnlicher räumlicher Auflösung zu produzieren um eine bequeme NV- und Spinselektivität zu erreichen [60, 62]. Für eine selektive Messung an einzelnen Spins sollten bestehende optische superauflö-

sende Techniken weiterentwickelt werden [44, 45, 63, 64].

Mit dem möglichen Fortschritt der oben genannten Diamant- und NV-Produktionstechniken sollten die Speicherzeiten von Quantenzuständen in den Sekundenbereich rücken, während die Zeiten von kontrollierten Quantengattern im Bereich von etwa 10 µs liegen. Mit diesem Verhältnis von Speicherzeit zu Gatterlaufzeit wird ein Quantenregister aus Spins in Diamant in der Tat für Anwendungen in der Quanteninformationsverarbeitung interessant.

Die erste Anwendung von NV basierten Quantenregistern wird aber sicherlich in der Quantenmetrologie liegen. Da das NV Zentrum schon sehr erfolgreich als Magnet- und Elektrischer Feldsensor eingesetzt wurde [65, 66, 67, 75], wird ein kleines Register von mehreren Spins erst einmal die Aufgabe haben die Sensitivität solcher Sensoren zu verbessern. Die vorgeschlagene Anwendung des NV Zentrums mit benachbarten Kernspins für die Quantenkommunikation [68] scheint auch in greifbarer Ferne. Die dafür benötigte Verschränkung des Elektronenspins mit einem emittierten Photon konnte bereits demonstriert werden [69].

Abgesehen von rein NV basierten Ansätzen für einen Quantencomputer werden zurzeit auch hybride Systeme diskutiert. In solch einem Prozessor sollen die guten Eigenschaften eines jeden Teilsystems in einer vorteilhaften Weise miteinander kombiniert werden. Zum Beispiel wurde bereits die Kopplung zwischen den Spins von NV Zentren mit supraleitenden Resonatoren und Quantenbits gezeigt [70, 71]. Weiterhin werden Ideen durchdacht wie man mehrere Spins mithilfe von nanomechanischen Resonatoren koppeln könnte [72].

Obwohl sich diese Arbeit mit der Untersuchung von Quantenregistern auf Basis einzelner NV Zentren im Diamant beschäftigt, kann man all jene Ergebnisse, welche sich rein auf das NV Zentrum und seinen ^{14}N Kernspins beziehen, auch für Ensembles von NV Zentren anwenden, da auch hier fast jedes NV Zentrum einen ^{14}N Kernspin besitzt. So könnte man die Auslesegenauigkeit eines Ensemble-basierten Magnetometers auch mit den hier vorgestellten Methoden verbessern [73, 74, 67].

Gliederung der Arbeit In Kapitel 1 wird ein kleiner Überblick über den Quantencomputer gegeben bevor in Kapitel 2 das zu studierende System, das NV Zentrum in Diamant, eingeführt wird und grundlegende experimentelle Techniken beschrieben werden. In Kapitel 3 wird gezeigt wie Kernspins als Quantenbits genutzt werden können. Das schließt die Kopplung zu mehreren Spins und deren Initialisierung sowie letztendlich die Verschränkung in einem System aus dem NV Elektronenspin und zwei ^{13}C Kernspins ein. Außerdem wird die Auswirkung des ^{13}C Kernspinbades auf den NV Elektronenspin untersucht. Unsere neuesten Erkenntnisse über Elektronenspinresonanzexperimente im angeregten Zustand des NV Zentrums bei Raumtemperatur sind in Kapitel 4 zusammengefasst. Dieses Wissen ermöglicht eine neuartige Methode zur Kernspininitialisierung und damit verbunden eine Möglichkeit zur verbesserten Elektronenspinmessung. Letztendlich ermöglicht dieses neue Wissen auch, QND Messungen an einem einzelnen Kernspin vorzunehmen. Die drei letzten Themen sind in Kapitel 5 dargestellt. Im letz-

ten Kapitel (6) sind die Experimente am ersten gekoppelten Paar von zwei NV Zentren präsentiert.

Im Anhang A sind einige Konventionen dieser Arbeit sowie nützliche Informationen über Diamant und Defekte und Spins in ihm zusammengefasst. Anhang B enthält detailliertere Angaben zum experimentellen Aufbau und beschreibt einige Messtechniken genauer. Detailliertere Informationen zum Spinsystem des NV Zentrums sind in Anhang C gegeben und das Hidden-Markov-Modell wird in Anhang D erklärt.

1. The quantum computer — A short introduction

During the last decades an ever increasing community of physicists, mathematicians and engineers is participating in the race to build a practical quantum computer. This includes the development of a theoretical framework, the investigation of the actual physical systems that realize the qubits and the fabrication and improvement of the final quantum processor. The current status of quantum computers, the physical systems and technologies involved and potential applications are reviewed in [76]. According to this reference the main systems to date are photons, trapped atoms, nuclear spin ensembles, quantum dots and dopants in solids (including the NV center in diamond) and superconducting devices. However, there are other existing or upcoming technologies and as the final goal seems to be still some way ahead these might render more promising in the future or even completely new ways of building a quantum computer might show up.

A quantum computer unlike a classical one should store, process and transmit "quantum" information. Thus, whereas first computers relied on mechanics or classical physics and even nowadays' information processing can be in principle explained by the same type of operation a quantum computer would exploit quantum features of the corresponding quantum system. This field of computation is so much different from its classical counterpart that the number of algorithms or even software for QIP is sparse. It is in particular this last point that makes it sometimes difficult to convince people of the advantages of a potential quantum computer. Apart from the small number of nowadays quantum algorithms it is still not clear whether a large scale quantum computer will ever be feasible whereas small versions are already available even commercially [77]. In addition, there is the question whether there will ever be something like a personal quantum computer working at room temperature on your desk [78].

In the following, first the special properties of qubits and qubit registers for quantum computing will be explained. Then the requirements for a practical quantum computer are given and finally some applications which can be envisioned today are presented.

1.1. The qubit register

The quantum bit is usually realized in a quantum mechanical two level system (e.g. electron and nuclear spins with $S = 1/2$ or $I = 1/2$ or any two levels which are decoupled

from other existing levels). A pure state of a two level system can be visualized as a point on the so called Bloch sphere (see appendix C.2) where North and South Pole usually represent the eigenstates and all other points are superposition states. Hence, also the state of a qubit can be any point on that sphere as compared to a classical bit which exists only in one of two states ("0" and "1"). If the state of a qubit is measured, however, it will collapse into one of its two eigenstates (i.e. North or South Pole of the Bloch sphere, "0" and "1" respectively) which is then the measurement result and can be identified with the two states of a classical bit. Apparently, a quantum algorithm acting on a qubit can work also with a superposition state as input which in a way is like processing both "0" and "1" at the same time and leads to "quantum parallelism" [2]. This opens up the ability to construct parallel computing algorithms which is nicely demonstrated by the Deutsch-Jozsa-algorithm [3] for example. In general quantum computing is not restricted to quantum bits as smallest carrier of quantum information but can also use d-dimensional quantum systems called qudits (e.g. qutrit as the triplet electron spin system of the NV center). In addition, several qudits can be assembled to form a logical qubit which would allow quantum error correction (QEC) within the logical qubit for example.

Another main resource of qubits arises when moving from one qubit to a register of many qubits. As the superposition state is special for the qubit compared to the classical bit, entanglement is the unique feature of a quantum register compared to a classical one (see section 3.3.3). Using entanglement we are able to exploit the full Hilbert space of a n-qubit register with a dimension of 2^n which is not possible without entanglement. In the former case the logic space can be described by the group $\mathrm{SU}(2^n)$ whereas in the latter case the group $\mathrm{SU}(2)^{\otimes n}$ resembles n independent qubits [76]. A system of n qubits where entanglement is possible can not be emulated by n qubits without entanglement or n classical bits [76] and that is what makes up the power of "quantum parallelism" [2].

Next to the Deutsch-Jozsa-algorithm there are other famous algorithms that would make a quantum computer very useful. One example is Grover's search algorithm which can search unsorted databases quadratically faster than classical algorithms [5]. It has been implemented in NMR spin ensembles [79, 80] and in a register of trapped ion qubits [81]. Last but not least there is the Shor-algorithm for factorizing large numbers in polynomial time as compared to classical algorithms which solve this task in super-polynomial time [4]. As nowadays cryptography schemes rely on the fact that factorization large numbers is far too time-consuming Shor's algorithm can pose a real thread to these schemes if the appropriate quantum computer would be available. This algorithm has been demonstrated for a nuclear spin ensemble based quantum register [8].

1.2. Requirements for a practical quantum processor

Although, nowadays many physical systems can be used as quantum bits no practical quantum computer has been built yet. This is mainly due to the fragility of quantum information and the related lack of ability to achieve large scale entanglement. In 2000 David DiVincenzo has developed a list of requirements which have to be met in order to build a quantum computer and which are often referred to as DiVincenzo criteria [82]. These criteria are:

1. A scalable physical system with well characterized qubits.
2. The ability to initialize the state of the qubits to a simple fiducial state.
3. Long relevant decoherence times, much longer than the gate operation time.
4. A "universal" set of quantum gates.
5. A qubit-specific measurement capability.
6. The ability to inter-convert stationary and flying qubits.
7. The ability faithfully to transmit flying qubits between specified locations.

Requirements 6 and 7 apply mainly to quantum communication. In the following we briefly explain the DiVincenzo criteria.

At first, we need well characterized qubits which we can assemble into a quantum register in a scalable way. Here, the word "scalable" is the crucial part. As the size of the Hilbert space grows exponentially when adding qubits to a system the resources that are needed to build, maintain and operate the system should not grow exponentially in order to retain the advantages of a quantum computer. Resources are typically time, space and energy and contain also the whole infrastructure of the computer or even the creation [76]. After all, the complete Hilbert space has to be accessible (i.e. entanglement is required). In this work we will show that spins associated with the NV center in diamond can be well characterized and that small quantum registers can be build (see sections 2.2, 3 and 6) which also allow the access of the whole Hilbert space (see especially 3.3). In principle, the operation of larger quantum registers of this type should be possible; however, the fabrication of these systems is still under development to date.

The second criterion requires an appropriate initialization mechanism which again should be scalable. The unique features of the NV center allow initializing its electron spin state (see section 2.2.6) and in sections 3.2, 5.1 and 5.3 new methods for the initialization of associated nuclear spin qubits are presented. All of these methods seem to be scalable as the corresponding resources scale linearly in the number of qubits.

To meet the third requirement the quantum system itself should be as well separated as possible from essentially everything. This would allow the quantum state to evolve

in a reproducible and predictable manner. However, nothing is perfect and without any interaction there is also no way to manipulate and read a quantum state. Thus, we have to find a compromise. And finally this compromise should be good enough to let QEC protocols do the rest. It is actually this third criterion which is nowadays the most challenging one. But all above mentioned candidate systems have their own strategy of how to decouple from the environment. Photons are usually well isolated qubits which can be sent over kilometers before losing their quantum information [83, 84]. Trapped atoms or ions are usually isolated in high vacuum held in optical, magnetic or electric traps [12, 85, 86]. Nuclear spins are anyway only weakly interacting with their environment and are therefore possible qubit candidates [87]. Dopants in solids have to be cooled [88] and decoupled from nuclear spins [89, 90] and superconducting devices also have to be cooled for the superconductivity and for a vanishing thermal photon population [91]. The single spins in the NV quantum register usually fulfill the coherence requirement quite well where they can be manipulated with rates in the MHz to GHz range which is much faster than the decoherence rate which is on the order of kHz or slower (see sections 2.2.4 and 3). However, controlled gates used for entanglement are on the order of several ten kHz or 100 kHz which can be in conflict with coherence times (see section 6.4). To improve the ratio between gate speed and decoherence rates we need to engineer the diamond properties (see section 3.1.5), control the creation of the quantum register (see section 6.2) and decouple the quantum information from its environment either by storage in nuclear spin registers or/and by dynamical decoupling (see section 5.3 and appendix C.3).

A universal set of quantum gates includes the ability to create any state of a single qubit by single qubit gates which is straight forward in spin manipulation by the use of resonantly oscillating magnetic fields (radiofrequency (rf) or microwave (mw) fields). But also laser light and static magnetic fields can be used in the case of the NV center (see sections 2.2.3 and 3.2). As mentioned above the resources needed for the gate operations should not scale exponentially with the number of qubits of the system. In addition to single qubit gates a small number of controlled gates needed for entanglement are required. In this work these gates are mediated by the hyperfine and magnetic dipole interaction between the spins (see sections 3.3 and 6.4) but also other schemes are possible which involve photons [68] or coupling to mechanical resonators [72].

Last but not least for a quantum computer we need to selectively measure or readout the qubits. This is possible for the electron as well as for the nuclear spins of a single NV center register (see [26, 27] and sections 2.2.6 and 3.1) where the nuclear spins can also be employed to improve the readout mechanism (see [53] and sections 5.2 and 5.3). For a system of several NV centers, however, new methods are needed as the conventional readout would address several NV centers at once. Storing quantum information on nuclear instead of electron spins only partially solves the issue as still all NV centers contribute noise. Other techniques like selective excitation using patterned illumination like stimulated emission depletion (STED) [44] or frequency selectivity at low temperatures [92] can be applied.

Although this work is mainly attributed to investigate locally confined NV center spin registers there are ideas to build larger quantum networks based on the NV center [68] where spin state dependent optical transitions should be used to create entanglement between distant network nodes for example. In that case associated nuclear spin registers should be used for QEC. One prerequisite for this has been achieved by entangling the state of an emitted photon with that of the NV electron spin [69]. Eventually, it is likely that requirements 6 and 7 which are necessary for long range quantum communication can be realized with the NV center in diamond.

1.3. Applications

The straight forward application of a quantum computer is — according to its name — performing quantum algorithms. Some of the most popular algorithms to date have already been introduced in 1.1. Another related application is the simulation of quantum phenomena in inaccessible systems by an accessible quantum computer as only a quantum computer can efficiently simulate other complex quantum systems [1]. A third field of application is quantum communication where mainly photons are used as "flying" qubits to transmit quantum information over larger distances and at the same time allow secure quantum key distribution [6]. Last but not least quantum computation schemes will certainly play a role in quantum metrology where the susceptibility of quantum systems and in particular cases the high spatial confinement will be exploited to detect environmental influences with unmatched precision and in some cases with ultra-high spatial resolution. It is widely believed that the biggest part of potential quantum computing applications cannot be foreseen nowadays [76].

Concerning the applications mentioned above the NV center in diamond is already used for quantum metrology purposes (e.g. for sensing magnetic and electric fields [66, 65, 75]). Here, the NV center including surrounding spins is a field sensor with a quantum processor directly attached to it. In this work it is shown how the quantum register is used to improve the NV as a field sensor (see section 5.2, 5.3 and appendix C.5) and in [55] further improvements are suggested for larger quantum registers. In addition quantum computational algorithms can further improve metrology applications [93, 94].

Regarding quantum computational tasks the register associated with the NV center is still too small (3 qubits + 2 qutrits [42]). However, the scaling up of the system is promising and some of the routes are demonstrated in this work (see sections 3, 6) and small algorithms are demonstrated in [37, 95]. Ideas in quantum communication were already mentioned [68, 69] and first small simulations have also been performed [96].

Although the NV center in diamond might be capable of comprising a quantum computer on its own, it is also possible that it might be incorporated into a hybrid design where the superior coherence times can be exploited whereas other parts of a hybrid device might be more susceptible to the environment and are therefore faster to manip-

ulate like superconducting resonators and associated qubits [70]. Also the coupling to nano-mechanical resonators is in principle possible [97].

1.4. The Kane Proposal

This section is devoted to a very particular idea of how to build a quantum computer, namely the so called Kane proposal from 1998 [90]. I want to recall it here for two reasons. First of all it is implemented in Silicon which is a solid state system like diamond. Secondly, it is very intriguing because it is based on the already existing well developed silicon technology and should therefore be applicable right away in principle (of course with some technological effort). It is this proposal that makes people really believe in quantum computation as something really achievable.

In the approach of Kane the qubits are realized by nuclear spins of ^{31}P donors in silicon. The register would comprise of an array of these donors where above each donor a so called A-gate is placed and between adjacent donors a so called J-gate is fabricated. The A-gates will tune the individual resonances by distorting the electron spin density at the nuclei whereas the J-gates allow or suppress electron spin mediated spin-spin interaction among two adjacent nuclei. Thus, individual qubits can be deliberately tuned into resonance with a rf field to realize single qubit gates and controlled gates among selective neighboring nuclei can be switched on and off. For the readout of the spin states the nuclear spin state is transferred to the electron spin which is then readout.

Kane lists a few obstacles or requirements on the way to a silicon quantum computer. These are a nuclear spin free silicon lattice, a lattice that lacks other defects, the possibility to accurately place the dopants, precise gates and the reduction of gate induced decoherence. As it turns out, these are almost the same challenges that arise for the NV center in diamond. Neither for diamond nor for silicon these problems could be fixed up to now.

2. Single NV centers in diamond

As this work is focused on the NV color center in diamond and its spin and optical properties this chapter is dedicated first of all to diamond as the host material, second to the NV center more specifically and at last to the main experimental setup for the investigation of single spins in single color centers in diamond.

2.1. Diamond — the host material

Diamond is a very exceptional material with widespread applications. First of all it is certainly the most famous gemstone due to its special optical properties. Apart from that its unsurpassed hardness and thermal conductivity pave the way for various applications such as for grinding and polishing tools as well as for heat sinks. Other upcoming applications are in the field of conventional semiconductors like Si or GaAs. Although diamond is perfectly stable under ambient conditions it is not the stable allotrope of carbon. All of its special properties originate from its lattice properties.

2.1.1. Characteristics

The diamond lattice consists of covalently bond carbon atoms. Each of the four valence electrons of the sp^3-hybridized carbon participates in bonds to neighboring atoms (distance 1.44 Å). This leads to a face-centered cubic (fcc) lattice structure with two-atomic basis where one fcc sub-lattice is shifted against the other one fourth along the space diagonal of the unit cell (lattice constant 3.57 Å, see figure 2.1). The covalent bonds make the diamond very stiff and the completely saturated valence electrons lead to a huge bandgap (5.48 eV). Hence, diamond is a formidable insulator and is optically transparent deep into the UV. It also possesses a large refractive index of 2.42.

In addition, its hardness makes it unlikely for other impurity atoms to enter the lattice, except for boron and nitrogen which are the major lattice impurities. Actually, a small amount of impurities can give diamond specific colors. Boron, for instance, leads to blue diamonds whereas nitrogen colors them yellow and irradiation damaged crystals appear green or brown. An increasing content of NV centers leads first to pink, later to purple and finally to almost black diamonds.

Naturally, diamonds are formed under high pressure and high temperature conditions in the earth crust. This is the stable region of diamond in the phase diagram of carbon.

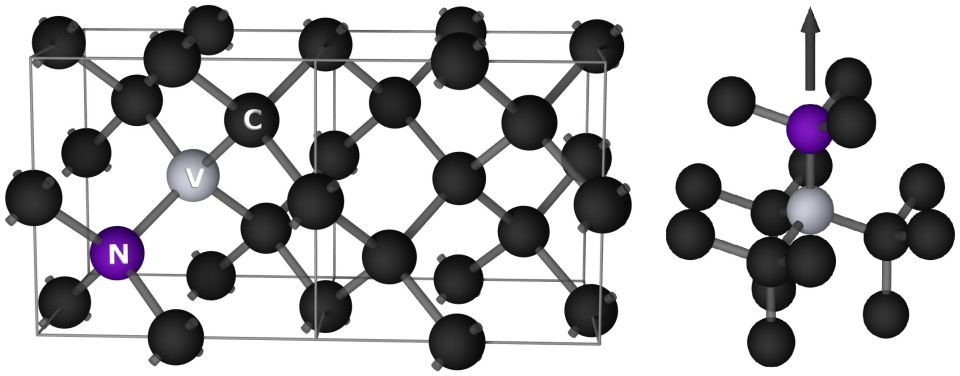

Figure 2.1.: Diamond lattice structure and NV defect center. left, Two unit cells of the diamond lattice where the one contains an NV color center. The unit cell boundaries are $\langle 001 \rangle$ directions. Carbon atoms ("C") are dark gray, the substitutional nitrogen atom is marked with "N" and the vacancy with "V". Lattice relaxation due to the NV center is neglected. **right,** NV center and two shells of nearest neighbor carbon atoms around the vacancy. The c_{3v} symmetry axis or NV axis is pointing upwards (dark arrow) and coincides with the $\langle 111 \rangle$ direction of the diamond lattice.

Most of the artificially created diamonds are also generated by applying high temperatures and pressures but with the addition of catalysts. These diamonds are therefore called high pressure high temperature (hpht) diamonds. A second way is chemical vapor deposition (CVD) (more specifically microwave plasma assisted CVD). As most of the diamonds used in this work are CVD diamonds we explain this technique is explained in more detail below.

The CVD diamond growth is a homoepitaxial technique (i.e. one needs a diamond surface as a seed layer) and the process is described according to [98, 99]. Often, a [001] surface orientation is chosen as a seed layer because less defects are created during growth [100, 101, 102]. The seed crystal is put into a plasma growth chamber on a heater which holds the diamond at around 800 °C at a pressure of ~ 30 mbar. Above the diamond a plasma of hydrogen mixed with methane ($0.5 - 5\,\%$) is created by microwave radiation of several hundred Watts at ~ 2 GHz. The plasma is fed by a constant stream of new gas at a rate of several hundred standard cubic centimeters per minute. The gas for the plasma can also contain argon [98] or the hydrogen part can be replaced by deuterium which drastically increases sample quality [99]. The hydrogen or deuterium in the plasma is converted to highly reactive atomic H or D which etches particularly non-diamond bonded material and graphite and can also etch diamond layer by layer. Most importantly it creates dangling bonds of the carbon atoms by breaking the bonds of the reconstructed surface. When methane is added to the plasma it can be converted to CH_3 or CD_3 which is also reactive and its carbon atom can bind to the dangling bonds of the carbon atoms of the diamond surface. This way the diamond grows layer by layer due to addition of carbon atoms from the methane. The quality of the gas mixture can

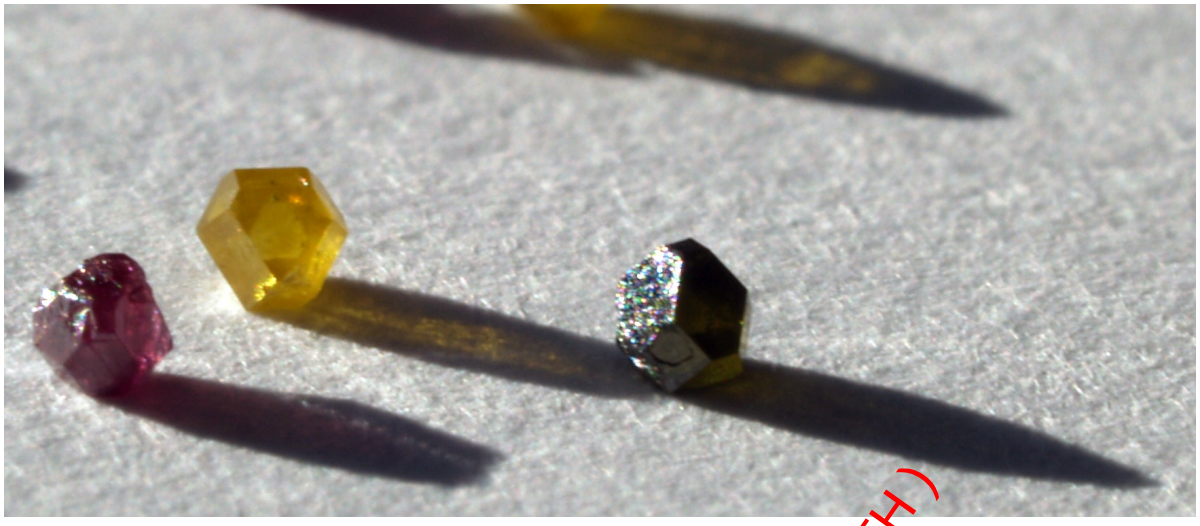

Figure 2.2.: Colored diamonds with different defects. Micrometer sized diamonds with different defects after different preparation steps. The yellow diamond contains large amounts of substitutional nitrogen ($\ll 1$ ppm). The green diamond is an electron irradiated version of the yellow one (i.e. it contains many vacancies). After annealing the green diamonds the violet ones appear due to the creation of NV centers.

be controlled to a very high degree such that the purity of the diamond crystal is also very high. Particularly, the nitrogen content of the final CVD diamond can be lowered below 1 ppb (i.e. 176 nitrogen atoms per µm³ or an average nitrogen-nitrogen distance of 178 nm, compare appendix A). With the control of the growth speed it is possible to reduce structural defects in the diamond lattice. In addition to the reduction of the nitrogen content during growth also the isotropic composition of the used carbon can be controlled such that diamonds with ^{12}C concentrations down to 99.99 % were produced for this work. On the other end of this scale hpht diamonds with 100 % ^{13}C have been produced. In this work natural as well as artificial hpht and CVD diamonds with various ^{12}C contents are used.

2.1.2. Lattice defects

Although diamond has a very stiff lattice there are many known defects existing and it is out of the scope of this work to name all of them. First of all we only concentrate on point defects. Of these only the very prominent ones and those related to the present work are shortly introduced. Since we are interested in the optical and spin properties of the NV center we are concerned about optical and spin properties of other defects as well.

The most trivial intrinsic defect is the vacancy where a single carbon atom in the lattice is missing. It can act as electron donor as well as acceptor and can thus be

type	N content	sub-type	feature	[N] in ppm
I	high	Ia	aggregates of N	< 3000
		Ib	single substitutional N	< 500
II	low	IIa	very low N content	$<\sim 1$
		IIb	significant boron content $\rightarrow$ p-type semiconductor	$<\sim 1$

Table 2.1.: Types of diamond regarding their most abundant impurities (N, B). Additional sub-types exist for type Ia [105].

paramagnetic ($S = 1/2$ and $S = 3/2$ for positively and negatively charged vacancy [103]). In addition it is weakly optically active [19, 103] and colors diamond green (see figure 2.2). Vacancies in the diamond lattice become mobile above $\approx 600\,^{\circ}\mathrm{C}$ [19]. On their way through the lattice they can form multi-vacancy complexes that are immobile or they can be trapped by other lattice defects (e.g. by nitrogen [19]). Multi-vacancies can be paramagnetic and give the diamond a brown color in high concentrations. One possible way of producing vacancies is the irradiation with particles such as high energy ions or electrons [103]. This is also true for carbon interstitial related defects where one or more carbon atoms are displaced from their lattice position (e.g. due to more than one atom per lattice site). These are also optically active and paramagnetic.

Apart from these intrinsic defects diamond can contain other atoms such as nitrogen or boron. Both have roughly the same size as carbon and thus fit well into the lattice. However, they have either one electron more or less than carbon (i.e. they act as donor or acceptor respectively). Usually nitrogen is much more abundant in diamond than boron. This holds for natural as well as artificially created diamonds. Nitrogen is a paramagnetic defect and due to its high abundance well studied. Especially in natural diamond samples defects comprised of aggregates of nitrogen atoms can be found because over the ages nitrogen migrated through the lattice until less mobile nitrogen clusters were formed. These can be paramagnetic as well. In fact, diamonds can be categorized mainly according to their impurity contents of nitrogen and boron [104, 105] (see table 2.1).

Apart from the above mentioned lattice defects some kind of inhomogeneity arises from the isotropic composition. Mostly carbon is present as $^{12}\mathrm{C}$ (98.9%) and seldom as $^{13}\mathrm{C}$. In contrast to the first the latter contains a nuclear spin of $I = 1/2$ which influences the electron spin of the NV center.

2.2. The NV-center

The NV center is formed by two lattice defects that were already introduced in the previous section, namely a nitrogen atom and a vacancy [19, 106, 107]. It is both strongly optically active and paramagnetic. Hence it has been identified by optical and spin resonance experiments on diamond samples containing large ensembles of various defects. In optical studies it was referred to as 1.945 eV vibronic band which mainly appears in type Ib diamonds after creation of radiation damage and subsequent heat treatment [19]. As type Ib diamond contains single substitutional nitrogen impurities and radiation creates vacancies that become mobile at elevated temperatures Davies and Hamer suggested a single nitrogen atom and a vacancy as constituents. Further optical studies under uniaxial stress revealed the NV center to have trigonal symmetry with an optical excitation between electronic levels exhibiting E and A_1 symmetry. Summarizing, Davies and Hamer suggested nowadays structure of the NV center [19]. In former days' EPR studies the negatively charged NV center has been called W15 center [107]. It is a spin triplet defect with a spin level splitting of ≈ 2.88 GHz at zero magnetic field due to the crystal field. It was realized that optical excitation leads to an increased EPR signal which is attributed to intersystem crossing (ISC) between singlet and triplet levels. However, a metastable triplet and singlet ground and excited states were proposed those days. By spectral hole burning experiments using one laser for hole burning and one to scan across the persistent hole Reddy, Manson and Krausz revealed the 2.88 GHz feature known from EPR which was unexpected for singlet ground and excited states. They proposed the model of triplet ground and excited states and a singlet metastable state which is nowadays accepted [108].

In the following the exact structure and abundance of NV centers is given as well as methods for NV center fabrication. Furthermore the electronic, spin and optical properties of the NV center are introduced in detail. In a separate section the suitability of the NV center spin as a qubit is pointed out by summarizing its properties and by explaining in detail how the electron spin is polarized on the one hand and how its state can be read out optically on the other hand.

2.2.1. Structure

The nitrogen-vacancy center in diamond consists of a substitutional nitrogen atom with a carbon vacancy on an adjacent lattice site (see figure 2.1). The defect exhibits a c_{3v} symmetry where the nitrogen and the vacancy form the symmetry axis which is often referred to as NV axis in this work. Apparently, the NV axis coincides with $\langle 111 \rangle$ directions of the diamond lattice. As there are four of distinct [111] directions there are also four different NV center orientations.[1] Symmetry and structure of the NV center

[1] Spin as well as optical properties do not depend on the order of nitrogen and vacancy along a certain [111] axis.

determine the electronic properties of the NV center which in turn influence the spin and optical properties.

2.2.2. NV center generation

Single NV centers are usually found in any natural diamond sample [20] because nitrogen as a major impurity in diamond is always present and over the ages vacancies migrated to some of these nitrogen atoms forming NV centers. Also in CVD and hpht diamonds NV centers are present because of their formation during the growth process. For ultrahigh purity diamond samples, however, there might be only a single NV center within $10^4\,\mu m^3$.

In samples with high nitrogen content the amount of NV centers can be increased by creation of vacancies. One method to achieve that goal is high energy electron irradiation of diamond samples which creates a homogeneous density of vacancies over several µm depth. At temperatures above 600°C the vacancies start to become mobile whereas the nitrogen atoms stay at their lattice site. Therefore, vacancies migrate to nitrogen impurities forming NV centers when the diamond sample is annealed at such temperatures usually for several hours [19]. It has been shown that this a versatile method to create a high density of NV centers in nitrogen rich diamond which is especially useful for NV production in nanodiamonds [109]. When ions are implanted the vacancies are created very locally. As a consequence it is possible to implant nitrogen ions into low nitrogen content diamond to introduce nitrogen atoms and vacancies locally confined. It was shown that the implanted nitrogen ions and the hereby created vacancies indeed form NV centers upon annealing [85] but that also intrinsic nitrogen atoms can be converted into NV centers by the produced vacancies [34].

Usually the yield of NV center creation decreases when the ion implantation energy is decreased from ∼ MeV down to a few keV [29] because the amount of created vacancies is reduced. In addition also the implantation depth decreases from ∼ µm down to a few nm. Therefore the surface is very close and created vacancies more easily heal out before they are trapped by the nitrogen atom. In these cases additional vacancies can be created by subsequent carbon ion implantation at the right depth [59].

2.2.3. Electronic and optical properties

Electronic structure

The electronic structure of the NV center is mainly governed by the dangling bonds of the three carbon atoms and the one nitrogen atom surrounding the vacancy [110, 111]. Thus, the overall number of electronic states is 8. Given the number of electrons in the dangling bonds the neutral NV center (NV^0) possesses 5 electrons and an electron spin of $S = 1/2$. Depending on the Fermi level in the diamond lattice either the neutral or the negative charge state is the dominating one [112, 113]. There are also cases where

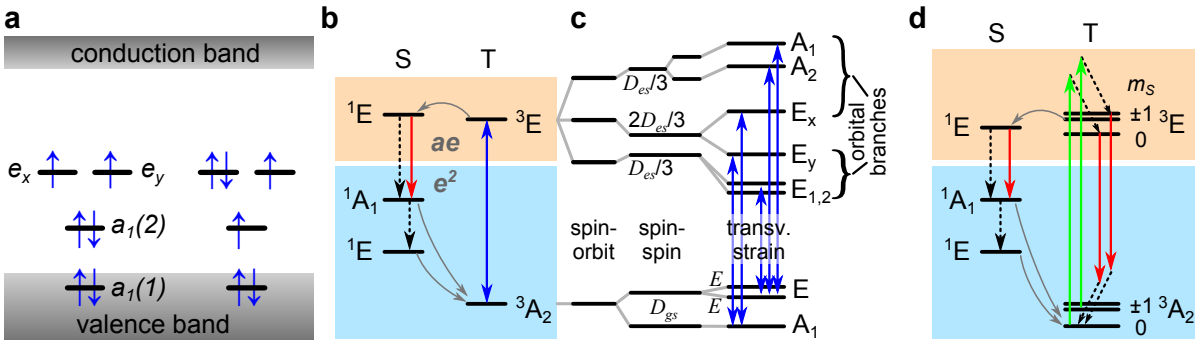

Figure 2.3.: Electronic structure of the NV center. a, Electronic levels of the NV center within the bandgap of diamond [119, 111]. Left and right are electronic ground and first excited state configuration respectively. **b,** From the electronic levels singlet (S) and triplet (T) states are formed (names according to symmetry properties). The blue shaded region contains the electronic ground and the orange shaded region the excited states. Optical transitions are shown as blue arrows, ISC as gray arrows and non-radiative decay as dashed arrows [120, 121]. **c,** Triplet level structures depending on interactions [47]. Most important in this work are $D_{ss,gs}$ and E parameters which are mainly due to spin-spin interaction. **d,** Level structure as it appears at room temperature. Non-resonant optical excitation into the phonon sidebands is illustrated by green arrows. Fluorescence (red arrows) also ends up most likely in the phonon sidebands. ISC is strongly spin state dependent.

the NV center can change its charge state emitting either NV^0 or NV^- fluorescence [114, 115]. However, in the samples investigated in this work, the negatively charged NV center (NV^-) possessing 6 electrons and an electron spin of $S = 1$ in the ground state is much more abundant. In the following we will concentrate exclusively on the negatively charged NV center and therefore the "$-$" sign is omitted in the rest of this work.

Deducing the electronic configurations of ground and excited states can be done using either a 6 electron model [110, 116, 117] or a two hole model [118]. Group theoretical approaches arrive at the single electron level scheme displayed in figure 2.3a where the lower two states ($a_1(1)$, $a_1(2)$) of a_1 symmetry are fully occupied in the ground state. The highest two states are degenerate and form a pair (e_x, e_y) of e symmetry. In the ground state the remaining electrons or the two holes occupy the two e states and form an antisymmetric orbital. Thus the electron spins form a triplet (i.e. $S = 1$, see figure 2.3). The corresponding spin singlet states (i.e. $S = 0$) for the three symmetric orbital wavefunctions are lying higher in energy ([122, 123, 120, 74]).

Concentrating on the triplet system we can give a general Hamiltonian summarizing the interactions that influence the energy levels in ground and excited state [47] (compare figure 2.3c):

$$\hat{H} = \hat{H}_{so} + \hat{H}_{ss} + \hat{H}_{str} \ . \tag{2.1}$$

Here, the first and the largest interaction (at least in the excited state) is spin orbit interaction $\hat{H}_{so}$, followed by spin-spin interaction $\hat{H}_{ss}$ (see section 2.2.4) and finally

strain $\hat{H}_{str}$.

The first excited state lies 1.945 eV above the ground state [19] and is reached when one hole is promoted from the e states to the $a_1(2)$ state. Again there are singlet and triplet states (see figure 2.3b,c). The triplet system experiences spin orbit coupling as the major energy contribution that shifts the energy levels. However, there are two levels with defined spin projection, namely E_x and E_y with $m_S = 0$ [47]. Thus, these levels are not shifted by spin-orbit coupling. For the remaining levels the spin projection m_S is not a good quantum number. Apart from spin-orbit coupling spin-spin interactions shift the energy levels (see section 2.2.4). The triplet system can split up into two orbital branches each containing 3 states if the symmetry of the NV center is broken (e.g. by transverse strain or electric fields). In addition to the triplet system there are two orbital states that form spin singlets.

The spin density of the NV center has been modeled for the ground and excited state in [111, 124]. It could be shown that in the ground state the major part of the spin density is located at the first shell carbon atoms and almost no spin density is found at the nitrogen [125]. Actually, the spin density at the nitrogen atom is even slightly negative. Some spin density is found roughly in the plane perpendicular to the NV axis reaching out up to 5 Å [111]. In the excited state of the NV center, however, a substantial amount of spin density is found at the nitrogen atom. The simulations show that the positions of the carbon and nitrogen atoms around the vacancy change upon excitation [111, 124].

Optical properties

At cryogenic temperatures optical transitions from the triplet ground to the triplet excited state are narrower than the spacing of the sublevels shown in figure 2.3c. Therefore, individual transitions from ground state spin levels to excited state orbital and spin sublevels can be addressed selectively [25]. There are two possible transition dipoles associated with the excitation of one hole from either e_x or e_y to the $a_1(2)$ level which are both perpendicular to the NV axis and perpendicular on each other. Thus excitation with a laser beam along the NV axis is most efficient. Upon relaxation into the ground state photons can be emitted with a rate of $\approx 1/12\,\mathrm{ns}^{-1}$. The part of the photons that is emitted into the zero-phonon line (ZPL) is about 4 %, the remaining photons relax into the phonon sidebands that stretch from 637 nm up to $\approx$ 750 nm with a maximum at around 680 nm [21] and are therefore red shifted. This enables resonant optical excitation spectroscopy where the signal is the red-shifted fluorescence light. In contrast to studies on ensembles of NV centers which exhibit an inhomogeneous optical linewidth of several GHz [25] the linewidth of single NV centers is in the MHz range. Actually, the optical linewidth is only limited by the excited state lifetime [126]. This allows to selectively address spin conserving vertical transitions as well as excitations in Λ-type systems where two distinct levels in the ground state can be optically coupled to the same excited state level [127, 128].

The broad linewidth of the ensemble studies originates from the huge variation of the local strain and electric fields from one NV to another. This is perfectly verified when investigating several single NV centers. The reduced symmetry that shifts the optical transition frequencies can be compensated by applying external electric fields to shift optical resonance lines of individual NV centers into resonance [92].

In addition to resonant excitation the NV center can also be excited at shorter wavelength to induce transitions into the excited state phonon sidebands (see figure 2.3d). This excitation mechanism is commonly used at room temperature. Due to the availability usually 532 nm laser light is used for optical excitation. Under ambient conditions the ZPL is severely broadened to a width of several nm. Hence, spin state selective optical excitation is not possible. To detect single NV centers usually the whole red shifted fluorescence intensity I_{PL} is detected.

So far, only radiative decay to the ground state has been discussed and we have concentrated on the triplet system. However, the spin-orbit coupling leads to ISC (see figure 2.3b,d). Thus, in the excited state the NV center can switch into the singlet system. Up to now, it is under debate which way the NV takes to reach the final triplet ground state and what the order of the singlet energy levels is. There are strong hints for a transition from the triplet excited state into the singlet ^1E excited state [120, 74] (see figure 2.3b,d). From there the NV relaxes most likely via non-radiative decay into the $^1A_1$ state and much less likely via emission of an infrared photon [120]. Finally, the NV returns into the triplet ground state either directly via ISC from $^1A_1$ into the $^3A_2$ states or via the ^1E singlet state [121]. Electron-vibration interaction is supposed to play a major role in this process [121]. The ^1E or the $^1A_1$ ground states appear to be metastable because the whole trip from the excited into the ground state via the singlet system takes ≈ 250 ns [122] and the lifetime of the ^1E excited state has been measured to be < 1 ns [74].

As it turns out ISC is strongly spin state dependent ([106, 129, 130]). This leads to one of the main exotic properties of the NV center, namely optical spin polarization and optical spin readout [131] which is explained in detail in section 2.2.6. More specifically, from the triplet excited states E_x and E_y with spin projection $m_S = 0$ intersystem crossing is suppressed and mainly radiative decay to the ground state occurs whereas for the other triplet excited states the intersystem crossing rate is comparable to the radiative decay rate. Therefore, the lifetime of the excited states with $m_S \neq 0$ is shorter than for those with $m_S = 0$. After a passage through the singlet system the NV center finally relaxes back into the triplet ground state but preferably into the $m_S = 0$ sublevel. This step happens with very high fidelity [129, 130, 132]. Optical spin polarization and readout works at cryogenic as well as at room temperature.

Due to the spin-dependent ISC the fluorescence lifetimes are spin-dependent as well. For $m_S = 0$ the lifetime is ≈ 12 ns and for $m_S = \pm 1$ it is ≈ 7.8 ns [126].[2] The observed fluorescence count rates upon continuous optical excitation are much smaller than an-

[2] The stated lifetimes apply to NV centers in bulk diamond. For nanodiamonds, however, lifetimes are usually higher due to the reduced optical mode density.

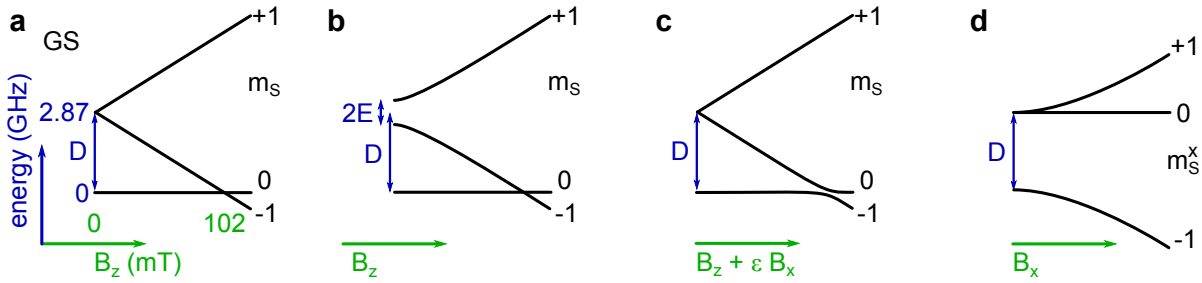

Figure 2.4.: Electron spin energy levels for various magnetic fields. a, Electron spin levels of the NV center in the ground state (GS) for the main setting throughout this work. That is a ZFS parameter $E \approx 0$ and the magnetic field is parallel to the NV axis. Therefore, m_S is always a good quantum number. **b,** Same condition as before but with $E \neq 0$. For eZ$\gg E$ m_S is a good quantum number otherwise $m_S = \pm$ form new eigenstates. **c,** Energy levels for $E \approx 0$ and a slightly misaligned magnetic field which leads to a level anti-crossing in the ground state (gsLAC) at $\approx 102\,\mathrm{mT}$. **d,** Energy levels for $E \approx 0$ and magnetic field aligned perpendicular to the NV axis (e.g. along x). In the high field regime (eZ$\gg D$) m_S^x with respect to the new quantization axis x is a good quantum number.

ticipated from the excited state lifetimes. This is mainly due to shelving some part of the population into the metastable singlet state (life time of $\approx 250\,\mathrm{ns}$). In addition, recently a dark state has been unraveled where the NV center is partially pumped by green excitation [132].

2.2.4. Spin properties

As pointed out in the previous section the ground state is a spin triplet without spin orbit coupling. Thus the main influences on the electron spins are spin-spin interaction and electron Zeeman shift [106, 107] (see figure 2.3c).[3]

The general spin Hamiltonian $\hat{H}$ for a triplet system will be given in the basis $m_S = +1, 0, -1$ where m_S is the spin quantization along the z-direction [133, 134]. In this work usually the z-direction coincides with the NV axis.

$$\begin{aligned}\hat{H} &= \underbrace{D_x\hat{S}_x^2 + D_y\hat{S}_y^2 + D_z\hat{S}_z^2}_{\text{ZFS}} - \underbrace{\tilde{\gamma}_e \underline{B}\cdot\underline{\hat{S}}}_{\text{eZ}} \\ &= \begin{pmatrix} D/3 & 0 & E \\ 0 & -2D/3 & 0 \\ E & 0 & D/3 \end{pmatrix} - \tilde{\gamma}_e \begin{pmatrix} B_z & \frac{B_x - iB_y}{\sqrt{2}} & 0 \\ \frac{B_x + iB_y}{\sqrt{2}} & 0 & \frac{B_x - iB_y}{\sqrt{2}} \\ 0 & \frac{B_x + iB_y}{\sqrt{2}} & -B_z \end{pmatrix}\end{aligned} \tag{2.2}$$

The first term in the Hamiltonian eq. (2.2) is the zerofield splitting (ZFS) tensor $\mathbf{D}$. As the name suggests it leads to a level splitting even in the absence of an external magnetic

[3] the hyperfine interaction to proximal nuclear spins will be introduced in chapter 3.

field. The reason for this is the magnetic dipole interaction of the two unpaired electron spins forming $S = 1$ [133]. Any deviation from a spherical spin density leads to this splitting. In the NV center the main deviation occurs along the NV axis as compared to transverse directions which leads to $D_z \neq D_{x,y}$. In case of a distortion of the c_{3v} symmetry also $D_x \neq D_y$; otherwise $D_x = D_y$. Tensor $\mathbf{D}$ is traceless such that $D_{x,y,z}$ can be replaced by

$$D = \frac{3}{2} D_z \tag{2.3a}$$

$$E = \frac{D_x - D_y}{2} \ . \tag{2.3b}$$

Usually $E \approx 0$ as compared to $D = 2870\,\mathrm{MHz}$ [135]. The sign of D is positive [129] which is consistent with a more disk-like shape of the spin density (see section 2.2.3) as compared to a rod-like shape [136]. Transverse electric fields [137, 75] and transverse strain [138] lead to $E \neq 0$ (see figure 2.4b and appendix C.1). Usually, the observed values of E are below a few MHz for bulk diamond samples (see figure 2.4a) whereas they can go up to several tens of MHz for NV centers in nanodiamonds where strain is often particularly high (see figures 2.4b and 4.2b). The second term in equation eq. (2.2) is the electron Zeeman (eZ) energy where $B_{x,y,z}$ are the respective magnetic field components and $\tilde{\gamma}_e = g_e\,\mu_B/h$ is the gyromagnetic moment of the NV electron spin devided by 2π with the NV spin g-factor $g_e = 2.0028$ [107], the Bohr magneton μ_B and the Planck constant h. The Hamiltonian delivers eigenenergies in units of frequencies. For more details about the spin Hamiltonian see table A.3 in appendix A.

In many parts of this work the magnetic field is aligned along the NV axis and the E parameter of the ZFS is negligible which leads to a diagonal Hamiltonian in the current basis (see eq. (2.2) and figure 2.4a). Usually we shift the Hamiltonian upwards in energy by the amount $2D/3$ such that it reads

$$\hat{H} = D\hat{S}_z^2 - \tilde{\gamma}_e\, B_z \hat{S}_z \ . \tag{2.4}$$

Magnetic fields which are misaligned from the parallel orientation lead to mixing of the former m_S levels into new eigenstates (see figures 2.4c,d).

Spin transitions are driven by an oscillating magnetic field $B_1(t)$ which is applied using microwave (mw) radiation. Usually these fields are linearly polarized and the strength is low enough to concentrate only on the transverse part $B_{1x}(t)$. The corresponding time dependent Hamiltonian $\hat{H}_1$ reads as follows

$$\begin{aligned} \hat{H}_1 &= \underbrace{-\tilde{\gamma}_e \overbrace{B_{1x}^0 \cos(\omega t)}^{B_{1x}(t)}}_{\Omega_x} \hat{S}_x \\ &= \frac{1}{\sqrt{2}} \left[\Omega_+ \begin{pmatrix} 0 & e^{-i\omega t} & 0 \\ e^{i\omega t} & 0 & e^{-i\omega t} \\ 0 & e^{i\omega t} & 0 \end{pmatrix} + \Omega_- \begin{pmatrix} 0 & e^{i\omega t} & 0 \\ e^{-i\omega t} & 0 & e^{i\omega t} \\ 0 & e^{-i\omega t} & 0 \end{pmatrix} \right] \end{aligned} \tag{2.5}$$

where the linearly polarized field of strength Ω_x has been replaced by the sum of two counter-rotating circularly polarized fields with strengths $\Omega_+ = \Omega_- = \Omega_x/2$. After changing into the rotating frame[4] and applying the rotating wave approximation eq. (2.4) changes to

$$\hat{H}_I = \begin{pmatrix} \Delta_+ & \frac{\Omega_+}{\sqrt{2}} & 0 \\ \frac{\Omega_+}{\sqrt{2}} & 0 & \frac{\Omega_-}{\sqrt{2}} \\ 0 & \frac{\Omega_-}{\sqrt{2}} & \Delta_- \end{pmatrix} \tag{2.6}$$

where $\Delta_\pm = D \mp \tilde{\gamma}_e B_z - \nu$ is the detuning of mw frequency ν from the respective resonance. Hence, Rabi oscillations between different spin projections $m_S = 0 \leftrightarrow -1$ and $0 \leftrightarrow +1$ are driven by transverse circularly polarized mw fields.[5] For misaligned magnetic fields the situations changes (see appendix C.1). The corresponding evolution of the spin state can be visualized on the Bloch sphere (see appendix C.2). The Rabi frequencies achieved in the current setup go up to several 100 MHz (see section 2.3).

Among the excited state triplets there are only two states with a defined electron spin projection; these are E_X and E_Y with no spin-orbit shift where $m_S = 0$. The other states exhibit large spin-orbit coupling such that m_S is not a good quantum number anymore. However, as it will turn out in chapter 4 at room temperature the spin-orbit coupling averages out so fast that an effective spin Hamiltonian similar to eq. (2.2) without spin-orbit coupling can describe the system.

The electron spin state of the NV center in diamond is mainly affected by magnetic fields that originate from either external fields or fields generated in the diamond itself (e.g. by other electron or nuclear spins). Surprisingly this effect inside the diamond lattice is very weak even at room temperature such that the longitudinal electron spin relaxation time T_1 is up to several tens of milliseconds [32]. The other two sources of magnetic fields can be controlled very well in diamond such that coherent superpositions of NV electron spin states possess a very long coherence time of up to a few milliseconds [56] (see section 3.1.5). The way how coherence lifetimes are measured is explained in section 2.3 and appendix C.3.

2.2.5. Coupling to phonons

Here, I want to quickly review how optical and spin properties are affected by vibrations of the diamond lattice and of atoms comprising the NV center point defect. As pointed out earlier the diamond lattice is exceptionally stiff due to the covalent bonds. This reflects in a very high Debye temperature of 1860 K [139]. Therefore, at room temperature the amount of phonon excitations is low and their effect on defect centers is smaller than in most other host crystals. The less phonons are present in the crystal the less phonons

[4] The transformation U into the rotating frame was done using $U = \exp(i\omega \hat{S}_z^2 t)$ to account for the ZFS which is usually the strongest part of the Hamiltonian.

[5] At cryogenic temperatures the effect of electromagnetically induced transparency (EIT) can be used to manipulate spin states by laser fields [128].

can couple to localized vibration modes at the defect center. Local vibration modes would affect the wave function of the electrons making up the electronic configuration of the defect center. On the other hand changes of the electronic state by optical excitation can change inter-atomic distances and therefore excite vibrations [124, 140].

Especially for the electron spin coherence properties it is of importance that no oscillating magnetic fields around the Larmor frequency are generated by vibrations in the lattice or by local vibrational modes as this would lead to longitudinal relaxation accompanied by transverse relaxation. In addition vibrations could couple via spin-orbit coupling to the spin states and lead to spin flips or changes of the Larmor frequency. Finally, in the case of the NV center the singlet ground state is far detuned such that the ISC rate is small which is beneficial for the longitudinal relaxation time T_1. For the NV center it turns out that all these processes are negligible leading to exceptional coherence properties and a long T_1 time.

As mentioned above optical excitation and relaxation of the NV center is accompanied by a change of the atomic distances with the defect. This leads to the excitation of phonons and hence the excitation and emission spectra a severely broadened. In addition the ratio of light emitted into the zero-phonon line is very small compared to that emitted into the phonon sidebands. This manifests in a Debye-Waller-factor of 0.04 which is typical for light impurity atoms associated to vacancies; in contrast, many other color centers in diamond containing heavier atoms show a much stronger ZPL [141, 142].

Recently, it has been considered that electron-vibration interaction in the NV center might play a crucial role for the optical electron spin polarization process [121].

2.2.6. Optical spin polarization and readout

Here, the previously mentioned mechanism for the optical spin polarization and readout is explained in more detail.

To begin with, we start with the spin state initialization procedure. As can be seen in figure 2.5a spin state $m_S = 0$ has a very low probability to perform intersystem crossing in the excited state and thus leads to cycling optical transitions upon optical pumping whereas $m_S = \pm 1$ states have roughly an equal probability for radiative decay and intersystem crossing from the excited state. Once the NV is in its metastable state, however, the decay back into the triplet ground state occurs preferentially into the $m_S = 0$ state with high fidelity [129]. Hence, the spin state will eventually be $m_S = 0$ after optical pumping regardless of its former state. This spin state remains until the spin is either flipped by purpose or due to longitudinal relaxation.

Although, laser illumination initializes the electron spin state it is also useful to gather information about the spin state prior to illumination. Therefore, the first fluorescence photons after laser switch on have to be counted until the spin state is reset to $m_S = 0$ (see figure 2.5b). If the electron spin state was $m_S = 0$ prior to laser illumination it would remain there and continuously undergo optical excitation and fluorescence emission cycles. This leads to a continuously high level of fluorescence except for the beginning

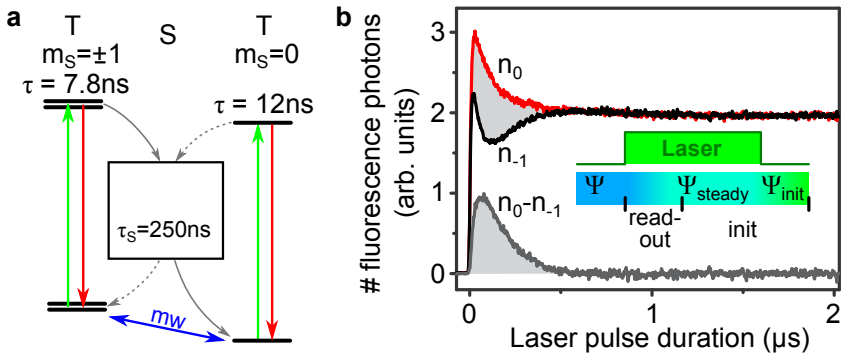

Figure 2.5.: Optical spin initialization and readout. a, Electronic level structure of ground and excited state divided into triplet with different m_S values and singlet states. For simplification the singlet level details are neglected. Optical transitions (green and red arrows), ISC (curved arrows), mw transitions (blue arrows) and lifetimes are given. Dashed lines illustrate weak transitions. **b,** Readout of electron spin state Ψ and initialization into $\Psi_{\text{init}} = |m_S = 0\rangle$ via the steady state Ψ_{steady} by a single laser pulse (see inset and text). For $\Psi = |0\rangle$ the fluorescence is always highest (red curve, n_0) and for $\Psi = |\pm\rangle$ it drops significantly lower (black curve, n_{-1}) before reaching Ψ_{steady}. The difference of the fluorescence levels are the "signal photons" $n_0 - n_{-1}$. The steady state fluorescence is lower than the initial one because of a considerable amount of population in the metastable singlet state.

where a small ISC rate leads to the initial fluorescence decrease. If, however, the spin state was $m_S = \pm 1$ the ISC rate is higher and the electron spin will eventually pass from the excited state triplet to the excited singlet state during laser illumination. When this happens the fluorescence count-rate will break down until finally the NV returns to its ground state with $m_S = 0$. This yields on average a 30% lower fluorescence level. In the end the same high fluorescence level is restored as for $m_S = 0$. Thus no further information about the previous spin state can be acquired. Therefore, we would like to call the difference in number of photons that are emitted for $m_S = 0$ and for $m_S = \pm 1$ the signal photons (see figure 2.5b).

As the signal photons are accumulated only for about 300 ns and the maximally achieved fluorescence count-rate so far is ≈ 0.8 Mcps on average only 0.24 photons are detected which results in 0.07 signal photons on average before the spin state is reset. Therefore, we have to average over many runs of an experimental measurement sequence to obtain a result that differs from the shot noise significantly.

The presented readout mechanism is sequential, i.e. laser pulse readout and initialize the spin system and in between two laser pulses coherent spin manipulation is possible. This coherent manipulation includes electron spin as well as nuclear spin manipulation. By transferring nuclear spin quantum states to the electron spin also their state can be readout. In essence any change of the electron spin state which is achieved during two readout laser pulses is detected in the fluorescence response. In contrast to the sequential readout, laser and appropriate mw fields can also be switched on simultaneously and

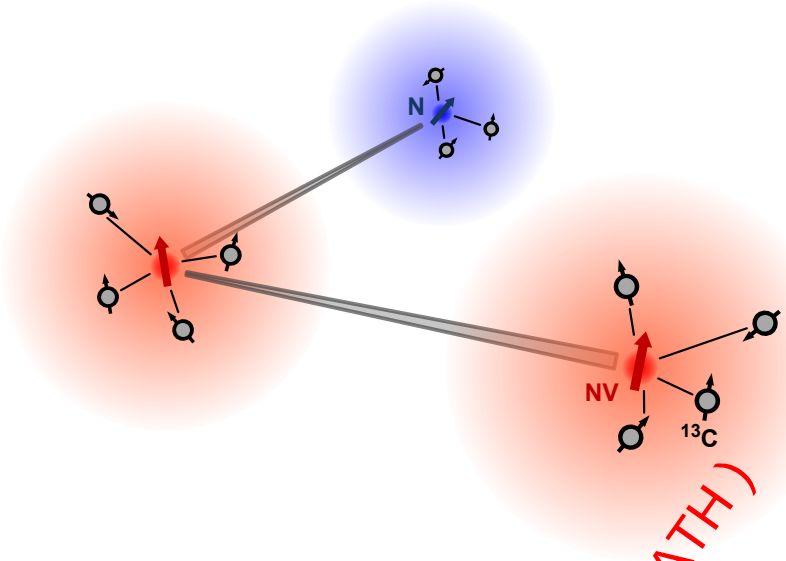

Figure 2.6.: Illustration of NV quantum register. ^{13}C or other nuclear spins coupled to NV center spins or other electron spins form local qubit clusters which are interconnected by the interaction of the electron spins among each other.

the spin state is read out in a cw manner. This can be applied to record EPR spectra (see section 2.3) but with some restrictions also for Rabi oscillations [26]. A detailed description of the sequential and the cw readout mechanism is given in appendix B.4.

The optical spin state readout presented here is usually referred to as optically detected magnetic resonance (ODMR). As explained above the ODMR signal is proportional to populations of spin states in contrast to conventional electron paramagnetic resonance (EPR) where excitations of coherences are detected. In our case the fluorescence level drops once the electron spin is flipped (e.g. by resonant mw fields) with respect to its initialized state. For the NV center in diamond the signal is large enough to detect ODMR of a single defect [20].

2.2.7. The master qubit

The NV center in diamond has several advantageous properties making it a qubit candidate. It possesses an electron spin $S = 1$ in the ground state which is the actual qubit or even a qutrit. This spin possesses both long transverse and longitudinal relaxation times under ambient conditions [56]. Intersystem crossing during optical pumping leads to polarization of that spin into its $m_S = 0$ state of the electronic ground state. Furthermore, the fluorescence of the NV center upon optical excitation depends on the spin state and thus enables optical spin state readout. Eventually, the electron spin state can be manipulated (e.g. by resonant mw radiation). The NV center is sufficiently stable under optical excitation (i.e. it does not blink or bleach and particularly nuclear spin

states are preserved).

In this work the NV center spin is coupled to various other spins which are usually not directly accessible on the single level (see figure 2.6). Using their coupling to the NV center, however, individual control is possible. For example the NV center spin is used for the initialization and the readout of surrounding spin qubits. Apart from directly manipulating the quantum states of proximal spins, these states can also be transferred from and to the NV center. This is why we call it the master qubit sometimes also called a bus qubit [143, 144]. The coupling strength to other spins is switchable. For instance by changing into the $m_S = 0$ level interactions can be decreased. In addition to the coupling to dark spins several NV centers can also be coupled with each other (see figure 2.6).

The NV center has additional promising applications in the field of metrology. Apart from coupling to other single spins the magnetic dipole moment of the NV center electron spin is particular susceptible to external magnetic fields. Due to its strong confinement to much less than 1 nm^3 the NV center allows magnetic field measurements with nanometer resolution and close proximity to the sample irrespective of the environmental conditions [66, 65]. The external magnetic field which can be sensed by the NV spin could indeed also origin from a single external electron or nuclear spin [145]. In addition to magnetic fields the NV center spin levels are susceptible to electric fields and crystal strain. Thus, electric field sources (such as charges) in the vicinity of the NV center as well as crystal strain around the NV position can be detected [75]. The quantum registers examined in this work have also very useful applications for future metrology devices based on the NV center spin and surrounding ones.

The NV center with its above mentioned properties is quite unique at present. However, there are strategies of how to search for defect centers with similar capabilities. The list of requirements for such a center reads like a "wanted" poster of the NV center [146]. Other materials where similar defect centers exist are SiC, MgO or CaO [146, 147]. In diamond itself there are also other center that might be suitable for QIP such as the Si-V^0 defect center with a spin triplet ground state and optical spin polarization [148]. However, so far the very short longitudinal spin relaxation time of the Si-V^0 seems to be incompatible with an application [148].

2.3. The room temperature experimental setup

It is the task of this setup to investigate single NV centers in diamond samples by optical microscopy and to perform spin resonance experiments on single electron and nuclear spins. Therefore, special requirements have to be met. One of the first systems where single molecule detection in a solid was possible are pentacene molecules in a para-terphenyl crystal [149, 150]. There a narrow-band laser excites a small volume of the crystal which still contains many pentacene molecules. However, the large inhomogeneous spread of excitation frequencies allows to spectrally select single molecules

and detect their red shifted fluorescence. This was possible because (i) the pentacene molecules have a sufficiently large absorption cross-section for the excitation light, (ii) the rate of the subsequent emission is higher than the detector dark count and (iii) the molecules are stable enough to emit a detectable amount of photons before either their excitation frequency changes or the molecules bleach or go off by some other process. Later also ODMR could be performed in the metastable spin triplet state of single pentacene molecules [151, 14]. All afore mentioned experiments were conducted at cryogenic temperatures of $\approx 2\,\mathrm{K}$. Later, however, it was demonstrated that also at room temperature single emitters can be addressed individually which is especially important for biological research. For example single nile red and green fluorescent proteins could be imaged individually by preparing dilute matrices and by confining the excitation light using total internal reflection [152, 153]. The latter two techniques are extremely important as the proteins cannot be selected by their excitation spectrum like in the case of pentacene. Eventually, single molecule detection and single molecule ODMR have also been demonstrated for the NV center in diamond [20, 154, 155, 25]. The NV center could be investigated under cryogenic as well as under ambient conditions.

In this work we use a room temperature experimental setup which is able to investigate single color centers in diamond optically. In addition electron as well as nuclear spins can be manipulated. Therefore it consists of a homebuilt confocal microscope [156], an adjustable magnetic field system and mw and rf equipment.

Figure 2.7a shows a sketch of the setup and is explained in the following. In the microscope part a collimated 532 nm laser (diode pumped solid-state laser (DPSSL), 100 mW) beam is first send trough an acousto-optic modulator (AOM) for switching and then focused using an oil immersion objective. The laser focus can be placed at the position of a color center by a 3D piezo scanner with nm precision. The fluorescence of an excited emitter and part of the excitation light is collected by the same objective, collimated and then focused onto a pinhole for spatial filtering. The confocal pointspread function (PSF) [156] (i.e. the region which is illuminated on the one hand and from which light is detected on the other hand) has a lateral extend of about 300 nm and an axial extend of roughly 1 µm.[6] In a next step a long pass filter (647LP) blocks light with wavelengths shorter than 647 nm including the excitation light and transmits the fluorescence light. The latter is split by a 50/50 beam splitter (BS) and focused onto two single photon counting avalanche photodiodes (APDs) . The latter part is a so called Hanbury-Brown and Twiss setup that enables recording the second order autocorrelation function

$$g^{(2)}(\tau) = \frac{\langle I_{PL}(t) I_{PL}(t+\tau) \rangle}{\langle I_{PL}(t) \rangle^2} \tag{2.7}$$

[6] The excitation volume (i.e. the focal volume of the laser light) and the detection volume (i.e. volume from where emitted light can pass through the pinhole) should coincide. In other words the focus of the laser coincides with the image of the pinhole. Therefore, this microscopy technique is called confocal microscopy.

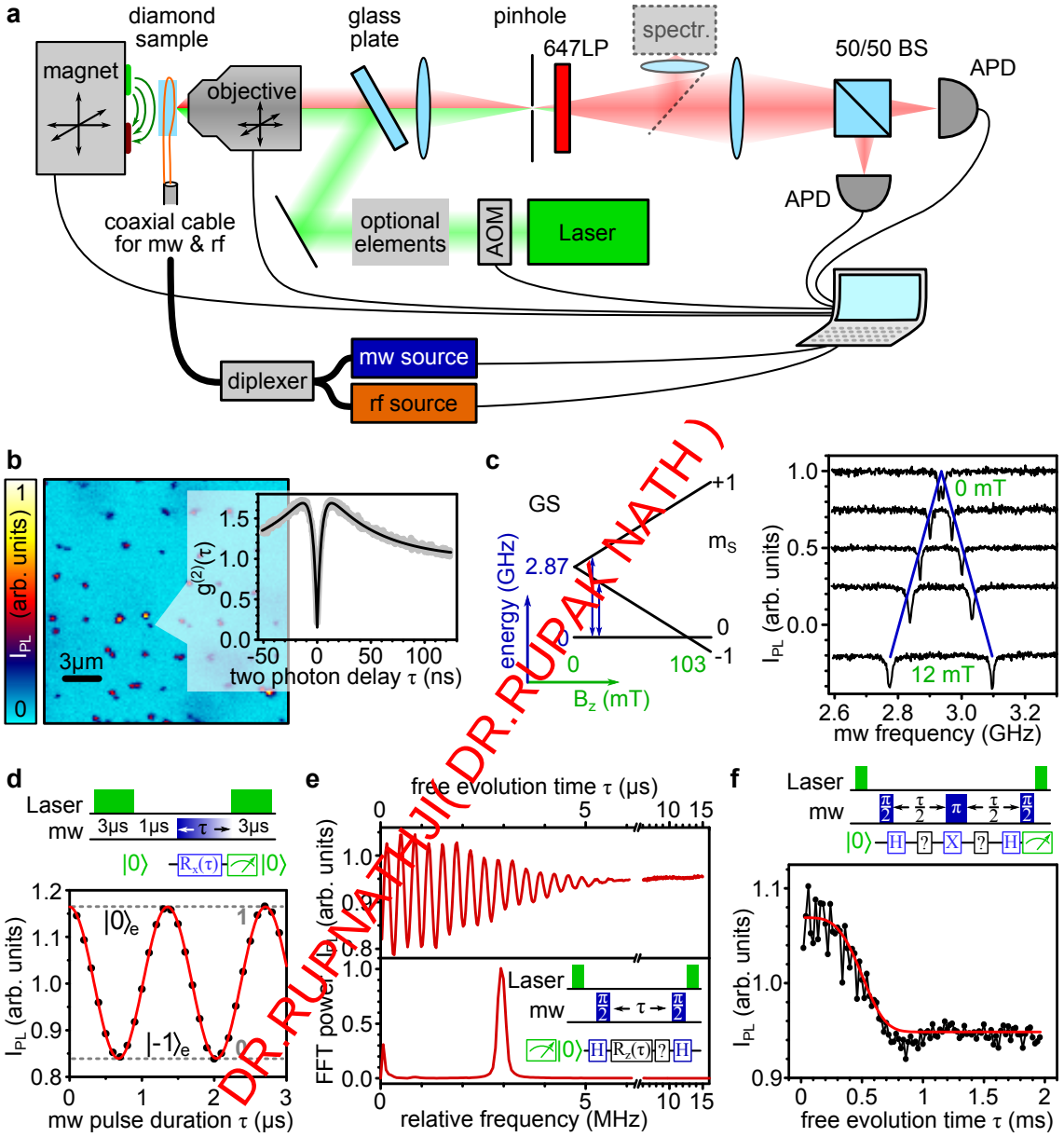

Figure 2.7.: Experimental setup and basic experiments. **a,** Experimental setup comprised of a homebuilt confocal microscope, an adjustable magnetic field and the mw and rf equipment (see text). **b,** Image of a lateral scan of the microscope inside the diamond sample showing many NV centers (high fluorescent spots). The fluorescence intensity autocorrelation function $g^{(2)}(\tau)$ reveals single emitters. **c,** Spin energy level splitting depending on axial magnetic field strength (left part). Spin transitions (blue arrows) are detected in the corresponding ODMR spectra (right side). **d,** Rabi oscillation of the NV center electron spin. For explanation of the pulse sequence see text. **e,** Ramsey oscillation of the electron spin coherence (upper part). The lower part displays the Fourier transform of the upper curve. **f,** ESEEM using a Hahn echo pulse sequence (see inset and text).

where $I_{PL}(t)$ is the photoluminescence intensity at time t and the brackets indicate a time average. Single emitters show the characteristic antibunching dip ($g^{(2)}(0) = 0$) (see figure 2.7b) whereas two equal emitters would lead to $g^{(2)}(0) = 1/2$. Background radiation leads to higher values of $g^{(2)}(0)$ than expected theoretically.

As an optional instrument a spectrometer (spectr. in figure 2.7a) can be mounted to analyze the fluorescence spectrum. In addition, the excitation laser light can be further manipulated by optional elements such as $\lambda/2$ plates for polarization adjustment or phase plates to create non-Gaussian field distributions at the position of the NV center.

To manipulate energy levels of spins an (electro- or permanent) magnet with an inhomogeneous field can be arbitrarily positioned with sub-µm accuracy in order to achieve any desirable field at the position of an NV center. Finally, mw and rf radiation is applied to NV centers by guiding it through coaxial cables close to the diamond sample where it is than coupled into either a copper wire or a coplanar waveguide. The corresponding ac current flowing in the wire or waveguide results in a linearly polarized oscillating magnetic field that affects the spins. Usually circularly polarized mw fields are needed to drive EPR transitions (see eq. (2.6) and appendix C.1). Therefore, the direction of the magnetic field in the plane perpendicular to the NV axis is not important.

The laser and rf and mw radiation can be adjusted up to several GHz and the collected photons can be registered with a timing accuracy of up to 100 ps. All parts of the setup are presented in more detail in the appendix B.

A basic measurement routine is first to scan with the laser illuminated confocal volume of the microscope across an area inside the bulk diamond, on its surface or on the surface of a cover slip with nanodiamonds deposited on top. The number of fluorescence photons collected by the APDs is recorded for each position in that area and is usually color-coded in a scan image such as figure 2.7b. Single NV centers show up as bright spots with a signal to background ratio of ~ 30. Depending on the type of sample one can deduce the number of NV centers inside the confocal volume from the fluorescence intensity. If this is not possible or if one wants to be sure the second order fluorescence autocorrelation function $g^{(2)}(\tau)$ can be recorded (see figure 2.7b). A value of $g^{(2)}(0) < 1/2$ usually confirms a single emitter. For two or more emitters with different fluorescence rates values of $g^{(2)}(0) < 1/2$ can also be achieved.

Once a suitable NV center is found it is moved into the confocal volume and this position is checked from time to time. In the meantime the NV center can be investigated. With a rough knowledge about the magnetic field mw radiation is applied to the NV in a suitable frequency range (see figure 2.7c). While the mw frequency is swept the laser continuously illuminates the NV center and the fluorescence intensity drops down when an EPR resonance is hit and is constantly high otherwise (cw ODMR spectrum).[7] The two fluorescence dips visible in the ODMR spectra correspond to electron spin transitions from $m_S = 0$ into either $m_S = -1$ or $+1$ (i.e. both transitions can be addressed selectively). The ODMR line pair splits upon the application of a magnetic field ac-

[7] continuous wave (cw) refers to continuously applied mw or laser radiation without pulsing.

cording to the energy level shifts (see figure 2.7c). Usually either laser or mw power broaden these resonance lines and determine their amplitude (see appendix B.4). For high resolution ODMR spectra (linewidth $\lesssim 1\,\mathrm{MHz}$) it is advisable to interleave laser and mw pulses in an appropriate way to get a much faster signal acquisition [51] (see appendix B.4). We refer to these as pulsed ODMR spectra as compared to cw ODMR spectra.

From the ODMR spectra the accurate resonance frequencies can be deduced. Prior to any coherent spin manipulation like the application of certain quantum gates the Rabi frequency has to be measured (see eq. (2.6)) [26]. Therefore, the experiment is performed in a pulsed manner (see figure 2.7d). First, the spin is initialized by a green laser pulse of 3 µs duration followed by a waiting time of 1 µs to ensure relaxation into the ground state (see figure 2.5b). Secondly, a microwave pulse of length τ is applied. The former two pulses comprise one measurement step of a sequence. Actually, the laser pulse of this step is at the same time the readout pulse for the previous measurement step. In the run of that sequence τ is increased from one measurement step to the next and finally the whole sequence is repeated many times ($> 10^5$). The fluorescence photons for all runs of the whole sequence are accumulated retaining 1 ns timing resolution within the sequence. This way we are able to analyze fluorescence responses for each value of τ separately (i.e. one fluorescence response pulse as in figure 2.5b in section 2.2.6 is obtained for each τ). Therefore, we can distinguish between the photons that arrive during the readout and reinitialization period and those that arrive later to the end of the laser pulse. The former photons contain the signal photons whereas the latter ones correspond to the high fluorescence rate. Usually, we normalize the signal photons to the number of photons that arrive at the high fluorescence rate. This yields I_{PL}. Figure 2.7d shows the resulting Rabi oscillation as the variation of fluorescence photons. The resulting Rabi frequency Ω is slightly below 1 MHz and is taken at a magnetic field of 50 mT.[8] In later chapters (5) it is demonstrated that Rabi frequencies of up to several 100 MHz can be achieved in this setup. The Rabi oscillation in figure 2.7d does not show any noticeable decay because the longitudinal relaxation time T_1 and the inverse of the inhomogeneous linewidth ($1/\gamma_{\mathrm{inh}} \propto T_2^*$) are much longer than the spin manipulation time τ. The contrast corresponds to the maximally achievable amplitude A_0 because the driving field is resonant (see eq. (2.6)). On some occasions it is useful to normalize I_{PL} to this maximum contrast. The behavior of the Rabi oscillation for non-resonant driving fields is described in appendix C.2.

From this Rabi oscillation some basic quantum gates can be deduced like the Hadamard (H) gate or the X gate which are both single qubit gates. Using these gates quantum wire diagrams can be drawn to illustrated the measurement sequences (see figures 2.7d–f). A summary of all quantum gates used in this work and a more detailed explanation is given in appendix C.2.

[8] At this field the nuclear spin associated with the nitrogen atom of the NV center is polarized and the bare electron spin behavior is observed (see section 5.1).

With a calibrated mw field we can now measure the so called T_2^* and T_2 times (see appendix). The T_2 time is a measure for how long the phase of a superposition state evolves coherently within a single measurement step whereas the T_2^* value is a measure for how strongly the Larmor precession frequency varies during many measurement steps (i.e. for the inhomogeneous linewidth of the EPR transition). For both measurements a coherent superposition state is required which is prepared by performing a $\pi/2$-pulse or Hadamard gate (see figure 2.7e, appendix C.3). In the case of the T_2^* measurement a waiting time τ is inserted during which the spin state evolves freely (i.e. it undergoes Larmor precession ($R_z(\tau)$) according to the present Hamiltonian). The final phase is converted back into spin state population by a second $\pi/2$-pulse which is readout by the subsequent laser pulse. The visible damped oscillation in figure 2.7e is also referred to as Ramsey oscillation or free induction decay (FID). Decoherence due to interaction with the environment (symbolized by "?") leads to decay of the Larmor precession amplitude. The Fourier transform of the oscillation shows the inhomogeneously broadened EPR line (see figure 2.7e). In the case of the T_2 measurement the free evolution period τ is interrupted by a π-pulse which acts as an inversion of the phase evolution (see figure 2.7f). Therefore, if no change of the Hamiltonian happens during τ the phase in the end will be the same as in the beginning.[9] This measurement follows the principle of a Hahn echo measurement (see appendix C.3.2). However, it is not the actual echo that is recorded but just one point of an echo, namely that for a symmetric pulse sequence where the first and the last evolution time are equal. This echo amplitude is recorded for several interval lengths τ. Therefore, this measurement is rather referred to electron spin echo envelope modulation (ESEEM, see figure 2.7f and appendix C.3.2). Apparently, both the echo as well as the Ramsey signal decay after some time (T_2 and T_2^* respectively).

Usually, the NV spin Hamiltonian varies slowly ($\sim T_2$) but the range of possible detunings (see eq. (2.6)) is rather large compared to $1/T_2$ which manifests in $T_2 \gg T_2^*$ (compare figures 2.7e and f). This dynamics is mainly governed by the nuclear spin bath (see section 3.1.5). Its effect on T_2 can be suppressed by specially designed echo sequences known from conventional EPR [157] (see appendix C.3).

The most straight forward way to measure the longitudinal relaxation time T_1 is to prepare a laser pulse train with increasing pulse distance. At some point the laser pulse distance is longer than T_1, populations will equilibrate and finally the fluorescence changes. T_1 values measured in this work are between 5 and 10 ms, however, values of more than 20 ms have already been measured [32].

[9] If interacting spins are included in the Hamiltonian even a static Hamiltonian can affect the final phase of the Hahn echo sequence (see section 3.1.5).

3. Nuclear spins as qubit resource

In the previous chapters the applicability of the electron spin of the NV center in diamond as quantum bit was pointed out. However, more sophisticated quantum effects can be studied if the electron spin qubit is coupled to other isolated quantum systems. Single nuclear spins in the vicinity of the electron spin are probably the most obvious ones. Due to their extremely weak interaction with their environment they could serve as ideal storage qubits. Although, the state of a coupled nuclear spin cannot be read out optically as for the electron spin of the NV center it can be indirectly measured by correlating its spin state with the one of the NV center and reading out the latter.

Also in other solid state systems nuclear spins are expected to be ideal candidates for QIP as for example in the Kane proposal where the ^{31}P nuclear spin qubit is introduced [90] (see section 1.4). Experiments using the phosphorus donor electron spin in silicon have recently achieved single shot readout of that spin [158]. Other approaches in silicon are the use of ^{29}Si nuclear spin chains in otherwise spinless ^{28}Si [159]. In the case of diamond also other spins can be used as qubits as for example electron and nuclear spins associated with single substitutional nitrogen impurities [29] or spins inside fullerenes [160].

In diamond there are mainly two different nuclear spin species. Namely the nitrogen nuclear spin of isotopes ^{15}N and ^{14}N associated to the color center itself and the carbon nuclear spins of the ^{13}C isotopes spread over the whole lattice (see table 3.1 and figure 3.1). The coupling to these spins is mediated by hyperfine interaction. For a coherent coupling between electronic and nuclear spin the strength of that coupling must be stronger than the decoherence rates of both spins. Despite this requirement numerous nuclear spins in the vicinity of a NV center might serve as qubits. In this chapter their interaction with the electron spin is discussed in detail. Furthermore, quantum gates like the CNOT and the Toffoli gate are applied to generate highly entangled states among electronic and nuclear spins.

Results of this chapter are published in [42, 36].

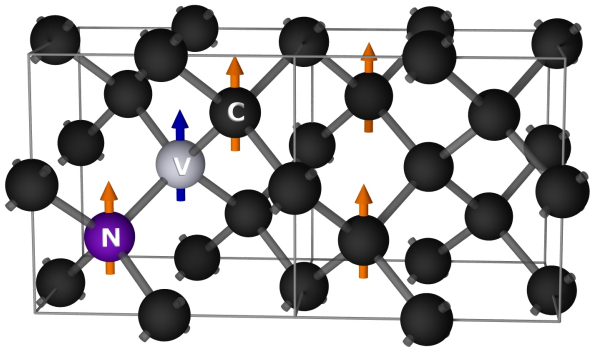

Figure 3.1.: NV center and proximal nuclear spins Two unit cells of the diamond lattice (C-carbon) containing an NV center (N-nitrogen, V-vacancy) and exemplary nuclear spins. The NV center electron spin is shown as blue arrow and the nuclear spins as orange arrows. From left to right the nuclear spins are that of nitrogen, ^{13}C in the first shell and two ^{13}C in the third shell.

isotope	natural abundance (%)	nuclear spin I	g_n-factor and gyromagnetic ratio $\tilde{\gamma}_n$ (kHz/mT)	
^{13}C	1.1	½	1.40482	10.7051
^{14}N	99.63	1	0.4037607	3.0766
^{15}N	0.37	½	−0.566380	−4.3156

Table 3.1.: Isotopes with nuclear spins Most abundant isotopes with nuclear spins in the diamond lattice. In addition to the abundance the nuclear spin I, nuclear spin g_n-factor and the gyromagnetic ratio devided by 2π are given.

3.1. Interaction of a single electron spin with nearby nuclear spins

3.1.1. Nuclear spin Hamiltonian

The Hamiltonian $\hat{H}_n$ of a nuclear spin surrounding an NV center in diamond can be divided into three parts [133].

$$\hat{H}_n = \hat{H}_{hf} + \hat{H}_{nZ} + \hat{H}_Q \tag{3.1}$$

The first one is the hyperfine (hf) interaction with the NV electron spin, the second term is the nuclear Zeeman (nZ) Hamiltonian depending on the static external magnetic field and the last term describes the zero field energy for nuclear spins where $I > 1/2$. Note, that the interaction with other nuclear spins is omitted here because it is negligible in strength due to their small concentration respectively their large average distance. The effects of individual parts of the Hamiltonian are illustrated in figure 3.2.

The hyperfine Hamiltonian $\hat{H}_{hf}$ comprises of two contributions [133]. One is the

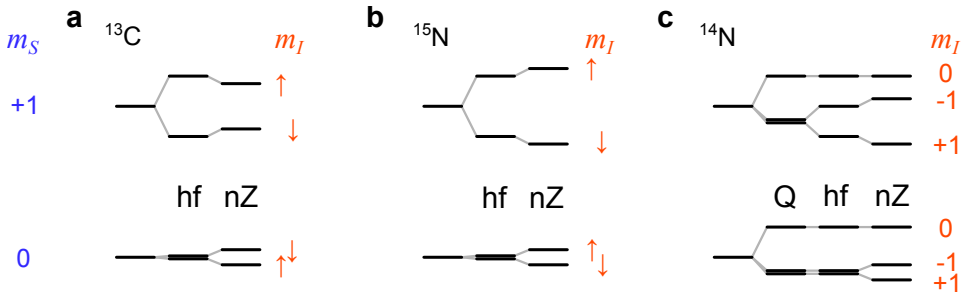

Figure 3.2.: Nuclear spin Hamiltonian and energy levels. **a,** Energy levels $m_I = \uparrow, \downarrow$ for a ^{13}C nuclear spin for two electron spin projections ($m_S = 0, +1$) are displayed. Subsequently different parts of the Hamiltonian are switched on (see text). **b,** Energy levels for ^{15}N. **c,** Energy levels for ^{14}N exhibiting additional quadrupole splitting Q.

isotropic Fermi Contact interaction $\hat{H}_F$ and the other one is the anisotropic electron-nuclear magnetic dipole-dipole interaction $\hat{H}_{dd}$.

$$\hat{H}_{hf} = \hat{H}_F + \hat{H}_{dd} \tag{3.2a}$$

$$\hat{H}_F = -\frac{2\mu_0}{3}\tilde{\gamma}_e g_n \mu_n \left|\psi^e_{@n}\right|^2 \underline{\hat{S}} \cdot \underline{\hat{I}} \triangleq a_{iso} \underline{\hat{S}} \cdot \underline{\hat{I}} \tag{3.2b}$$

$$\hat{H}_{dd} = \frac{\mu_0}{4\pi}\tilde{\gamma}_e g_n \mu_n \frac{\underline{\hat{S}} \cdot \underline{\hat{I}} - 3\left(\underline{\hat{S}} \cdot \underline{e}_r\right)\left(\underline{e}_r \cdot \underline{\hat{I}}\right)}{r^3} \tag{3.2c}$$

The Fermi contact interaction is proportional to the electron spin density at the location of the nucleus $\left(\left|\psi^e_{@n}\right|^2\right)$. Therefore, it is only of importance for nuclear spins that are very close the NV center and thus can possess a reasonable amount of spin density (compare section 2.2.3). The magnetic dipole-dipole interaction in contrast is a long range one, which however decreases very fast as $1/r^3$ with electron-nuclear spin distance r. As can be seen from equation (3.2c) an anisotropy enters which depends on the orientation of the two spins with respect to each other. Here $\underline{e}_r$ is the unit vector connecting them. For proximal nuclei a point dipole approximation in eq. (3.2c) might not be valid anymore and one would have to integrate $\hat{H}_{dd}$ for all r weighted by the electron spin density.

Often, the two contributions to the hyperfine interaction are summarized into one tensor $\mathbf{A}$ resulting in

$$\hat{H}_{hf} = \underline{\hat{S}} \cdot \mathbf{A} \cdot \underline{\hat{I}}. \tag{3.3}$$

In its eigensystem the tensor is diagonal of the form $\mathbf{A} = \mathrm{diag}(A_\perp, A_\perp, A_\parallel)$.[1] The isotropic part of the interaction can be calculated as $a_{iso} = (A_\parallel + 2A_\perp)/3$ and the anisotropic one as $b = (A_\parallel - A_\perp)/3$. Conversely, $A_\perp = a_{iso} - b$ and $A_\parallel = a_{iso} + 2b$.

The nuclear Zeeman splitting is expressed in the following way

$$\hat{H}_{nZ} = -\tilde{\gamma}_n \underline{B} \cdot \underline{\hat{I}} \tag{3.4}$$

[1] This is strictly true only for the point dipole approximation in eq. (3.2c). However, the hyperfine tensors of nuclei surrounding the NV are usually well approximated by $A_\perp$ and $A_\parallel$ [161].

nuclear spins	observable hyperfine splitting (MHz)
^{13}C	0 . . . 126
^{14}N @ NV	−2.16
^{15}N @ NV	3.03

Table 3.2.: Hyperfine interaction strengths. Hyperfine splittings of NV center ESR lines due to nearby nuclear spins. For the carbon nuclear spins several lattice positions with respect to the NV center are possible leading to different values.

and the quadrupole splitting which, in the diamond lattice, applies only to the ^{14}N nuclear spin (see table 3.1) can be written as

$$\hat{H}_Q = Q\hat{I}_z^2 \ . \tag{3.5}$$

As illustrated in figure 3.2c Q for ^{14}N is negative and its value is −4.945 MHz (see section 5.2).

3.1.2. Secular approximation and non-secular terms

In most cases the electron Zeeman energy and the electron spin zero-field splitting are orders of magnitude larger than the hyperfine interaction (see table 3.2). Thus the electron spin states are almost unaffected by the nuclear spins. This allows for the secular approximation of equations (3.2) and (3.3). For a magnetic field applied parallel to the NV axis (z-direction) only z-terms of the electron spin ($\hat{S}_z$) need to be taken into account here. Hence, the eigenstates of the electron spin cannot be changed by the nuclear spins. Only their energy can be altered by the nuclear spins.

The secular approximation allows illustrating the interactions of the nuclear spins in an intuitive way. Namely, the nuclear spins on the one hand exert a magnetic field on the electron spin, of which, however, only the z-component has an effect on the energy levels of the electron spin but not on its eigenstates. On the other hand the quantization axis and the energy level splitting of the nuclear spins are determined by an effective magnetic field B_{eff} which comprises of the external static magnetic field and the magnetic field generated by the electron spin including $\hat{H}_F$ and $\hat{H}_{dd}$ (see figure 3.3a). Quantization axes as well as energy level splittings in general are different for the three electron spin states. There are two special cases. One is when the nuclear spin quantization axes for all the electron spin sublevels are parallel and the other is when the quantization axes for $m_S = \pm 1$ and $m_S = 0$ are orthogonal (case 1. and 2. in figure 3.3a). This has some consequences for the electron spin transitions. Assuming hyperfine interaction with a spin ½ nucleus (e.g. ^{15}N), each electron spin level is split into two nuclear spin sublevels by an amount given by the nuclear spin Hamiltonian $\hat{H}_n$ (see figure 3.3b). For electron spin transitions between levels $m_S = 0$ and $m_S = \pm 1$ the

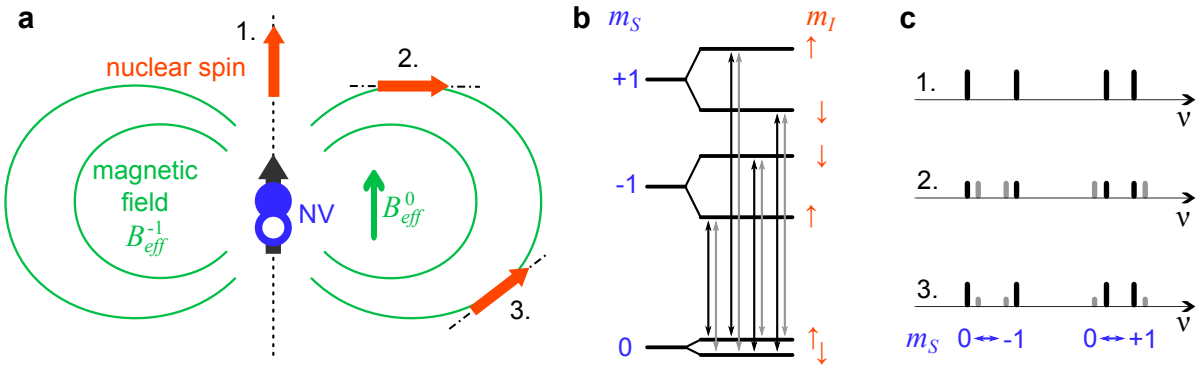

Figure 3.3.: Hyperfine interaction and secular approximation. **a,** The electron spin state of the NV center determines the effective magnetic field for $m_S = 0$ (B_{eff}^{0}, bare external field) and for $m_S = -1$ (B_{eff}^{-1}) which acts on the nuclear spins (1.–3.) and sets the quantization axes. The axes might be different for different m_S values which affect the visible ESR transitions. The field exerted by the nuclear spins on the electron spin only shifts its energy levels but does not change the quantization axis. **b,** Electron and nuclear spin energy level scheme including ESR transitions. Black vertical arrows are "allowed" and gray arrows "forbidden" transitions. **c,** Stick spectra showing allowed and forbidden transitions for the 3 different nuclear spins.

nuclear spin remains unchanged. Thus in the case of parallel nuclear spin quantization axes (case 1.) for all electron spin sublevels only "allowed" transitions occur and the respective nuclear spin quantum number does not change (see figure 3.3c). This is different, however, if the quantization axes are not parallel (cases 2. and 3.). In this case a nuclear spin eigenstate in one electron spin sublevel would be promoted into a superposition of eigenstates of another electron spin sublevel upon electron spin transition. Thus the nuclear spin quantum number will change according to the new quantization axis and so called "forbidden" transitions occur. In the ESR spectrum this manifests as additional lines (see figure 3.3c). Depending on the angle between the nuclear spin quantization axes of two electron spin sublevels the strength of allowed and forbidden electron spin transitions changes. Both strengths are equal for orthogonal axes (case 2.) and the forbidden line vanishes and only the allowed line remains for parallel axes (case 1.). In the case of the NV center ESR lines allowed and forbidden transitions are often hidden within the linewidth because of the small gyromagnetic ratio of the nuclear spin that leads to the level splitting of the $m_S = 0$ sublevels.

Another consequence of different nuclear spins quantization axes in different electron spin levels are nuclear spin Larmor precessions that differ not only in frequency but also in their rotation axis. This behavior can be exploited to generate arbitrary controlled quantum gates on the nuclear spin [38].

In the case of the secular approximation sublevels of each electron spin projection only differ by their nuclear spin projection. Thus, magnetic dipole transitions between these levels can be induced by an oscillating magnetic field at the frequency of the respective

energy splitting (i.e. the nuclear spin Larmor frequency). These transitions have to obey the selection rules $\Delta m_I = \pm 1$. Usually the Rabi frequencies achievable for these transitions are much smaller than for electron spin transitions because of the much smaller nuclear gyromagnetic ratio compared to that of the electron spin.

Although, the secular approximation is valid most of the time for the NV center, there are experimental observations that can only be explained by the non-secular terms, namely a nuclear Zeeman splitting that is stronger than expected for a bare nuclear spin and in the same way faster nuclear spin Rabi frequencies [31]. The effect of the non-secular terms is a tiny admixture of electron spin character to nuclear spin states (i.e. nuclear spin states that are supposed to be within the same electron spin sublevel have in fact slightly different electron spin states). This has some consequences for example for the effective nuclear spin gyromagnetic ratio. Although the admixture might be tiny the effective nuclear spin gyromagnetic ratio would be greatly increased because of the much larger gyromagnetic ratio of the electron spin that mixes in. Thus especially in the $m_S = 0$ sublevel nuclear spin levels are split by a larger amount than expected and might become larger than the ESR linewidth and thus visible in the ESR spectrum (see figure 3.3b,c). Another consequence of the enhanced gyromagnetic ratio is a faster nuclear Rabi frequency. This whole effect is called hyperfine enhancement.

In the case of the NV center the enhancement of nuclear gyromagnetic ratios of surrounding nuclear spins is strongly magnetic field dependent. Thus the gyromagnetic ratio is not isotropic but can be rather described by a tensor. A detailed analysis for this is shown in [31]. There it turns out that the hyperfine enhancement is maximal for a magnetic field oriented perpendicular to the NV axis and minimal for parallel orientation. To suppress the hyperfine enhancement further the magnetic field has to be increased such that electron and nuclear Zeeman energies become more and more off-resonant [54].

3.1.3. Examples of nearby nuclear spins

Every NV center has at least hyperfine interaction with one nuclear spin, namely that of the associated nitrogen atom. Its nuclear spin is usually $I = 1$ but might also be $I = 1/2$ depending on the isotope (see table 3.1). Due to a small electron spin density at the nitrogen nucleus the hyperfine interaction is comparatively small. Depending on the nitrogen isotope the splitting of the ESR line is $\approx 2.2\,\mathrm{MHz}$ (^{14}N) or $\approx 3\,\mathrm{MHz}$ (^{15}N). For the ^{15}N nucleus the NMR resonance frequency can be directly deduced from the ESR spectrum. It is the visible hyperfine splitting plus the nuclear Zeeman slitting. In the case of ^{14}N the nuclear quadrupole splitting has to be taken into account in addition. For moderate fields of up to 50 mT the observed nuclear Rabi frequencies are higher than expected due to hyperfine enhancement (see section 3.1.2).

Apart from the fact that the nitrogen nuclear spin is present in every NV center it is also special regarding symmetry. The nuclear spin is lying on the NV axis ($z-$axis) and its hyperfine tensor therefore is rotationally symmetric and collinear with the NV axis.

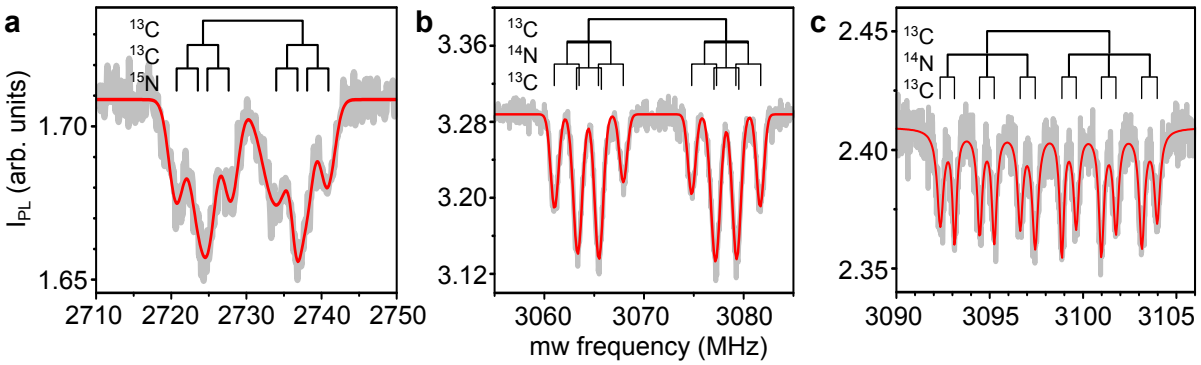

Figure 3.4.: ODMR spectra with ^{13}C hyperfine splitting. **a,** This spectrum shows the $m_S = 0 \leftrightarrow -1$ transition at $\approx 5\,\mathrm{mT}$. The visible ^{13}C hyperfine interactions are 13.2 MHz and 4.2 MHz. The ^{15}N nuclear spin creates an additional splitting of $\approx 3\,\mathrm{MHz}$. A concatenated stick spectrum illustrates the interactions. **b,** This spectrum shows the $m_S = 0 \leftrightarrow +1$ transition at $\approx 11\,\mathrm{mT}$. ^{13}C and ^{14}N hyperfine interaction is visible with the respective splittings 13.8 MHz, 2.2 MHz and 2.6 MHz. **c,** The same situation as in panel **b** but with hyperfine interactions 6.5 MHz, 2.2 MHz and 0.8 MHz.

Thus according to the secular approximation the hyperfine field which the electron spin exerts on the nuclear spin points into the $z-$direction as well (assuming small magnetic fields or fields in $z-$direction). It follows that for parallel aligned magnetic fields the nuclear spin quantization axes are parallel in all electron spin levels. This results in allowed electron spin transitions only (see figure 3.3 case 1).

In addition to the nitrogen nuclear spin every NV center is usually surrounded by numerous ^{13}C nuclear spins (see figure 3.1). Depending on their position in the lattice the hyperfine interaction strength varies drastically. A ^{13}C atom on a lattice site next to the vacancy (i.e. in the first coordination shell) generates a hyperfine splitting of 126 MHz [27]. In this coordination shell there are three indistinguishable positions. In general those lattice sites around an NV center form one coordination shell that can be converted into each another by symmetry operations of the c_{3v} group with respect to the center. The next smaller observable hyperfine splitting is $\approx 14\,\mathrm{MHz}$, followed by $\approx 13\,\mathrm{MHz}$, $\approx 9\,\mathrm{MHz}$, $\approx 6\,\mathrm{MHz}$, $\approx 2\,\mathrm{MHz}$ and $\approx 0.8\,\mathrm{MHz}$ ... [162]. A few corresponding ESR spectra exhibiting these splittings are displayed in figure 3.4. An assignment to distinct coordination shells or lattice sites is not straight forward, because the electron spin density is neither decreasing isotropically nor monotonically with distance from the vacancy. There are *ab initio* supercell calculation studies of the electron spin density in the ground state of the NV$^-$ center and accompanying calculations of hyperfine interactions [111] which underline this behavior (see section 2.2.3). Data from this reference is compared to the experimentally observed hyperfine splittings in table 3.3 and a tentative assignment is given.

Due to the wide spread of nuclear spin resonance frequencies and hyperfine splittings,

exp. hf splitting (MHz)	calc. hf splitting (MHz)	calc. V-^{13}C distance (Å)
126	158.5	1.61
13.8	17.5	3.85
13.2	16.2	3.86
6.5	7.3	2.49
4.2	4.0	2.93
2.6	2.8	4.99
0.8	?	?

Table 3.3.: Hyperfine interactions of various ^{13}C spins (experiment and theory). Experimentally observed ^{13}C hyperfine splittings (col. 1) compared to results from *ab initio* supercell calculations (col. 2–3) (calculated results taken from [111]). The last column gives the distance of the corresponding nuclear spin to the vacancy. The question marks in the last row indicate that no calculated values have been available for such small coupling.

many different nuclei may be individually addressed at the same time. Therefore it is necessary that apart from having different frequencies the linewidth in ESR and NMR spectra has to be smaller than the frequency difference of neighboring lines. For the example spectra in figure 3.4 the lines are well separated. This is also true for the respective nuclear spin frequencies because there the linewidth is usually much narrower. Taking into account the different nuclear spins in the list of reference [111] and additional experimentally observed ones there are at least 12 different nuclear spin positions that can be addressed individually. If nuclear spins with even smaller hyperfine splittings are taken into account, this number will increase. However, the distinguishability will also go down because the hyperfine splitting is than in the range of the ESR line width (compare figure 3.6a).

Apart from using nuclear spins in different coordination shells, more than one spin from the same coordination shell could be used. There, however, individual addressing might be difficult because especially nuclear spin transitions are almost equal. The reason for this is the small interaction of the nuclear spins among each other. However, if the interaction with the electron spin is strong enough, a nuclear-nuclear interaction can be mediated. Especially in the case of two ^{13}C atoms in the first coordination shell a level scheme arises where 4 distinct nuclear spin transitions are present (see section 3.3.1).

In a natural diamond crystal only 1.1 % of all carbon atoms possess a nuclear spin. Thus the probability to find an NV center with a considerable amount of nuclear spins in close coordination shells is very low and decreases exponentially with the number of desired spins. Although, looking for such a center might pay off one can think of other ways to increase the probability. For example one might implant molecules containing nitrogen atoms and a high amount of ^{13}C atoms to locally enhance the spin density. An easier approach is to fabricate diamond crystals with enriched ^{13}C content. In this case,

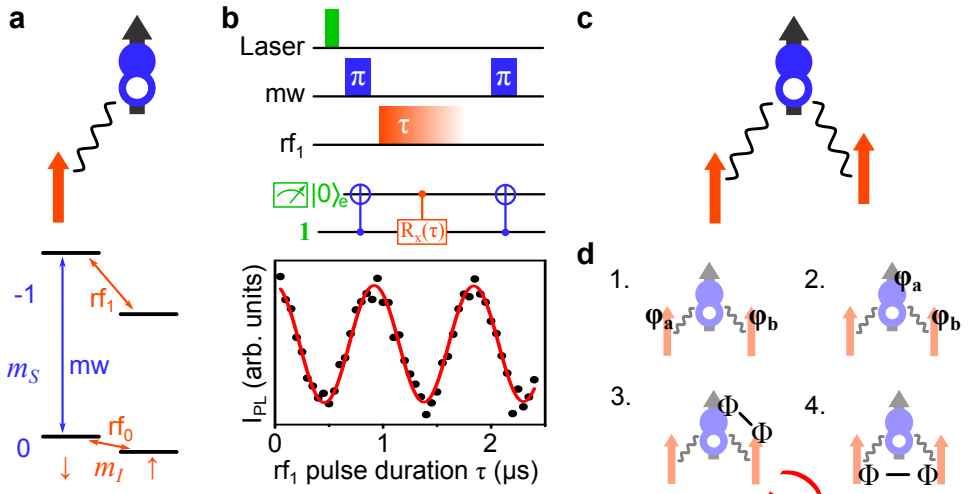

Figure 3.5.: Nuclear spins and controlled qubit gates. **a,** Illustration of a first shell ^{13}C nuclear spin coupled to an NV electron spin (top). The coupling is visualized by the wavy line. The corresponding energy level scheme is shown at the bottom. Blue and orange arrows illustrate EPR and NMR transitions respectively. **b,** Nuclear spin Rabi oscillation in the $m_S = -1$ electron spin sublevel (CROT gate, bottom) and corresponding pulse sequence (top, see text). **c,** NV center spin coupled to two nuclear spins. The direct coupling among the nuclear spins is too weak to perform quantum gates. **d,** Two qubit gates among nuclear spins exploiting the coupling to the common electron spin (see text).

however, the nuclear spin bath is not dilute anymore and the effects on the NV electron spin have to be considered (see section 3.1.5).

3.1.4. Quantum gates using nuclear spins

As for the electron spin every superposition of nuclear spin states can be created by rf pulses and phase shift gates that act on the nuclear spin directly. However, these gates are usually not single qubit gates but controlled two qubit gates (i.e. they depend on the electron spin state). Because of the different hyperfine coupling strengths in m_S manifolds 0 and ± 1, rf pulses that are resonant in one manifold are off-resonant in the other (see figure 3.5a). As long as one is only working in one electron spin manifold, however, these gates can be considered as effective single qubit gates. Again many gates can be extracted from the nuclear Rabi oscillations [27] (see figure 3.5b). Single qubit phase shift gates can be realized straight forward by adjusting the phase of the driving RF field or by using ancilla qubits.

The first demonstration of the "controlled" character of nuclear spin Rabi oscillations in the case of the NV center in diamond was demonstrated in [27] where a controlled rotation gate (CROT) was realized in a register out of an NV electron spin and the nuclear spin of a ^{13}C atom in the first coordination shell (see figure 3.5a,b). Because of

the large hyperfine interaction in this system it is easily possible to flip the electron spin conditional on the nuclear spin state and vice versa. Note that the corresponding ESR and NMR pulses therefore comprise CNOT gates. To demonstrate this, the electron spin was first polarized into its $m_S = 0$ state. By a nuclear spin state selective ESR π-pulse (CNOT gate) the nuclear spin state $|\downarrow\rangle_n$ is prepared in the $m_S = -1$ sublevel. Now, an electron spin state selective NMR pulse (CNOT gate) rotates the nuclear spin from $|\downarrow\rangle_n$ into $|\uparrow\rangle_n$ in the $m_S = -1$ sublevel which results in nuclear spin Rabi oscillations. Thus, this is a controlled rotation and therefore a CROT gate (see figure 3.5b). As the fluorescence of the NV center usually depends only on the electron spin state, the nuclear spin Rabi oscillation performed here would not result in an oscillation of the fluorescence intensity. Therefore, the nuclear spin state of interest, namely the one in the $m_S = -1$ sublevel has to be correlated with the electron spin state, which is finally read out. This correlation is achieved by performing again the first CNOT gate on the electron spin.

In addition to driving the nuclear spin directly via rf radiation the different hyperfine couplings in different m_S manifolds can be used to manipulate the spin state. In section 3.1.2 it is shown how the quantization axis and the effective magnetic field at the nuclear spin depend on the m_S manifold and the external magnetic field. Larmor precessions around non-parallel quantization axes can finally be used to perform controlled quantum gates on the nuclear spin [38]. An application of this method is shown in section 3.2.

In principle it is possible to compose a single qubit rotation by applying two controlled rotations each of which is controlled by another control qubit state.

So far, controlled gates have involved the electron spin and a nuclear spin. This has been particularly easy because of the hyperfine coupling among them. The coupling among two nuclear spins, however, is usually by far weaker and therefore not suitable to enable controlled gates (see figure 3.5c). Nevertheless, controlled gates can be achieved. A straight forward way would be to use the electron spin as a bus qubit (see figure 3.5d). By swapping one nuclear spin qubit state onto the electron spin and performing the desired controlled operation with the second nuclear spin qubit and swapping it back onto the first nuclei, the interaction strength between the two qubits has been virtually switched on for computation and off afterwards. A detailed theoretical analysis of how nuclear spin qubit gates can be realized in system comprised of an NV electron spin and proximal nuclear spins is given in [38].

3.1.5. The nuclear spin bath

Previously, the use of nuclear spins as qubits has been discussed. But apart from being a qubit resource nuclear spins first of all form a spin bath that is affecting the electron spin of the NV center. Because of the small natural abundance of the ^{13}C isotope (1.1%), spins in natural diamond possess favorable coherence properties. Apart from ^{13}C nuclear spins electron spins associated with nitrogen defects in diamond are another main source of decoherence [41]. The diamond samples that are mainly used throughout

this work, however, contain only a very small fraction of nitrogen impurities ($\ll 1\,\mathrm{ppm}$, some even $< 1\,\mathrm{ppb}$). Thus even the dilute nuclear spin bath becomes the main source of decoherence [42]. In this section the influence of the nuclear spin bath on the coherent superposition states of the NV electron spin will be explained. In addition the effect of nuclear spin baths with different densities will be analyzed.

Experimental conditions The scene of many experiments on the NV center spins is similar to the following. The ZFS parameter D is the strongest energy term for the electron spin Hamiltonian. Second largest and usually commuting with D is the electron Zeeman energy eZ. The smallest contribution is the coupling to other spins (electronic and nuclear ones). Usually the latter is so small that only contributions commuting with D and eZ need to be taken into account. Thus a secular approximation is valid. For the nuclear spins however the situation is different. Depending on the strength of the magnetic field and the distance to the NV center either the hyperfine interaction hf (table 3.2) with its electron spin or the nuclear Zeeman energy nZ (see table 3.1) is strongest and usually both are not commuting. The interaction with other bath nuclear spins is much smaller ($\sim 10\,\mathrm{Hz}/\%$, see appendix A). As a consequence switching the electron spin from one spin orientation m_S to another changes the quantization axis of the nuclear spin which leads to an interesting behavior of the nuclear spin bath affecting the electron spin coherence of the NV center [31] (see section 3.1.2).

The interaction of NV center spins with surrounding ^{13}C nuclear spins has been first observed in ensemble experiments [163] and the case of a single NV electron spin was first observed and explained in [31]. In general the interaction of a solid state electron spin with a nuclear spin bath can be calculated with a cluster expansion method as demonstrated for Si:P in [164]. There it could be shown that this fully quantum mechanical approach yields better results than classical stochastic modeling. The term cluster relates to clusters of more strongly interacting nuclear spins which are indeed allowed to interact with each other whereas weaker interactions among nuclei are neglected. It could be shown that already small cluster sizes allow modeling the decay of electron spin coherence measured by a Hahn-echo sequence. However, larger cluster sizes are required to model echo modulations. The application of cluster expansion methods to the NV electron spin and the surrounding nuclear spin bath was first demonstrated in [165]. It turned out that some effects of this interaction can be only explained by quantum phenomena.

Electron spin decoherence There are two main ways how the coherent evolution can be monitored. First of all there is the Ramsey type experiment where a coherent superposition between two electron spin states of the NV center is created, evolves freely and is eventually read out (see section 2.3 and appendix C.3.1). We have to average over many runs, thus a time average is obtained. During the many runs many different statistically chosen nuclear spin bath settings are present whereas during one run the

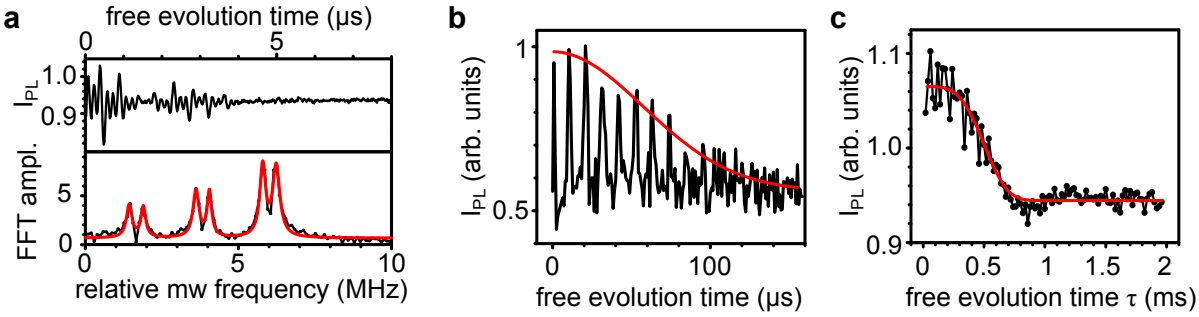

Figure 3.6.: Ramsey and Hahn echo experiments affected by nuclear spins. **a,** Ramsey oscillations and corresponding FFT spectrum showing the coupling to the ^{14}N nucleus and most likely a weakly coupled ^{13}C nuclear spin. **b,** ESEEM of for Hahn echo an NV center showing collapses and revivals due to ^{13}C nuclear spin bath. **c,** ESEEM for higher magnetic fields where collapses are suppressed.

nuclear spin setting hardly changes. Each setting creates a different local magnetic field at the NV center position which can be explained as classical field fluctuation. This leads to a Gaussian decay of the spin coherence (see figures 2.7e and 3.6a, [166]). Especially proximal nuclear spins have interaction strengths of up to $\sim 1\,\mathrm{MHz}$. Hence, the Ramsey signal decays on the time scale of a few µs (see figure 3.6a). This yields the T_2^* time or the inhomogeneous linewidth

$$\Delta\nu_{inh} = 2\sqrt{\ln 2}/(\pi\, T_2^*). \tag{3.6}$$

Experimentally it turns out that the afore mentioned nuclear spin bath configurations change slowly from one to another ($\sim 2\,\mathrm{kHz}$) compared to $\Delta\nu_{inh}$. This is exploited and thus made visible by the second coherence monitoring method. For a single measurement run a free evolution due to a certain bath configuration can be refocused by a Hahn echo sequence. Hence, the coherence can be retained for up to $T_2 \approx 500\,\mu\mathrm{s}$ (see figure 3.6c). To monitor the coherence the electron spin echo envelope modulation (ESEEM) is recorded (see section 2.3 and appendix C.3.2). Therefore, usually a superposition of $m_S = 0$ and $m_S = -1$[2] evolves for time τ, a mw π-pulse on the corresponding transition acts as a time reversal for all static environmental influences and after another evolution time τ the originally generated superposition is restored. Nevertheless, for different τ the final state might differ from the original one which is visible as a modulation of the echo amplitude (see figure 3.6b). The modulation and the decay of the echo amplitude can not be explained by classical noise anymore.

When the magnetic field is parallel to the NV center axis (i.e. D and eZ commute) and is small such that nZ and hf are similar, the ESEEM shows distinct collapses and revivals (see figure 3.6b). These can be explained by an entanglement and disentanglement of the electron spin with the bath nuclear spins [31]. Two quantum gates are needed to

[2]Superpositions of states $m_s = 0$ and $+1$ or of $m_S = -1$ and $+1$ are also possible.

entangle two qubits. These are the Hadamard gate that creates a coherent superposition on one qubit (here: creation of electron spin superposition state by a mw pulse) followed by a CNOT gate that flips the second qubit conditional on the state of the first one. The CNOT gate is realized by the hyperfine interaction between electron and nuclear spin that causes two different nuclear spin quantization axes for electron spin projections $m_S = 0$ and $m_S = -1$. Thus for the right waiting time the originally identical nuclear spin states in the two electron spin manifolds can evolve into orthogonal states. When this has happened electron and nuclear spin are maximally entangled and the former electron spin coherence is transferred to the entangled state. For the interaction with a single nuclear spin this leads to coherent modulation of the ESEEM signal ([31] and figure 3.9a). The modulation amplitude is largest when the first echo waiting time leads to the above mentioned CNOT gate (i.e. electron and nuclear spin entanglement). During the second waiting time the spins are disentangled again. A coupling to a whole bath of nuclear spins, however, this leads to a collapse of the ESEEM because of the superposition of many independent modulations which cancel each other and thus look like a decay of spin coherence. Not all nuclear spins can be maximally entangled with the electron spin. Indeed, rather many nuclear spins are partially entangled which leads to the same collapse of the ESEEM.

The revival of the electron spin coherence is caused by the common Larmor precession frequency ω_{L0} of the nuclear spins in the $m_S = 0$-manifold. This common Larmor precession reverts all CNOT and partial CNOT gates after a common time period, namely $t = \omega_{L0}^{-1}$. If one echo waiting time is ω_{L0}^{-1} the revivals appear. Finally also these revivals decrease and eventually disappear. Reasons for this are for example non-uniform nuclear Larmor precession in the bath due to coupling to the NV spin, strong couplings of nearest neighbor ^{13}C nuclei or decoherence due to electron spins [165].

If we deviate from the usual scenario explained in the beginning and increase the magnetic field, the nuclear Zeeman energy becomes larger than the hyperfine interaction for almost all nuclear spins. This reduces the possibility to entangle electron and nuclear spins and thus the collapses disappear (see figure 3.6c).

In some cases one can find a proximal ^{13}C nuclear spin with a hyperfine interaction that is stronger than the inhomogeneous linewidth (see table 3.2). Depending on the magnetic field setting some of these nuclear spins entangle beautifully with the electron spin. Because the large hyperfine splitting this process is so fast that its coherent evolution can be observed in the ESEEM before the collapse due to the rest of the bath spins occurs [31] (see also figure 3.9a). The same behavior can be observed for the ^{15}N nuclear spin and it can be exploited for nuclear spin initialization (see section 3.2).

Nuclear spin bath of varying density In this paragraph experiments on diamond samples with artificially tailored ^{13}C concentration c_{13} are summarized [42]. Therefore, samples with enriched as well as lowered ^{13}C concentration were fabricated by collab-

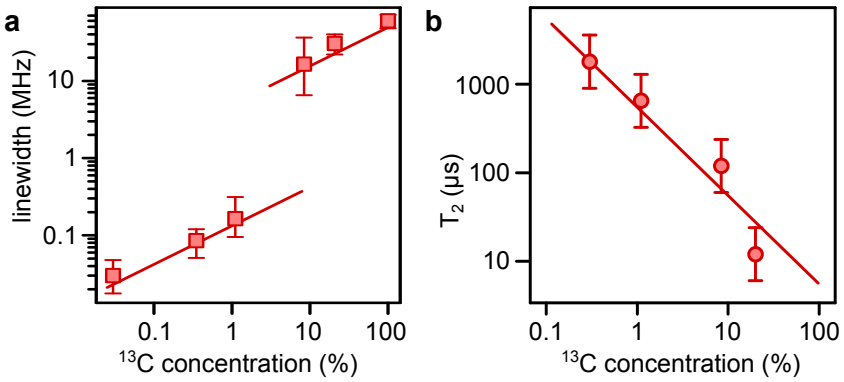

Figure 3.7.: Dependence of NV center electron spin coherence properties on ^{13}C concentration. **a,** Inhomogeneous linewidth of the NV electron spin EPR transition for various ^{13}C concentrations. Clearly two regimes are visible (see text). **b,** Phase memory time T_2 of the NV center electron spin for various ^{13}C concentrations (see text).

oration partners (i.e. c_{13} =100 %†, 20.7 %, 3.4 %, 1.1 %, 0.35 % and 0.03 %†).[3] All samples exhibit low nitrogen content such that the nuclear spin bath is the dominating decoherence source for the NV electron spin.

For all samples homogeneous and inhomogeneous linewidth (i.e. T_2 and T_2^* respectively) have been determined. Therefore ODMR spectra were taken, Ramsey experiments were conducted and the ESEEM has been recorded. In the case of the 100 % sample no ESEEM was possible due to the fast dephasing. For samples with concentrations $c_{13} \leq 1.1\,\%$ T_2^* was derived from the ODMR linewidth (eq. (3.6)); for the other samples by fitting the Ramsey decay.

When looking at the inhomogeneous linewidth as a function of c_{13} two regimes become visible (see figure 3.7a). Whereas in both regions the linewidth scales as $\sqrt{c_{13}}$ [42, 167, 168] there is an offset between both regimes of a factor of ≈ 50. The reason for this behavior is the very localized electron spin density of the NV center. For concentrations $\leq 1.1\,\%$ it is unlikely that a ^{13}C atom is present in the closest shells around the NV center (i.e. within the high electron spin density region). Thus the nuclear spins have a small interaction with the NV spin mainly due to dipole-dipole coupling ($\approx 20\,\mathrm{kHz}\,\frac{\mathrm{nm}^3}{r^3}$, see table A.2). Hence, even if there is a ^{13}C in the closest shells once in a while it produces a visible splitting of the ODMR line that is not blurred by interactions of the other spins. If however the concentration exceeds 1.1 % an increasing number of nuclear spins is occupying the closest shells. Here the Fermi contact interaction is dominating over pure dipole-dipole interaction. Thus if the number of nuclear spins in

[3] The samples were provided by Element Six Ltd. and Tokio Gas Co., Ltd. All samples except the ones marked with † were produced by MW plasma-assisted homoepitaxial chemical vapor deposition growth (CVD) using different ratios of $^{12}CH_4$ and $^{13}CH_4$. The samples marked with † were produced by high pressure high temperature technique (hpht).

that region is sufficient to smear out individual hyperfine split ODMR lines an effective broadening occurs with the same scaling as for the dipole-dipole case but with a much larger prefactor.

The phase memory time T_2 is also increasing with decreasing ^{13}C concentration. The mechanism of decoherence during a Hahn echo measurement can be simulated using the disjoint cluster approach [165]. Here the nuclear spin bath is subdivided into clusters of a few more strongly interacting nuclear spins. Within these clusters spin-spin interactions among the nuclei are taken into account whereas this interaction is neglected among different clusters. This approach predicts a dependence of the T_2 time on the average nuclear spin-spin interaction within the bath C and the characteristic interaction strength between electron and nuclear spins A_c (i.e. $T_2 \propto 1/\sqrt{CA_c}$). Because A_c and C both depend on c_{13} (i.e. $A_c,\ C \propto c_{13}$) the overall concentration dependence of the phase memory time is $T_2 \propto 1/c_{13}$. This predicted behavior is verified by our experiment. In figure 3.7b the concentration dependence of the T_2 time is displayed and it is nicely fitted by an inverse proportionality.

The Frozen core around the NV center contains those nuclear spins that possess a stronger hyperfine coupling to the NV center electron spin than the width of the energy level splitting of the bath nuclear spins. In turn these nuclear spins are decoupled from flip-flops with the rest of the bath spins due to an energy mismatch. All nuclear spins that fall into the frozen core are potential qubit candidates.

To estimate the frozen core we collect some numbers. The hyperfine coupling among the NV electron spin and a ^{13}C bath nuclear spin is on the order of 20 kHz for a distance of 1 nm (i.e. $E_{en} \approx 20\,\mathrm{kHz\,nm^3}$, see appendix A). The average distance of the nuclear spins for a concentration of 1 % is almost 1 nm and the corresponding dipole-dipole interaction among them is on the order of 10 Hz (see appendix A). Indeed, experimental results show NMR linewidths of the ^{13}C spin transition of ≈ 7 Hz [169]. The average coupling among the bath spins scales proportional to the concentration (i.e. $\tilde{E}_{nn} \sim 10\,\mathrm{Hz/\%}$ or $E_{nn} \sim 10\,\mathrm{Hz\,nm^3}$). Now we can estimate the volume of the frozen core to be $E_{en}/\tilde{E}_{nn} \sim 1000\,\mathrm{nm^3\,\%}$ (i.e. with an extend of ~ 10 nm and an inverse scaling with the concentration). Although the size of the frozen core changes the number of nuclear spins inside is constant with $E_{en}/E_{nn} \sim 1000$ spins.

The estimates for the frozen core are very rough. In addition they do not take into account the full dipole interaction with its angle dependence. However, the numbers provide a feeling for the dimensions. By the demonstrated tailoring of the nuclear spin bath it should be possible to extend the range of the frozen core further from ~ 10 nm for 1 % concentration to ~ 50 nm for 0.01 %. This becomes interesting if far away nuclear spins should be coupled to the NV spin or even nuclear spins outside the diamond lattice. After all one has to keep in mind that the frozen core only exists for electron spin projections $m_S = \pm 1$ whereas $m_S = 0$ does not possess a magnetic dipole moment which could produce a frozen core.

3.2. Initialization of a nuclear spin qubit

In the previous paragraphs nuclear spins have been introduced as qubit candidates. However, in contrast to the electron spin they are not a priori initialized (i.e. polarized in a specific nuclear spin state). In order to build a scalable quantum processor this prerequisite has to be met. A successful realization of this task is given in [32] where the electron spin polarization has been partially transferred to a particular ^{13}C nuclear spin. In a subsequent step the electron spin is repolarized while maintaining the nuclear spin polarization. A few repetitions of this sequence deterministically polarize a particular nuclear spin to a high degree. This polarized nuclear spin could then be used to store quantum information for up to 20 ms [32]. In the following the polarization method is explained in detail and its application to the ^{15}N nuclear spin is presented.

The polarization technique is realized using laser and microwave pulses to manipulate the electron spin. In addition precise control of the applied magnetic field is needed to adjust especially the nuclear spin quantization axes in different electron spin manifolds (compare section 3.1.2). The goal is to achieve a large angle η (ideally $\eta = \pi/2$) between nuclear spin quantization axes in m_S manifolds 0 and 1 [134]. The spin Hamiltonian for electron spin states $m_S = 0, 1$ and a nuclear spin $I = 1/2$ can be written as

$$\begin{aligned}\hat{H}_n &= |1\rangle\langle 1| \otimes \omega_{nL1}\hat{I}_{x1} + |0\rangle\langle 0| \otimes \omega_{nL0}\left(\hat{I}_{x1}\cos\eta + \hat{I}_{x2}\sin\eta\right) \\ &= \begin{pmatrix} \frac{\omega_{nL1}}{2} & 0 & 0 & 0 \\ 0 & -\frac{\omega_{nL1}}{2} & 0 & 0 \\ 0 & 0 & \frac{\omega_{nL0}}{2}\cos\eta & \frac{\omega_{nL0}}{2}\sin\eta \\ 0 & 0 & \frac{\omega_{nL0}}{2}\sin\eta & -\frac{\omega_{nL0}}{2}\cos\eta \end{pmatrix}\end{aligned} \tag{3.7}$$

Here ω_{nLi} are the nuclear Larmor frequencies for the respective electron spin manifolds and $\hat{I}_{x1}$ and $\hat{I}_{x2}$ are the nuclear spin operators for the perpendicular directions x_1 and x_2. The matrix representation is expressed in the basis $|m_S\rangle \otimes |m_{Ix1}\rangle = |m_S, m_{Ix1}\rangle$. Note that for small magnetic field strengths (i.e. $|\tilde{\gamma}_e B| \ll D$) the m_S quantum number is still a good quantum number regardless of the field orientation. Furthermore, for the ^{15}N nuclear spin ω_{nL1} and $x_1 = z$ are mainly determined by the hyperfine interaction[4] whereas ω_{nL0} and η are determined by the magnetic field strength and direction and are therefore adjustable. Proper field alignment is thus capable to adjust $\eta = \pi/2$. This is achieved by aligning the magnetic field B roughly perpendicular to the NV axis, say along x such that $B = B_x$ and $x_2 = x$ (see figures 3.8a,b). Hence, nuclear Zeeman interaction aligns the quantization axis roughly along x. To zero order there is no hyperfine interaction in $m_S = 0$ but to first order $m_S = 0$ acquires a magnetic moment in $-x$ direction for increasing B_x leading to a hyperfine field in this direction adding to the nuclear Zeeman field (see appendix C.1). Consequently, nZ and hf determine the nuclear spin quantization axis in $m_S = 0$ to be $x_2 = x$ and thus $\eta = \pi/2$. As a

[4] The hyperfine tensor produces a hf field of ≈ 700 mT along z in the $m_S = \pm 1$ manifolds (see section 3.1.2).

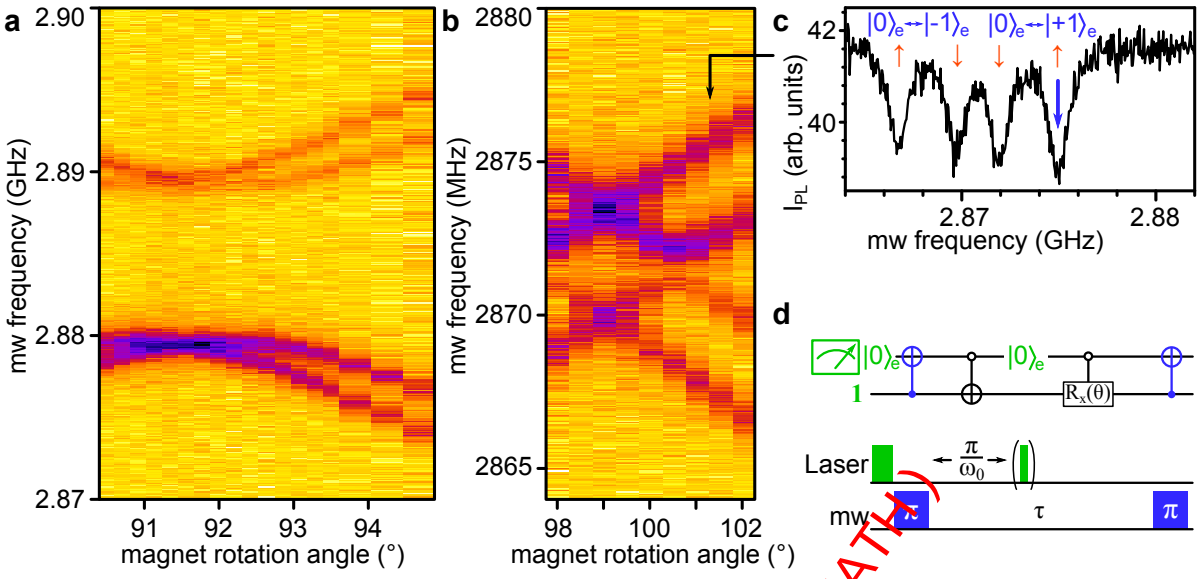

Figure 3.8.: Initialization of a single ^{15}N nuclear spin (I). a–b, ODMR spectra matrix for various magnetic field angles for magnetic field strengths 6.5 mT and 3.5 mT respectively. Where the two ODMR branches are closest the magnetic field is perpendicular to the NV axis. As explained in appendix C.1 here the hyperfine interaction is reduced. **c,** Single ODMR spectrum for 3 mT. The electron spin transitions and the nuclear spin states are marked. In addition, the working transition for nuclear spin initialization is marked by the blue arrow. **d,** Measurement sequence for nuclear spin FID with and without initialization (with and without second laser pulse, see text).

consequence, the nuclear spin states $m_{Ix} = \uparrow\downarrow$ in the $m_S = 0$ sublevel (i.e. $|0,\uparrow\downarrow\rangle$) are not eigenstates but equal superpositions states of those. For small magnetic fields in x direction $\omega_{nL0} \ll \omega_{nL1}$. In that case nuclear spin polarization is realized by the following sequence.

First, the NV center is polarized into the $m_S = 0$ state and the nuclear spin is in an incoherent superposition

$$\rho_i = |0\rangle\langle 0| \otimes \tfrac{1}{2}\left(|\downarrow\rangle\langle\downarrow| + |\uparrow\rangle\langle\uparrow|\right) \tag{3.8}$$

(see figure 3.8d). Afterwards, a nuclear spin selective electron spin π-pulse performs a CNOT gate flipping the electron spin for nuclear spin state $m_I = \uparrow$ (see figure 3.8c). The respective Rabi frequency Ω has to be chosen such that $\omega_{nL0} \ll \Omega < \omega_{nL1}$. The new state is

$$\rho_{nc} = \tfrac{1}{2}\left(|1,\uparrow\rangle\langle 1,\uparrow| + |0,\downarrow\rangle\langle 0,\downarrow|\right) . \tag{3.9}$$

During a free evolution time $\tau = (2\,\omega_{nL0})^{-1}$ under the Hamiltonian of equation (3.7) state ρ_{nc} precesses about axis x_2 conditional on electron spin state $m_S = 0$ into

$$\rho_f = \tfrac{1}{2}\left(|1\rangle\langle 1| + |0\rangle\langle 0|\right) \otimes |\uparrow\rangle\langle\uparrow| . \tag{3.10}$$

Thus the free evolution period acts as a CNOT gate flipping the nuclear spin conditional on the electron spin state. Please note further that the two different CNOT gates are similar to a SWAP gate.[5] Finally, a short laser pulse of duration $t_L \ll \omega_{nL0}^{-1}$ repolarizes the electron spin into the $m_S = 0$ state resulting in

$$\rho_0 = |0,\uparrow\rangle\langle 0,\uparrow| \ . \tag{3.11}$$

This however, is only true if the nuclear spin is not affected during the laser excitation cycle. A detailed theoretical analysis of this problem is presented in [33]. Experimental results show that under the given circumstances the effect of laser excitation on the nuclear spin is negligible [32].

In the experiment a small magnetic field roughly perpendicular to the NV axis is applied. This is verified by taking ODMR spectra at two field strengths for various magnetic field angles (see figure 3.8a,b). An ESEEM at the higher field reveals the two Larmor frequencies $\omega_{nL0} \approx 1/4\,\mathrm{MHz}$[6] and $\omega_{nL1} \approx 3\,\mathrm{MHz}$ and the depth of the modulation as compared to the Rabi amplitude gives an estimation of $\eta \approx 1$ (see figure 3.9a). A full contrast is achieved for $\eta = \pi/2$.

The nuclear spin Larmor frequency ω_{nL0} in $m_S = 0$ can also be obtained from a nuclear Ramsey measurement. We perform this at a lower magnetic field because finally we need a small ω_{nL0}. The Ramsey oscillation is realized by two consecutive CNOT gates on the electron spin separated by a free evolution time τ (see figure 3.8d). The first CNOT gate creates the quantum state ρ_{nc} where the nuclear spin in the $m_S = 0$ manifold precesses about x_2 during τ. Finally, the second CNOT gate converts the phase of this precession into a detectable population difference of the electron spin sublevels.

$$\begin{aligned}\rho_{\mathrm{fid}}(\tau) = &\tfrac{1}{2}\sin^2(\pi\tau\omega_{nL0})\,|1,\uparrow\rangle\langle 1,\uparrow| \\ &+\tfrac{1}{2}|0\rangle\langle 0| \otimes (|\uparrow\rangle\langle\uparrow| + \cos^2(\pi\tau\omega_{nL0})\,|\downarrow\rangle\langle\downarrow|)\end{aligned} \tag{3.12}$$

As can be seen from equation (3.12) and figure 3.9b the FID will oscillate with frequency $\omega_{nL0} \approx 0.06\,\mathrm{MHz}$[7] and half amplitude in theory and almost half amplitude in the experiment (the field and therefore also ω_{nL0} is reduced as compared to the ESEEM measurement). Exactly at half of one oscillation period ($\tau = (2\,\omega_{nL0})^{-1}$) the polarization has been swapped from the electron to the nuclear spin and the nuclear spin state to the electron spin (eq. (3.12)). This is where a short laser pulse ($\approx 20\,\mathrm{ns}$) has to be inserted in order to repolarize the electron spin (see figure 3.8c). The subsequent passage through the metastable state takes $\approx 250\,\mathrm{ns}$. Therefore, ω_{nL0} has to be sufficiently small to allow a relaxation before the nuclear spin state precesses too far. After that laser pulse the polarized quantum state will go on oscillating in the $m_S = 0$ state (see figure 3.9c).

[5] The actual swap gate would require an additional proceeding electron spin π-pulse (CNOT gate). This, however, is not necessary for our purposes.

[6] The bare ^{15}N Larmor frequency for the applied 6.5 mT would be 28 kHz as compared to the hyperfine enhanced 250 kHz.

[7] Without hyperfine enhancement ω_{nL0} would be 15 kHz.

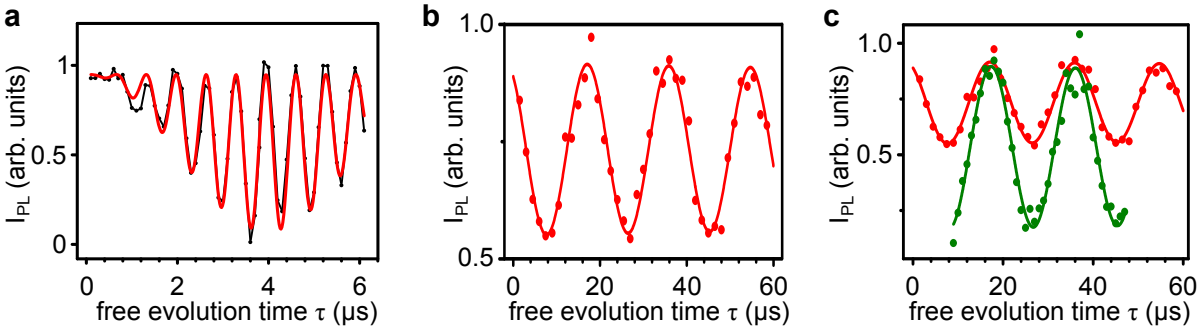

Figure 3.9.: Initialization of a single ^{15}N nuclear spin (II). **a,** ESEEM of ^{15}NV showing modulation due to the nitrogen nuclear spin. The fast oscillation is due to the hyperfine interaction in $m_S = -1$ and the slow oscillation due to the level splitting in $m_S = 0$. **b,** Ramsey oscillation of the nitrogen nuclear spin in the $m_S = 0$ manifold. **c,** A polarization laser pulse united almost all population into one nuclear spin state (doubled Ramsey amplitude of green curve).

This oscillation is probed again by a CNOT gate on the electron spin conditional on the nuclear spin state $m_I = \uparrow$. The final population in the $m_S = 1$ state is

$$\mathrm{Tr}(|1,\uparrow\rangle\langle 1,\uparrow| \rho_{\mathrm{fid}}(\tau,\mathcal{P})) = p_0 + \mathcal{P}\sin^2(\pi\tau\omega_{nL0})\Big|_{\tau>(2\,\omega_{nL0})^{-1}} \tag{3.13}$$

and we would like to define the polarization as the oscillation amplitude. Using this technique the degree of polarization reached is $\mathcal{P} = 0.76$. The equivalent nuclear spin temperature in this case is $\approx 1.5\,\mu$K.[8] In the presented experiment maximum polarization is achieved already after one cycle. Further cycles have not improved $\mathcal{P}$.

Summarizing, we can say that the proposed method is a versatile tool for qubit initialization. The crucial point for it to work is the preservation of the nuclear spin state during laser excitation and relaxation. Obviously, the time in the triplet excited state and the metastable singlet state are short enough to inhibit potential interactions that might flip the nuclear spin. The SWAP gate presented here relied on nuclear spin CNOT gates realized by Larmor precession. In a potential application with more than one nuclear spin it might become necessary to change the magnetic field strength and direction to address different spins. In such a situation it might become more efficient to realize the CNOT gates by applying the appropriate NMR frequency radiation on the nuclear spins.

3.3. Non-local states — The heart of a quantum processor

In [27] it was shown that controlled qubit gates can be realized in a system comprising of an NV electron spin and the nuclear spin of a ^{13}C atom in the first coordination

[8] 1.5 μK would lead to thermal spin polarization of $\mathcal{P} = 0.76$ for a level splitting of $\omega_{nL0} = 0.06$ MHz.

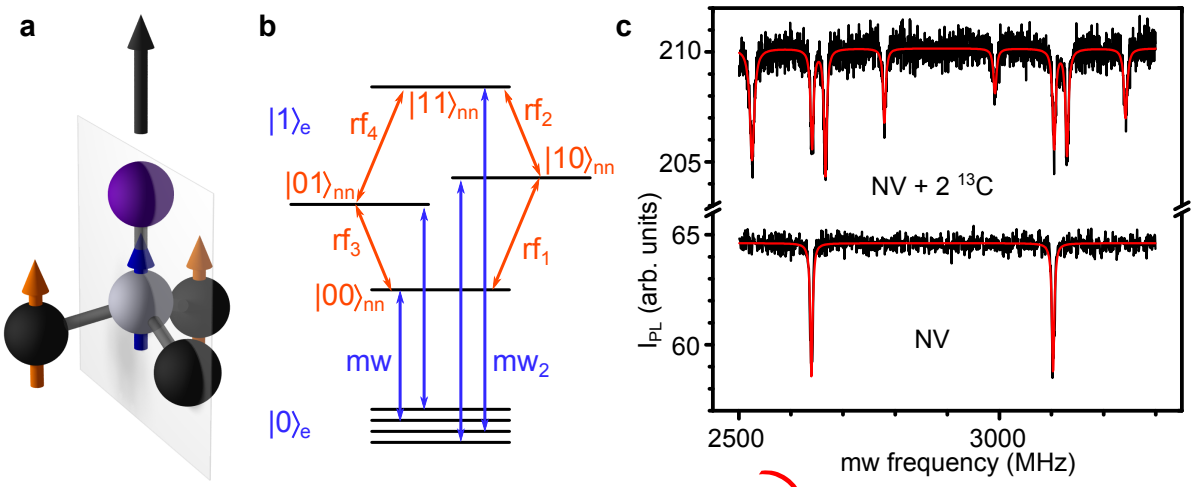

Figure 3.10.: NV center with two ^{13}C nuclei in the first coordination shell. **a,** NV center in the diamond lattice including first coordination shell of carbon atoms, two of which are ^{13}C isotopes. **b,** Spin energy level spectrum including electron spin $m_S = 0, -1$ ($|0\rangle_e$, $|1\rangle_e$) levels times the four levels corresponding to the 2 nuclear spins with $I = 1/2$. For the names see text. **c,** Upper ODMR spectrum at 8.32 mT shows large hyperfine splitting due to the 2 nuclear spins. Both EPR transitions are show, the red curve is a fit. Lower ODMR spectrum is a bare NV center at the same magnetic field as comparison.

shell. Finally, one would like to create non-local states in such registers. Therefore, the generation and tomography of entangled states in a three qubit quantum register is presented next. The register comprises of the NV electron spin plus two ^{13}C nuclear spins in the first coordination shell (i.e. one ^{13}C nuclear spin more than in the case of [27]). This enables to generate entanglement in a purely nuclear spin environment. If the electron spin is included in addition, tripartite entanglement can be generated.

3.3.1. Two nearest neighbor ^{13}C nuclear spins

At first, the system is introduced focusing on interaction strength, energy levels and eigenstates. The NV defect with two ^{13}C isotopes in the first coordination shell is depicted in figure 3.10a. In addition a mirror plane is highlighted showing the reduced symmetry when taking into account the nuclear spins. The NV spin exerts a large hyperfine field on both nuclei and vice versa. This yields the ODMR spectrum shown in figure 3.10c.

The spin Hamiltonian describing the system and finally the spectrum can be written in the following way,

$$\begin{aligned} \hat{H} &= \hat{H}_{NV} + \hat{H}_{n1} + \hat{H}_{n2} \\ &= \hat{H}_{NV} + \hat{H}_{nZ1} + \hat{H}_{nZ2} + \underline{\hat{S}} \cdot \sum_{i=1..2} \mathbf{A}_i \cdot \underline{\hat{I}}_i \end{aligned} \tag{3.14}$$

where the subscript i enumerate the ^{13}C nuclear spins. Please note that both hyperfine tensors $\mathbf{A}_i$ posses the same constants $a_{iso} = 150.33\,\text{MHz}$ and $b = 27.33\,\text{MHz}$ [106]. But their symmetry axis is not parallel to the one of the NV center. This implies that both tensors are also not parallel and therefore have different reference frames and thus different representations in the lab frame.

According to secular approximation the two central lines in figure 3.10c would fall together. However, as can be seen the hyperfine constants are still smaller than D but are sufficiently strong such that the non-secular terms should not be neglected. Thus, the hyperfine interaction between electron and nuclear spins leads to a certain mixing of the electron spin states $m_S = 0, \pm 1$. Second order perturbation theory taking into account also the non-secular terms leads to a splitting of the formerly degenerate central lines [133] (cf. 3.10c, appendix C.1). This gives a qualitative explanation of the spectrum and even the strength of the splitting is quite well reproduced.

Another consequence of the perturbation approach are the new eigenstates. As the two nuclear spins are a priori not distinguishable the single spin product basis is not appropriate. Indeed the approximation mentioned above assumes the nuclear spin eigenstates to be triplets and a singlet whereas the electron spin states are only changed slightly. The different orientations of the hyperfine tensors of the two nuclei, however, distort the singlet - triplet eigenfunctions. The indistinguishability of the two nuclear spins can be lifted by variations in the very local environment of the nuclei or by magnetic or electric fields that do not possess the shown mirror symmetry. The correct eigenstates and eigenenergies can be obtained by diagonalizing the spin Hamiltonian (3.14). In the appendix C.1 the resulting energy levels and the electron and nuclear spin resonance spectra are shown. Especially the EPR spectrum of figure 3.10c was well reproduced.

In the energy level scheme obtained above qubits can be encoded. The whole spin state $\Psi = \Psi_e \otimes \Psi_n$ can be written as a product state of a mainly electronic spin part Ψ_e and a mainly nuclear spin part Ψ_n. The electronic spin part represents one qubit E. Starting in the $m_S = -1$ manifold which we label $\Psi_e = |E = 1\rangle_e$ ($m_S = 0 \rightarrow \Psi_e = |E = 0\rangle_e$) we can encode two nuclear spin qubits N_1 and N_2 as $\Psi_n = |N_1\, N_2\rangle_{nn}$ in the 4 nuclear spin energy levels. This is done straight forward according to the NMR transitions that can be driven (cf. 3.10b). Please note that the qubit states are encoded in the given eigenstates and can therefore not be identified with single nuclear spin product states (i.e. $|m_{I1}\rangle_{n1} \otimes |m_{I2}\rangle_{n2}$) in general [170, 171]. Whereas this is possible for the states $|00\rangle_{nn} = |\uparrow\rangle_{n1} \otimes |\uparrow\rangle_{n2}$ and $|11\rangle_{nn} = |\downarrow\rangle_{n1} \otimes |\downarrow\rangle_{n2}$ it is not possible for states $|01\rangle_{nn}$ and $|10\rangle_{nn}$ where $|01\rangle_{nn}$ has strong singlet character and $|01\rangle_{nn}$ has triplet character (see appendix C.1).

3.3.2. Characterization of the qubit system

The system comprised of qubits E, N_1 and N_2 has to be characterized for the use as a quantum register. Therefore, the energy level scheme calculated from the Hamiltonian has to be verified, basic qubit gates have to be implemented and an initialization proce-

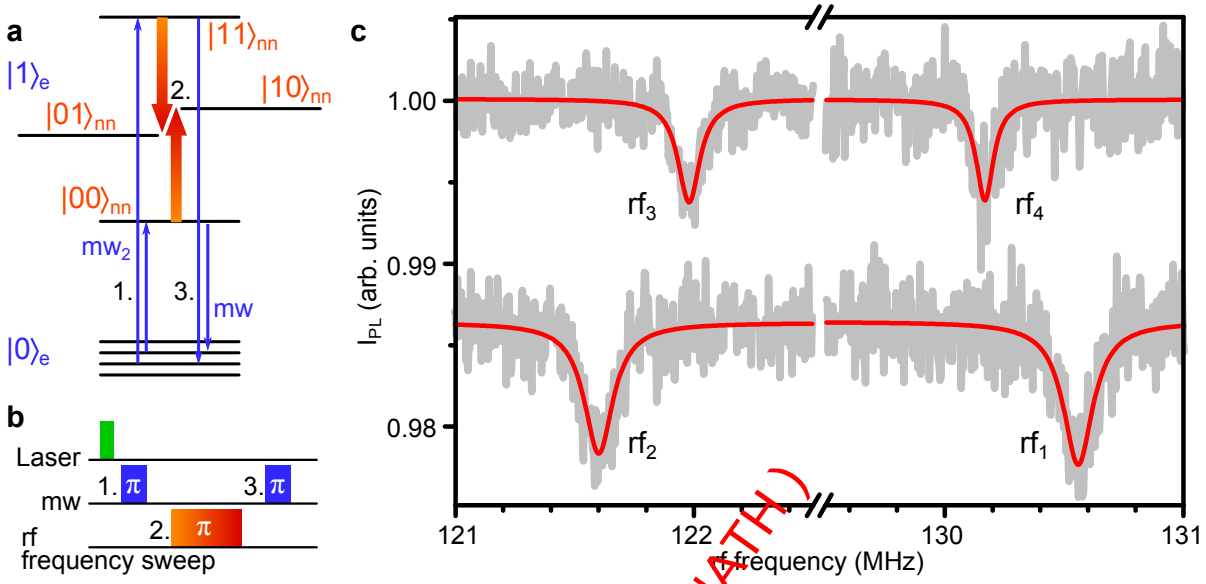

Figure 3.11.: ENDOR spectra of ^{13}C nuclear spins. **a,** Energy level scheme containing mw and rf pulses to find rf resonance frequencies. Bold orange arrows with changing color indicate frequency sweeps. **b,** Measurement sequence containing laser initialization, mw π-pulse (either mw or mw_2) and rf π-pulse with swept frequency. A spectrum is recorded as the rf frequency is swept while the sequence is running. **c,** Actual spectra showing the correct transition frequencies for figure 3.10b.

dure is needed.

After the application of a green laser pulse the electron spin state is polarized into $\Psi_e = |0\rangle_e$ and the nuclear spins are in an incoherent mixture $\rho_{nn} = \mathbf{1}_{nn}$. The nuclear spins can be either initialized by an additional procedure (e.g. one of those presented in sections 3.2 (p. 70) and 5.1 (p. 100)) or probabilistic initialization of the nuclear spin in a certain electron spin sublevel can be performed by the application of a nuclear spin state selective π-pulse on the electron spin (CNOT gate). Here, we apply a CNOT gate on the electron spin conditional on the nuclear spin state $\Psi_n = |00\rangle_{nn}$. Because of the incoherent mixture of nuclear spin states in the first place this CNOT will result in $\Psi = |1\rangle_e \otimes |00\rangle_{nn}$ which occurs only in one fourth of the time. Only then the following operations will have an effect on the final fluorescence signal.

To manipulate the nuclear spin qubits in the $|1\rangle_e$ level we have to know the exact nuclear spin transition frequencies (see figure 3.11a). As a starting point the results of the diagonalized Hamiltonian are appropriate. To refine the transition frequencies electron-nuclear double resonance (ENDOR) spectra are taken (see figure 3.11 and appendix B.4). Starting with the initialized state $\Psi = |1\rangle_e \otimes |00\rangle_{nn}$ an rf pulse almost in resonance with transition $|1\rangle_e \otimes |00\rangle_{nn} \leftrightarrow |1\rangle_e \otimes |01\rangle_{nn}$ or $|1\rangle_e \otimes |00\rangle_{nn} \leftrightarrow |1\rangle_e \otimes |10\rangle_{nn}$ is applied. Please note that this operation is a CROT gate. The resulting nuclear spin state is measured by correlation with the electron spin state via a CNOT gate. Afterwards the electron spin

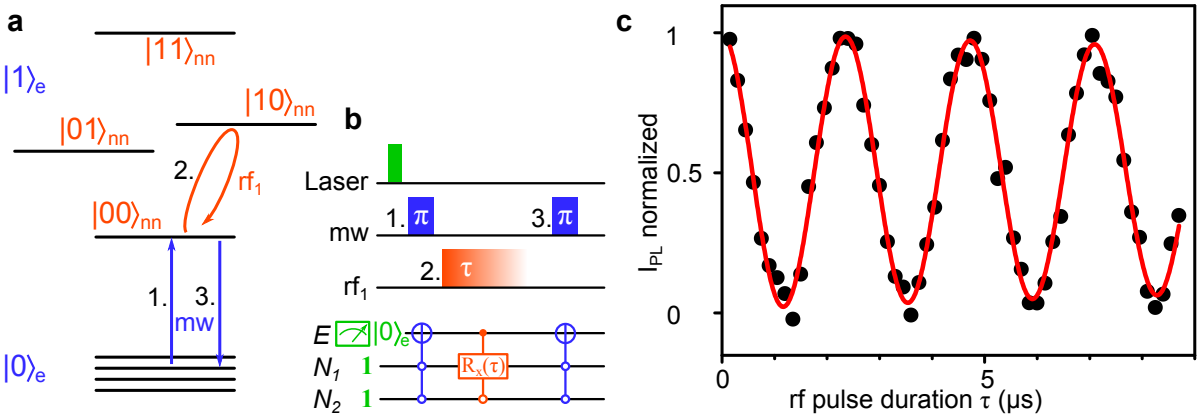

Figure 3.12.: Coherent manipulation of ^{13}C nuclear spins. **a,** Energy level scheme with arrows corresponding to mw and rf transitions used for monitoring nuclear spin Rabi oscillations. **b,** Pulse sequence for the experiment. A laser pulse initializes the electron spin into $|0\rangle_e$, then a mw π-pulse flips the electron spin for nuclear spin state $|00\rangle_{nn}$ and a subsequent rf pulse resonant for the illustrated transition rotates the nuclear spin. Finally, spin state $|1\rangle_e|00\rangle_{nn}$ is probed by a second mw pulse and the laser pulse of the next sequence. **c,** Measurement outcome. The fluorescence level oscillates while the nuclear spin is rotated. The vertical axis corresponds to the population that is found in state $|1\rangle_e \otimes |00\rangle_{nn}$.

state is measured by a readout laser pulse. When the rf frequency is swept around the expected transition frequencies the resonances appear (cf. 3.11a,c). The rf frequencies for transitions $|1\rangle_e \otimes |11\rangle_{nn} \leftrightarrow |1\rangle_e \otimes |01\rangle_{nn}$ and $|1\rangle_e \otimes |11\rangle_{nn} \leftrightarrow |1\rangle_e \otimes |10\rangle_{nn}$ are obtained in a similar fashion but starting with state $|1\rangle_e \otimes |11\rangle_{nn}$ instead of $|1\rangle_e \otimes |00\rangle_{nn}$.

Due to the finite rf pulse lengths of a few µs (see figure 3.11b) the linewidth is limited. Nuclear spin Ramsey measurements reveal a nuclear spin T_2^* of more than several hundred µs and a T_2 time that is limited by the electron spin T_1 time.

Knowing the exact resonance frequencies we can start driving coherent Rabi oscillations on these transitions from which we deduce $\pi/2$ and π pulse lengths. As these Rabi oscillations are conditional rotations the $\pi/2$ and π pulses are conditional Hadamard and CNOT/Toffoli gates respectively. The corresponding pulse sequences and Rabi oscillations are shown in figure 3.12. Apparently, the Rabi frequency is very high for nuclear spins which can be attributed to hyperfine enhancement (compare section 3.1.2). In addition the Rabi oscillations exhibit a cosine form without any decay underlining the superior coherence properties of nuclear spins as compared to electron spins.

3.3.3. Generation and detection of entanglement

Generation of entangled states Up to now we have generated only superposition states of one qubit (e.g. $|0\rangle_1 + |1\rangle_1$). When working with several qubits there is as well the possibility to create these superposition states on each qubit individually leading

to a separable or product state (e.g. $(|0\rangle_1 + |1\rangle_1) \otimes (|0\rangle_2 + |1\rangle_2)$). In addition a new kind of superposition states arises, namely the entangled state. Bluntly speaking these are superpositions of states which differ in more than one qubit (e.g. $(|0\rangle_1 \otimes |0\rangle_2) + (|1\rangle_2 \otimes |1\rangle_2)$). More precisely, entanglement is present if a state $|\Psi\rangle$ is not separable, i.e. it cannot be written as a product state. In order to access the whole Hilbert space spanned by the present qubits we also have to be able to generate all product states and all entangled states.

In the following the generation and detection of the most basic and most popular entangled states namely the Bell states is presented and in addition entanglement among 3 qubits by generation and detection of the so called GHZ and W states.

The Bell states

$$\Psi^{\pm} = |01\rangle_{nn} \pm |10\rangle_{nn} \tag{3.15a}$$
$$\Phi^{\pm} = |00\rangle_{nn} \pm |11\rangle_{nn} \tag{3.15b}$$

are encoded among the nuclear spins in the electron state $\Psi_e = |1\rangle_e$. Starting with $|00\rangle_{nn}$ a conditional Hadamard gate one the first qubit generates $(|00\rangle_{nn} + |10\rangle_{nn})$ and a final CNOT gate on the second qubit leads to Φ^+ if the former CNOT gate is conditional on the state "0" the resulting state would be Ψ^+. By adjusting the Hadamard gate also Ψ^- and Φ^- can be generated.

The generation of the GHZ state starts with the Bell state Φ^+. Because this Bell state is present in the electronic spin state $\Psi_e = |1\rangle_e$ a Toffoli gate on the electron spin conditional on state $\Psi_n = |00\rangle_{nn}$ results in the GHZ state

$$\mathrm{GHZ} = |0\rangle_e \otimes |00\rangle_{nn} + |1\rangle_e \otimes |11\rangle_{nn}\,. \tag{3.16}$$

The W state is the following equal superposition state of three eigenstates,

$$\mathrm{W} = |0\rangle_e \otimes |11\rangle_{nn} + |1\rangle_e \otimes |10\rangle_{nn} + |1\rangle_e \otimes |01\rangle_{nn}\,. \tag{3.17}$$

Its creation is a bit more complex. We start with state $|1\rangle_e \otimes |11\rangle_{nn}$. A CROT gate on qubit N_2 with a rotation angle of about $\alpha = 70.5°$ $(= 2\arccos\sqrt{2/3})$ results in $\sqrt{1/3}\,|1\rangle_e \otimes |10\rangle_{nn} + \sqrt{2/3}\,|1\rangle_e \otimes |11\rangle_{nn}$. Then a CROT gate on qubit N_1 with a rotation angle of $\pi/2$ leads to $|1\rangle_e \otimes |10\rangle_{nn} + |1\rangle_e \otimes |11\rangle_{nn} + |1\rangle_e \otimes |01\rangle_{nn}$. Finally, a toffoli gate on the electron spin conditional on the nuclear spins state $|11\rangle_{nn}$ leads to the W state.

The pulse sequences and the quantum circuit diagrams corresponding to the generation of the mentioned entangled states are shown in figure 3.13 and summarized in tables 3.5, 3.6 and 3.7.

Detection of entangled states The entanglement can be measured in different ways. Monitoring the coherent evolution of the phase of the entangled states as presented in

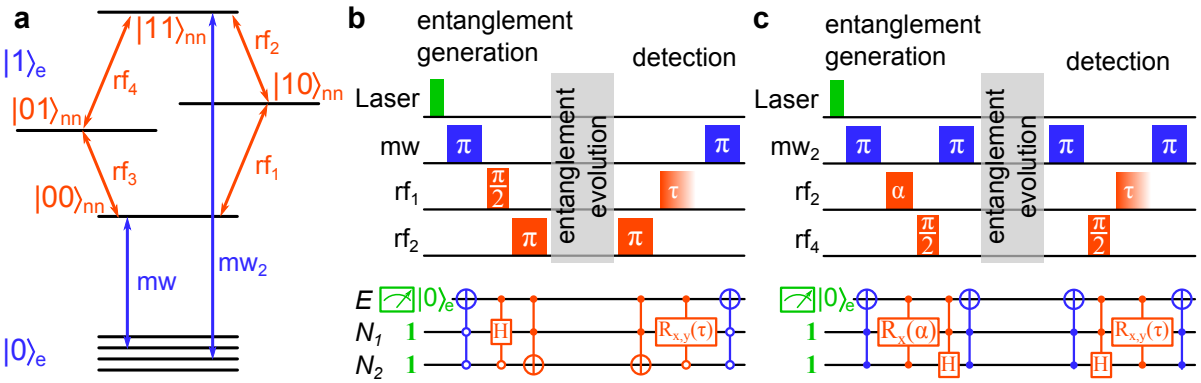

Figure 3.13.: Sequence for entanglement generation and detection. **a,** Energy level scheme showing contributing spin states and mw and rf transitions used. **b,** Exemplary sequence to generate and detect the Φ^- Bell state (see text). The other Bell states are created by changing the frequency of the rf_2 pulse and length and frequency of the rf_1 pulse. To record Ramsey oscillations the free evolution time is varied and the final rf_1 pulse is a $\pi/2$-pulse. For state tomography the final rf_1 pulse length is varied (Rabi oscillation) for two 90° phase shifted rf fields. **c,** Sequence to generate and detect the W state (analogous to Bell states, see text).

[87] is one possibility doing a quantum state tomography is another one.

The phase of an entangled state evolves characteristically with respect to the driving fields that are used to generate the entangled state. This evolution can be monitored in a Ramsey type of experiment which yields oscillation amplitude, frequency and phase. The frequency and phase are necessary to identify the entangled state and the amplitude can be used to estimate the amount of entanglement. In the case of the Bell states for the generation of entanglement two rf driving fields are used. These are rf_1 and rf_2 for the $\Phi^\pm$ states and rf_1 and rf_3 for the $\Psi^\pm$ states (see figure 3.10b). Both driving fields can have a detuning from resonance $\Delta\nu_i$. The phase of the Bell states depends on these detunings in the following way,

$$\Psi^+: \quad \varphi_\Psi^+ = 2\pi(\Delta\nu_1 - \Delta\nu_3)\tau \tag{3.18a}$$
$$\Psi^-: \quad \varphi_\Psi^- = 2\pi(\Delta\nu_1 - \Delta\nu_3)\tau + \pi \tag{3.18b}$$
$$\Phi^+: \quad \varphi_\Phi^+ = 2\pi(\Delta\nu_1 + \Delta\nu_2)\tau \tag{3.18c}$$
$$\Phi^-: \quad \varphi_\Phi^- = 2\pi(\Delta\nu_1 + \Delta\nu_2)\tau + \pi \tag{3.18d}$$

where τ is the free evolution period of the entangled state in the Ramsey experiment.

The actual experimental sequence can be divided into three steps. First, starting from state $\psi_i = |00\rangle_{nn}$ (in electron spin manifold $|1\rangle_e$) the entangled state is generated, afterwards it evolves freely for time τ and eventually it is unitarily transformed back to a final state ψ_f (see figure 3.13b). If $\tau = 0$ no phase is accumulated and the final state is $\psi_i = \psi_f = |00\rangle_{nn}$ which is read out by correlating it with electron spin state $|0\rangle_e$. If

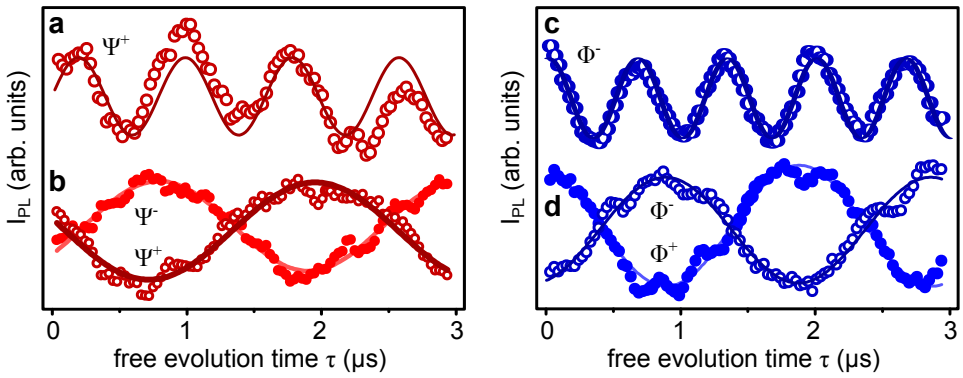

Figure 3.14.: Ramsey interferometry with entangled states. **a,** Ramsey oscillation of Ψ^+ Bell state. The frequency should be $\Delta\nu_1 - \Delta\nu_3 = 1\,\mathrm{MHz} - (-0.3\,\mathrm{MHz}) = 1.3\,\mathrm{MHz}$ and the fit yields 1.25 MHz. **b,** Ramsey oscillations of Ψ^+ and Ψ^- reveals their π phase shift. **c,** Ramsey oscillation of Φ^- Bell state. The frequency should be $\Delta\nu_1 + \Delta\nu_2 = 0.5\,\mathrm{MHz} + 1\,\mathrm{MHz} = 1.5\,\mathrm{MHz}$ and the fit yields 1.51 MHz. **d,** Ramsey oscillations of Φ^+ and Φ^- reveals their π phase shift.

however $\tau \neq 0$ a phase is accumulated and the population of state $|00\rangle_{nn}$ evolves as

$$\left|\langle\psi_f|00\rangle_{nn}\right|^2 = A\cdot\cos^2\left(\frac{\varphi^{\pm}_{\Psi,\Phi}}{2}\right) + p_0. \tag{3.19}$$

The fluorescence intensity is modulated in the same way. Here A is a measure for the amount of entanglement and p_0 is a population offset that can be larger than 0 if $A < 1$. The maximum value of A is 1 which corresponds to a maximally entangled Bell state. Figure 3.14 shows the measurement results for detunings $\Delta\nu_i$ given in the caption. Obviously the Ramsey frequencies and the detunings obey equations (3.18). In addition the "+" and "−" versions of the Ψ and Φ Bell states show Ramsey oscillations that are phase shifted by π as compared to their counterparts (see figure 3.14b,d).

A second possibility to unambiguously prove entanglement is quantum state tomography. Therefore, the whole density matrix of the entangled state has to be reconstructed. This includes all populations and the quantum coherences among them. The method to reconstruct the density matrix will be explained next on the example of the nuclear spin qubits in the $|1\rangle_e$ manifold exhibiting a 4×4 density matrix.

To begin with we have a look on the population and coherences in and among states $|00\rangle_{nn}$ and $|10\rangle_{nn}$ and neglect all other entries in the density matrix ρ (basis: $|11\rangle_{nn}$, $|10\rangle_{nn}$, $|01\rangle_{nn}$, $|00\rangle_{nn}$).

$$\rho = \rho_{t1} = \begin{pmatrix} \cdot & \cdot & \cdot & \cdot \\ \cdot & a & \cdot & b+ic \\ \cdot & \cdot & \cdot & \cdot \\ \cdot & b-ic & \cdot & d \end{pmatrix}; \quad \begin{array}{c} a,b,c,d \in \mathbb{R} \\ a,d \geq 0 \\ 0 \leq a+d \leq 1 \\ ad \geq b^2+c^2 \end{array} \tag{3.20}$$

Usually the entry $\rho_{4,4} = |00\rangle_{nn}\langle 00|_{nn}$ is probed by correlating it with electron spin state $|0\rangle_e$ and reading out the latter, which yields d. The value of a is measured by first applying a Toffoli gate on nuclear spin qubit N_1 controlled by $|1\rangle_e \otimes |0\_\rangle_{nn}$ (i.e. an rf π-pulse on transition rf_1 which transforms ρ into ρ_{t2}) and then reading out.

$$\rho_{t2}^{sub} = \begin{pmatrix} 0 & i \\ i & 0 \end{pmatrix} \begin{pmatrix} a & b+ic \\ b-ic & d \end{pmatrix} \begin{pmatrix} 0 & -i \\ -i & 0 \end{pmatrix} = \begin{pmatrix} d & b-ic \\ b+ic & a \end{pmatrix} \tag{3.21}$$

To measure the off-diagonal elements b and c, rf $\pi/2$-pulses (controlled Hadamard gates) on the same transition rf_1 are applied, once around the rotating frame x-axis and once around the y-axis each followed by a readout step.

$$x: \ \rho_{t3}^{sub} = \frac{1}{2}\begin{pmatrix} 1 & i \\ i & 1 \end{pmatrix} \begin{pmatrix} a & b+ic \\ b-ic & d \end{pmatrix} \begin{pmatrix} 1 & -i \\ -i & 1 \end{pmatrix} = \begin{pmatrix} \frac{a+d}{2}+c & b-i\frac{a-d}{2} \\ b+i\frac{a-d}{2} & \frac{a+d}{2}-c \end{pmatrix} \tag{3.22a}$$

$$y: \ \rho_{t4}^{sub} = \frac{1}{2}\begin{pmatrix} 1 & -1 \\ 1 & 1 \end{pmatrix} \begin{pmatrix} a & b+ic \\ b-ic & d \end{pmatrix} \begin{pmatrix} 1 & 1 \\ -1 & 1 \end{pmatrix} = \begin{pmatrix} \frac{a+d}{2} & b-\frac{a-d}{2}+ic \\ \frac{a-d}{2}+ic & \frac{a+d}{2}+b \end{pmatrix} \tag{3.22b}$$

These operations yield $\frac{a+d}{2}+b$ and $\frac{a+d}{2}-c$. Knowing a and d we can compute c and b.

So far we have worked on transition rf_1 which we call our "working transition". Using the working transition we have done tomography on a 2×2 sub-density matrix. Every other entry on the density matrix can be transferred to the working transition by Toffoli gates (i.e. appropriate rf π-pulses). As an example it is shown how the coherences $(\tilde{b}, \tilde{c})$ and populations $(\tilde{a}, d)$ of the $\Phi^{\pm}$ Bell states can be transferred to the working transition.

$$\begin{aligned} \rho_{t5} &= \begin{pmatrix} 0 & i & & \\ i & 0 & & \\ & & 1 & \\ & & & 1 \end{pmatrix} \overbrace{\begin{pmatrix} \tilde{a} & \cdot & \cdot & \tilde{b}+i\tilde{c} \\ \cdot & a & \cdot & b+ic \\ \cdot & \cdot & \cdot & \cdot \\ \tilde{b}-i\tilde{c} & b-ic & \cdot & d \end{pmatrix}}^{\rho} \begin{pmatrix} 0 & -i & & \\ -i & 0 & & \\ & & 1 & \\ & & & 1 \end{pmatrix} \\ &= \begin{pmatrix} a & \cdot & \cdot & -c+ib \\ \cdot & \tilde{a} & \cdot & -\tilde{c}+i\tilde{b} \\ \cdot & \cdot & \cdot & \cdot \\ -c-ib & -\tilde{c}-i\tilde{b} & \cdot & d \end{pmatrix} \end{aligned} \tag{3.23}$$

They are subsequently analyzed in the same way as the initial entries on the density matrix ρ_{t1}.

Instead of reading out only the entries $\rho_{4,4}$ of density matrices ρ_{t1}^{sub}, ρ_{t2}^{sub}, ... (i.e. a, b, c, d, $\tilde{a}$, $\tilde{b}$, $\tilde{c}$, ...) we have performed Rabi oscillations on the working transition rf_1 around the rotating frame axes x and y that comprise many different CROT gates including the above mentioned $\pi/2$- and π-pulses. These Rabi oscillations on rf_1 can be illustrated on the Bloch sphere and they show the conversion of populations into coherences and vice versa in a beautiful manner (see figure 3.15). The Rabi oscillations

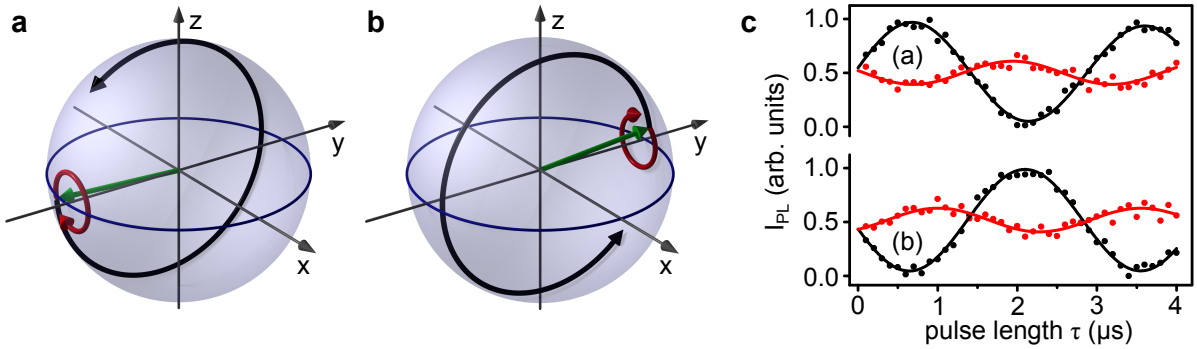

Figure 3.15.: Quantum state tomography — Rabi signal. **a,** Bloch sphere illustrating Rabi oscillations for quantum state tomography (see text). Here, the main density matrix entries of a Φ^- state (green arrow) have been transferred onto the working transition rf_1 (Bloch sphere) where the Rabi oscillations are performed around x (black line) and y axes (red line). **b,** Tomography of Φ^+. **c,** Actual measurement data of the Rabi oscillations (z-components of quantum states) for Φ^+ and Φ^- Bell states that lead to the state reconstruction shown in panel **a** (upper part) and panel **b** (lower part).

in figure 3.15c follow equations (3.24) and by fitting these formulas to the measured data we can reconstruct the density matrices.

$$x - \text{rotation} : A(t) = \frac{c+a}{2} + \frac{d-a}{2}\cos\Omega t - c\sin\Omega t \tag{3.24a}$$

$$y - \text{rotation} : A(t) = \frac{d+a}{2} + \frac{d-a}{2}\cos\Omega t + b\sin\Omega t \tag{3.24b}$$

Figures 3.15a,b illustrate the results of the Rabi oscillations for the $\Phi^{\pm}$ Bell states on the Bloch sphere.

The resulting density matrices for all four Bell states are shown in figure 3.16. They exhibit the characteristic features for entangled states. For the evaluation of entanglement we use different measures. These are the Fidelity $\mathcal{F}$, the partial transpose $\mathcal{T}_p$ and the concurrence $\mathcal{C}$ (see appendix C.4). The fidelity $\mathcal{F}$ is a measure of how well the actually generated state ρ matches the desired state σ. For a pure state σ (all Bell states are pure states) $\mathcal{F}$ can be calculated as follows.

$$\mathcal{F} = \mathrm{Tr}(\sigma\rho) \tag{3.25}$$

Here Tr is the trace of a matrix. The partial transpose $\mathcal{T}_p$ is the smallest eigenvalue of a partially transposed density matrix of two qubits. It has been shown that two qubits are entangled if and only if this partially transposed density matrix obtains a negative eigenvalue [172, 173]. Eventually, the concurrence $\mathcal{C}$ of a system of two qubits has to be larger than Zero for the entanglement of formation to be larger than Zero [174, 175]. Please note that $\mathcal{C}$ and $\mathcal{T}_p$ both are defined for systems comprising two qubits only. In table 3.4 all three mentioned entanglement measures for all four generated Bell states

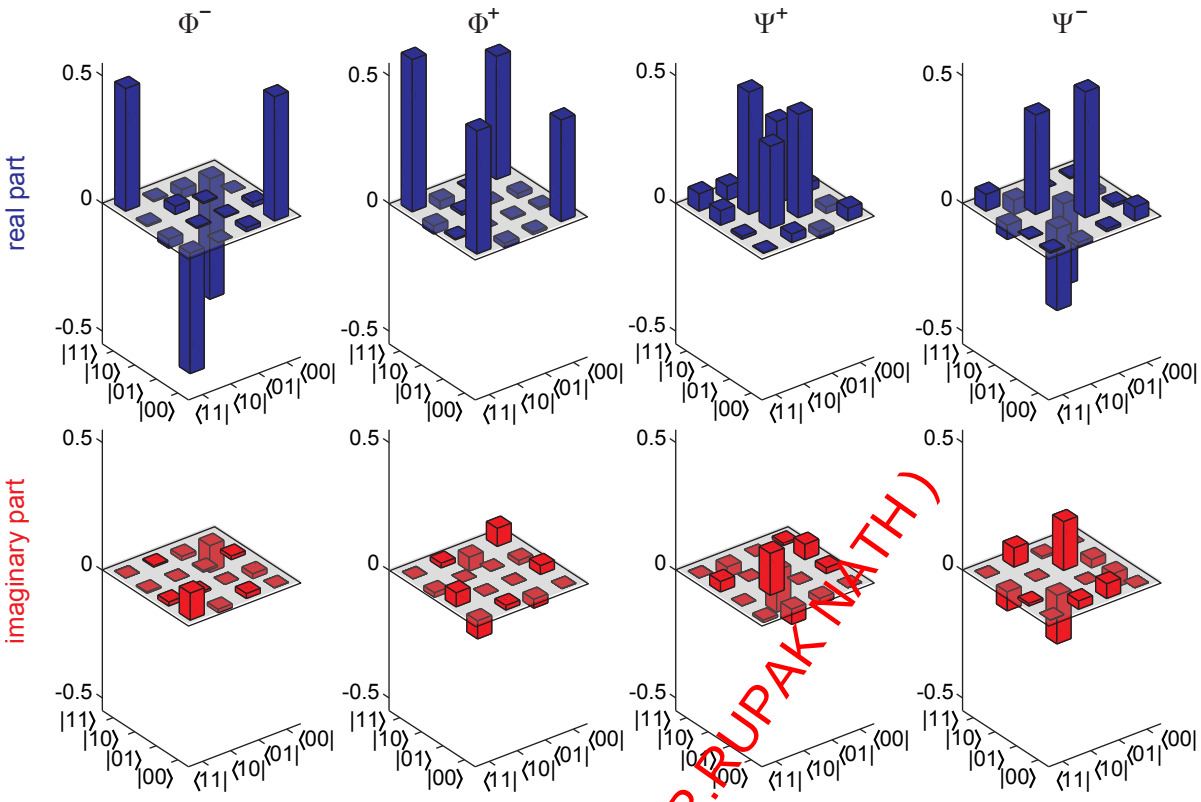

Figure 3.16.: Results of quantum state tomography for all four Bell states.

are presented. As can be seen the overlap of the generated state with the desired state is quite large. Especially for the Φ Bell states values of $\mathcal{F}$ close to one are reached; the Concurrence as well as the partial transpose verify that indeed entanglement has been created.

The deviation from the targeted Bell states can be explained by the rf pulses that were used for Bell state generation [176]. These are square pulses with lengths of a few µs. According to [176] the fidelity can be increased to values larger than 0.99 for all Bell states when specially designed robust rf pulses are used.

In addition to the degree of entanglement also the lifetime of the entangled states is of importance. Usually the coherence lifetime of an entangled state is different from that of a single qubit coherent superposition state. This behavior is expressed for instance by the phase dependence on the detuning of the driving fields as in eq. (3.18). The phase of the $\Phi^{\pm}$ Bell states for example depends on the sum of the detunings. Such a detuning can be produced by a magnetic field offset. Thus the phase of $\Phi^{\pm}$ is twice as sensitive to a magnetic field offset as the phase of a single qubit equal superposition state. This is appreciable for sensing of the magnetic field [177] but in terms of decoherence due to fluctuating magnetic fields this increased sensitivity decreases the coherence lifetime of this entangled state.

	Fidelity $\mathcal{F}$	Concurrence $\mathcal{C}$	partial transpose $\mathcal{T}_p$
Ψ^+	0.80 ± 0.07	$0.65^{+0.15}_{-0.08}$	$-0.31^{+0.05}_{-0.06}$
Ψ^-	0.81 ± 0.06	0.59 ± 0.11	$-0.32^{+0.04}_{-0.05}$
Φ^+	0.98 ± 0.05	$0.96^{+0.04}_{-0.09}$	$-0.49^{+0.04}_{-0.02}$
Φ^-	0.96 ± 0.05	$0.92^{+0.07}_{-0.08}$	$-0.47^{+0.05}_{-0.06}$
GHZ	0.87 ± 0.06	—	—
W	$0.85^{+0.05}_{-0.1}$	—	—

Table 3.4.: Entanglement measures for the generated Bell states and the GHZ and W states. The partial transpose and the Concurrence are only defined for two qubit systems.

Some entangled states exhibit reduced phase sensitivity on global magnetic fields (i.e. magnetic fields that have an equal effect on both qubits making up the entangled pair) and thus a reduced decoherence rate. As an example we have a look on the $\Psi^{\pm}$ Bell states. They are made up out of superpositions of states $\Phi_n = |01\rangle_{nn}$ and $|10\rangle_{nn}$ whose energy splitting is less sensitive to magnetic field changes. Hence, the phase of the $\Psi^{\pm}$ Bell states is more robust against global magnetic field variations. Ideally these global magnetic field changes are exactly canceled [178, 179]. In our case however states $\Phi_n = |01\rangle_{nn}$ and $|10\rangle_{nn}$ are not product states of single qubit states. This changes their respective magnetic field dependence.

To monitor the coherence lifetime of the entangled states we measure the amount of coherence for different free evolution times. It turns out that every Bell state has a coherence lifetime of $\approx 4\,\mathrm{ms}$ which is similar to the electron spin T_1 time of the NV center (see figure 3.17). Thus decoherence of the nuclear spin Bell states is mainly limited by the longitudinal relaxation time of the electron spin. Differences between decoherence rates of Φ and Ψ Bell states might have shown up for longer T_1 times of the electron spin.

In this register of two ^{13}C nuclear spins first quantum algorithms have been implemented. In [37] the entanglement was used to perform superdense coding and the Deutsch algorithm.

Three-partite entanglement The detection of three-partite entanglement is done analogous to the bipartite case. Thus, one possibility is to analyze the evolution of the entangled state's phase (i.e. φ_{GHZ} for the GHZ state). It should evolve as the sum of the detunings $\Delta\nu_i$ of the driving fields in the corresponding rotating frame.

$$\mathrm{GHZ}: \quad \varphi_{\mathrm{GHZ}} = 2\pi(\Delta\nu_1 + \Delta\nu_2 + \Delta\nu_3)\tau \tag{3.26}$$

Here, $\Delta\nu_1$ and $\Delta\nu_2$ are the detunings of the rf driving fields (compare eq. (3.18c)) and $\Delta\nu_3$ is the detuning of the microwave field resonant with transition $|0\rangle_e \leftrightarrow |1\rangle_e$ for $\Psi_n = |00\rangle_{nn}$. However, due to the fast dephasing of electron spin coherence similar

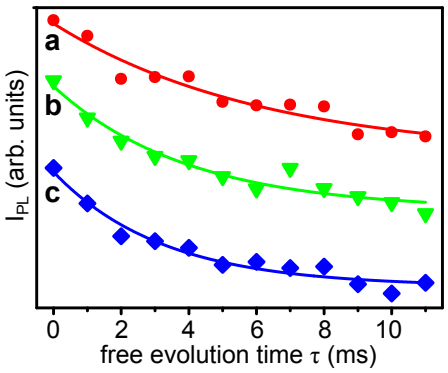

Figure 3.17.: Decay of Bell state coherence. a,b, and **c** show the decay of electron spin state polarization (T_1) and coherence (T_2) of Φ and Ψ Bell states respectively. Obviously, all decay rates are comparable.

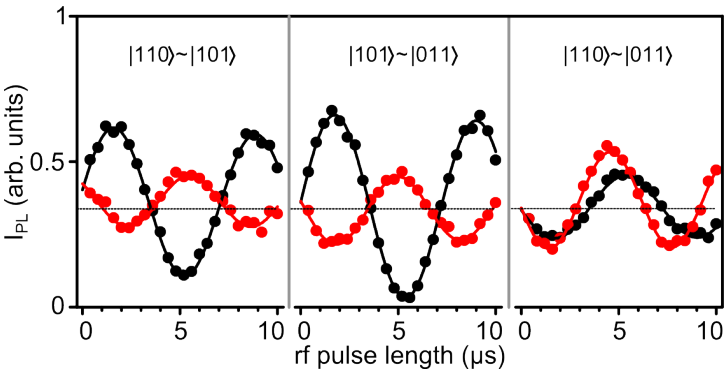

Figure 3.18.: Quantum state tomography of W state. Partial tomography of W state (see text). Populations of the main density matrix entries and respective coherences can be deduced from the presented Rabi oscillations. They correspond to transitions $|110\rangle \leftrightarrow |101\rangle$, $|101\rangle \leftrightarrow |011\rangle$ and $|110\rangle \leftrightarrow |011\rangle$ (from left to right).

Ramsey fringes as shown in figure 3.14 can not be obtained with a detectable detuning dependence.

Instead of performing Ramsey experiments the density matrix has been partially reconstructed. Namely all entries necessary for fidelity calculation (see appendix C.4) have been measured in a similar way as in the two qubit case (i.e. by Rabi oscillations of the corresponding density matrix elements on the working transition). The pulse sequences are shown in figure 3.13c and tables 3.6 and 3.7 and the acquired density matrix entries for the GHZ and the W state are shown in figure 3.19a,b (upper parts) and the resulting fidelities are presented in table 3.4.

Please note that whereas the GHZ state contains three qubit entanglement the W state does not. The W state rather contains two qubit entanglement which manifests in the following way. If any qubit of the W state is measured projectively the other two are either in an eigenstate or in a maximally entangled Bell state conditional on the result of the projective measurement. Thus, even when tracing out one qubit the other two have some degree of entanglement. This behavior becomes visible when looking at the time evolution of the coherences of the entangled states.

The evolution of coherences of the entangled states is monitored by performing partial density matrix reconstruction after several free evolution times of the entangled states. For the GHZ state only one coherence (namely the one between $\Psi = |0\rangle_e \otimes |00\rangle_{nn}$ and $|1\rangle_e \otimes |11\rangle_{nn}$) has to be monitored. Because of the much shorter coherence lifetime of the electron spin which is part of the entanglement now the coherence of the GHZ state decays within 2 µs (see figure 3.19c). Please note that the measurement sequence is of Ramsey type (see figure 3.13). Thus we see decay due to inhomogeneous broadening with lifetime T_2^*. In addition to the partial density matrix reconstruction of the initial

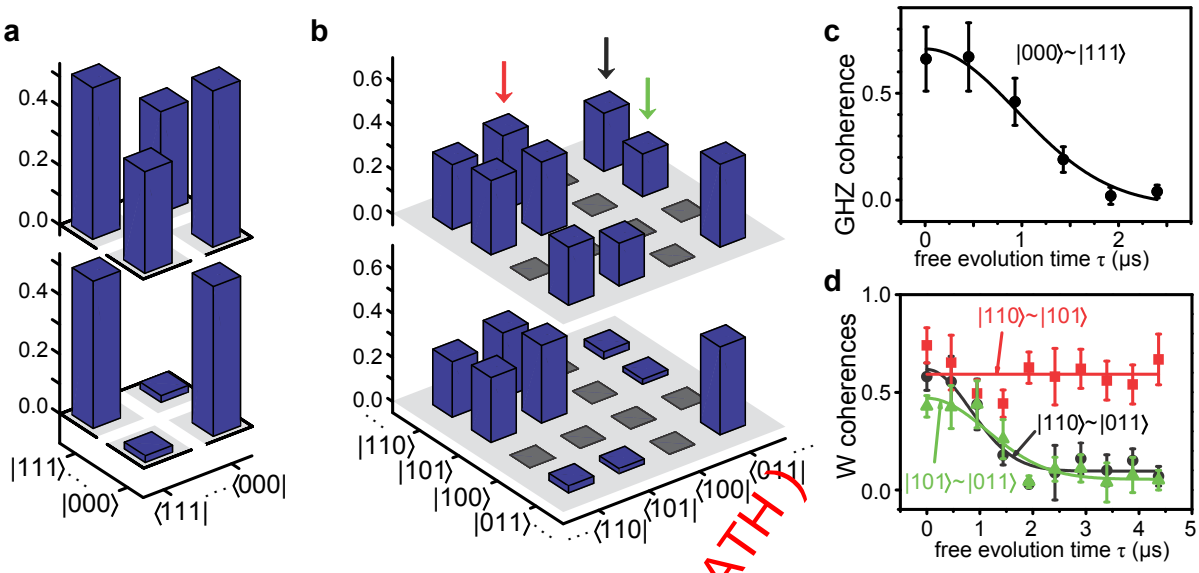

Figure 3.19.: Results of quantum state tomography of GHZ and W states. **a,** Partial tomography of the GHZ state showing only the main density matrix entries. The upper part is for zero evolution time (see figure 3.13) and the lower part shows the decayed coherences after 2.4 µs. **b,** Partial tomography of the W state (gray entries have not been measured). Red, green and black arrows mark the three different coherences. The upper topography is taken right after generation the lower one after an evolution time of 4.4 µs. The bare nuclear spin coherence (red arrow) survives longest. **c, d,** Decay of GHZ and W states' coherences respectively for increasing free evolution time. For the GHZ state the decay of the single coherence (off-diagonal density matrix entry) is shown whereas for the W state three coherences decay (for color coding see panel **b**).

GHZ state another reconstruction is shown for an evolution time $> T_2^*$ (see figure 3.19a lower part). As expected the populations of states eigenstates $\Psi = |0\rangle_e \otimes |00\rangle_{nn}$ and $|1\rangle_e \otimes |11\rangle_{nn}$ remained but the coherence among them has decayed. Hence, only classical correlations are left.

When monitoring the evolution of the W state we have to keep track of three coherences (namely those among $\Psi = |0\rangle_e \otimes |11\rangle_{nn}$, $|1\rangle_e \otimes |10\rangle_{nn}$ and $|1\rangle_e \otimes |01\rangle_{nn}$, see figure 3.18). Taking a closer look at these states we recognize that a phase between states $|1\rangle_e \otimes |01\rangle_{nn}$ and $|1\rangle_e \otimes |10\rangle_{nn}$ does not possess electron spin character whereas the other two phases (i.e. the ones between one of the former two states and $|0\rangle_e \otimes |11\rangle_{nn}$) do. Thus we expect different decay characteristics for these coherences. Indeed, figures 3.19b,d show that two coherences of the W state decay within 2 µs whereas one coherence persists for at least 4 µs. It is the purely nuclear spin coherence that remains.

The fast decay of the electron spin coherence can be explained as a measurement of the electron spin state by the environment. This measurement happens much faster for the electron spin than for the nuclear spins because the much larger electron spin magnetic moment. The measurement has two possible outcomes, electron spin state "0"

or “1”. Whereas the “1” case delivers an entangled nuclear spin state case “0” delivers a nuclear spin eigenstate. This is verified by the density matrix reconstruction that was measured for phase accumulation time $\tau > 2\,\mu s$ (lower part of figure 3.19b).

id	transition	pulse	phase
	Bell state generation		
1.	Laser pulse, initialize $\|0\rangle_e\langle 0\|_e \otimes \mathbf{1}_{4\times4}$	$3\,\mu s$	—
2.	mw, $(\|0\rangle_e \leftrightarrow \|1\rangle_e) \otimes \|00\rangle_{nn}$	π	0
3.	rf, $\|1\rangle_e \otimes \begin{matrix}\|00\rangle_{nn} \leftrightarrow \|10\rangle_{nn} & (\Phi^{\pm}) \\ \|00\rangle_{nn} \leftrightarrow \|01\rangle_{nn} & (\Psi^{\pm})\end{matrix}$	$\pi/2$ or $3\pi/2$, $(\pm)$	0
4.	rf, $\|1\rangle_e \otimes \begin{matrix}\|10\rangle_{nn} \leftrightarrow \|11\rangle_{nn} & (\Phi^{\pm}) \\ \|00\rangle_{nn} \leftrightarrow \|10\rangle_{nn} & (\Psi^{\pm})\end{matrix}$	π	0
	transfer partial density matrices to working transition $\|1\rangle_e \otimes (\|00\rangle_{nn} \leftrightarrow \|10\rangle_{nn})$		
$\begin{pmatrix}\rho_{22} & \rho_{24}\\ \rho_{42} & \rho_{44}\end{pmatrix}$	—	—	—
$\begin{pmatrix}\rho_{11} & \rho_{14}\\ \rho_{41} & \rho_{44}\end{pmatrix}$	rf, $\|1\rangle_e \otimes (\|10\rangle_{nn} \leftrightarrow \|11\rangle_{nn})$	π	0
$\begin{pmatrix}\rho_{11} & \rho_{12}\\ \rho_{21} & \rho_{22}\end{pmatrix}$	rf, $\|1\rangle_e \otimes \begin{matrix}1. & \|00\rangle_{nn} \leftrightarrow \|10\rangle_{nn} \\ 2. & \|10\rangle_{nn} \leftrightarrow \|11\rangle_{nn}\end{matrix}$	π π	0 0
	transfer partial density matrices to working transition $\|1\rangle_e \otimes (\|00\rangle_{nn} \leftrightarrow \|01\rangle_{nn})$		
$\begin{pmatrix}\rho_{33} & \rho_{34}\\ \rho_{43} & \rho_{44}\end{pmatrix}$	—	—	—
$\begin{pmatrix}\rho_{22} & \rho_{23}\\ \rho_{32} & \rho_{33}\end{pmatrix}$	rf, $\|1\rangle_e \otimes (\|00\rangle_{nn} \leftrightarrow \|10\rangle_{nn})$	π	0
$\begin{pmatrix}\rho_{11} & \rho_{13}\\ \rho_{31} & \rho_{33}\end{pmatrix}$	rf, $\|1\rangle_e \otimes \begin{matrix}1. & \|10\rangle_{nn} \leftrightarrow \|11\rangle_{nn} \\ 2. & \|00\rangle_{nn} \leftrightarrow \|10\rangle_{nn}\end{matrix}$	π π	0 0
	Analyze partial density matrices on working transition		
1.a 1.b	corresponding working transition	variable (Rabi)	0 $\pi/2$
2.	mw, $(\|0\rangle_e \leftrightarrow \|1\rangle_e) \otimes \|00\rangle_{nn}$	π	0
3.	Laser, readout $\|1\rangle_e\langle 1\|_e \otimes \mathbf{1}_{4\times4}$	$3\,\mu s$	—

Table 3.5.: Bell state generation and tomography. upper part, Bell state generation sequence. Point three and four are different for Φ and Ψ states. In addition, for different phases of the Bell states different pulse lengths at point three have to be chosen. **middle parts,** After any free evolution of the Bell states the tomography is performed by first transferring any partial density matrix of interest to the working transition. The sequences are shown for all available partial density matrices and their corresponding working transitions. **lower part,** Analysis of any partial density matrix by Rabi oscillations on the working transition. Two oscillations are performed with two $\pi/2$ phase shifted rf fields (see text). Finally, mw and laser pulses deliver the result.

	id	transition	pulse	phase
		GHZ state generation		
	1.	Laser pulse, initialize $\|0\rangle_e\, 0 \otimes \mathbf{1}_{4\times4}$	$3\,\mu s$	—
	2.	mw, $(\|0\rangle_e \leftrightarrow \|1\rangle_e) \otimes \|00\rangle_{nn}$	π	0
	3.	rf, $\|1\rangle_e \otimes (\|00\rangle_{nn} \leftrightarrow \|10\rangle_{nn})$	$\pi/2$	0
	4.	rf, $\|1\rangle_e \otimes (\|10\rangle_{nn} \leftrightarrow \|11\rangle_{nn})$	π	0
	5.	mw, $(\|0\rangle_e \leftrightarrow \|1\rangle_e) \otimes \|00\rangle_{nn}$	π	0
		transfer partial density matrix to working transition $\|1\rangle_e \otimes (\|00\rangle_{nn} \leftrightarrow \|10\rangle_{nn})$		
$\begin{pmatrix}\rho_{11} & \rho_{18}\\ \rho_{81} & \rho_{88}\end{pmatrix}$	1.	mw, $(\|0\rangle_e \leftrightarrow \|1\rangle_e) \otimes \|00\rangle_{nn}$	π	0
	2.	rf, $\|1\rangle_e \otimes (\|10\rangle_{nn} \leftrightarrow \|11\rangle_{nn})$	π	0
		Analyze partial density matrix on working transition		
	1.a	$\|1\rangle_e \otimes (\|00\rangle_{nn} \leftrightarrow \|10\rangle_{nn})$	variable (Rabi)	0
	1.b			$\pi/2$
	2.	mw, $(\|0\rangle_e \leftrightarrow \|1\rangle_e) \otimes \|00\rangle_{nn}$	π	0
	3.	Laser, readout $\|1\rangle\langle 1\|_e \otimes \mathbf{1}_{4\times4}$	$3\,\mu s$	—

Table 3.6.: GHZ state generation and tomography. Detailed pulse sequences for the generation and tomography of the GHZ state. **upper part,** GHZ state generation. **middle part,** After any free evolution of the GHZ state the tomography is performed by first transferring the main partial density matrix to the working transition. **lower part,** Analysis of the partial density matrix by Rabi oscillations on the working transition. Two oscillations are performed with two $\pi/2$ phase shifted rf fields (see text). Finally, mw and laser pulses deliver the result.

id	transition	pulse	phase
	W state generation		
1.	Laser pulse, initialize $\|0\rangle_e\langle 0\|_e \otimes \mathbf{1}_{4\times4}$	$3\,\mu s$	—
2.	mw, $(\|0\rangle_e \leftrightarrow \|1\rangle_e) \otimes \|11\rangle_{nn}$	π	0
3.	rf, $\|1\rangle_e \otimes (\|01\rangle_{nn} \leftrightarrow \|11\rangle_{nn})$	$2\arccos\sqrt{2/3}$	0
4.	rf, $\|1\rangle_e \otimes (\|10\rangle_{nn} \leftrightarrow \|11\rangle_{nn})$	$\pi/2$	0
5.	mw, $(\|0\rangle_e \leftrightarrow \|1\rangle_e) \otimes \|11\rangle_{nn}$	π	0
	transfer partial density matrices to working transition $\|1\rangle_e \otimes (\|10\rangle_{nn} \leftrightarrow \|11\rangle_{nn})$		
$\begin{pmatrix}\rho_{33} & \rho_{35}\\ \rho_{53} & \rho_{55}\end{pmatrix}$	mw, $(\|0\rangle_e \leftrightarrow \|1\rangle_e) \otimes \|11\rangle_{nn}$	π	0
$\begin{pmatrix}\rho_{22} & \rho_{23}\\ \rho_{32} & \rho_{33}\end{pmatrix}$	rf, $\|1\rangle_e \otimes (\|10\rangle_{nn} \leftrightarrow \|11\rangle_{nn})$	π	0
$\begin{pmatrix}\rho_{22} & \rho_{25}\\ \rho_{52} & \rho_{55}\end{pmatrix}$	1. mw, $(\|0\rangle_e \leftrightarrow \|1\rangle_e) \otimes \|11\rangle_{nn}$	π	0
	2. rf, $\|1\rangle_e \otimes (\|01\rangle_{nn} \leftrightarrow \|11\rangle_{nn})$	π	0
	3. rf, $\|1\rangle_e \otimes (\|10\rangle_{nn} \leftrightarrow \|11\rangle_{nn})$	π	0
	Analyze partial density matrices on working transition		
1.a	$\|1\rangle_e \otimes (\|01\rangle_{nn} \leftrightarrow \|11\rangle_{nn})$	variable (Rabi)	0
1.b			$\pi/2$
2.	mw, $(\|0\rangle_e \leftrightarrow \|1\rangle_e) \otimes \|11\rangle_{nn}$	π	0
3.	Laser, readout $\|1\rangle_e\langle 1\|_e \otimes \mathbf{1}_{4\times4}$	$3\,\mu s$	—

Table 3.7.: W state generation and tomography. Detailed pulse sequences for the generation and tomography of the W states. **upper part,** W state generation. The odd rotation angle of point three assures that finally an equal superposition of all three participating states is achieved. **middle part,** After any free evolution of the W state the tomography is performed by first transferring any partial density matrix of interest to the working transition. This is shown for all three partial density matrices which are of interest for calculation of the fidelity. **lower part,** Analysis of any partial density matrix by Rabi oscillations on the working transition. Two oscillations are performed with two $\pi/2$ phase shifted rf fields (see text). Finally, mw and laser pulses deliver the result.

4. The excited state spin Hamiltonian

The majority part of this thesis is mainly concentrated on the use of the electron spin of the NV center in diamond and proximal nuclear spins while the system is in its electronic ground state. So far the excited and metastable states have only been regarded as a tool to read out the electron spin state and to initialize it (see chapter 2.2.3). The current chapter, however, will elucidate the electron spin level structure in the first electronic excited state of the NV center. Eventually the results of this chapter pave the way for the fascinating experiments of chapter 5.

In this work the NV center in diamond is predominantly used under ambient conditions (i.e. at room temperature, ambient pressure, etc.). It will turn out that the electron spin level structure at cryogenic temperatures ($\approx 4\,\mathrm{K}$) and room temperature are fundamentally different. Therefore, in the beginning of this chapter we recall some facts about the NV center at cryogenic temperatures. In the main part the spin levels of the excited state are presented for ambient conditions. As the results for ambient and cryogenic conditions are quite opposite finally the intermediate regime is elucidated.

The experiments regarding EPR in the excited state at room temperature are published in [46].

4.1. At cryogenic temperatures

The electronic level structure and optical properties of the NV center are given in section 2.2.3. Especially figure 2.3 describes the level scheme and the triplet and singlet system. At cryogenic temperatures spin selective optical transitions of single NV centers from the ground to the first excited spin triplet states can be addressed individually due to the narrow optical linewidth. Therefore, the excited state level structure can be analyzed in detail which is not possible at room temperature.

As it turns out, there is a huge variation of local strain from one NV to another. Transverse strain reduces the symmetry of the NV center and leads to a splitting of the 6 excited state triplet levels into two orbital triplets [47]. In turn, the optical transition frequencies are very different from one NV to another leading to a huge inhomogeneous linewidth in ensemble studies. Furthermore, not only the splitting of the orbital doublets changes but also the splitting among levels within one orbital branch. Thus, EPR transitions in the excited state are also expected to vary drastically from one NV center

to another with changes on the order of several GHz [47]. Because of spin orbit interaction in the excited state in general $m_S = 0, \pm 1$ are no good quantum numbers anymore. Thus a magnetic field along the symmetry axis would usually not be commuting with Hamiltonian eq. (2.1). Due to this mixing of the spin states EPR transitions among almost every level of the excited state triplet have to be considered.

Summarizing, electron spin transitions among excited state levels can hardly be observed in ensemble measurements because the inhomogeneous linewidth of these transitions would be in the GHz range probably even larger than the Larmor frequency itself. For single NV centers, however, this should be possible because here the linewidth is on the same order as the optical linewidth of that center ($\sim 20\,\mathrm{MHz}$, figure 4.3b). Electron spin Rabi frequencies in this range would flip the spin in the excited state before the NV relaxes back into the ground state.[1]

4.2. At room temperature

Excited state ODMR signatures According to the experiments at cryogenic temperatures electron spin levels of the NV excited state at room temperature are also expected to vary drastically from one NV to another. In addition high Rabi frequencies are needed to observe the related spin flips. That's why these transitions have not been observed so far. The more surprising where the following results that were obtained at the same time also by G. Fuchs and coworkers [48].

A new sample holder design (see appendix B.3) and powerful microwave amplifiers allowed to drive Rabi frequencies up to a few hundred MHz, by far enough to drive excited state spin flips. Consequently, ODMR spectra of several NV centers showed always a similar pair of fluorescence dips around 1.4 GHz like those at around 2.9 GHz that belong to ground state spin flips (see figure 4.1a). Compared to the ground state ODMR lines the new lines around 1.4 GHz are broader. In addition an applied magnetic field along the NV symmetry axis B_z leads to the same linear splitting of both the 2.9 GHz and the 1.4 GHz doublet (see figure 4.1b) according to

$$\Delta\nu_{\pm} = 2\frac{\gamma_e}{2\pi} \cdot B_z \ . \tag{4.1}$$

These experiments were also repeated for NV centers in nanodiamonds where it is very likely to find NV centers with high strain which manifests in an observable E_{gs} parameter of the ZFS in the ground state. Also these NV centers showed a pair of fluorescence dips around 1.4 GHz, but with a larger E_{es} parameter than for the ground state ODMR lines at around 2.9 GHz (see figure 4.2b).

If these new fluorescence dips belong to the excited state there would be two main surprising issues. At first there is the uniformity of the resonance frequencies among the observed NV centers even for apparently high strain NVs. This contradicts the observed

[1] These experiments have not been conducted so far.

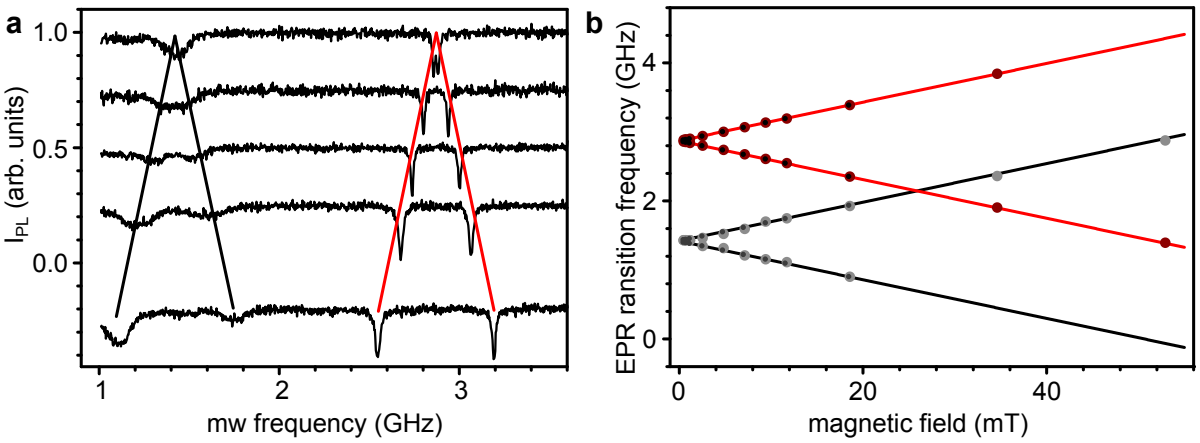

Figure 4.1.: ODMR spectra of ground and excited state electron spin transitions. **a,** ODMR spectra for increasing magnetic fields (from top to bottom) reveal ground and excited state resonance lines at around 2.87 GHz and at around 1.42 GHz respectively. Red and black lines are a guide to the eye for the evolution of the line positions of ground and excited state spin transitions respectively. **b,** Comparison of magnetic field dependence of EPR transitions for ground (red) and excited (gray) state. Both show the same slope for a magnetic field along the NV axis.

variety of energy level spacing for single NVs at cryogenic temperatures. The second surprise is the linear energy level splitting for increasing magnetic field (i.e. m_S is a good quantum number in the excited state and $g_e = -2$). This is again in contradiction to cryogenic experiments. However, the enhancement of E_{es} compared to E_{gs} would be explained by the excited state. Thus, test experiments are needed to verify that these new ODMR lines have their origin in the excited state.

At first the microwave power is varied. It turns out that as the ODMR linewidth of the 2.9 GHz line pair narrows due to decreased power broadening the 1.4 GHz line is not decreasing its width. This can be explained by the excited state decay rate Γ that sets the minimum EPR linewidth to $\gamma_{es} \approx \Gamma/2\pi$. In addition the 1.4 GHz feature reduces in contrast and finally vanishes whereas the 2.9 GHz line pair almost keeps its ODMR contrast. This would happen when the Rabi frequency in the excited state becomes much smaller than γ_{es}.

Secondly, the cw-ODMR scheme is changed to a pulsed one (i.e. microwave and laser radiation are periodically switched on and off). In an experimental sequence where laser and mw are in phase (i.e. on at the same time) the spectrum does not change (see figure 4.2a). If, however, the mw and laser are interleaved the 1.4 GHz line pair vanishes but not the 2.9 GHz line pair. This is expected for excited state ODMR, where the laser has to pump the NV center into its excited state while the mw is driving the spin transition. In the interleaved case the NV is in its ground state while the mw tries to drive the excited state transition there. Thus, only the ground state line pair is expected to show up in both spectra whereas the excited line is expected to vanish in the interleaved

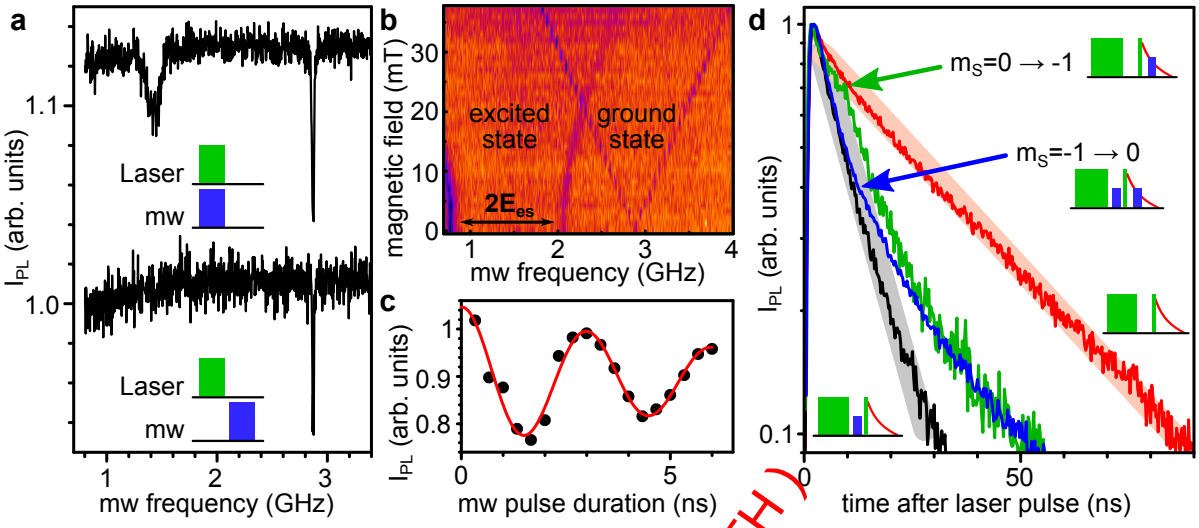

Figure 4.2.: Excited state spin manipulation. **a,** ODMR spectra taken in pulsed mode (see inset and text). The upper graph shows ground and excited state EPR transitions for synchronous laser and mw pulses. The lower graph shows only the ground state EPR transition because of interleaved laser and mw pulses. **b,** ODMR spectra of ground and excited state for an NV center in a nanodiamond for various magnetic fields parallel to the NV axis. A large ZFS E_{es} parameter for the excited state is visible possibly due to large strain in the nanodiamond. The ground state E_{gs} is negligible. **c,** Rabi oscillation of the NV electron spin with frequency of 335 MHz. **d,** Fluorescence decay of an NV center in $m_S = 0$ and $m_S = -1$ (red and black line respectively). The green line shows a flip of the electron spin in the excited state from $m_S = 0$ to -1 which manifests in a change of the fluorescence decay rate. The blue line corresponds to a flip from $m_S = -1$ to 0 in the excited state. Respective pulse sequences are illustrated (see text).

experiment.

The previous experiments showed that the ODMR line pair at 1.4 GHz originates from spin flips in the excited state. These spin flips obviously lead to an enhanced intersystem crossing rate which is the reason for the ODMR dip (similar to the ground state ODMR mechanism). However, it is still not clear whether the spin flips occur in the emitting excited state or in another excited state level. In the following we perform an experiment to address this question.

The idea is to excite the NV center with a ps laser pulse and measure the transient fluorescence response while manipulating the electron spin. According to [126] the fluorescence should decay exponentially with the excited state decay constant Γ depending on the electron spin state (i.e. $\Gamma_{\pm 1} = 1/7.8\,\mathrm{ns}^{-1}$ for $m_S = \pm 1$ and $\Gamma_0 = 1/12\,\mathrm{ns}^{-1}$ for $m_S = 0$). If a mw pulse hits the spin transition in the excited state shortly after a ps laser pulse the decay rate of the corresponding fluorescence should change. In order to perform this experiment a sample with nanodiamonds has been prepared on a coplanar waveguide structure. This approach has two main advantages. At first, the coplanar

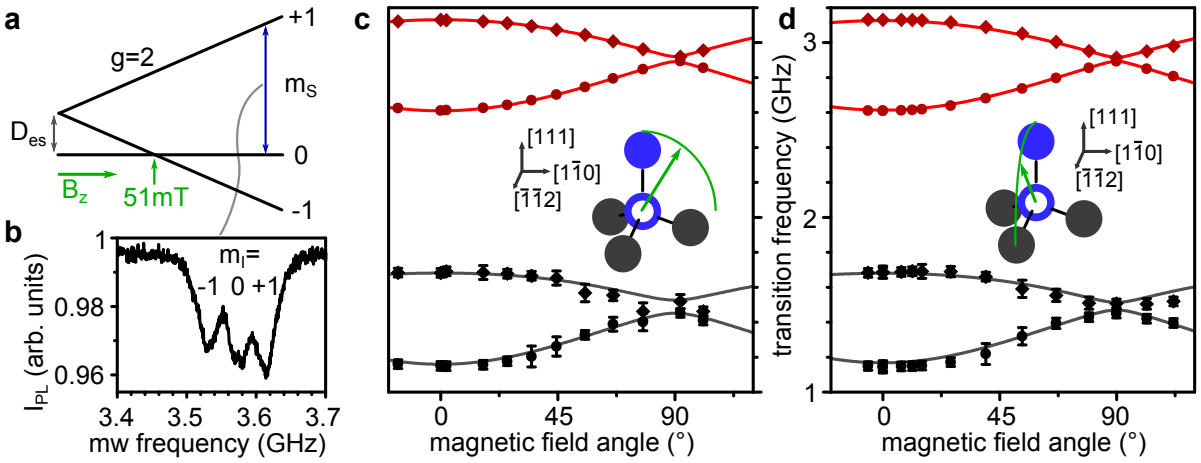

Figure 4.3.: Excited state spin Hamiltonian. a, Spin energy level structure of the excited state (see text). The vertical blue arrow is an EPR transition which is magnified below. Due to the lower D_{es} value in the excited state the electron spin level anticrossing is already at a magnetic field of 51 mT. **b,** Excited state ODMR spectrum showing hyperfine coupling to a ^{14}N nuclear spin. **c,** Change of EPR line frequencies as a magnetic field of 9.2 mT is rotated from parallel alignment (along NV axis) around axis $[\bar{1}\bar{1}2]$. Ground and excited state transitions behave similar. The fit assumes the ZFS tensor given in the text. **d,** EPR line frequencies for magnetic field rotation around axis $[1\bar{1}0]$.

waveguide allows to achieve higher mw fields which lead to faster Rabi oscillations of the electron spin. A corresponding Rabi oscillation is shown in figure 4.2c revealing a Rabi frequency of $\Omega \approx 336\,\mathrm{MHz}$. Secondly, the fluorescence decay rate Γ varies drastically from one NV center to another in nanodiamonds. Thus we have chosen an NV center with a small decay rate which allows the mw π-pulse to be short compared to the excited state lifetime. The bare transient fluorescence responses are displayed in figure 4.2d and reveal $\Gamma_{\pm1} = 1/13\,\mathrm{ns}^{-1}$ and $\Gamma_{\pm1} = 1/36\,\mathrm{ns}^{-1}$. In figure 4.2d the same experiment with an additional mw π-pulse on the spin transition in the excited state is shown. The mw pulse occurs roughly 10 ns after the laser pulse (i.e. when the NV center is in the emitting exiting state) while the spin projection was initially $m_S = 0$. Apparently, the fluorescence decay rate changes from Γ_0 to $\Gamma_{\pm1}$. Thus, the spin transitions of the ODMR spectrum originate indeed from the emitting excited state of the NV center.

Excited state spin Hamiltonian From the previous results we can draw a preliminary excited state level structure (see figure 4.3a). In a low strain case $m_S = 0, \pm1$ is a good quantum number and in zero magnetic field we measure a ZFS between $m_S = 0$ and $m_S = \pm1$ of $D_{es} = 1.42\,\mathrm{GHz}$. An axial magnetic field B_z leads to a linear splitting of the former degenerate levels $m_S = -1$ and $+1$ according to eq. (4.1). The suggested

excited state spin Hamiltonian $\hat{H}_{es}$ is similar to the ground state one (see eqs. 2.2, 3.1).

$$\hat{H}_{es} = \underbrace{D_{es}\hat{S}_z^2 + E_{es}\left(\hat{S}_x^2 - \hat{S}_y^2\right)}_{\underline{\hat{S}}\cdot\mathbf{D}_{es}\cdot\underline{\hat{S}}} - \tilde{\gamma}_e \underline{B}\cdot\underline{\hat{S}} + \underline{\hat{S}}\cdot\mathbf{A}_{es}\cdot\underline{\hat{I}} \tag{4.2}$$

First measurements (see figure 4.1) propose a rotationally symmetric $\mathbf{D}_{es}$ tensor with a principle axis along the NV center axis and a value of $D_{es} = 1.42\,\text{GHz}$. In a low strain case E_{es} is zero. The g_e-factor is the same as in the ground state and the hyperfine interaction to the nitrogen nuclear spin $\mathbf{A}_{es}$ generates an ODMR line splitting of about 60 MHz for the ^{15}N isotope [48].

The following experiment verifies that the ZFS tensor $\mathbf{D}_{es}$ is indeed axially symmetric and parallel to the NV center symmetry axis. Therefore, the magnetic field is rotated around two different crystallographic directions that are perpendicular to the NV center axis (i.e. [111]) and the corresponding ODMR spectra are monitored. In figure 4.3c,d the excited and ground state EPR line frequencies are plotted against the magnetic field angle of rotations around the $[1,-1,0]$ and $[-1,-1,2]$ axis. Given the magnetic field strength of 9.2 mT and a ZFS parameter of $D_{es} = 1.42\,\text{GHz}$ the transitions frequencies can also be calculated from Hamiltonian eq. (4.2). Apparently, experimental values and the data match which suggests that our model for the excited state spin Hamiltonian is correct.

In the ground state the ZFS constant D_{gs} is positive [129] (i.e. levels $m_S = \pm 1$ have a higher energy than the $m_S = 0$ level). This sign is yet unknown for the excited state and will be revealed by the following experiments which rely on the knowledge of the ground state sign of D_{gs}. The type of experiment is the same as demonstrated in figure 4.2d (i.e. a mw π-pulse in the excited state will change the transient fluorescence decay and thereby reveal a spin flip). In the first place the electron spin is initialized into the ground state $m_S = 0$ level and a mw π-pulse prepares the $m_S = -1$ state. Note that the mw frequency for transition $m_S = 0 \leftrightarrow -1$ is lower as compared to transition $0 \leftrightarrow +1$ in the given magnetic field range (see figure 4.2b). If the sign of D_{gs} would be negative the latter roles were reversed. In the next step, excited by a ps laser pulse the fluorescence will decay with rate $\Gamma_{\pm 1}$ (see figure 4.2d, blue curve). However, a mw pulse on the $m_S = -1 \leftrightarrow 0$ in the excited state can flip the spin and change the fluorescence decay rate into Γ_0. The right resonance frequency of this π-pulse depends on the sign of D_{es}. If $D_{es} > 0$ the lower ODMR resonance frequency will flip the spin and if $D_{es} < 0$ this is accomplished by the higher one (see figure 4.2b). It turns out that the lower EPR frequency of the excited state flips the spin and thus changes the fluorescence decay rate (see figure 4.2d, blue curve). Hence, the sign of D_{es} is indeed positive as depicted in figure 4.2a and therefore the spin density still has a rather disk-like shape as in the ground state (compare section 2.2.4).

Finally we have also determined the hyperfine interaction in the excited state between NV electron spin and the ^{14}N nuclear spin. As mentioned above the ^{15}N nuclear spin produces a hyperfine split doublet ($I_{^{15}\text{N}} = 1/2$) of the excited state ODMR line of $\approx$

60 MHz [48] which is roughly 20 times larger than the ground state hyperfine splitting of that isotope. Thus also the ^{14}N nuclear spin produces a larger hyperfine splitting in the excited state. By reducing the mw power such that the electron spin is hardly driven during the excited state lifetime we were able to record an excited state ODMR spectrum that exhibits the expected hyperfine split triplet ($I_{^{14}\mathrm{N}} = 1$) with a splitting of ≈ 40 MHz (see figure 4.3b). Again, this is roughly 20 times the ground state value. The large increase of the hyperfine interaction strength can be explained by the excited state spin density. Whereas the ground state spin density is mainly distributed among the bonds to the three nearest neighbor carbon atoms the excited state spin density has a substantial amount at the position of the nitrogen atom as well [124]. The performed measurements cannot determine the sign of the hyperfine interaction. However, simulations using *ab initio* supercell calculations [124] show that the signs of the hyperfine interaction with the nitrogen nuclear spin are different for ground and excited state. The reason for this is the small negative spin density at the nitrogen nucleus in the ground state and the large positive spin density in the excited state [111]. Thus, it turns out that the excited state hyperfine coupling constant for the nitrogen nuclear spin is negative for ^{15}N and positive for ^{14}N.

Magnetic field sweeps In magnetic field sweeps around 50 mT and 100 mT usually break down of the NV center fluorescence response is detected [28] (see appendix C.1). In the case of the 100 mT feature a level anti-crossing (LAC) at the ground state and accompanied electron spin oscillations are responsible. However, the 50 mT feature coincides with the degeneracy of the NV spin transition $m_S = 0 \leftrightarrow -1$ and a dopant electron spin $^1/_2$ transition. Indeed, substitutional nitrogen has been identified as a reason for this breakdown mediated by electron-electron spin flip-flops [28, 29]. On the other hand the breakdown of ODMR at around 50 mT keeps showing up also for high purity type IIa diamonds with a very dilute electron spin bath. In that case the flip-flops can be excluded as the dominating mechanism as it is far too slow. It is more likely a similar electron spin dynamics as for the gsLAC (see appendix C.1) and indeed this could be verified by exploiting this dynamics for nuclear spin manipulation which is demonstrated in section 5.

4.3. In between (T=4 . . . 300K)

In the previous two sections quite different level structures of the excited state have been deduced from measurement results at low temperature on the one hand and at room temperature on the other hand. The intermediate temperature region is elucidated in [47] in order to find a reason for these different behaviors. There, in a first step the excited state ODMR spectrum (compare figure 4.1a) is recorded for intermediate temperatures. It turns out that the contrast of the excited state ODMR lines decreases with decreasing temperature until it is vanished below ≈ 120 K. An explanation for this be-

havior is an averaging process between the two orbital branches (compare figure 2.3c) of the excited state which sets in at elevated temperatures. If such a process would induce fast transitions between these branches ($\gg \Gamma$) but would not flip the electron spin it would average out spin orbit interaction and parts of the spin-spin interaction. There would be a remaining splitting of levels with $m_S = \pm 1$ from those with $m_S = 0$ by an amount of 1.4 GHz [47]. This would allow driving the excited state ODMR transitions found at room temperature.

The reason for the averaging of the orbital branches is expected to be phonon related [47, 180, 49]. In [49] it is shown in addition that the most possible reason is the dynamic Jahn-Teller effect in the excited state of the NV center. Interesting behavior might be found in particular NV centers in nanodiamonds where the strain splitting in the excited state is larger than the temperature related broadening of the ZPL. In some cases a ZPL splitting of ~ 10 nm was observed which might prevent orbital averaging by the DJT [181]. In that case individual orbital addressing might be possible by optical wavelength selection or polarization selection. In addition these NV centers might preserve the individual spin levels of the corresponding orbitals including reduced hyperfine interaction. The latter point might be interesting for protection of quantum information on nuclear spins while the NV center is optically excited.

5. Nuclear spins — Advanced dynamics

In the previous chapters it was demonstrated how electron and nuclear spins can be manipulated in a coherent fashion to create arbitrary quantum states in qubit registers consisting of several spins. This was mainly achieved by the application of appropriate mw and rf driving fields or by free evolutions in tailored static Hamiltonians. At the end of such experiments there is usually the only incoherent and statistical process, namely the readout step which consists of a green laser excitation pulse (saturation intensity and duration of $\geq 3\,\mu s$) and simultaneous fluorescence detection. In a great majority of all presented experiments so far the result of this readout pulse was the following. The fluorescence depended on the electron spin state which was furthermore reinitialized into its ground state $m_S = 0$ level. Populations of all nuclear spin states have been found randomly redistributed during these laser pulses leading to an equal incoherent mixture of nuclear spin states. However there are a few exceptions. One is the nuclear spin polarization mechanism presented in [32] and applied to the nitrogen nuclear spin in section 3.2 (pp. 70). Here a very short laser pulse ($\approx 20\,ns$) retained nuclear spin populations but only under special conditions regarding the hyperfine interaction tensor. A theoretical analysis of how the nuclear spin is randomized by laser excitation is presented in [33]. Furthermore, it was shown in [29] that proximal electron spins can be spin polarized by an incoherent optical pumping process.

In this chapter we show how the incoherent nature of laser excitation and subsequent decay and the recently obtained knowledge about the excited state spin level structure can be exploited to efficiently polarize proximal nuclear spins, how this polarization mechanism can be used for the enhancement of the electron spin readout and finally how nuclear spins can be efficiently decoupled from common flip-flops with the electron spin. Whereas the polarization and the readout enhancement lead to an initialization of the nuclear spins in a particular state and thus erasing information of a previous state the decoupling leads to a protection of the present nuclear spin state populations against laser excitations eventually allowing the detection of quantum jumps of a single nuclear spin. This implies that the nuclear spin state is projectively measured in a QND measurement scheme. Eventually, this allows initializing a quantum system by measuring its state.

After all we would like to point out that the initialization of a quantum system for QIP is crucial for its applicability. Without proper initialization the success rate of any algorithm decreases exponentially with the size of the Hilbert space. Especially the results

of section 5.1 provide a versatile method to initialize several qubits simultaneously. In addition the improvement of the readout procedure has great impact on both quantum information processing as well as on metrology applications using the NV center. The method demonstrated in section 5.2 for example allows a three times faster acquisition of information and is at the same time easy to implement. Finally, the results of section 5.3 demonstrate the superb control about our quantum register. It allows measuring the spin states with a new quality and for the first time gives also more quantitative insight into our quantum system. In addition it allows using the nuclear spin as formidable memory during the readout of quantum information which can make the readout up to 400 times faster than with the conventional readout.

The results of this chapter are published in [50, 51, 54].

5.1. Cooling of nuclear spins

The electron spin of the NV center is polarized (or cooled) using optical pumping as described in chapter 2.2.4. Here we show how to use the electron spin level anti-crossing (esLAC) in the excited state at around 50 mT to simultaneously polarize certain proximal nuclear spins. We demonstrate this mechanism using the nitrogen nuclear spin as well as the nuclear spin of a first shell ^{13}C atom.

Under usual magnetic field conditions during our experiments (i.e. small fields compared to D_{gs} and D_{es}) electron and nuclear spin magnetic quantum number are good quantum numbers. This is because of a small hyperfine interaction compared to the electron spin zerofield splitting and Zeeman energy. In addition the large energy mismatch between electron spin levels and nuclear spin levels prevents flip-flops between both spin species. All previously mentioned experiments with spin registers are conveniently performed under these conditions. For the polarization of the nuclear spins, however, it would be desirable to bring electron and nuclear spins into resonance to enhance flip-flops in order to transfer polarization of the electron spin onto the nuclear spins.

The idea of the following experiment is to bring both spin species into resonance in the excited state, namely at a magnetic field corresponding to the excited state LAC. Several optical excitation cycles would then lead to shelving into a stable spin configuration ($m_S = 0,\ m_I = \uparrow$ see figure 5.1a). This has several advantages over previous nuclear spin polarization mechanisms. At first, this mechanism is readily switchable going from an experimentally convenient magnetic field range in the ground state to a flip-flop dominated situation in the excited state. Secondly, several nuclear spins can be polarized at the same time. Thirdly, the electron spin is also polarized (i.e. this is not just a polarization swap between electron and nuclear spin). Last but not least the hyperfine interaction strength in the excited state can be different as for the nitrogen nuclear spin where the excited state value is 20 times larger than the ground state value. As a consequence the polarization speeds up without using any mw or rf power. Simply

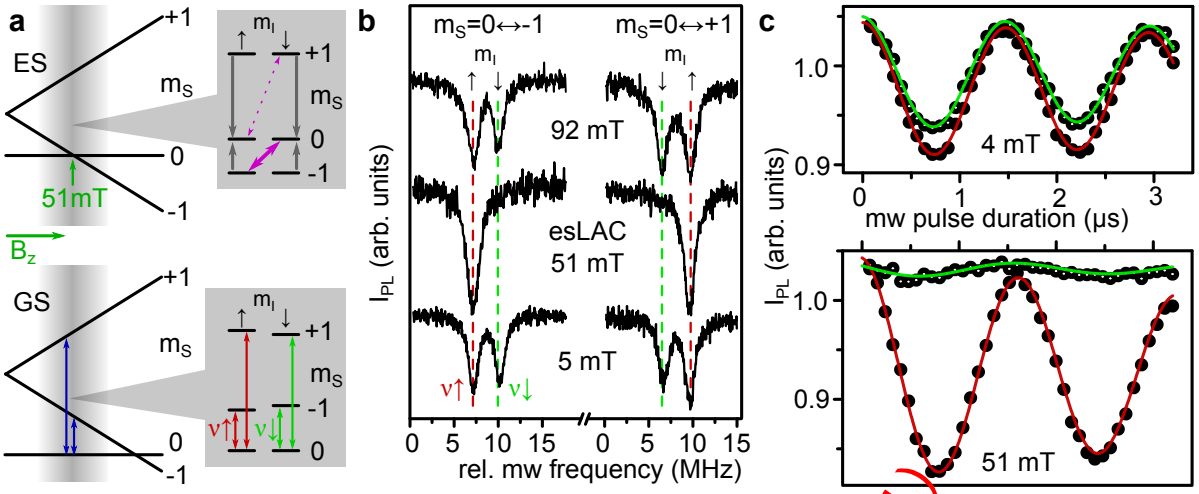

Figure 5.1.: Signature of dynamic nuclear spin polarization. **a,** Energy level scheme of ground (bottom) and excited state (top) depending on axial magnetic field B_z. Around 51 mT the esLAC occurs. Here hyperfine interaction to the ^{15}N nuclear spin leads to spin flip-flop rates (solid purple arrow in inset, dotted arrow illustrates suppressed flip-flops). Electron spin polarization by ISC is depicted by gray arrows. In the ground state EPR transitions can be driven (solid vertical arrows). The lower inset reveals nuclear spin state selective EPR transitions (red curve $m_I = \uparrow$, green curve $m_I = \downarrow$). **b,** Hyperfine resolved ODMR spectra of both EPR transitions ($m_S = 0 \leftrightarrow \pm 1$) for three magnetic fields. Apparently, at 51 mT one nuclear spin orientation is dominant ($m_I = \uparrow$) and the other one is suppressed ($m_I = \downarrow$). **c,** Nuclear spin state selective electron spin Rabi at 4 mT (upper graph) and at the esLAC (lower graph). At the esLAC the Rabi amplitude for spin projection $m_I = \uparrow$ is increased whereas the amplitude for $m_I = \downarrow$ is suppressed as compared to 4 mT.

shining green laser light onto the NV center under the right magnetic field conditions is sufficient. This polarization mechanism is also referred to as dynamic nuclear spin polarization (DNP).

Before a deeper analysis of this mechanism the signature of nuclear spin polarization is shown in figure 5.1b. Here we see three ODMR spectra of the electron spin transition $m_S = 0 \leftrightarrow -1$ (left side) and $m_S = 0 \leftrightarrow +1$ (right side) exhibiting a hyperfine split doublet due to the ^{15}N nuclear spin (taken at increasing magnetic field strengths from top to bottom). Apparently, for magnetic fields below and above the value for the esLAC the doublet is clearly visible with equal contributions of both nuclear spin projections whereas at ≈ 51 mT one of the hyperfine lines is missing and the other one is enhanced. We attribute this to the polarization of the nuclear spin and define the degree of polarization as

$$\mathcal{P} = \frac{A_{\nu\uparrow} - A_{\nu\downarrow}}{A_{\nu\uparrow} + A_{\nu\downarrow}} \tag{5.1}$$

where $\nu_\downarrow$ and $\nu_\uparrow$ are the resonance frequencies of both hyperfine split transitions (see figure) and $A_{\nu_\downarrow/\nu_\uparrow}$ denotes the corresponding area of the resonance peak. Additionally, we

have performed Rabi oscillations on the electron spin selectively for each of the nuclear spin projections, once at small fields and once at the excited state LAC. The resulting oscillations (see figure 5.1c) support the polarization result of the ODMR spectra. Using eq. (5.1) we arrive at a degree of polarization of $\mathcal{P} = 0.98 \pm 0.02$. This is far from equilibrium at room temperature. The temperature to achieve $\mathcal{P}$ by thermalization is $\sim 1\,\mu\text{K}$ regarding an energy level splitting of the nuclear spin of 200 kHz.

For the derivation of the polarization mechanism we first introduce the electron and nuclear spin Hamiltonian for the excited state.

$$\hat{H}_{es} = D_{es}\hat{S}_z^2 - \underbrace{\tilde{\gamma}_e B_z}_{b_e}\hat{S}_z + \underbrace{A_\parallel \hat{S}_z\hat{I}_z + A_\perp/2\left(\hat{S}_+\hat{I}_- + \hat{S}_-\hat{I}_+\right)}_{\underline{\hat{S}}\cdot\mathbf{A}\cdot\underline{\hat{I}}} - \underbrace{\tilde{\gamma}_n B_z}_{b_n}\hat{I}_z \tag{5.2}$$

Obviously it is the transverse part $A_\perp$ of the hyperfine coupling tensor $\mathbf{A}$ that induces the spin flip-flops ($A_\parallel = -60\,\text{MHz}$, $A_\perp = -40\,\text{MHz}$ [48, 124]). At the excited state LAC only two electron spin levels are involved ($m_S = 0, -1$) whereas the $m_S = +1$ level is far detuned. Thus, we concentrate on a 4×4 part $\tilde{H}_{es}$ of the Hamiltonian. In the product basis of the two spins ($|m_S = 0, -1\rangle \otimes |m_I = \uparrow, \downarrow\rangle$) the matrix representation of the sub-Hamiltonian is

$$\tilde{H}_{es} = \begin{pmatrix} -\frac{b_n}{2} & \cdot & \cdot & \cdot \\ \cdot & \frac{b_n}{2} & \frac{A_\perp}{\sqrt{2}} & \cdot \\ \cdot & \frac{A_\perp}{\sqrt{2}} & D_{es} + b_e + \frac{-A_\parallel - b_n}{2} & \cdot \\ \cdot & \cdot & \cdot & D_{es} + \frac{b_e + A_\parallel + b_n}{2} \end{pmatrix}. \tag{5.3}$$

Apparently, the states $|0, \uparrow\rangle = |0\rangle \otimes |\uparrow\rangle$ and $|-1, \downarrow\rangle = |-1\rangle \otimes |\downarrow\rangle$ remain eigenstates throughout the whole LAC region, i.e. where the detuning from the esLAC $\Delta \sim 0$ with

$$\Delta(B_z) = D_{es} + b_e(B_z) - b_n(B_z) - A_\parallel/2\,. \tag{5.4}$$

However, $|0, \downarrow\rangle$ and $|-1, \uparrow\rangle$ are eigenstates only far away from the LAC region but are mixed and form new eigenstates closer to the LAC (see figure 5.2a):

$$|+\rangle = \alpha\,|0, \downarrow\rangle + \beta\,|-1, \uparrow\rangle \tag{5.5a}$$

$$|-\rangle = \beta\,|0, \downarrow\rangle - \alpha\,|-1, \uparrow\rangle \tag{5.5b}$$

$$\alpha = \sqrt{\frac{1}{2} + \frac{\Delta}{2\Omega}} \tag{5.5c}$$

$$\beta = \frac{A_\perp}{\Omega\sqrt{1 + \frac{\Delta}{4\Omega}}} \tag{5.5d}$$

$$\Omega = \sqrt{2A_\perp^2 + \Delta^2}\,. \tag{5.5e}$$

Taking into account also the optical electron spin polarization any $m_S = -1$ contribution would be converted into $m_S = 0$ by optical pumping. Hence, optical pumping

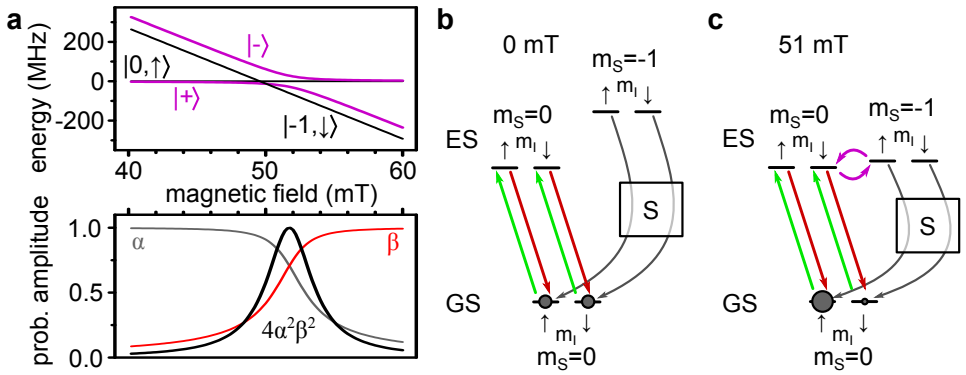

Figure 5.2.: Energy levels at the esLAC and polarization mechanism. a, (top) Energy levels of quantum states participating in the esLAC for axial magnetic field strength around 51 mT. Two levels are crossing and two are anticrossing (see text). (bottom) Probability amplitudes of quantum states $|+\rangle$ and $|-\rangle$ close to the esLAC. **b,** Energy levels and transition rates (arrows) away from the esLAC for ground and excited state during laser excitation and decay. The metastable singlet state (S) is illustrated as a box. The arrow colors green, red and gray correspond to laser excitation, fluorescence decay and passage through the metastable state. The NV center is polarized into $m_S = 0$ and the population (gray spheres) is equally distributed among the two nuclear spin orientations. **c,** Energy levels and transition rates (arrows) at the esLAC during illumination. The coherent evolution from state $|0,\downarrow\rangle$ into $|-1,\uparrow\rangle$ is illustrated as purple curved arrows. Polarization occurs into $|0,\uparrow\rangle$.

combined with the hyperfine interaction in the excited state will only leave spin state $|0,\uparrow\rangle$ unaltered. If the spin state in the ground state is $|0,\downarrow\rangle$, however, promotion into the excited state leads to a superposition state $|0,\downarrow\rangle = \alpha\,|+\rangle + \beta\,|-\rangle$ whose phase oscillates with Ω. This oscillation is accompanied by an at least partial evolution into the spin "flip-flopped" state $|-1,\uparrow\rangle$

$$\begin{aligned} \alpha\,|+\rangle + \beta\,|-\rangle &\rightleftarrows \alpha\,|+\rangle - \beta\,|-\rangle \\ \alpha\,|+\rangle - \beta\,|-\rangle &= (\alpha^2 - \beta^2)\,|0,\downarrow\rangle + 2\alpha\beta\,|-1,\uparrow\rangle\,. \end{aligned} \tag{5.6}$$

In general the maximum population in this spin "flip-flopped" state $|-1,\uparrow\rangle$ during the oscillation follows a Lorentzian dependence on the magnetic field.

$$p_+^{max}(B_z) = 4\alpha^2\beta^2 = \frac{A_\perp^2}{A_\perp^2 + \Delta^2(B_z)/2}\,. \tag{5.7}$$

Especially at the esLAC (i.e. $\Delta = 0$ and $\alpha = \beta = 1/\sqrt{2}$) this oscillation converts the non-eigenstate $|0,\downarrow\rangle$ completely into $|-1,\uparrow\rangle$ and back again.

During the coherent oscillation in the excited state statistically the electronic state can decay either via the radiative path directly to the ground state or via ISC to the metastable singlet state accompanied with final polarization of the electron spin state into $m_S = 0$. ISC occurs preferably for the $m_S = \pm 1$ spin states. Thus, whenever $|0,\downarrow\rangle$

oscillates partially into $|-1,\uparrow\rangle$ there is a chance to pass via the metastable state which polarizes the electron spin and finally leads to the stable spin state $|0,\uparrow\rangle$. Because the oscillation frequency $\Omega > 56\,\mathrm{MHz}$ (eq. (5.5e) and [124]) is on the same order or faster than the excited state decay rate $\sim 100\,\mathrm{MHz}$ we can approximate the average probability p_+ for a nuclear spin evolution from $m_I = \downarrow$ to $\uparrow$ to be proportional to p_+^{max}, namely

$$p_+(B_z) = p_+^{max}(B_z)/2 \ . \tag{5.8}$$

All afore mentioned considerations hold as well for a reversed magnetic field such that $m_S = 0$ and $m_S = +1$ have an anti-crossing and the nuclear spin will be polarized into $m_I = \downarrow$ instead.[1] In that case the spin flip probability into $m_I = \downarrow$ is

$$p_-(B_z) = p_+(-B_z) \tag{5.9}$$

In the following we deduce a rate equation to calculate the dependence of the polarization on the magnetic field. Starting in the electronic ground state with a spin state $a^2\,|0,\uparrow\rangle\langle 0,\uparrow| + b^2\,|0,\downarrow\rangle\langle 0,\downarrow|$ the polarization of eq. (5.1) can be written as $\mathcal{P} = a^2 - b^2$. The rates for polarization into $m_I = \uparrow$ and $\downarrow$ and for depolarization are modeled by

$$k_+ = b^2 p_+ \Gamma = (1-\mathcal{P}) p_+ \Gamma/2 \tag{5.10a}$$
$$k_- = a^2 p_- \Gamma = -(1+\mathcal{P}) p_- \Gamma/2 \tag{5.10b}$$
$$k_{eq} = -k_{eq}^0 \mathcal{P} \ . \tag{5.10c}$$

Here Γ expresses the rate for a nuclear spin conserving decay of $m_S = \pm 1$ states via the metastable state accompanied by electron spin polarization into $m_S = 0$. The constant k_{eq}^0 summarizes all forces that drive the nuclear spin polarization to its equilibrium value (i.e. $\mathcal{P} \approx 0$ at present conditions). The steady state condition $k_+ + k_- + k_{eq} = 0$ leads to the following magnetic field dependence of

$$\begin{aligned} \mathcal{P}(B_z) &= \frac{p_+ - p_-}{p_+ + p_- + 2k_{eq}^0/\Gamma} \\ &= \frac{p_+(B_z) - p_+(-B_z)}{p_+(B_z) + p_+(-B_z) + 2k_{eq}^0/\Gamma} \ . \end{aligned} \tag{5.11}$$

Obviously this function is antisymmetric with respect to B_z and resembles a Lorentzian profile around the esLAC which can be approximated by

$$\mathcal{P}(B_z) \approx \left. \frac{1}{1 + \tilde{k}_{eq} + \frac{\tilde{k}_{eq}\Delta^2}{2A_\perp^2}} \right|_{B_z>0,\ \text{around esLAC}} \ . \tag{5.12}$$

[1] We can not distinguish between the two opposite magnetic field orientations. Thus we only measure $|\mathcal{P}|$. This treatment however affects the magnetic field dependence of $\mathcal{P}$.

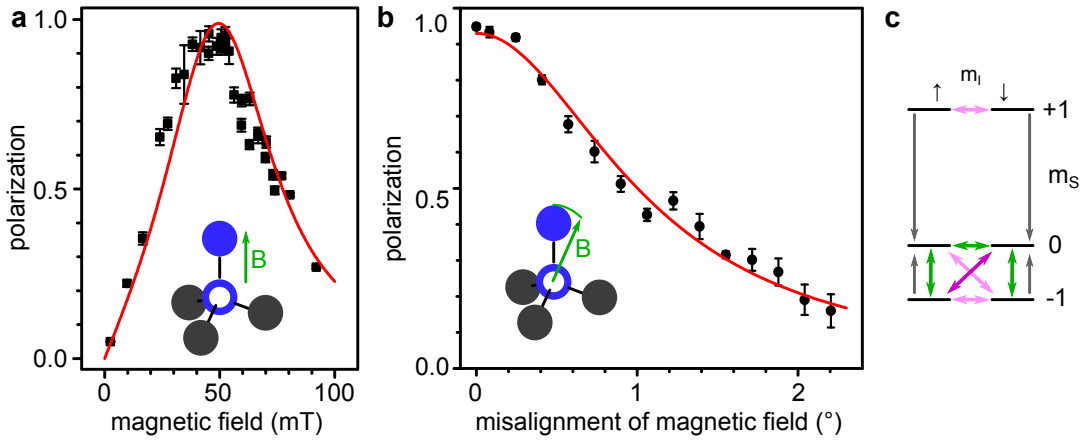

Figure 5.3.: Magnetic field dependence of nuclear spin polarization. **a,** Degree of nuclear spin polarization $\mathcal{P}$ for a parallel aligned magnetic field (see inset). For the fit function see text. **b,** Dependence of $\mathcal{P}$ on the misalignment angle of the magnetic field (see inset) for a field strength of 47 mT. **c,** Energy levels and transition rates at the esLAC. Polarization is achieved by interplay of ISC (gray arrows) and hyperfine induced spin flip-flops (purple arrow). A slightly misaligned magnetic field leads to rates shown as green arrows. Nuclei with a misaligned hyperfine tensor lead to rates illustrated as light purple arrows.

Here, $\tilde{k}_{eq}$ combines effects of k^0_{eq}/Γ and p_- as depolarization effects and apparently the rate of depolarization affects both the amplitude and the width of the polarization function $\mathcal{P}(B_z)$.

The magnetic field dependence of $\mathcal{P}$ has been measured by aligning the magnetic field parallel to the NV axis, changing its strength and simultaneously acquiring ODMR spectra as the ones shown in figure 5.1b. Figure 5.3a shows the deduced polarization and a function according to eq. (5.11) nicely fits the data. Apparently, the distribution is very broad and has an almost perfect maximum which suggests only little depolarization effects. Even close to zero magnetic field the polarizing terms $k_\pm$ prevail over the depolarizing ones k_{eq} which is expressed by the steep slope of the fitting function. This slope is an effect of the two opposing polarization terms k_+ and k_- which cancel at zero magnetic field and thus lead to $\mathcal{P} = 0$. Thus substantial spin dynamics in the excited state is present even close to zero magnetic field.

The width of this distribution also makes this polarization procedure less magnetic field dependent. However, care must be taken when setting the angle of the magnetic field as figure 5.3b underlines. The degree of polarization decreases as the angle between magnetic field and NV axis is increased accompanied by a drop in fluorescence due spin state mixing at the esLAC (see sections 4.2 and C.1).

The described mechanism for the nuclear spin polarization fits perfectly only to nuclear spins that have a collinear hyperfine tensor with the NV center which usually only applies to spins on the NV symmetry axis. In addition an aligned magnetic field is

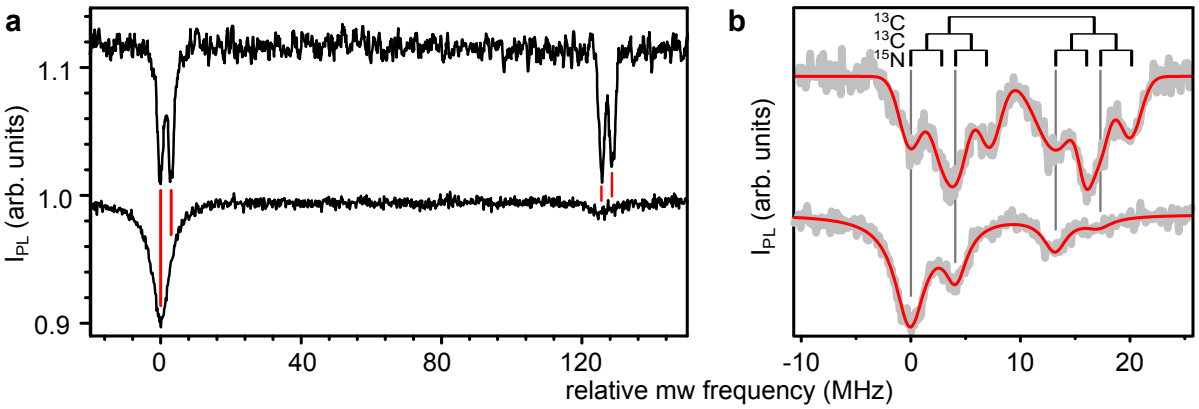

Figure 5.4.: Simultaneous polarization of several nuclear spins. a, ODMR spectra of an NV center with one ^{13}C nuclear spin in the first coordination shell and a ^{15}N nuclear spin. The upper spectrum is taken at low fields and thus does not show signs of polarization whereas the lower graph is taken at $\approx 50\,\mathrm{mT}$. Here, both nuclear spins are polarized to a high degree. **b,** Simultaneous polarization of two ^{13}C nuclei in different lattice positions and a ^{15}N nuclear spin. Due to non-axial hyperfine tensors of the ^{13}C nuclei their degree of polarization is not ideal.

necessary. Now we describe how deviations from these requirements affect polarization. Considering a slightly misaligned magnetic field at the esLAC the electron spin levels $m_S = 0$ and -1 would immediately be mixed with each other leading to the rates highlighted in figure 5.3c as green arrows. Also the nuclear spin levels for $m_S = 0$ mix whereas the nuclear spin levels for $m_S \pm 1$ are "protected" by the hyperfine interaction with the electron spin. However a few degree of misalignment are sufficient for these rates to be larger than the hyperfine interaction. If the hyperfine tensor is not collinear with the NV center axis additional rates appear illustrated as light purple arrows in figure 5.3c. Depending on the strength of these rates compared to the polarization rate high degrees of nuclear spin polarization can still be obtained.

In figure 5.4a the simultaneous polarization of a ^{13}C nuclear spin in the first shell and a ^{15}N nuclear spin is demonstrated which almost perfect for both nuclei. The degree of polarization of the ^{13}C spin is $\mathcal{P} = 0.90 \pm 0.01\,\%$. In figure 5.4b additional ^{13}C nuclear spins on different lattice sites are presented. The polarization of the nuclear spin exhibiting the larger splitting of $\approx 13\,\mathrm{MHz}$ is $\mathcal{P} = 0.7$ and the other ^{13}C nucleus is polarized to $\mathcal{P} = 0.4$. A more detailed analysis of achievable polarizations for different ^{13}C positions around the NV is presented in [162].

5.2. Nuclear spins for readout enhancement

In the previous section a nuclear spin polarization mechanism was demonstrated that leads to almost perfect spin initialization especially for nitrogen nuclear spins associated with the NV center but also for other proximal spins. Now we show how the flip-flop

process involved in polarization is exploited to enhance the readout of the NV center spin. Therefore, we work again at magnetic fields at the esLAC but in contrast to the previous section we use the ^{14}N nuclear spin instead of ^{15}N . The only difference is the nuclear spin of $I = 1$ instead of $I = 1/2$. The degree of nuclear spin polarization for ^{14}N is the same as for ^{15}N and the final initialized nuclear spin state is $m_I = +1$.

In the usual readout sequence the electron spin is initialized by a laser pulse into $m_S = 0$ which is the stable spin configuration that allows a cycling optical transition that emits a high level of fluorescence photons (see figure 2.5b in chapter 2.2.6). If the spin is flipped to another state (e.g. $m_S = \pm 1$) a subsequent laser will first promote the NV center into the metastable singlet state which reduces fluorescence. Eventually, spin state $m_S = 0$ is restored accompanied with the higher fluorescence level (see figure 2.5b in chapter 2.2.6). At this point in time the read out is finished because no further information about the former spin state can be extracted (i.e. the spin system is reset). Thus, only a limited amount of photons carries information about the spin state which leads to considerable shot noise. More precisely, on average only up to 0.2 photons are collected during readout (see chapter 2.2.6). The actual signal is $\approx 30\%$ of it which leads to a signal to noise ratio (SNR) for one readout step of SNR ≈ 0.1.

In the novel approach presented here the state of nuclear spin ^{14}N is correlated with that of the electron spin. Thus, the system now consists of 2 spins such that repolarizing the electron spin alone is insufficient for a reset. The initial state now includes the nuclear spin, it is

$$\Psi_{\text{init}} = |m_S = 0, m_I = +1\rangle \ . \tag{5.13}$$

The nuclear spin polarization mechanism will reinitialize the nuclear spin as well but "quantum by quantum" ($|\Delta m_I| = 1$ per optical excitation step) and force the electron spin each time through the metastable singlet yielding additional fluorescence photons.

To begin with, the level structure is presented in figure 5.5a (for Hamiltonian see section 3.1.1) and the corresponding ODMR spectrum at small magnetic fields and at the esLAC are shown in figure 5.5c. Apparently, also the ^{14}N nuclear spin can be polarized to a high degree (compare section 5.1 and see flip-flop rates in figure 5.5a). The corresponding esLAC is depicted in figure 5.5b. A similar sub Hamiltonian as eq. (5.3) describes it. Here the probability amplitudes that describe the state mixing are α, β, γ and δ and $2\alpha^2\beta^2$ and $2\gamma^2\delta^2$ are the corresponding spin flip-flop probabilities.

For the correlation of the nuclear with the electron spin state it is necessary to manipulate the nuclear spin directly via rf radiation (see figure 5.5a). Therefore, the corresponding ENDOR spectra have to be measured. In figure 5.6 the measurement sequence and the ENDOR spectra are shown. Some ENDOR lines appear stronger than others. This is already a direct consequence of the novel readout enhancement (see below).

Whenever the quantum state of the electron spin after a unitary operation is measured the number of response fluorescence photons can vary between the maximum $N_{|0,+1\rangle}$ for spin state $|0, +1\rangle$ and the minimum $N_{|-1,+1\rangle}$ for state $|-1, +1\rangle$ (see red and gray curve figure 5.7a); the actual maximum number of signal photons N_S corresponding to a spin

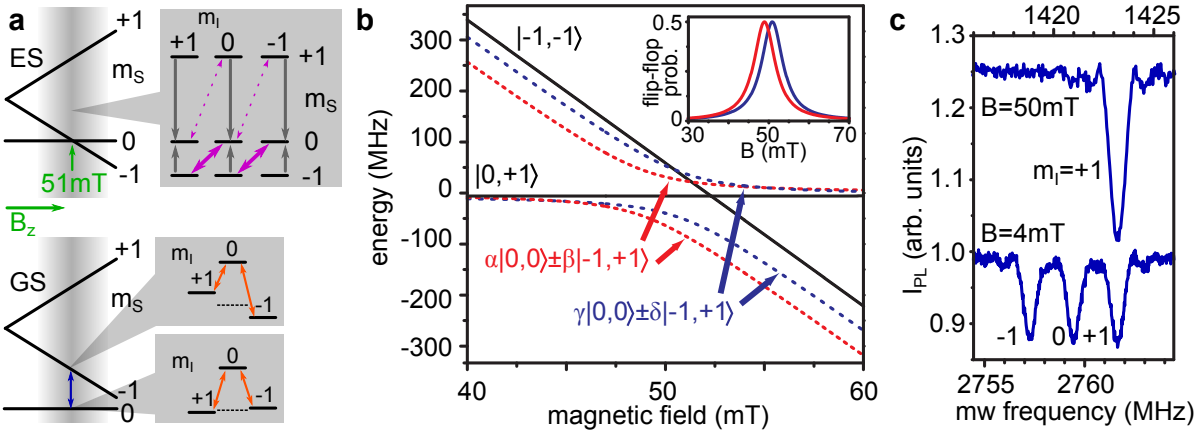

Figure 5.5.: ODMR spectra and level scheme of ^{14}NV at the esLAC. a, Electron spin energy levels in ground (GS) and excited (ES) state for an increasing axial magnetic field B_z. EPR transitions driven in this experiment are highlighted by the blue arrow. The upper inset illustrates transition rates at the esLAC for a ^{14}N nuclear spin. Gray arrows represent electron spin polarization rates due to ISC and purple arrows represent spin flip-flops due to hyperfine interaction. The lower inset illustrates the hyperfine substructure of levels $m_S = 0, -1$ due to the ^{14}N nuclear spin. The NMR transitions driven in this experiment are highlighted by orange arrows. **b,** Energy levels at the esLAC showing crossings and avoided crossings (compare figure 5.1). The spin state mixing at the esLAC leads to flip-flops whose probability is displayed in the inset. **c,** ODMR spectrum at small magnetic fields and at the esLAC for transition $m_S = 0 \leftrightarrow -1$. At the small field the hyperfine lines are visible whereas at the esLAC the nuclear spin is polarized into $m_I = +1$.

flip is the difference between these two (light gray area). One can say, the signal photons are acquired during the passage through the metastable state (see section 2.2.6). In this conventional approach the nuclear spin state remains constant. A typical unitary operation is a Rabi oscillation between $|0,+1\rangle$ and $|-1,+1\rangle$ (see figure 5.8a)

$$\Psi_{\mathrm{rot}}^{\mathrm{conventional}} = \cos\frac{\omega\tau}{2}\,|0,+1\rangle + \sin\frac{\omega\tau}{2}\,|-1,+1\rangle \tag{5.14}$$

The corresponding fluorescence result for varying rotation angles $\omega\tau$ is shown in figure 5.8b. In the novel approach electron spin state $m_S = -1$ is correlated with nuclear spin state $m_I = -1$ after the unitary operation by applying two consecutive rf π-pulses that flip the nuclear spin $m_I = +1$ into $m_I = -1$ only in the $m_S = -1$ manifold (i.e. we apply two CNOT gates, see figure 5.7b). The resulting spin state prior to the readout is thus

$$\Psi_{\mathrm{rot}}^{\mathrm{enhanced}} = \cos\frac{\omega\tau}{2}\,|0,+1\rangle + \sin\frac{\omega\tau}{2}\,|-1,-1\rangle \ . \tag{5.15}$$

Obviously, in this approach the minimum number of photons $N_{|-1,-1\rangle}$ corresponds to state $|-1,-1\rangle$. As apparent from figure 5.7 the maximum number of signal photons N_S which again is the difference between maximum and minimum numbers of fluorescence

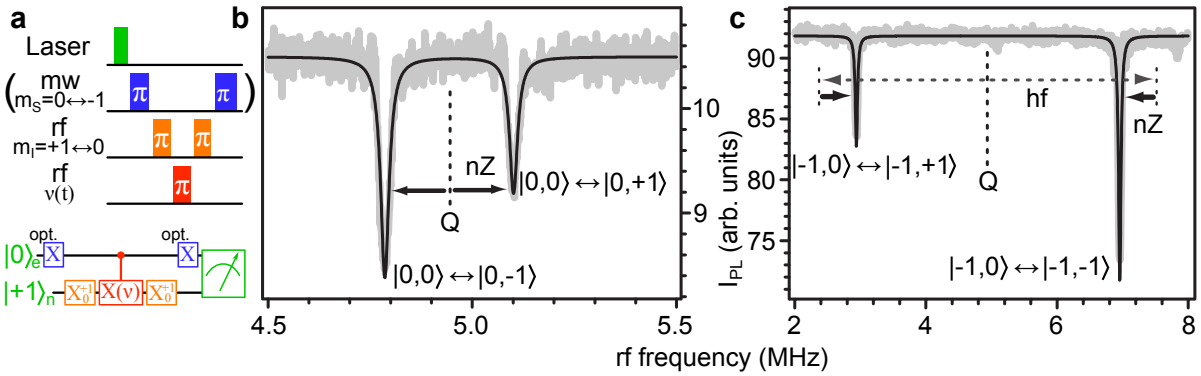

Figure 5.6.: ENDOR spectra of the ^{14}N nuclear spin. **a,** Pulse sequence to record ENDOR spectra. The laser initializes electron and nuclear spin into $|0,+1\rangle$. To work in the $m_S = -1$ level additional mw π-pulses are needed. These are hard pulses that flip the electron spin regardless of the nuclear spin state. The first orange rf π-pulse prepares nuclear spin state $m_I = 0$ and the last one transfers population from $m_I = 0$ to $+1$. The red rf pulse changes its frequency. When it hits one of the two rf resonances (see figure 5.5a) the fluorescence drops. **b–c,** ENDOR spectrum for $m_S = 0$ and -1 respectively. Lineshifts due to hyperfine (hf), quadrupole (Q) and Zeeman (nZ) interaction are marked. The fluorescence drop is created by the readout enhancement technique (see text) which is stronger for the $m_I = 0 \leftrightarrow -1$ transition. Note that the hard mw pulses do not correlate electron and nuclear spin state as in conventional ENDOR described in chapter 3.1.4.

photons is three times enhanced and the accumulation of the signal (i.e. the reinitialization process) takes roughly three times longer. The resulting Rabi oscillation using the enhanced readout mechanism is shown in figure 5.8b and exhibits the same three times enhanced contrast.

The explanation of the enhanced number of signal photons accompanied with a longer accumulation time is illustrated in figure 5.7b. Once the correlation of nuclear and electron spin state is performed the laser is switched on. The first signal photons (gray circles in figure 5.7b) are acquired when state $|-1,-1\rangle$ decays by a passage through the metastable state and transforms into $|0,-1\rangle$.[2] After that the same laser pulse re-excites the NV center and the spin state $|0,-1\rangle$ will eventually flip-flop into $|-1,0\rangle$ and decay via the metastable state yielding additional signal photons and spin state $|0,0\rangle$.[3] The NV center will now be excited a third time by the same laser and again a flip-flop and a passage through the metastable state yield signal photons and finally the spin system is reinitialized into $\Psi_{\text{init}} = |0,+1\rangle$. At this stage no additional signal photons can be extracted.

In the following we calculate the maximum SNR of both methods. Therefore, both

[2] States $|-1,-1\rangle$ as well as $|0,+1\rangle$ are flip-flop protected whereas states $|0,-1\rangle \leftrightarrow |-1,0\rangle$ and $|0,0\rangle \leftrightarrow |-1,+1\rangle$ are linked by flip-flops at the esLAC (see figure 5.5a).

[3] The flip-flop accompanied by a passage through the metastable singlet state does not occur with 100 % probability. But finally it will occur and only than signal photons are generated. A non-unity probability can delay the readout process.

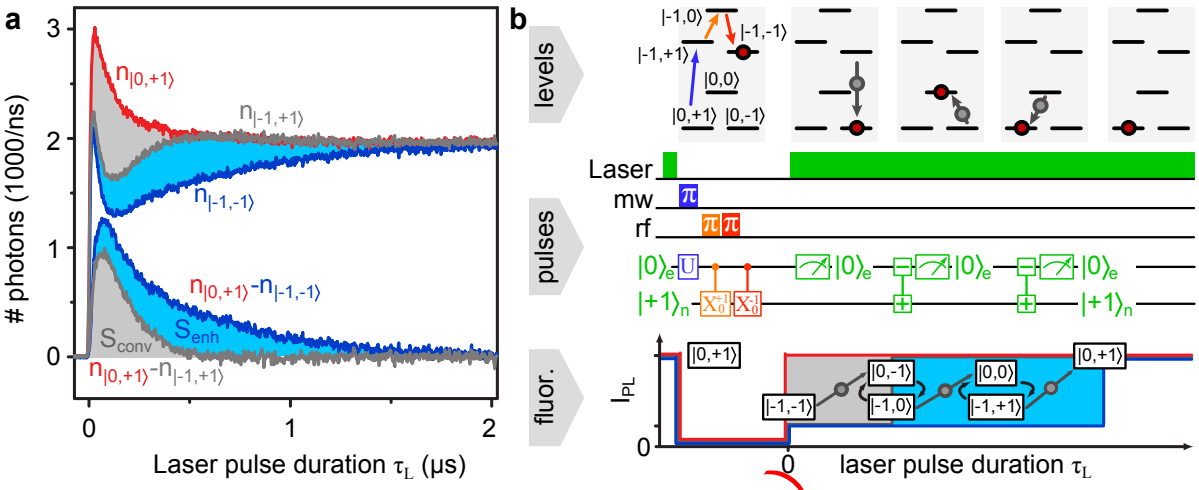

Figure 5.7.: Optical spin readout enhancement. **a,** Three different fluorescence responses to a laser pulse (upper three curves) corresponding to different initial spin states (compare section 2.2.6). Spin state $|0,+1\rangle$ (red curve), state $|-1,+1\rangle$ (gray curve) and state $|-1,-1\rangle$ (blue curve). Conventional signal photons are the difference between red and gray curve which yields the light gray area. The enhanced amount of signal photons corresponds to the light blue area. **b,** Mechanism behind enhanced readout in level scheme, pulse sequence and fluorescence response representation with common time axis. The mechanism is explained in the text. As a unitary transformation on the electron spin a π-pulse is chosen which yields the blue fluorescence response. If no mw pulse is present the red curve would be the fluorescence response.

methods have been applied simultaneously on the same spin to ensure equal conditions and equal signal accumulation time. Specifically, a lone laser pulse, a mw π-pulse followed by a laser pulse and a mw π-pulse plus nuclear spin correlation and laser pulse have been applied in an alternating fashion (see figure 5.8a). This yields the numbers of fluorescence photons $N_\psi = N_{|0,+1\rangle}$, $N_{|-1,+1\rangle}$ and $N_{|-1,-1\rangle}$ as they grow over laser duration τ_L by summing up the photons $n_\psi(t_i)$ of each interval t_i (see figure 5.7a).

$$N_\psi(\tau_L) = \sum_{t_i=0}^{\tau_L} n_\psi(t_i) \tag{5.16}$$

If the signal is taken to be the number of signal photons (e.g. $S_{\text{enh}} = N_{|0,+1\rangle} - N_{|-1,-1\rangle}$ for enhanced and $S_{\text{conv}} = N_{|0,+1\rangle} - N_{|-1,+1\rangle}$ for conventional readout) then the Noise due to shot noise is the square root of all collected fluorescence photons (e.g. $\sqrt{N_{|0,+1\rangle} + N_{|-1,-1\rangle}}$ for enhanced readout) and we arrive at a signal to noise ratio of

$$\text{SNR}(\tau_L) = \frac{N_{|0,+1\rangle}(\tau_L) - N_{|m_S,m_I\rangle}(\tau_L)}{\sqrt{N_{|0,+1\rangle}(\tau_L) + N_{|m_S,m_I\rangle}(\tau_L)}} \,. \tag{5.17}$$

The experimentally obtained SNR is plotted in figure 5.8c for both conventional and enhanced readout mechanisms. Apparently, the SNR of the enhanced readout is a factor

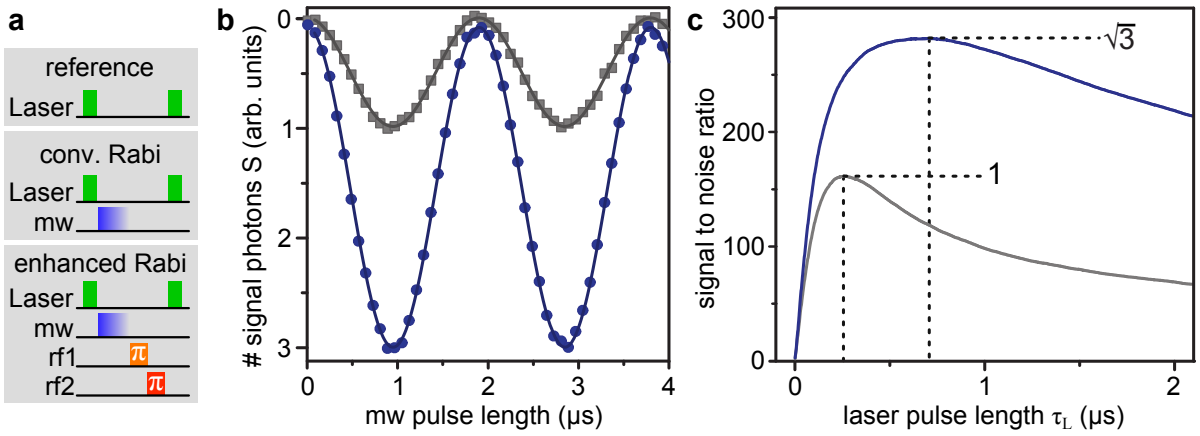

Figure 5.8.: enhanced signal to noise ratio. **a,** Pulse sequence to record a reference number of photons, conventionally readout photons for a Rabi oscillation and enhanced readout photons for a Rabi oscillation (from top to bottom). **b,** Rabi oscillation using conventional readout (gray curve) and enhanced readout (blue curve). The signal is given in accumulated signal photons normalized to the conventional signal. **c,** Signal to noise ratio SNR for increasing readout laser pulse length τ_L. The corresponding pulse sequence is shown in panel a where the mw pulse is a π-pulse. The maximum occurs because the number of signal photons saturates but the photon shot noise constantly increases. The maximum SNR for enhanced readout (blue curve) is $\sqrt{3}$ times bigger than for conventional readout (gray curve).

of $\sqrt{3}$ larger and occurs for a three times longer laser pulse duration. The explanation for this is straight forward. Because the novel method passes three times through the metastable state the signal is three times enhanced and the duration is three times longer. The longer accumulation time also leads to a larger shot noise increased by a factor of $\sqrt{3}$. Thus the SNR is $3/\sqrt{3} = \sqrt{3}$ larger. For laser pulse durations larger than the average time to pass the metastable state the SNR decreases again because no more signal is acquired but the noise still rises as $\sqrt{\tau_L}$.[4]

Although the polarization of nuclear spins works over a wide range of magnetic fields around the esLAC, the readout enhancement does not. As the detuning from the esLAC increases the time until a successful flip-flop in the excited state occurs increases as well. In turn, the signal photons are collected over a much longer time which leads to an increase of noise accompanied by a reduction of the SNR. This behavior is modeled in [55].

Finally, the SNR of a single readout step (i.e. a single laser pulse) is still smaller than one preventing to readout the electron spin state in a single shot. Thus, additional enhancement is needed. An option would be to extend the presented technique to n additional nuclei with spin I_n that show similar polarization dynamics. The improvement

[4] In a practical experiment all photons up to the maximum SNR are registered for the I_{PL} although the laser pulse might be longer. In the case of pulsed ODMR spectra (see figure 5.5c and appendix B.4) the laser pulse length matches the time for optimum SNR.

would be $\mathrm{SNR}_{\mathrm{enh.}}/\mathrm{SNR}_{\mathrm{conv}} = \sqrt{1+\sum_n 2I_n}$. Using nanodiamonds in our current setup count rates of $\approx 0.8\,\mathrm{Mcps}$ have been achieved which translates to a demand for ≈ 30 additional $I = 1/2$ nuclear spins to reach SNR = 1. Although, the current status of this technique does not allow single shot readout it facilitates the speedup of any experiment on the electron spin. If for instance the electron spin is used to sense a magnetic field exploiting a long T_2 time of up to a few milliseconds the time to establish the electron nuclear spin correlation and subsequent readout are negligible. Thus the measurement time to arrive at a similar uncertainty is three times shorter using the novel approach (see appendix C.5).

5.3. Protection of quantum information in a single nuclear spin

In the previous sections of this chapter it was demonstrated how spin dynamics in the excited state of the NV center can be exploited to polarize several proximal nuclear spins simultaneously on the one hand and how the polarization mechanism behind this is used to incorporate the nuclear spins into the readout process to enhance the signal on the other hand. All this is related to rather fast electron nuclear spin flip-flops that do not allow for instance the storage of quantum information in nuclear spin states.

In this section, on the contrary, we demonstrate the successful decoupling of the nitrogen nuclear spin from flip-flops with the electron spin of the NV center. By increasing the magnetic field strength far from the esLAC while keeping its direction very accurately parallel to the NV center axis it is possible to suppress electron and nuclear spin flip-flops to a very high degree. This way information stored in nuclear spins can survive multiple laser excitation and decay cycles. Hitherto quantum information can be protected using weakly coupled ^{13}C nuclear spins that exhibit only small hyperfine interactions with special tensor axes [53]. By repetitive readout of the quantum information stored on these nuclear spins before the decay of this information the SNR of a single readout step can be enhanced [53]. However, the small hyperfine coupling makes this approach very slow and an unfavorable hyperfine tensor limits the amount of repetitive readout steps and therefore the degree of SNR enhancement.

Up to now the single shot threshold has not been reached (i.e. knowledge about the quantum state could not be acquired before the state decays). However, the degree of decoupling presented here is sufficiently high to support enough readout steps to beat this limit. Moreover, even after gaining knowledge of the quantum state (i.e. projective measurement) the same quantum state is still present facilitating projective QND measurements [182]. Finally, the nature of the QND readout manifests in the observation of quantum jumps of a single nuclear spin (see figure 5.9b). In addition to the projective measurement of the nuclear spin which destroys any coherence it is possible to protect quantum coherence during laser excitation [55].

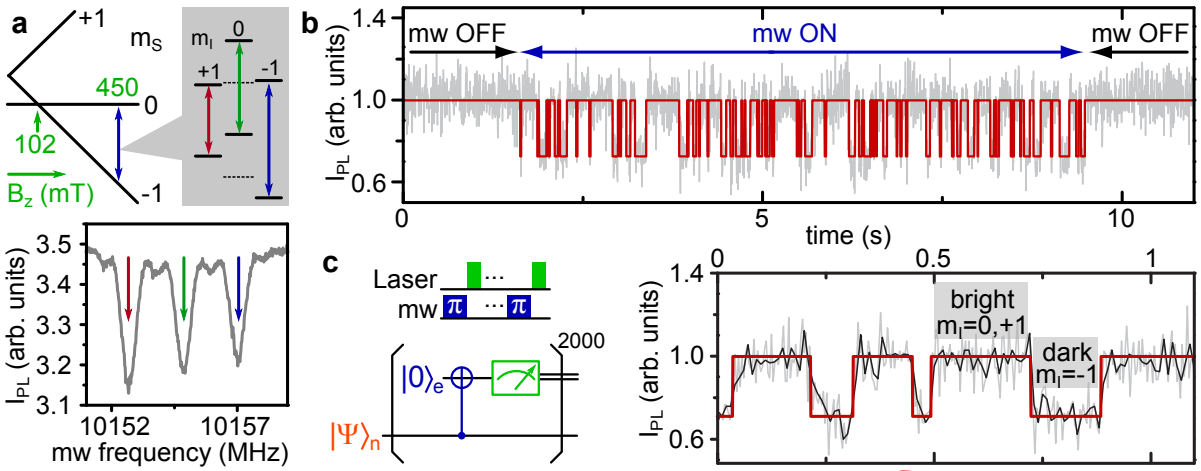

Figure 5.9.: Quantum jumps of a single nuclear spin. **a,** Energy level scheme of ground state spin levels in a large axial magnetic field (upper part). The EPR transitions are marked for different nuclear spin projections. In the lower part the corresponding ODMR spectrum is shown. **b,** Fluorescence time trace (gray curve) of projective nuclear spin state measurement. Abrupt jumps in fluorescence are due to quantum jumps of the nuclear spin state. A high level of fluorescence corresponds to spin states $m_I = 0, +1$ and low level to $m_I = -1$. For the measurement sequence (see panel c) the mw radiation has to be switched on. A zoom in (lower part) reveals the time scale of the jumps as several tens of ms. The red line resembles the quantum state trajectory obtained by HMM analysis. **c,** Measurement sequence for QND readout of nuclear spin state in pulse representation (upper part) and as quantum wire diagram. As illustrated the mw pulse is a nuclear spin state selective ($m_I = -1$) π-pulse with length 1300 ns. The laser pulse is 200 ns long followed by a 1000 ns waiting time.

5.3.1. Quantum jumps of a single nuclear spin

The measurement of the spin state of a single ^{14}N nucleus is straight forward. First, the electron spin is initialized by a laser pulse into $m_S = 0$. Afterwards, the electron spin state is correlated with that of the nuclear spin by a proper CNOT gate (e.g. $|m_S = 0, m_I = -1\rangle \rightarrow |-1, -1\rangle$ and $|0, 0\rangle \rightarrow |0, 0\rangle$, $|0, +1\rangle \rightarrow |0, +1\rangle$, see figure 5.9a,c). Finally, a laser pulse reads out the electron spin state and therefore also gives insight into the nuclear spin state (i.e. low fluorescence level: $m_S = -1$ and $m_I = -1$ ($|-1\rangle_n$); high fluorescence level: $m_S = 0$ and $m_I = 0, +1$ ($|0\rangle_n$, $|+1\rangle_n$)).[5] The final laser pulse is at the same time the electron spin initialization laser of the next readout step of this continuously repeating sequence. Experience shows that the state of the nuclear spin changes already after very few excitation cycles for standard measurement conditions (in particular for low magnetic fields compared to D_{gs} and laser pulse length $\approx 3\,\mu s$). It has therefore not been possible experimentally to gain enough information about the

[5] A single readout step is already projective although we can not collect the full information emitted.

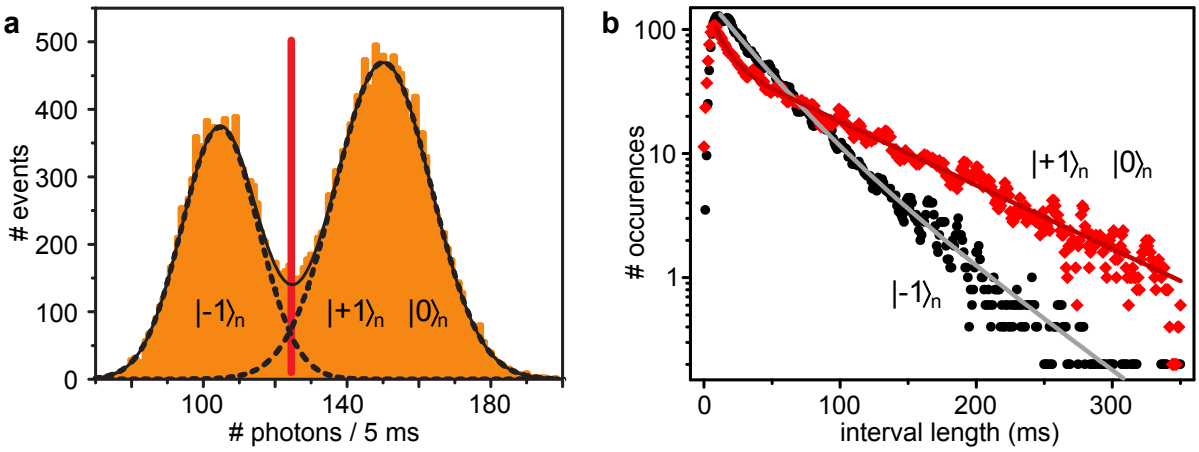

Figure 5.10.: Nuclear spin state lifetime. **a,** Histogram of a fluorescence time trace (see figure 5.9b) reveals two Poisson distributions belonging to different nuclear spin states. For the histogram fluorescence photons within 5 ms are binned. For longer binning times the limited spin state lifetime would distort the distributions from the Poissonian shape. The vertical red line marks the threshold to distinguish state $|-1\rangle_n$ from the other states. The overlap of the two Poissonians leads to a limited fidelity. **b,** Histogram of the average interval length of a particular fluorescence level as obtained from the HMM analysis of fluorescence time traces. The average length corresponds to the average nuclear spin state lifetime under the given experimental conditions. The black/gray curve corresponds to nuclear spin state $|-1\rangle_n$ and the red curve to $|0\rangle_n$, $|+1\rangle_n$.

spin state (i.e. distinguish the two fluorescence levels) before it decays.[6] In the present setting, however, the spin state remains unaltered long enough to achieve that.

Figure 5.9b shows an example fluorescence time trace acquired using the afore described measurement sequence. Apparently, the fluorescence suddenly jumps statistically between two levels corresponding to the different nuclear spin states. Thus, these changes in fluorescence monitor the quantum jumps of the nuclear spin. If the mw radiation that correlates electron and nuclear spin is switched off, however, the jumps disappear as expected and the fluorescence level remains high.

To further characterize the fluorescence time-trace a histogram of the number of photons in all time bins is presented in figure 5.10a. Clearly, two peaks are visible, one corresponding to the high fluorescence level and spin states $|0\rangle_n$, $|+1\rangle_n$ and the other one corresponding to the 30 % reduced level and nuclear spin state $|-1\rangle_n$. Both peaks are fitted by a Poissonian distribution. The shown fluorescence time trace exhibits a perfect playground to apply a Hidden Markov Model (HMM) analysis. The HMM can find the two individual histograms of each state and therefore the fluorescence levels, the transition rates $1/T_1$ between the two states and the most likely sequence of states

[6] In principle enough signal photons can be emitted during a single laser pulse to distinguish two spin states using the conventional readout scheme. In addition other readout schemes might be possible that gain information on the electron spin state before it is reinitialized.

([183, 184], see appendix D). Here, T_1 is the average lifetime of spin state $|-1\rangle_n$ which corresponds to the low fluorescence level. The lifetime $T_1^{0,+1}$ of the high level , however, corresponds to the two remaining states and is therefore roughly twice as long. The HMM analysis is able to some extend to check whether the number of states (two in this case) is appropriate. The two level model leads to a good agreement with the experimental data and the calculated most likely sequence of states shown as red line in figure 5.9b is a guide to the eye.

The average time between two jumps is on the order of several tens of milliseconds (see figures 5.9b, 5.10b). Hence, the information about the quantum state is not only acquired just before it is lost but it is conserved on the nuclear spin for even longer times. Therefore, the measurement is not only a single shot measurement but a projective QND measurement (see below).

5.3.2. Make nuclear spins robust against electron spin readout

To understand the mechanism that reduces the flip-flops among electron and nuclear spins the spin Hamiltonian has to be analyzed.

$$\hat{H} = \underbrace{D\hat{S}_z^2 - \tilde{\gamma}_e B_z \hat{S}_z}_{\hat{H}_e} + \underbrace{\hat{\underline{S}} \cdot \mathbf{A} \cdot \hat{\underline{I}}}_{\hat{H}_A} + \underbrace{Q\hat{I}_z^2 - \tilde{\gamma}_n B_z \hat{I}_z}_{\hat{H}_n} \tag{5.18}$$

The corresponding level structure is depicted in figure 5.11a,b. As can be seen from eq. (5.18) the magnetic field is supposed to be perfectly parallel to the NV center symmetry axis. If this is fulfilled only the hyperfine interaction term $\hat{H}_A$ contains off-diagonal elements (compare eqs. (5.2–5.3)).

$$\hat{H}_A = A_\parallel \hat{S}_z \hat{I}_z + A_\perp/2 \left(\hat{S}_+ \hat{I}_- + \hat{S}_- \hat{I}_+ \right) \tag{5.19}$$

In their present form eqs. (5.18–5.19) are valid for ground and excited state. The values of D and $\mathbf{A}$ have to be adjusted for specialization. In section 5.1 it was derived that $A_\perp$ leads to substantial electron nuclear spin flip-flops around the esLAC (see figure 5.11a,b).[7] Furthermore, it could be shown experimentally that even at almost zero magnetic field and up to the gsLAC the flip-flop terms are sufficiently strong to govern spin dynamics (see section 5.1). Therefore, it is absolutely necessary to increase the magnetic field far beyond the esLAC to reduce the spin flip-flops. In this case the Lorentzian function of the flip-flop probability p_+ (see eq. (5.8) and figure 5.11a) can be approximated by the following magnetic field dependence.

$$\begin{aligned} p_+(B_z) &\approx \left. \frac{4A_\perp^2}{\Delta^2(B_z)} \right|_{\Delta^2 \gg A_\perp^2} \\ &\approx \frac{4A_\perp^2}{(\tilde{\gamma}_e B_z - D_{es})^2} \end{aligned} \tag{5.20}$$

[7] The same behavior is present at the gsLAC [185], however, there the hyperfine strength is ≈ 20 times smaller. This effect is therefore neglected in the present analysis.

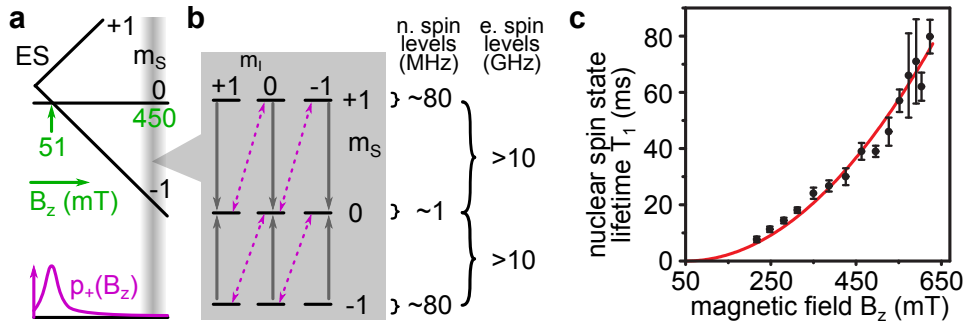

Figure 5.11.: Suppression of electron and nuclear spin flip-flops. **a,** Electron spin levels in the excited state for an axial magnetic field B_z. Many experiments in this chapter are carried out at around 450 mT. In the lower part the nuclear spin flip probability $p_+(B_z)$ due to hyperfine interaction is shown. **b,** Transition rates among spin levels in the excited state. The flip-flop rates (purple dashed arrows) are highly suppressed because of the large energy mismatch of nuclear and electron spin level spacings (see right part). The electron spin polarization through ISC (gray arrows) is still active. **c,** Nuclear spin state lifetime for various magnetic fields. The data is fit by a quadratic function centered at 50 mT.

Apparently p_+ decreases as the inverse square of the detuning from the esLAC. For nuclear spins of alkaline earth metal ions similar decoupling mechanisms have been proposed [186, 187].

As the flip-flop mechanism is decreased by high magnetic fields other sources that cause nuclear spin flips have to be considered. Nuclear spins in solids are usually strongly influenced by the bath of other electron and nuclear spins. In the case of diamond, however, both of these baths are very dilute such that coupling to these spins is much smaller than couplings to the NV center spin. Phonons can affect the nuclear spin state for instance by their influence on the electron spin via spin-orbit coupling. Again, this effect is minor for the NV center because of no spin orbit coupling in the ground state and averaged spin-orbit coupling in the excited state (see chapter 4). Another weak point might be the quadrupole tensor of the nuclear spin; it is usually very susceptible to changes of the electric field. Especially, possible ionizations of the NV center might therefore affect the quadrupole tensor and in turn might induce spin flips. As was shown in figure 5.3b,c of section 5.1 a misaligned magnetic field induces spin flips as well.

Eventually, it turns out that all other potentially detrimental effects are minor compared to the hyperfine induced nuclear spin flips. In [55] the nuclear spin polarization was studied far beyond the excited and ground state LAC and surprisingly still showed substantial but decreasing polarization. This behavior could be very well simulated by neglecting all other nuclear spin flip mechanisms. Eventually, the decoupling was good enough to see the nuclear spin quantum jumps.

To further support the magnetic field dependence of the nuclear spin robustness the average spin flip time T_1 visible in the time-traces is analyzed for an increasing magnetic

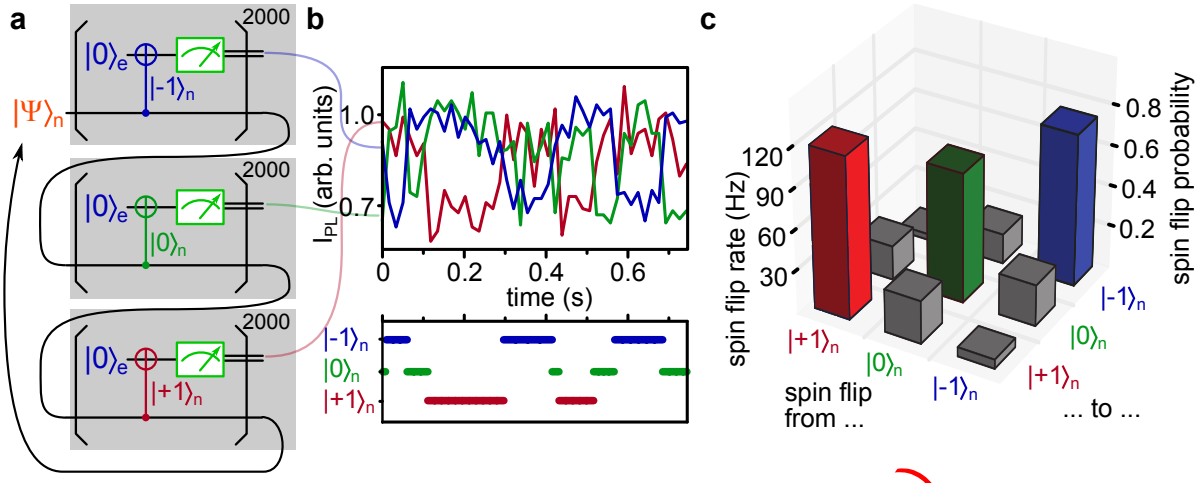

Figure 5.12.: Single shot readout of a spin triplet. a, Measurement sequence to distinguish all three projections of the ^{14}N nuclear spin triplet. The color coding of the CNOT gates illustrates the control qubit state (i.e. the mw frequency, compare figure 5.9a). **b,** Time traces for all three nuclear spin state readouts (upper part). Quantum state trajectory deduced from time traces (lower part). **c,** Matrix showing transition rates or spin flip probabilities from any spin projection to another.

field. As the T_1 time should be inverse proportional to the spin flip probability p_+ we expect the following dependence on the magnetic field.

$$T_1 \propto (\tilde{\gamma}_e B_z - D_{es})^2 \quad . \tag{5.21}$$

Experimentally we were able to detect quantum jumps in a magnetic field range of 200 mT up to 650 mT where the lower bound is due to the decreasing visibility of jumps and the higher limit is due to the limited strength of the used permanent magnet. Figure 5.11c shows that T_1 indeed nicely increases quadratically from ≈ 8 ms to ≈ 80 ms with increasing magnetic field.[8] Hence in the given field range the results support the theory of hyperfine induced electron nuclear spin flip-flops as the main mechanism affecting the nitrogen nuclear spin.

As flip-flops would only change the nuclear spin state by one quantum at a time only single quantum changes of the nuclear spin state are expected (i.e. $\Delta m_I = \pm 1$). So far we were only able to tell apart $|\Psi\rangle_n = |-1\rangle_n$ and $|\Psi\rangle_n \neq |-1\rangle_n$ (i.e. $|\Psi\rangle_n = |0\rangle_n, |+1\rangle_n$). To really distinguish all three states the CNOT gate has to change the corresponding control-qubit state in an alternating fashion. This is achieved by tuning the mw frequency into the corresponding resonance (see figures 5.9a and 5.12a). Part of the resulting time-trace that now distinguishes all three ^{14}N nuclear spin states in shown in figure 5.12b. An analysis of the whole time trace yields the transition rates between the individual states (see figure 5.12c). Apparently, mainly single quantum jumps occur.

[8] The T_1 time is the total time and includes periods where the laser is switched on and where it is switched off given the measurement sequence shown in figure 5.9c.

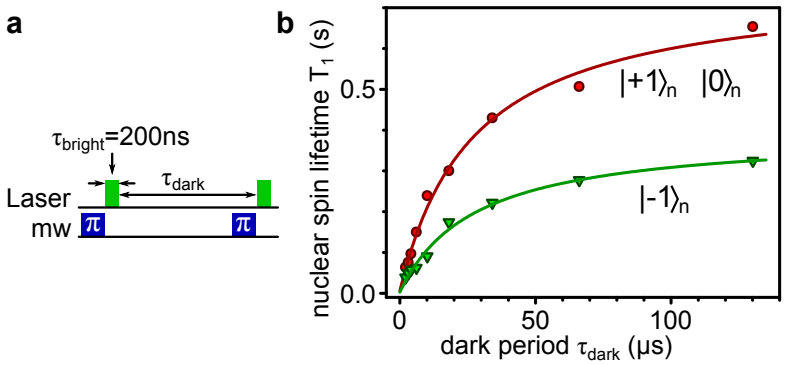

Figure 5.13.: Nuclear spin lifetimes with and without laser illumination. **a,** Pulse sequence to deduce nuclear spin lifetimes with and without illumination. **b,** Nuclear spin lifetime for increasing dark intervals for states $|-1\rangle_n$ and $|0\rangle_n$, $|+1\rangle$.

	low I_{PL} level ($|-1\rangle_n$)	high I_{PL} level ($|0\rangle_n$, $|+1\rangle_n$)
T_1^{dark} (ms)	390 ± 20	760 ± 30
T_1^{bright} (ms)	2.8 ± 0.2	5.6 ± 0.4

Table 5.1.: Nuclear spin T_1 times with and without laser illumination. Nuclear spin state lifetime T_1 for illuminated and dark case given for both high and low fluorescence level I_{PL} (i.e. for spin states $|0\rangle_n$, $|+1\rangle_n$ respectively $|-1\rangle_n$).

The few double quantum transitions can be attributed to the finite readout duration of 5 ms which in fact can include two single quantum jumps.

Up to now the hyperfine interaction in the ground state has been neglected as a reason for nuclear spin flips. Nevertheless, it will cause flips but on a much longer time scale. To increase the effect of the ground state hyperfine interaction the measurement sequence has been changed (see figure 5.13a). Additional "dark" intervals (i.e. laser and microwave are switched off) have been introduced to increase the time τ_{dark} without laser illumination. During this time only the ground state spin Hamiltonian governs the spin dynamics. The duration τ_{bright} of the laser illumination is kept constant. Figure 5.13b shows the increase of T_1 as the dark period is increased. If we assume an intrinsic spin lifetime for the illuminated case T_1^{bright} and the dark case T_1^{dark} the total lifetime should be

$$T_1 = \frac{\tau_{\text{bright}} + \tau_{\text{dark}}}{T_1^{\text{bright}}/\tau_{\text{bright}} + T_1^{\text{dark}}/\tau_{\text{dark}}} \,. \tag{5.22}$$

This equation is fit to the data in figure 5.13b and results in the intrinsic lifetimes values given in table 5.1. As expected the nuclear spin state lifetime is much longer under dark conditions. The flip-flop rate is expected to scale quadratically with the hyperfine interaction strength (see eq. (5.20)). Thus, if we set the hyperfine interaction of the excited state as the average interaction during illumination and the ground state

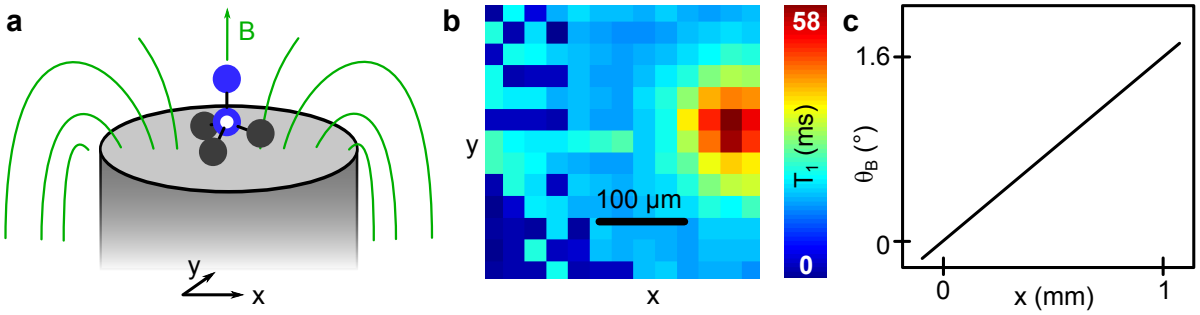

Figure 5.14.: Dependence of nuclear spin state lifetime on magnetic field alignment. a, Illustration of permanent magnet and the NV center in diamond under investigation. The magnet is a rod of 45 mm diameter and the NV has a distance of 2 mm. **b,** Nuclear spin T_1 map as function of lateral NV position. The magnetic field is aligned where T_1 is maximal. The FWHM is $\approx 100\,\mu m$. **c,** Magnetic field angle θ_B with respect to vertical axis as a function of lateral displacement x from center.

value for the dark period we would deduce a lifetime ratio of $\approx 20^2 = 400$. Instead, we have a ratio of ≈ 150. Apparently, we rather have an average hyperfine interaction during illumination because the NV resides also some amount of time in the ground and metastable state where hyperfine interaction is different.

Finally, the requirements for a stable and accurate magnetic field direction parallel to the NV center axis are demonstrated. A schematic magnetic field setup is shown in figure 5.14a. We use permanent magnetic rod with a magnetization along the rotation axis. The diamond has a [111] surface orientation and we are therefore able to select an NV center with its symmetry axis perpendicular to the diamond surface and parallel to the magnet symmetry axis. If the magnet in figure 5.14a is moved laterally the field angle changes slightly (see figure 5.14c). The corresponding nuclear spin T_1 time map (figure 5.14b) shows a distinct peak where perfect alignment is obtained. The FWHM is $\approx 100\,\mu m$ and the corresponding angle is $\approx 0.16\,°$.

Finally, another way of achieving higher robustness would be to use ^{13}C nuclear spins which lie on the NV center axis. These spins would exhibit the same hyperfine tensor symmetry as the nitrogen nuclear spins but with a much weaker interaction strength which would decrease the flip-flop rate drastically. The closest axial ^{13}C spins are those situated three bond lengths below or four bond lengths above the vacancy (compare figure 2.1). As the main part of the NV center's electron spin density is located in the dangling bonds of the carbon atoms and partially in the plane perpendicular to the NV axis [111, 124] the hyperfine interaction is expected to be comparably small. A point dipole approximation with the electron spin centered in the vacancy yields $A_\parallel$ values of 0.25 MHz and 0.1 MHz for the closer and the further apart ^{13}C spins mentioned above (see appendix A). For a diamond sample with a reduced ^{13}C concentration this is easily resolvable in an ODMR spectrum and therefore the required CNOT gates are feasible. The expected flip-flop limited T_1 time would be around 20 s according to eq. (5.20) and

table 5.1. Even at low magnetic fields the nuclear spin flip-flops with the electron spin can be suppressed to a higher degree as for the nitrogen nucleus at the high fields used.

5.3.3. Quantum nondemolition measurement

The character of the nuclear spin state measurement presented here is that of a QND measurement. The most striking feature is the correlation between the quantum state before and after a measurement. In the present case a projective measurement is performed as opposed to a weak measurement. Therefore, the correlation is present only for eigenstates as input states or for output states of consecutive measurements.

Imoto and coworkers have proposed a scheme to perform a QND measure to reveal the number of photons in a signal beam by introducing an interaction with a probe beam due to the optical Kerr effect [188]. In their paper they have given four requirements which should be met in order to realize a QND measurement. In our experiment these requirements impose restrictions on the system observable I_z with its Hamiltonian $\hat{H}_n$, the probe observable S_z with $\hat{H}_e$ and on the interaction Hamiltonian

$$\hat{H}_i = \hat{H}_A + \hat{H}_p \tag{5.23}$$

$$\hat{H}_p = \Omega_{mw} \left(\hat{S}_x \cos \omega t + \hat{S}_y \sin \omega t \right) \otimes |m_I = -1\rangle\langle m_I = -1| \tag{5.24}$$

where $\hat{H}_p$ describes the action of the mw pulse (CNOT gate) with frequency ω and strength Ω_{mw}. The pulse Hamiltonian $\hat{H}_p$ only acts for a time τ_π such that it realizes the CNOT gate whereas the hyperfine interaction $\hat{H}_A$ is always present, either in the ground state or, during electron spin state readout, in the excited state. The **QND requirements** are:

1. The system has to influence the probe sufficiently strong to convey information about the system state. Therefore, it is necessary that the interaction Hamiltonian $\hat{H}_i$ on the one hand depends on the system observable I_z.

2. On the other hand $\hat{H}_i$ should not commute with the probe observable S_z ($\left[\hat{H}_i, \hat{S}_z\right] \neq 0$). Obviously, eq. (5.24) fulfills these two requirements.

3. The system state has to be sufficiently stable (i.e. m_I should be a good quantum number). Therefore, the Hamiltonian governing the nuclear spin evolution must not contain any $\hat{I}_x$ or $\hat{I}_y$ components (i.e. no conjugate observables to $\hat{I}_z$). Otherwise, measurement backaction would increase the uncertainty of the observable's conjugates. As long as the magnetic field is perfectly aligned this condition is fulfilled (see section 5.1).

4. The system observable $\hat{I}_z$ should be very well isolated from the environment, especially from the probe observable $\hat{S}_z$. In other words neither the probe nor the environment should affect system state during measurement. This is ensured as

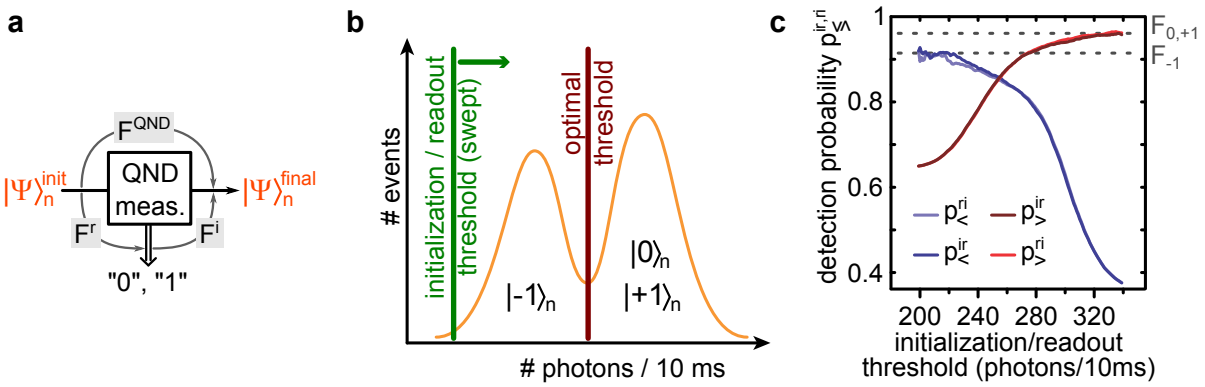

Figure 5.15.: Fidelities in a QND measurement. **a,** Schematic illustration of fidelities in a QND measurement and how they connect initial state Ψ_{init}, final state Ψ_{final} and measurement results "0", "1" (see text). **b,** Illustration of measurement scheme to deduce initialization and readout fidelity. The photon counting histogram shows the fixed optimal threshold (red) for state discrimination and a variable initialization/readout fidelity (green). The data of a fluorescence time trace will be analyzed using both thresholds. **c,** Correlation between two consecutive measurement outcomes in a time trace for different initialization/readout thresholds. Either the first measurement is below ("<") the initialization threshold and the second one below the optimal threshold ("ir") or the thresholds are in reversed order ("ri"). These two cases yield $\mathcal{F}_{-1}$ as the value for the initialization and readout fidelity for state $|-1\rangle_n$. If both measurement outcomes are above (">") the thresholds we initialize and readout states $|0\rangle_n$, $|+1\rangle_n$. This yields the corresponding initialization and readout fidelity $\mathcal{F}_{0,+1}$.

long as the interaction Hamiltonian commutes with the system observable (i.e. $\left[\hat{H}_i, \hat{I}_z\right] = 0$).

Especially condition 4 is very hard to realize experimentally. In diamond, however, spins and especially nuclear spins are very well isolated from the environment [56] such that the system state is almost unaffected during measurement. As pointed out earlier, the most severe interaction that does not fulfill condition 4 is the hyperfine interaction $\hat{H}_A$. However, by increasing the magnetic field (see section 5.3.2) the 4 conditions can be almost ideally fulfilled. The effect of the hyperfine interaction could be reduced such that its effect is only visible as quantum jumps on a timescale much longer than the measurement time.

To quantify how good a QND measurement is several correlation Fidelities can be determined [189]. In the following the fidelities will be given for one QND readout sequence which consists of 2000 steps where each step consists of a CNOT gate and a laser pulse (see figure 5.9c). The **correlations/Fidelities** are (see figure 5.15a):

- **Readout fidelity** $\mathcal{F}^{\text{r}}$: is the correlation of the input state with the measurement result. For projective measurements eigenstates are used as input states. If the fidelity is "1" the result always matches the input state.

- **QND fidelity** $\mathcal{F}^{\mathrm{QND}}$: correlates input and output state. In the case of projective measurements both should be eigenstates. For a fidelity of "1" the output state is unaltered and thus is equal to the input state.

- **Initialization fidelity** $\mathcal{F}^{\mathrm{i}}$: correlates the actual output state with the measurement result. The higher this value the more reliably a QND readout can be used for qubit initialization.

First, the QND fidelity is deduced. Therefore, it is sufficient to know the T_1 time of the nuclear spin during a QND measurement sequence and the length of the readout sequence t_{QND}. The QND fidelity is then

$$\mathcal{F}^{\mathrm{QND}} = \mathrm{e}^{\frac{-t_{\mathrm{QND}}}{T_1}} \quad . \tag{5.25}$$

For a maximum $T_1 = 80\,\mathrm{ms}$ and a readout time of 5 ms (2000 steps) this yields $\mathcal{F}^{\mathrm{QND}} = 0.94$.

In the presented experiments we do not initialize the nuclear spin deterministically but rely on the QND readout result. Therefore, our measurable correlations depend on readout and initialization fidelities. Thus these fidelities cannot be extracted directly. To estimate these fidelities we calculate correlations between two subsequent measurements using variable thresholds. In figure 5.15b it is shown that the optimal threshold for fluorescence counts to distinguish between the quantum states is set close to the minimum of the two overlapping Poisson distributions. This is optimum to distinguish between the two cases. If, however, the task is to initialize into state $|-1\rangle_n$ with highest possible fidelity, it is better to lower the "initialization" threshold (threshold for the first measurement) even further down. This of course excludes many events when $|-1\rangle_n$ was indeed present but the ratio between $|-1\rangle$ and $|0\rangle_n$, $|+1\rangle_n$ increases; and so does the initialization fidelity. The resulting probability $p^{ir}_{<}$ to find $|-1\rangle_n$ according to the optimum threshold after it has been detected using a very small initialization threshold is then taken as the lower bound for the readout fidelity $\mathcal{F}^{\mathrm{r}}$ (see figure 5.15c). The same can be done using a variable "readout" threshold (i.e. for the second measurement). In this case we can check how the first measurement result using the optimal threshold changes while the readout threshold is lowered ($p^{ri}_{<}$ in figure 5.15c). This yields the initialization fidelity $\mathcal{F}^{\mathrm{i}}$. Indeed, initialization and readout fidelities approach a maximum as readout/initialization fidelities are shifted down (see figure 5.15c).[9] Still, the results are lower bounds. Apparently, initialization and readout fidelities are equal and have a lower bound of $92 \pm 2\,\%$.

The number of 2000 readout steps per QND sequence was chosen such that the readout fidelity is roughly maximized (using the optimal threshold). This number is influenced

[9] The optimal threshold was used to determine initialization/readout fidelities. The lowered Initialization/readout thresholds were only used to find the maximum lower bound of the fidelities by sorting out more uncertain events.

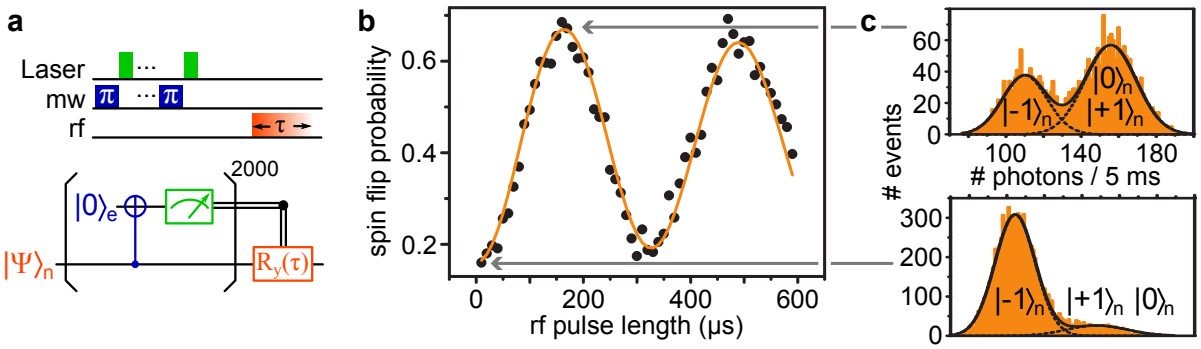

Figure 5.16.: Active feed-forward. **a,** Measurement sequence for a nuclear spin Rabi oscillation conditional on the previous nuclear spin readout result ($|-1\rangle_n$). The demonstrated nuclear spin rotation is comprised of CROT gates which can correlate the nuclear spin state with that of the electron spin (see text). **b,** Nuclear spin Rabi oscillation shown as spin flip probability from initial state $|-1\rangle_n$ to $|0\rangle_n$. **c,** Exemplary conditional photon counting histograms for no rf pulse (lower graph) and for a π-pulse (upper graph) on the nuclear spin.

by mainly two things. One is the limited spin state lifetime T_1 during readout and the other one is the number of fluorescence counts. As the number of fluorescence counts is increased the distance of the two Poisson distributions in figure 5.10a increases proportionally whereas the width only increases roughly as the square root of the photon count. Thus the overlap decreases and the fidelity increases as the photon count rises. The number of photons can be increased by extracting photons more efficiently[10] or by increasing the fluorescence rate [190, 191]. In addition, an increasing number of readout steps per QND sequence also yields more photons. On the other hand, increasing the number of steps also increases the probability for a spin flip during the QND sequence which in turn reduces the fidelity by increasing the overlap again.

5.3.4. Active feed-forward

The ability to perform projective QND measurements allows performing unitary operations and measurements conditional on the previous measurement result. This is usually referred to as active feed-forward and has applications for instance in one-way quantum computation [192] or quantum error correction.

We use active feed-forward to perform a nuclear spin Rabi oscillation only if the spin state is $|-1\rangle_n$ (see figure 5.16). The graph shows the spin flip probability over the length of the rf pulse. Obviously, the oscillation does not start at zero due to the limited fidelity. In fact, the oscillation starts at $2\mathcal{F}(1-\mathcal{F}) = 0.15$. Surprisingly, the oscillation is not symmetric with respect to 0.5 spin flip probability (i.e. it rises up to ≈ 0.68

[10] The [111] diamond sample here allows a better light extraction from NV centers oriented perpendicular to the surface because of the perfect alignment of their optical dipoles. Such an NV center is used here.

instead of up to the expected 0.85). This means that the rf π-pulse flips the nuclear spin in only 75 % of all cases. There are many possible reasons for this. One is improper electron spin initialization into $m_S = 0$ which would lead to an off-resonant rf π-pulse. Another reason might be improper rf pulses. Research to answer this question has been performed [132] and revealed an unperceived dark state of the NV center.

The demonstrated nuclear spin Rabi oscillation is a CROT gate as in all previous nuclear spin manipulations demonstrated in this work. As the demonstrated readout of the nuclear spin is far superior over the conventional electron spin state readout, it can be applied to assist the electron spin state readout. Therefore the electron spin state of interest has to be correlated with the nuclear spin with a CNOT gate (compare CROT gate in figure 5.16 and [53]). Finally, the nuclear spin state is readout using the demonstrated QND measurement. This method can be readily applied to quantum metrology applications using the NV center electron spin [65, 66, 56]. In that case the enhancement of the magnetic field sensitivity would be roughly 20 fold (see appendix C.5). The measurement results about the nuclear spin CROT gate presented in this section already do benefit from this readout enhancement as many thousand electron spin state readout steps follow only one application of the CROT gate compared to a one to one ratio in the case of the conventional readout scheme (compare figure 3.12).

Another straight forward application of the demonstrated active feed-forward would be the deterministic initialization of the nuclear spin qubit by transferring it into the desired state.

6. Coupling of two single NV centers — Scaling up the quantum processor

Up to now nuclear spins were investigated for their use as qubits to scale up the quantum register. However they possess a drawback that makes scaling slower. They need a bus-qubit to access the quantum information stored in them which is usually the NV center electron spin. In the present chapter we introduce a pair of coupled NV centers as a route towards an array of NV centers as a multi-qubit quantum processor (see figure 6.1). In such an array each NV center can be readout individually by a combination of optical and microwave means and no other bus-qubit is needed which makes scaling more favorable.

The interaction between the NV centers is mediated by magnetic dipole-dipole interaction which limits the maximum distance to a few tens of nanometers. This strong distance and angle dependence of the interaction is used to measure the exact relative orientation of the two NV centers. Additionally the first two qubit gates among different NV centers are performed and correlations among them are created.

To reduce influences from the nuclear spin bath we use an isotopically pure ^{12}C CVD diamond sample. The NV centers are created by high energy nitrogen ion implantation.

In addition to conventional optical and microwave techniques optical super-resolution methods are applied to characterize NV pairs.

The results presented in this chapter are published in [43].

6.1. Hamiltonian and magnetic dipolar coupling

The main interaction between the electronic spins of two NV centers A and B is the magnetic dipole-dipole interaction $\hat{H}_{dip}$.

$$\begin{aligned}\hat{H}_{dip} &= \frac{\mu_0}{4\pi}\frac{\tilde{\gamma}_e g_e \mu_B}{r^3}\left[\underline{\hat{S}}^A \cdot \underline{\hat{S}}^B - 3\left(\underline{\hat{S}}^A \cdot \underline{e}_r\right)\left(\underline{\hat{S}}^B \cdot \underline{e}_r\right)\right] \\ &= \underline{\hat{S}}^A \cdot \mathbf{M} \cdot \underline{\hat{S}}^B \\ &= \underline{\hat{S}}^A \cdot \mathbf{M}' \cdot \underline{\hat{S}}'^B\end{aligned} \tag{6.1}$$

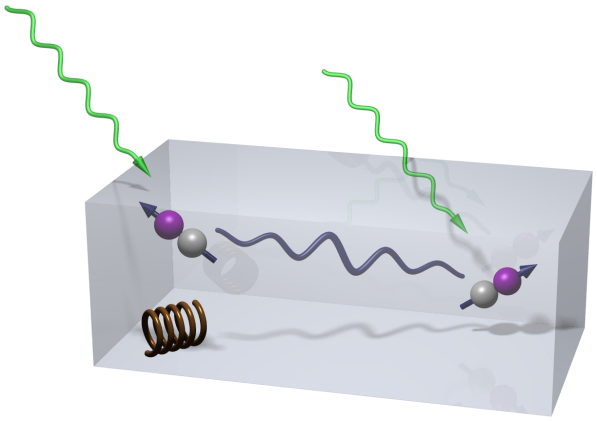

Figure 6.1.: Illustration of a coupled NV pair in the diamond lattice exhibiting two different NV axes. Both centers are manipulated by laser light and mw radiation.

Here g_e is the electronic g-factor, μ_B is the Bohr magneton and $r \cdot \underline{e}_r$ the vector connecting the two NV centers. The spin operators $\underline{\hat{S}}^A$ and $\underline{\hat{S}}^B$ are defined in a coordinate system where the z-axis coincides with the axis of NV A whereas $\underline{\hat{S}}'^B$ is defined in a system where the z'-axis coincides with the axis of NV B. The prefactor in equation (6.1) is equivalent to $\approx 50\,\mathrm{kHz}$ for a separation of 10 nm which is the relevant order of magnitude in this pair of coupled NV centers. Regarding typical spin coherence times of $T_2 \approx 2\,\mathrm{ms}$ for these kind of diamond samples this is sufficient for the creation of quantum correlations among this pair of spins for example.

In addition to the magnetic interaction there is an electrostatic interaction due to the charge of the NV center. The corresponding electric field induces a shift of the ground state electron spin levels on the order of MHz or less (see section 2.2.4 and C.1). All electrostatic effects, however, are constant when the NV center remains in its negative charge state and can therefore not be used for conditional quantum gates.

All NV pairs investigated so far had a distance of $\approx 10\,\mathrm{nm}$ or more. On that scale no overlap of the electronic wavefunction takes place. The corresponding interaction is therefore neglected.

The complete spin Hamiltonian for a pair of NV centers is therefore

$$\begin{aligned} \hat{H} &= \hat{H}_{\mathrm{NV\,A}} + \hat{H}_{\mathrm{NV\,B}} + \hat{H}_{dip} \\ \hat{H}_{\mathrm{NV}\,i} &= \underline{\hat{S}}^i \cdot \mathbf{D}^i \cdot \underline{\hat{S}}^i - \tilde{\gamma}_e \underline{B} \cdot \underline{\hat{S}}^i \ . \end{aligned} \tag{6.2}$$

Please note that each NV center in a pair can have a different orientation in the diamond lattice and therefore the ZFS tensor $\mathbf{D}$ might be different for the two centers (as it turns out that is the case for the present pair). In this spin Hamiltonian the nitrogen nuclear spins are neglected because they do not play a crucial role in the experiments presented in this chapter. Although the nuclear spins lead to a level splitting which is visible in the spectrum we can regard it as a splitting into three disjoint level schemes that behave

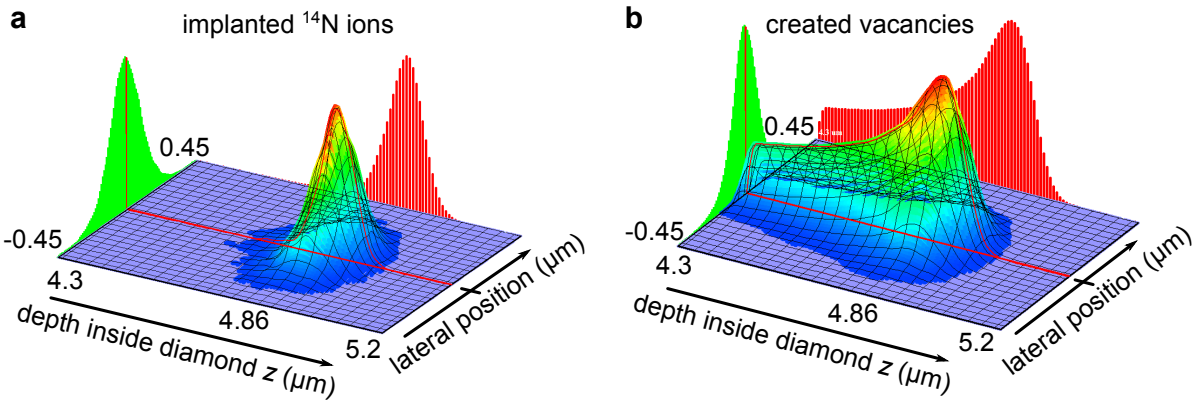

Figure 6.2.: Simulation of ion implantation by SRIM/TRIM ®. **a,** Probability distribution of an implanted ^{14}N ion in diamond. Depth and lateral distributions are shown. **b,** Probability distribution of the vacancies created by an implanted ^{14}N ion. One ion creates on average 2576 vacancies of which a considerable part is located in the area of the stopped ions where on average every nm of depth one vacancy is created per ion.

like three distinct NV electron spin levels without interchange. In future experiments the nuclear spins should be used to store the correlations created by the interaction of the electron spins.

The effect of the magnetic dipolar interaction on the energy levels and eigenstates is minor compared to the other contributions in eq. (6.2). In all experiments in this chapter energy level splittings will be much larger than 50 kHz. Thus a secular approximation is valid, i.e. energy level changes due to the interaction occur but changes of the eigenstates due to off-diagonal terms in $\hat{H}_{dip}$ can be neglected.

6.2. Creation of NV center pairs

ion implantation The present experiments are conducted in isotopically purified CVD diamond with a ^{12}C concentration of 99.99% and a (001) surface.[1] The nitrogen content in this sample is less than 1 ppb and it is therefore very unlikely to find a native NV center.[2] Thus the NV center pairs are created artificially, namely by ion implantation and subsequent annealing of the sample (see section 2.2.2).

The low ^{13}C content leads to long decoherence times and allows to study NV pair interaction in a clean environment. In addition the long coherence lifetimes allow smaller coupling strengths and thus larger distances between the NV centers within a pair. The low nitrogen content assures that the created NV centers are indeed formed out of the implanted nitrogen ions and not from residual nitrogen atoms in the lattice that capture

[1] The actual isotopically purified diamond is a several µm thick layer that was deposited on a synthetic diamond substrate by microwave plasma assisted CVD growth using purified methane.

[2] The approximate intrinsic NV density is $\sim 10^8\,\mathrm{cm}^{-3}$.

a produced vacancy.

As mentioned above NV distances on the order of a few 10 nm or less are necessary to achieve a coupled pair. This puts a high demand on the positioning accuracy of the implanted ions which has not been demonstrated so far. Actually many aspects affect the successful creation of a suitable pair of negatively charged NV centers:

- surface distance: Recently it has been shown that surface properties have a high influence on the NV center (e.g. charge state [112], spin environment [145]). Indeed, shallow implanted NV centers show inferior coherence properties and sometimes tend to change their charge state.

- conversion efficiency: To generate an NV center we need a substitutional nitrogen atom in the diamond lattice and proximal vacancies one of which should eventually bind to the nitrogen forming the color center. The probability to produce vacancies rises with implantation energy (see figure 6.2b). Indeed, low energy implants show low conversion efficiency to NV centers ($\approx 1\,\%$ [29]).

- implantation energy: A higher energy leads to a higher implantation depth. Before an implanted nitrogen ion comes to rest in the diamond lattice it straggles in lateral and axial direction (see figure 6.2a). The amount of straggle is increasing with increasing implantation energy. The freely available software SRIM ® [193] is used to simulate implantation events of ions into matter.

- ion beam focus: The high energy ion implantation facility used here has a focus of ≈ 200 nm.[3]

The last aspect, namely the beam spot size is the bottleneck when creating NV pairs for this experiment. On the other hand we can afford higher implantation energy such that the lateral straggle is roughly the beam size. This increases conversion efficiency and increases the distance to the surface thus decreasing deleterious surface effects.

Eventually the implantation energy used is 13 MeV per nitrogen ion which results in an implantation depth of $\approx 5\,\mu$m and straggle radius of ≈ 90 nm (i.e. the square-root of the variance of the radius, see figure 6.2a). With these settings multiple arrays of implantation sites were created where each site has a certain amount of implanted ions and this amount varies from one array to another (nominal number of ions per spot are in the range from 5 to 100, see figure 6.3a). Finally, the NV pair we use throughout this chapter was found in the array where each site nominally contains 6 implanted nitrogen ions (see figure 6.3b). From the average number of NV centers found in this array we deduce a conversion efficiency (from ion implantation to NV center formation) of 21 %.

optical characterization The technique of NV pair generation explained above has a very low success rate. Therefore, it is necessary to characterize the implantation sites

[3]The nitrogen ions were implanted by Jan Meijer at Rubion at University of Bochum.

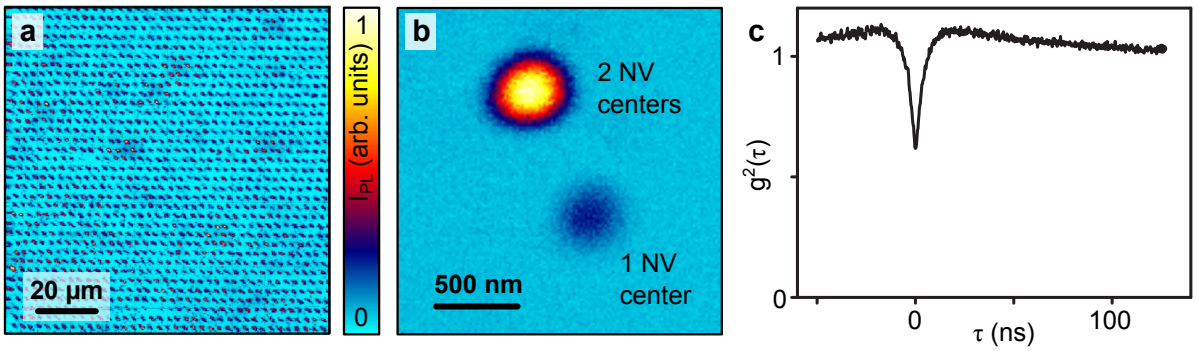

Figure 6.3.: Confocal scans of implantation area including NV pair. **a,** Implantation area with 10 N atoms per impact site. The colorbar indicates the fluorescence intensity I_{PL}. **b,** Zoom of implantation area with 6 N ions per site. Three ions have been converted, two as an NV pair and a separated one. **c,** Fluorescence autocorrelation function of the NV pair. Apparently, two single emitters are within the confocal volume.

of each array in order to find those sites that are likely to obtain a coupled NV pair. The following characterization steps are performed to narrow down the number of NV pair candidates:

1. Take a confocal scan image of an implantation array and find single fluorescent spots that contain more than one NV center. The fluorescence rate gives a rough estimate of the number of NV centers, later a fluorescence autocorrelation measurement can be done to verify the former finding (figure 6.3c).

2. Take a close-up of the former fluorescent spot (see figure 6.3b). Any visible deviation from the circular shape[4] originates from a lateral separation that is easily more than 10 nm. These spots can be rejected. (It is possible to check also the axial PSF shape; however, because of the lower resolution in this direction the implantation distribution should always fall well into the axial PSF.)

3. Take a super-resolution image of the remaining candidates using stimulated emission depletion (STED) [44] or ground state depletion (GSD) microscopy [63]. Resolutions of down to $\approx$ 5 nm have been demonstrated [44] which is sufficient to rule out any candidates that are too far apart in lateral and axial direction. We have only used lateral GSD scans on candidate pairs (see figure 6.4a and appendix B.1.2). Here a doughnut shaped illumination profile is used exhibiting a steep intensity gradient close to the center.

4. An alternative approach to resolve two NV centers with sub-wavelength separation is fluorescence lifetime imaging (FLIM) [194]. The basic idea of this method is to

[4]The actual shape might differ from a circle. The 2d PSF in the focal plane of a single emitter has to be taken to verify the shape.

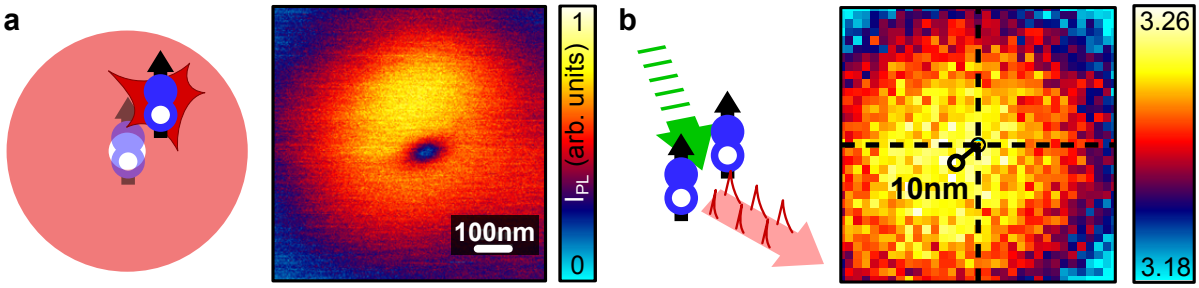

Figure 6.4.: Super-resolution images of the NV pair. **a,** GSD imaging mechanism (left, see text). A large area is illuminated except a very confined central region. Thus, even close NV centers can be separately excited. GSD scan (right) cannot resolve the NV pair. Obviously their separation is below the resolution limit of $\approx 20\,\mathrm{nm}$. The colorbar indicates the fluorescence intensity I_{PL}. **b,** Illustration of FLIM imaging (left, see text). Cross-correlation image of the two FLIM sub-images (see appendix B.1.1). The separation of the two centers is $\approx 10\,\mathrm{nm}$.

exploit different fluorescence lifetimes of the fluorescent objects under study to acquire a separate image for each fluorescent object (see appendix B.1.1). In the present case the fluorescence lifetimes of the two NV centers are made different by applying an appropriate magnetic field (see below).

Those NV pairs that pass all these tests will be investigated by means of EPR to gather information about their relative distance and orientation.

For the present diamond sample and the coupled NV pair under investigation the confocal images, the fluorescence autocorrelation measurement and the GSD are displayed in figures 6.3b,c and 6.4a. Next we go more into detail about the FLIM measurements. For this technique it is necessary for the two NV centers to have different fluorescence lifetimes. As it turns out the NV centers of the coupled pair have a different crystallographic orientation. Thus, by applying a sufficiently strong magnetic field ($\approx 70\,\mathrm{mT}$) along the symmetry axis of one center this one will be in its $m_S = 0$ state of the ground state after green laser illumination whereas the other center will be in a mixture of $m_S = 0, \pm 1$ (see section 2.2.4). Because of the different fluorescence lifetimes for $m_S = 0$ and $m_S = \pm 1$ the light emitted from the two NV centers is now distinguishable (see section 2.2.3).[5] Once this is assured 2 images (one for each NV, see figure B.1) are acquired where the pixel values of each image are the amplitudes the of the corresponding exponentially decaying fluorescence intensity. Finally both images can be accumulated long enough such that the uncertainty of the corresponding NV position is less than the distance between both centers. Here, we perform a cross-correlation of the two images to obtain the most likely lateral displacement of the two NV centers (see figure 6.4b). As it turns out the lateral separation is about 10 nm which might very well be sufficient

[5] If both centers have the same orientation an inhomogeneous (on the 10 nm scale) magnetic field could be applied. In addition this can be used to address two equally aligned NVs individually by mw radiation and for magnetic resonance imaging [65].

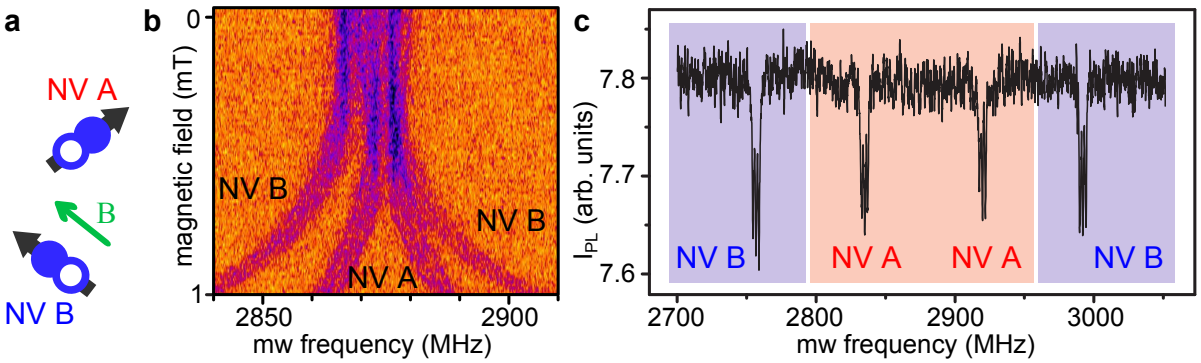

Figure 6.5.: ODMR spectrum of the NV pair. **a,** Sketch of the pair of NV centers and the magnetic field alignment. The field is applied along the axis of NV B. Thus, it is misaligned for NV A. **b,** Continuous acquisition of ODMR spectra while the magnetic field is slowly increased. Obviously, both centers have different values for ZFS parameters D and E. In addition, the resonance lines of NV B split further apart than the ones of NV A because of the aligned magnetic field. Caution: the magnetic field axis is not linear; only start and stop values are given. **c,** A single ODMR spectrum for a magnetic field of 4.3 mT aligned along NV B. The resonances for NV A and B are clearly distinguishable.

for coupling of the two spins. We have performed the FLIM measurement only in lateral direction, however an axial scan is possible as well. Again the lower axial resolution in conventional confocal microscopy would reduce the FLIM resolution in that direction as well.

6.3. Discrimination and individual addressing

In the following experiments we use conventional confocal microscopy to address both NV centers optically at the same time. Thus we also accumulate the fluorescence photons from both NV centers at the same time. Hence, we have no optical means to distinguish the two NV centers. They are distinguished by their different EPR transition frequencies instead.

Figure 6.5b shows the evolution of the ODMR spectrum of both centers (NV A and NV B) as the magnetic field is increased from zero to 1 mT. Here the field is aligned parallel to NV center B. In figure 6.5c a single ODMR spectrum of both centers for a magnetic field of 4.3 mT is shown. Obviously, both centers have different orientations in the crystal lattice (see figure 6.5a). As a consequence we can change the spin state of one center while the other spin remains in its $m_S = 0$ state for example. In that case the fluorescence intensity of the former center is modulated according to its spins state while the light emitted from the latter center remains constant. Consequently, the maximum achievable ODMR contrast when manipulating only one spin is half the usual contrast. In the following the contrast is normalized to the maximum achievable

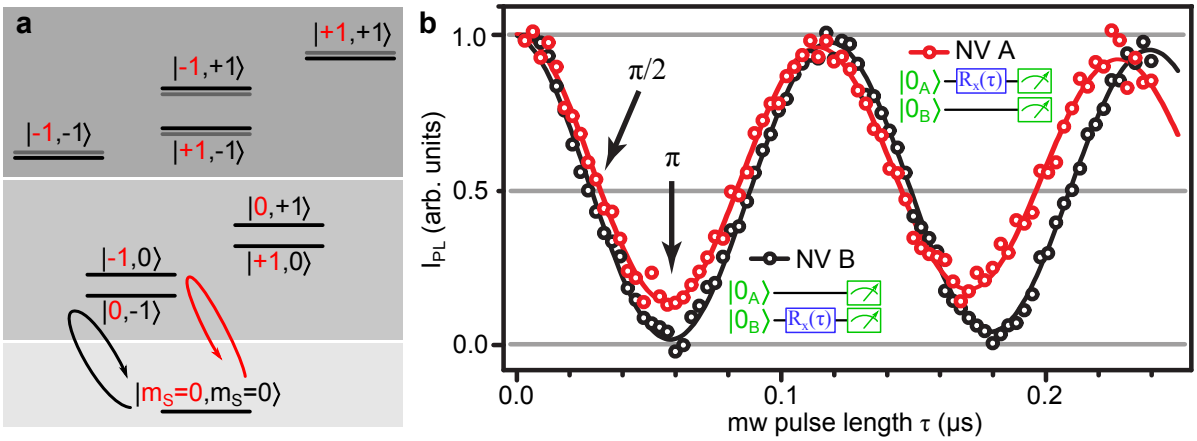

Figure 6.6.: Rabi oscillations of individual spins of an NV pair. a, Combined spin energy level scheme of the coupled NV pair. Black lines resemble energy levels for the uncoupled system and the gray lines indicate shifted levels due to the coupling according to approximation eq. (6.7). The background is shaded according to the level of fluorescence response (darker corresponds to less fluorescence). The performed Rabi oscillations are indicated by curved arrows with the same color coding as in **b,** Electron spin Rabi oscillation of the individual NV centers. Measurement sequence is the usual one (see section 2.3). Thus, the system is first initialized into $m_S = 0$ for both NVs.

contrast for manipulating one spin.

Another detail visible from the magnetic field sweep of the ODMR spectrum are surprisingly large zerofield splitting (ZFS) E values of 2.3 MHz for NV A and 5 MHz for NV B (i.e. the splitting of the levels $m_S = -1$ and $+1$ at zero magnetic field). This can be caused by an electric field or by strain of the lattice (see section 2.2.4). The electric field due to the charge of the NV centers itself, however, is not sufficient to account for the observed E values (these would be $E = 0.2$ MHz and $E = 0.4$ MHz for NV A and B respectively, see section C.1).

In the following we are using the combined spin energy level system displayed in figure 6.6a to explain the experiments. The names assigned to the energy levels correspond to $|m_S^A, m_S^B\rangle = |m_S^A{}_A\rangle \otimes |m_S^B{}_B\rangle$ where $m_S^{A,B}$ are the m_S quantum numbers of NV centers A and B respectively. The level scheme shows the case for a NV pair with an observable coupling and without (black and gray lines respectively). Apparently, to first order only levels with spin projections that are $\neq 0$ lead to a shift in the case of a coupling. Figure 6.6b shows two Rabi oscillations, one for an EPR transition of each center (see figure 6.6a). As a result coherent individual control of both NV center spins is possible. The contrast of NV A is slightly reduced compared to that of NV B because of the misaligned magnetic field.The misaligned field leads to a mixing of the spin levels and thus no pure $m_S = 0$ can be prepared by a laser pulse (see appendix C.1 for details). A smaller magnetic field would reduce this effect.

6.4. Controlled quantum gates and entanglement

For controlled quantum gates one NV spin state has to be changed conditional on the state of the other NV's spin which relies on an observable coupling. For our pair of NV centers this condition is realized by the magnetic dipole-dipole interaction (see eq. (6.1)). Hence, one NV center spin has to measure the magnetic field of the other NV's spin. As mentioned above off-diagonal Hamiltonian terms of the magnetic dipole-dipole interaction can be neglected. This allows some approximations because the eigenstates of both NVs are not influenced by each other.

In the following we use NV A as the sensing spin and NV B as the spin whose state is sensed. According to eq. (6.1) the magnetic field that spin B exerts on spin A is

$$\delta\underline{B}(\beta) = \mathbf{M}' \cdot \langle\beta_B| \, \underline{\hat{S}}'^B \, |\beta_B\rangle \tag{6.3}$$

and it depends only on the spin state $|\beta_B\rangle$ of NV B.[6] Hence, the partial interaction Hamiltonian of spin A for fixed $|\beta_B\rangle$ reads

$$\hat{H}^A_{dip}(\beta) = \underline{\hat{S}}^A \cdot \delta\underline{B}(\beta) \ . \tag{6.4}$$

In the case where the external magnetic field is applied along NV B and if $|\beta_B\rangle$ is an eigenstate, $\delta\underline{B}(\beta)$ depends only on the z' component of spin B which is m_S^B.

$$\begin{aligned} \delta\underline{B}(\beta) &= \langle\beta_B| \, \hat{S}'^B_z \, |\beta_B\rangle \sum_{m=x,y,z} \left(M'_{m,z'} \cdot \underline{e}_m\right) \\ &= m_S^B \sum_{m=x,y,z} \left(M'_{m,z'} \cdot \underline{e}_m\right) \end{aligned} \tag{6.5}$$

Eigenstates of NV A might change by the misaligned magnetic field. When the magnetic field is aligned along NV A, however, the eigenstates of NV B might differ from states with defined m_S^B but we only need to take into account the magnetic field component $\delta B_\parallel$ parallel to the NV A axis.

$$\delta B_\parallel(\beta) = \langle\beta_B| \sum_{n=x',y',z'} \left(M'_{z,n} \cdot \hat{S}'^B_n\right) |\beta_B\rangle \ . \tag{6.6}$$

For very small magnetic fields when m_S is a good quantum number for both NV spins we can approximate the magnetic field as

$$\delta B_\parallel(\beta) \approx M'_{z,z'} \cdot m_S^B \ . \tag{6.7}$$

The approximation in equation (6.7) implies that magnetic fields are only generated by eigenstates with $|m_S| = 1$ and fields are sensed by energy level shifts of eigenstates with $|m_S| = 1$. Deviations from this approximation occur (see appendix C.1) which are exploited to measure the relative positioning of the two spins (see section 6.5). In the next two paragraphs different schemes to detect couplings of the two NV centers and hence to achieve conditional quantum gates are discussed.

[6] Do not confuse β with the notation of spin down which is often used in NMR.

Ramsey experiments A straight forward way of testing for a coupling of the two NV centers is a Ramsey experiment (see section 2.3). The magnetic field is again aligned along NV B which leads to the level scheme shown in figure 6.7a. As NV A will be the sensing spin a coherent superposition between states $m_S^A = 0$ ($|0_A\rangle$) and $m_S^A = -1$ ($|-1_A\rangle$) of NV center A[7] is created using a Hadamard gate or $\pi/2$-pulse:

$$\Psi_{\text{single}}^A = \frac{1}{\sqrt{2}} \left(|0_A\rangle + |-1_A\rangle \right) \tag{6.8}$$

The Ramsey oscillation frequency of the phase ϕ of Ψ_{single}^A is shifted by

$$\delta\nu(\beta) = \langle -1_A | \hat{H}_{dip}^A(\beta) | -1_A \rangle - \langle 0_A | \hat{H}_{dip}^A(\beta) | 0_A \rangle \tag{6.9}$$

(see figure 6.7b). After a free evolution (or sensing) time τ the phase

$$\phi = 2\pi \cdot \delta\nu(\beta) \cdot \tau \tag{6.10}$$

of the superposition state has been altered by spin B and is probed by a second Hadamard gate on spin A and a final laser pulse for readout. In conclusion, using a Ramsey measurement spin A can detect the state of spin B by measuring the Ramsey oscillation frequency which is different for the three different eigenstates $|\beta_B\rangle$ of NV B. In addition, the phase evolution described in eq. (6.10) can be used to implement a controlled phase gate (see figure 6.7b).

Figure 6.7c shows the Fourier transform of three Ramsey oscillations of NV A each corresponding to one of the spin projections of NV B $|\beta_B\rangle = |0_B\rangle, |\pm 1_B\rangle$. The Fourier transform reveals the ODMR spectra containing inhomogeneously broadened resonance lines at three different frequencies one for each of the three different projections of NV B. Thus, the two NV centers show indeed an observable coupling with a strength of $\approx 40\,\text{kHz}$ (i.e. $\delta\nu(-1) = -\delta\nu(+1) \approx 40\,\text{kHz}$, $\delta\nu(0) \approx 0$).

The three spectra allow determining the degree of polarization of the electron spin of one NV center using the spin of the other. It is assumed that the electron spin state of the NV center is polarized with almost unity probability by shining green laser light. Indeed, the fact that we see three distinct peaks in figure 6.7c (one for each spectrum) strengthens this statement. If there would be only a small degree of polarization each spectrum would be a composition of three peaks (a strong one and two smaller ones). The ratio of the amplitudes of these peaks would correspond to the ratio of the populations of each spin projection. To estimate the degree of polarization each of the three spectra is fitted by three Lorentzian peaks (see figure 6.7c). The center of these Lorentzians corresponds to the center frequencies of the resonance lines and the amplitude is fitted. From these amplitudes we can then deduce the population ratios. With proper weighting using the accuracies of the fitted lines we arrive at a degree of polarization of $\mathcal{P} = 88 \pm 4\%$. We

[7] Due to the misaligned magnetic field for NV A the states $|0_A\rangle$ and $|-1_A\rangle$ will have some minor contributions of other m_S^A levels.

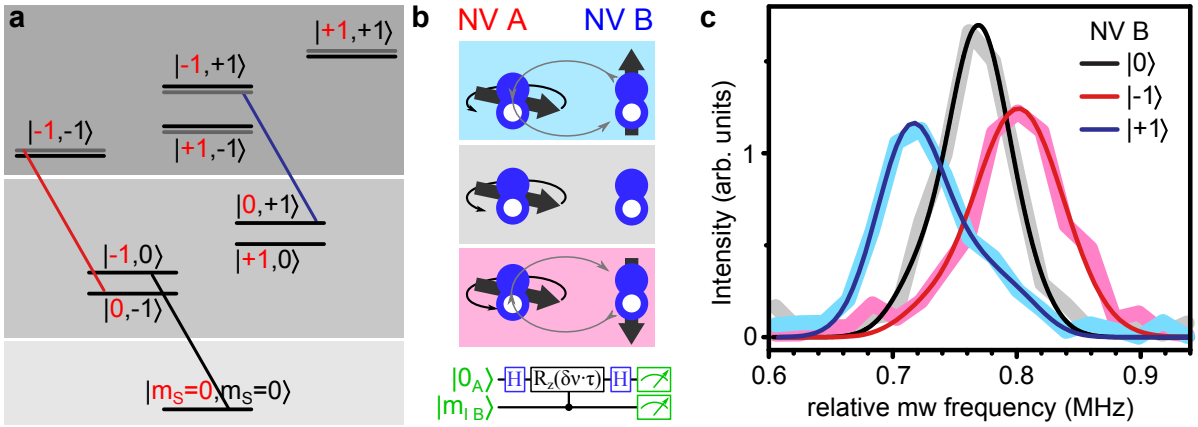

Figure 6.7.: Ramsey spectroscopy of a coupled NV pair. **a,** Combined spin energy level scheme of the coupled NV pair (compare figure 6.6). The transitions on which Ramsey spectroscopy has been performed are linked by color-coded lines. **b,** Illustration of measurement process. Superposition state of spin A senses field generated by different projections of spin B. **c,** Ramsey spectra reveal a line separation and thus a coupling strength of $\approx 40\,\mathrm{kHz}$ among both NV centers. Note that the displayed spectral range contains only the EPR transitions for nitrogen nuclear spin projection $m_I = 0$. Each spectrum is fit by three Lorentzians of varying amplitude corresponding to the maxima of the three spectra. Obviously, the spectrum for $m_S = 0$ of NV B is almost a single Lorentzian, thus NV B is well initialized (see text).

would like to call this value a lower bound because every pulse error would lower the real value to the measured one. In addition improper field alignment would spoil the degree of polarization. Finally, the surrounding of this NV pair has some deleterious effects on their coherence properties as will be discussed below. This could also spoil the degree of polarization.

Double electron-electron resonance (DEER) From the inhomogeneously broadened lines in figure 6.7c we deduce a maximum useful free evolution time τ of $T_2^* \approx 10\,\mu\mathrm{s}$ which is just long enough to reveal the coupling. However the sensing time τ of one spin could be prolonged by performing an echo measurement on the sensing spin ($\tau \to \tau_{\mathrm{echo}} \approx T_2 = 110\,\mu\mathrm{s}$, see section 2.3). An echo sequence will refocus every static magnetic field such as $\delta\underline{B}(\beta)$ in the Ramsey experiment above. A change of the spin state of NV B, however, can be detected. In double electron-electron resonance (DEER) experiments this change of spin B is done deliberately by appropriate mw radiation.[8] Therefore, a DEER measurement is capable of detecting deliberate spin state changes in contrast to the Ramsey sequence where rather the constant state of another spin is detected.

More specifically, in a DEER measurement the spin to be sensed (NV B) is flipped

[8] DEER is sometimes also referred to as electron electron double resonance (ELDOR).

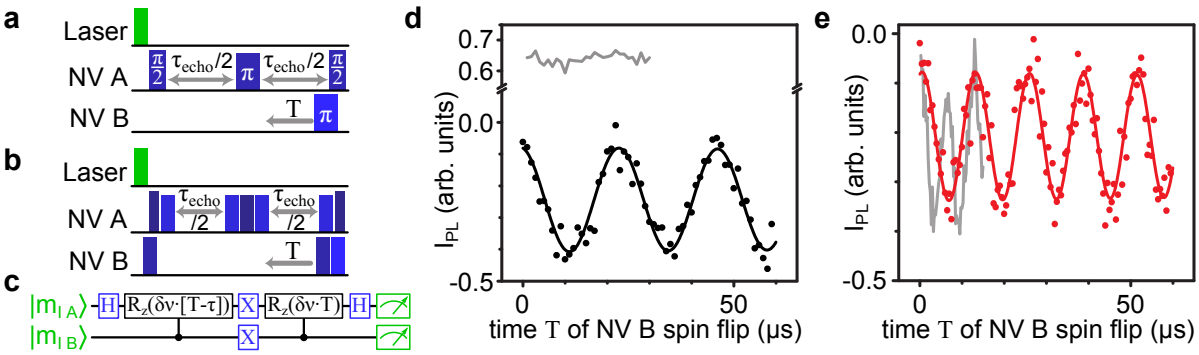

Figure 6.8.: DEER experiments on a coupled NV pair. a, Pulse sequence for "single" DEER. The laser initializes both NV centers into $m_S = 0$ and an echo measurement on NV A (superposition $m_S = 0 \leftrightarrow -1$) with fixed waiting time τ_{echo} is performed. During the second waiting time $\tau_{\text{echo}}/2$ NV B is flipped from $m_S = 0$ to $+1$. The latter flip is shifted backwards in time by T. High and thin Blue rectangles represent mw $\pi/2$-pulses and smaller thicker rectangles are π-pulses. Different shades of Blue represent different mw frequencies. **b,** Pulse sequence for "quattro" DEER. In contrast to single DEER the echo on NV A is performed with superposition $m_S = -1 \leftrightarrow +1$ and the spin of NV B is initially prepared in $m_S = -1$ and then flipped into $m_S = +1$. **c,** Quantum wire diagram of DEER sequences. For single, double and quattro DEER the proper two qubit states of the three NV spin states have to be selected (see text). **d,** Black curve, "single" DEER modulation (42.7 ± 0.4 kHz) due to phase accumulation of NV A spin caused by spin flip of NV B. Gray curve is for detuned pulse on NV B, i.e. no flip occurs and thus no modulation is visible and the fluorescence level is higher. **e,** "Double" (red line, 78.4 ± 0.8 kHz) and "quattro" (gray line, 160 ± 2 kHz) DEER oscillations. For "double" DEER spin B is flipped from $m_S = -1$ to $+1$ and "quattro" DEER is illustrated in b.

in the second free evolution time of the Hahn echo sequence of the sensing spin (NV A) (see figure 6.8a–c). First, spin B is flipped right at the end of the echo sequence of spin A. In this way spin A has no time ($T = 0$) to accumulate any phase that was influenced by the flip of the second spin. Then this spin flip is shifted towards earlier points in time (increasing T). Consequently, spin A can accumulate a phase

$$\Delta\phi = 2\pi \cdot \underbrace{(\delta\nu(\beta_i) - \delta\nu(\beta_f))}_{\Delta\nu(\beta_i,\beta_f)} \cdot T \tag{6.11}$$

during the interval $0 < T < \tau_{\text{echo}}/2$ which depends on initial and final states of spin B $|\beta_{i\,B}\rangle$ and $|\beta_{f\,B}\rangle$ respectively (compare eq. (6.9)). Eventually the accumulated phase will be converted into a population difference and the fluorescence signal will be modulated like

$$A_{\text{DEER}} = \cos(\Delta\phi). \tag{6.12}$$

In figure 6.8d,e the results of the DEER measurements are presented. In panel d spin B is flipped from state $|0_B\rangle$ to $|+1_B\rangle$. Therefore, the visible coupling frequency is

$\Delta\nu(0,+1) \approx -\delta\nu(+1)$. Due to the longer T_2 time compared to T_2^* the coupling frequency can be deduced more precisely than from the Ramsey fringes.

Please note that the NV B spin is flipped from one eigenstate to another in any case. Thus the fluorescence intensity will not be modulated by shifts of the NV B spin flip in time; it will only be modulated due to the changing spin state of NV A that is in fact induced by the sensing time of the flipped NV B spin. If we perform the same DEER measurement with an off-resonant microwave pulse on spin B than this spin is not flipped (see figure 6.8d upper curve). Consequently no change in magnetic field is felt by spin A and the modulation is gone. In addition we have an offset in fluorescence intensity because NV B stays all the time in its bright state $|0_B\rangle$. This is a test experiment to exclude other effects like ac-Zeeman effect as the source of the fluorescence modulation.

In a DEER sequence the spin of NV B can also be flipped from $|-1_B\rangle$ to $|+1_B\rangle$. This leads to a larger change of the local magnetic field from $\delta\underline{B}(-1)$ to $\delta\underline{B}(+1)$ and consequently the phase oscillation frequency $\Delta\nu(-1,+1) \approx 2\delta\nu(-1)$ roughly doubles. This effect can indeed be verified in figure 6.8e (red curve). One can go even one step further and use a different superposition state for the sensing of the magnetic field change, namely $\Psi^A_{\text{double}} = \frac{1}{\sqrt{2}}(|-1_A\rangle + |+1_A\rangle)$. The phase of this state is twice as sensitive as the phase of Ψ^A_{single} (compare eq. (6.9)):

$$\begin{aligned}\delta\nu_{\text{double}}(\beta) &= \langle -1_A|\, \hat{H}^A_{dip}(\beta)\, |-1_A\rangle - \langle +1_A|\, \hat{H}^A_{dip}(\beta)\, |+1_A\rangle \\ &\approx 2 \cdot \delta\nu(\beta)\end{aligned} \tag{6.13}$$

Hence, this leads to an even faster oscillation frequency

$$\begin{aligned}\Delta\nu_{\text{double}}(\beta_i,\beta_f) &= \delta\nu_{\text{double}}(\beta_i) - \delta\nu_{\text{double}}(\beta_f) \\ &\approx 2\Delta\nu(\beta_i,\beta_f)\end{aligned} \tag{6.14}$$

(compare eq. (6.11)) which eventually arrives at $\Delta\nu_{\text{double}}(-1,+1) \approx 4\cdot\delta\nu(-1)$ (see figure 6.8e gray curve). Summarizing, we can say that combining the two latter effects we arrive at a gate speed which is four times increased.

As in the case of the Ramsey experiment the influence of NV B spin on the phase of NV A spin resembles a controlled phase rotation (see figure 6.8c). A controlled phase rotation can be transformed into a CROT gate around x or y by encompassing it with two Hadamard gates on the target spin. That is actually exactly what is done during the Ramsey sequence. If the rotation angle is π the CROT is actually a CNOT gate. The DEER sequence is not exactly a CROT gate; it rather rotates the target spin if the control spin is flipped (not if it is in a particular state). Nevertheless, this is sufficient for entanglement creation.

Entanglement Now that we have CNOT gates (or something similar) at hand and we can perform Hadamard gates we are able to create entangled states namely Bell states. As usual, the sequence therefore is starting with a defined initial state. After

this a Hadamard gate creates a superposition state on one spin and finally a CNOT gate completes the Bell state.

In our case the initial state is

$$\Psi_i = |0_A\rangle \otimes |0_B\rangle = |0,0\rangle \tag{6.15}$$

which is created by laser illumination (see figure 6.9b). As a second step we start with an echo (DEER) sequence on NV A which is part of the later CNOT gate.

$$\Psi = \frac{1}{\sqrt{2}}\left(|0_A\rangle + |-1_A\rangle\right) \otimes |0_B\rangle \tag{6.16}$$

After a waiting time $\tau_{\text{echo}}/2$ the π pulse of the echo sequence inverts the phase evolution of spin A. At the same time a Hadamard gate ($\pi/2$-pulse) is applied to spin B.

$$\begin{aligned}\Psi &= \frac{1}{2}\left(|0_A\rangle + |-1_A\rangle\right) \otimes \left(|0_B\rangle + |-1_B\rangle\right) \\ &= \frac{1}{2}\left(|0,0\rangle + |0,-1\rangle + |-1,0\rangle + |-1,-1\rangle\right)\end{aligned} \tag{6.17}$$

This Hadamard gate creates a superposition state on spin B and at the same time starts the controlled phase gate. Now the phase accumulated for time T by spin A depends on spin B which leads to a phase change of term $|-1,-1\rangle$ in eq. (6.17). For a $\tau_{\text{echo}}/2 = T = 1/\left(2 \cdot \Delta\nu(0,-1)\right)$ the quantum state is

$$\Psi = \frac{1}{2}\left(|0,0\rangle + |0,-1\rangle + |-1,0\rangle - |-1,-1\rangle\right). \tag{6.18}$$

The final pulse of the echo (DEER) sequence can be either a $\pi/2$-pulse or a $3\pi/2$-pulse on spin A which leads to

$$\Psi_{f1} = \Psi_\Phi = \frac{1}{\sqrt{2}}\left(|0,0\rangle + |-1,-1\rangle\right) \text{ or} \tag{6.19a}$$

$$\Psi_{f2} = \Psi_\Psi = \frac{1}{\sqrt{2}}\left(|0,-1\rangle + |-1,0\rangle\right) \tag{6.19b}$$

respectively (see red and black solid lines in figure 6.9a). If the phase accumulation time $T = \tau_{\text{echo}}/2$ is varied the final states oscillate between the entangled states $\Psi_{f1} = \Psi_\Phi$, $\Psi_{f2} = \Psi_\Psi$ for $T/\Delta\nu(0,-1) = 1/2, 3/2, 5/2, \ldots$ and the unentangled states

$$\Psi_{f1} = \frac{1}{\sqrt{2}}\left(|0,-1\rangle + |0,0\rangle\right) \tag{6.20a}$$

$$\Psi_{f2} = \frac{1}{\sqrt{2}}\left(|-1,-1\rangle + |-1,0\rangle\right) \tag{6.20b}$$

for $T/\Delta\nu(0,-1) = 0, 1, 2, \ldots$ (red and black dashed lines in figure 6.9a). In both cases the two states have different fluorescence intensities. The entangled states both have

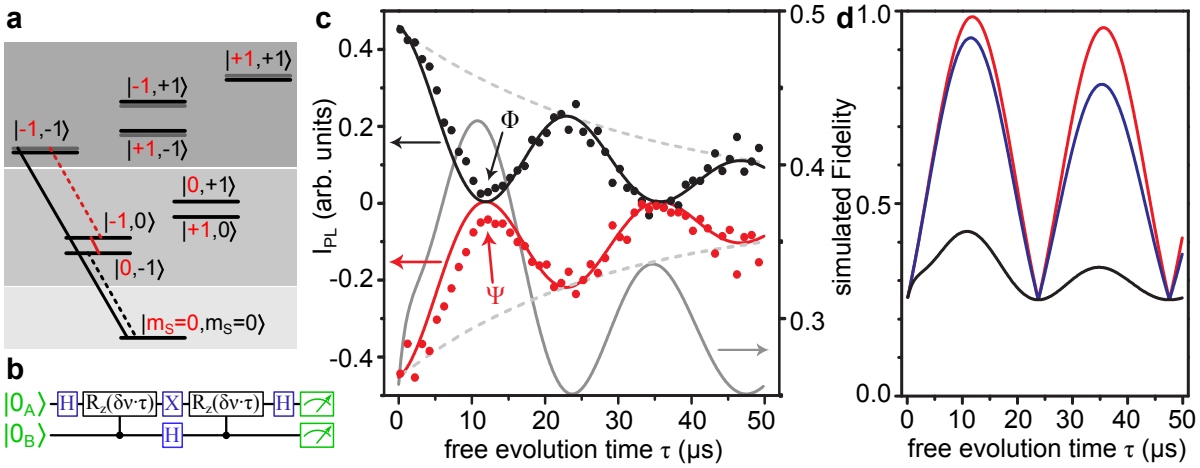

Figure 6.9.: Entanglement in a coupled NV pair. **a,** Energy level scheme with marked entangled (solid lines) and unentangled (dashed lines) states which occur during variation of τ (see text). **b,** Pulse sequence for the creation of entanglement (see text). **c,** Fluorescence response during entanglement creation for Bell states Φ (black) and Ψ (red). The fluorescence response is simulated (solid black and red lines). As a result the simulated fidelity of the created entangled states is given (gray line). **d,** Simulation of the fidelity of the entangled states for longer T_2 values of both centers. Black line corresponds to the actual setting, blue line both centers have $T_2 = 200\,\mu s$ and red line both NVs have $T = 1\,ms$.

average intensity (let's set it to 0.0), whereas the intensity of Ψ_{f1} goes up to 0.5 and for Ψ_{f2} goes down to -0.5 for the unentangled states (see figure 6.9c).

The T_2 and T_2^* times mentioned so far were only measured for NV center A. Due to some yet unknown reason NV center B exhibits much shorter coherence times (i.e. $T_2 = 2\,\mu s$, see below). Thus for a coupling strength of $\approx 40\,kHz$ no entanglement can be achieved only classical correlations are possible. Nevertheless, we have applied the entanglement sequence with a variable phase accumulation time T and monitored the fluorescence modulations to estimate the amount of correlation generated (see figure 6.9c). The oscillations follow our expectations and the point in time of maximum entanglement is marked. They exhibit decay which is due to the echo decay. Given the value of T_2 for NV B and the measured value for the coupling $\Delta\nu(0,-1)$ we have simulated the fluorescence modulations by adjusting T_2 of NV A (see solid lines in figure 6.9c). From the quantum states of the simulation we have deduced the Fidelity of the entangled states (see gray solid line in figure 6.9c). As the coherence of NV B is negligible due to the short T_2 value no entanglement is present. Thus, the maximum fidelity we can achieve is 0.5 for the case of maximum classical correlations:

$$\rho_{f1}^{\text{exp. max}} = \frac{1}{2}\left(|0,0\rangle\langle 0,0| + |-1,-1\rangle\langle -1,-1|\right) \tag{6.21a}$$

$$\rho_{f2}^{\text{exp. max}} = \frac{1}{2}\left(|0,-1\rangle\langle 0,-1| + |-1,0\rangle\langle -1,0|\right) \ . \tag{6.21b}$$

The simulation yields a maximum fidelity of 0.43. In figure 6.9d the expected fidelity is shown if both NV centers would have T_2 values of 200 µs (like NV A) or 1 ms and more like intrinsic NV centers in that diamond sample.

The reason for the short coherence times of NV center B could not be determined. A local variation of the nuclear spin concentration can be excluded. A locally increased electron spin concentration which might be due to implanted nitrogen or other implantation related defects might account for the coherence properties. However, efforts to decouple possible proximal electron spins by strong driving of the respective spin transitions did not work out. On the other hand the ODMR spectra in figure 6.5b reveal high E values of the ZFS parameters. Thus, it appears very likely that the lattice close to NV centers is strained. This might be due to implantation damage comprising lattice defects (see section 2.1.2) that were not cured by the subsequent annealing step. These damages can have fluctuating charges or spins and might affect the coupling to phonons (see section 2.2.5). Further investigation of implantation damage is needed to clarify this effect. Although it has been shown that high temperature annealing can improve the coherence properties of implanted NV centers [195] this techniques has not worked out for this particular center so far.

6.5. Relative position measurements

According to eq. (6.1) the interaction strength of the two NV centers can be adjusted by controlling strength and relative orientation of the corresponding magnetic dipoles. This can be used to determine the relative position of the two spins [196]. However, the magnetic dipole strengths and orientations of the two NV centers' spins are mainly fixed by their respective crystal fields $\mathbf{D}^{A,B}$. The defect's symmetry axis sets the direction of the magnetic dipole and the ZFS favors $m_S = 0, \pm 1$ as electron spin eigenstates. For the present pair the symmetry axes are different, hence their relative angle is 109.47°. Using these zero order approximations and a coupling strength of 40 kHz we can calculate a surface of possible positions of one NV center if the other is located at the origin (see figure 6.11c). There the light gray surface is for negative coupling between like spin states (e.g. $|-1_A\rangle$ and $|-1_B\rangle$) and the darker gray one for positive coupling as in the present case ($\delta\nu(-1) > \delta\nu(+1)$, see figure 6.7).

Although the ZFS tensor sets strong bounds on the spin projection of the eigenstates, it is possible to alter them sufficiently enough to see an effect on the coupling strength. A magnetic field applied along the symmetry axis of one NV center commutes with its ZFS term. Thus, the spin eigenstates are not changed. However, any perpendicular component of the magnetic field does change the eigenstates according to first order perturbation theory. Consequently, the magnetic dipole moment of the eigenstates changes (see figure 6.10 and appendix C.1). If the z direction corresponds to the NV symmetry axis a magnetic field in x direction tilts the magnetic moment of the $m_S = \pm 1$ spin eigenstates towards the x direction and the $m_S = 0$ level which had no magnetic moment

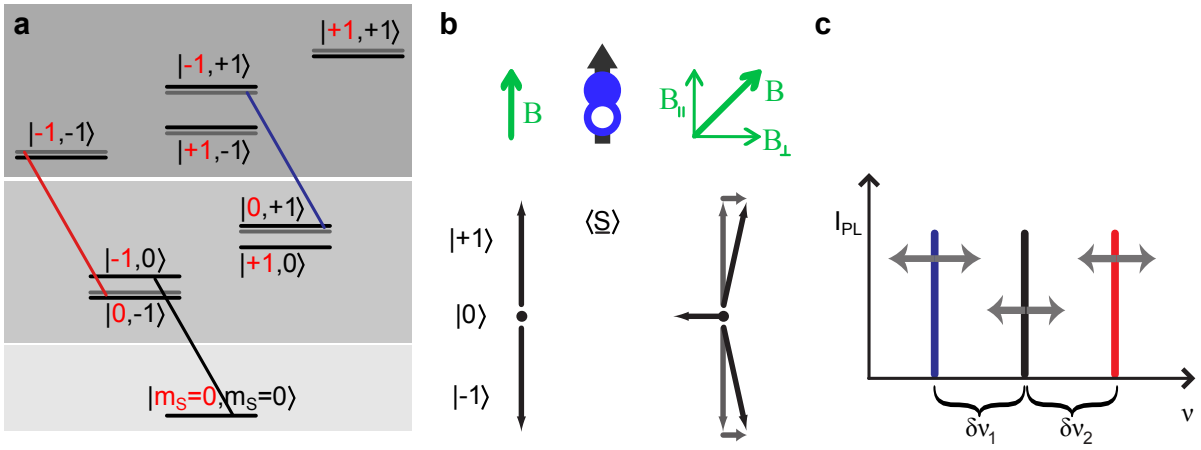

Figure 6.10.: NV pair coupling affected by magnetic field. a, Energy level scheme of coupled NV pair similar to figure 6.5a. The magnetic field is tilted against NV A which induces an additional level shift of levels containing $m_S^A = 0$. **b,** Effect of a tilted magnetic field on the spin eigenstates of the NV center. The magnetic moments $\langle \hat{\underline{S}} \rangle$ of the individual levels changes as illustrated. **c,** Stick spectrum showing transition frequencies corresponding to a). A former equal line spacing can become unequal ($\delta\nu_1 \neq \delta\nu_2$).

before acquires a moment in negative x direction (see figure 6.10b). Thus by applying a magnetic field vector $\underline{B} \nparallel z$ all spin eigenstates of the NV center have magnetic moments lying in a plane spanned by z and $\underline{B}$. Changing just the strength of that field changes the directions of the magnetic moments. This influences the energy level scheme of the coupled NV pair (see figure 6.10a). If as in the present case the magnetic field is parallel to NV B it is tilted against NV A and therefore the previous $m_S = 0$ state of NV A acquires a magnetic moment and the respective energy levels are shifted. In turn this also affects the Ramsey spectrum (see figure 6.10c). Whereas the line splitting was equal previously it can now be different ($\delta\nu$, $\delta\nu \rightarrow \delta\nu_1$, $\delta\nu_2$).

It is necessary to be able to generate magnetic dipole moments of the NV center spins that span the 3d space to do a relative position measurement. As shown above even for the NV center with its high ZFS this is possible. In the experiment it is very convenient to first apply a magnetic field parallel to one NV center (here NV A and B_1, see figure 6.11a) and measure the coupling strength via a DEER sequence for different magnetic field strengths (see figure 6.11b). In this way the magnetic dipole moments of the second NV center's spin eigenstates will change and the ones of the first NV remain constant. The Hamiltonian is now evaluated while the relative position is iteratively adjusted such that the calculated coupling strengths match the measured ones. The red circles in figure 6.11c show the possible positions corresponding this first range of DEER measurements. A single value of the coupling strength has narrowed down the possible positions to a surface. Now the position is further limited to a line. In a final DEER series a point will be achieved. Therefore, the magnetic field is roughly aligned along the symmetry axis

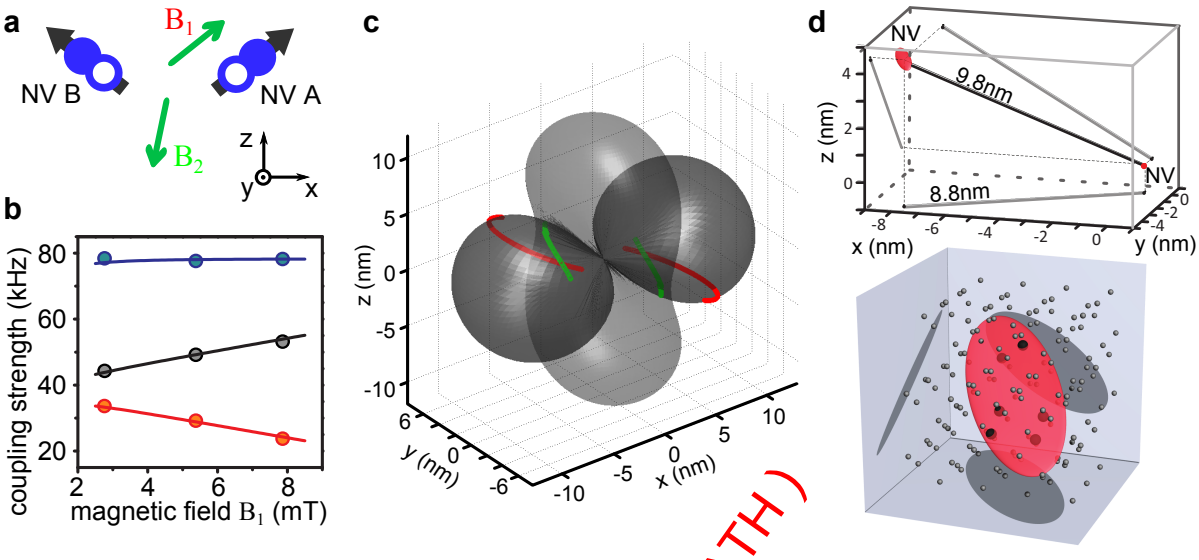

Figure 6.11.: Distance measurement of NV pair by EPR. a, A magnetic field is first applied along NV A (B_1) and later misaligned to both NV centers (B_2). DEER measurements are performed for different strengths of both fields. **b,** Resulting coupling strengths out of DEER measurements for increasing B_1. Therefore, an echo is performed on NV A spin transition $m_S = 0 \leftrightarrow -1$ and the spin of NV B is flipped ($m_S = 0 \rightarrow -1$ (red curve), $0 \rightarrow +1$ (black curve) and $-1 \rightarrow +1$ (blue curve)). Red and black curves are analogous to $\delta\nu_1$ and $\delta\nu_2$ in figure 6.10. **c,** Relative position of NV centers where one NV is located at zero and the other on the gray surface. DEER Results for different B_1 restrict the position to the red line whereas DEER results for fields B_2 restrict to the green line. **d,** Taking all DEER results into account the position can be narrowed down to the red uncertainty area (upper part). A zoom in (lower part) shows individual carbon atoms (gray spheres) in addition. Six atoms lie in the uncertainty area (bigger black spheres).

of a third NV center close by (see figure 6.3b) and points in a different direction than NV A and NV B (see figure 6.11a). The magnetic field is further adjusted such that the NV pair constituents can still be distinguished via ODMR. Again the magnetic field strength is increased and the coupling strengths are measured. As before, the relative position guess is changed such that the Hamiltonian delivers the measured couplings. As expected the calculated position is now a point surrounded by an error volume (see figure 6.11c,d).

A. Physical constants and conventions

In this part of the appendix a lot of useful information is gathered that appears in this work. Table A.3 contains physical constants, conventions and basic spin operators that appear in the Hamiltonians of this work. Furthermore, table A.1 contains some information about sizes, ranges and concentrations within the diamond lattice. Finally, table A.2 gives some interactions strengths of spins in the diamond lattice.

Table A.1.: Details about the diamond lattice.

detail	value
lattice constant	$3.57\,\text{Å}$
bond length	$1.44\,\text{Å}$
carbon atom density	$176\,\text{nm}^{-3}$ $176 \times 10^{9}\,\mu\text{m}^{-3}$ $176 \times 10^{21}\,\text{cm}^{-3}$
average distance between impurities with concentration c	$17.8\text{ nm}\sqrt[3]{\frac{\text{ppm}}{c}}$
impurity density depending on concentration c	$176 \times 10^{3}\,\frac{\text{atoms}\,c}{\mu\text{m}^3\,\text{ppm}}$ $176 \times 10^{15}\,\frac{\text{atoms}\,c}{\text{cm}^3\,\text{ppm}}$

Table A.2.: Details about spins in diamond. The actual interaction strengths depend on the relative position of the spins and the orientations of their quantization axes. The numbers given here are the pre-factors of eqs. (3.2c) and (6.1) respectively.

interaction	strength	
interaction with ^{13}C nuclear spin ½	$19.9\,\text{kHz}\,\frac{\text{nm}^3}{r^3}$	$0.71\,\mu\text{T}\,\frac{\text{nm}^3}{r^3}$
interaction with electron spin ½	$52\,\text{MHz}\,\frac{\text{nm}^3}{r^3}$	$1.9\,\text{mT}\,\frac{\text{nm}^3}{r^3}$
interaction among ^{13}C nuclear spins	$7.6\,\text{Hz}\,\frac{\text{nm}^3}{r^3}$	$13.5\,\text{Hz}/\%$
interaction among electron spins	$52\,\text{MHz}\,\frac{\text{nm}^3}{r^3}$	$9.2\,\text{kHz}/\text{ppm}$

Table A.3.: Hamiltonian related details.

expression	description
g_e	$= -2.0023$, electron spin g-factor; $g = -2.0028$ for the NV center spin [107]
g_n	nuclear spin g-factor; depends on isotope, see table 3.1
μ_B	$= 927.400949 \times 10^{-26}\,\mathrm{J\,T^{-1}}$, Bohr magneton
μ_n	$= 5.05078343 \times 10^{-27}\,\mathrm{J\,T^{-1}}$, nuclear magneton
γ_e	$= g_e\,\mu_B/\hbar = -2\pi\,28.03\,\mathrm{MHz/mT}$, gyromagnetic ratio of the electron spin
γ_n	$= g_n\,\mu_n/\hbar$, gyromagnetic ratio of a nuclear spin; depends on isotope, see table 3.1
$\tilde{\gamma}_e$, $\tilde{\gamma}_n$	$= \frac{\gamma_e,\gamma_n}{2\pi}$ spin transition frequency in Hz/T due to Zeeman interaction
D_{gs}	$= 2870\,\mathrm{MHz}$, zerofield splitting in the ground state of the NV center
D_{es}	$= 1420\,\mathrm{MHz}$, zerofield splitting in the excited state of the NV center
S	electron spin angular momentum (e.g. $S = 1/2, 1, \ldots$); please note the omitted $\hbar$
$\hat{S}_{x,y,z}$	$= \frac{1}{\sqrt{2}}\left(\begin{smallmatrix}0&1&0\\1&0&1\\0&1&0\end{smallmatrix}\right)$, $\frac{1}{\sqrt{2}}\left(\begin{smallmatrix}0&-i&0\\i&0&-i\\0&i&0\end{smallmatrix}\right)$, $\left(\begin{smallmatrix}1&0&0\\0&0&0\\0&0&-1\end{smallmatrix}\right)$, matrix representation for electron spin operators for $S = 1$ in the z-basis; please note the omitted $\hbar$
I	nuclear spin angular momentum (e.g. $I = 1/2, 1, \ldots$); please note the omitted $\hbar$
$\hat{I}_{x,y,z}$	nuclear spin operators; see $\hat{S}_{x,y,z}$ for $I = 1$ and $I_{x,y,z} = 1/2\,(\mathrm{X}, \mathrm{Y}, \mathrm{Z})$ for $I = 1/2$; please note the omitted $\hbar$
$\hat{H}$	Hamilton operator. The energy is given in units of mw and rf frequencies (MHz, GHz) rather than energy. Usually, it is not given in units of the magnetic field because unlike in conventional ESR and NMR we work at a constant field but change the mw and rf frequencies.
$\mathrm{X}, \mathrm{Y}, \mathrm{Z}$	$= \left(\begin{smallmatrix}0&1\\1&0\end{smallmatrix}\right), \left(\begin{smallmatrix}0&-i\\i&0\end{smallmatrix}\right), \left(\begin{smallmatrix}1&0\\0&-1\end{smallmatrix}\right)$, Pauli matrices

B. Experimental setup

In section 2.3 a compact description of the experimental setup is given. This is valid for most of the experiments performed during this thesis. However, sometimes special equipment is used and some parts of the setup are only briefly explained such that additional details are presented here.

B.1. The confocal microscope

In this thesis we are going to investigate single quantum systems where the only way to interrogate them is via laser excitation and subsequent detection of the emitted fluorescence. As the fluorescence count rate is low compared to ambient light we need to setup a very sensitive microscope. Confocal microscopy is a well-known tool to acquire high resolution and highly sensitive optical microscopy images of an appropriate sample (see figure 2.7a). A very comprehensive review is given in [156].

Confocal microscopy is a scanning technique, i.e. only one point of the sample is illuminated and its response is registered at a time. Therefore it is sufficient to have a single photon detector. Light originating from the emitter of interest is collected by the objective and further projected onto a pinhole that transmits light only from within the zeroth diffraction order.[1] All the light from regions with too much axial or lateral displacement from the emitter (i.e. from outside the diffraction limited detection volume) will not pass the pinhole. Finally, light passing the pinhole in our case is filtered by a 647 nm longpass and registered by the photon detector. In this way we get rid of the laser light and the associated Raman-shifted photons but we keep almost all fluorescence photons from the negatively charged NV center. Although the pinhole suppresses light from outside the focal volume the integral of the light coming from every spot in the sample can lead to a substantial amount of noise photons. In confocal microscopy, however, unlike wide-field microscopy only the emitter of interest is illuminated reducing background noise. Therefore, the fundamental mode of a laser ($TEM_{0,0}$, Gaussian beam) is focused by an objective onto the sample. Hence, the illuminated volume is diffraction limited as well. For illumination and subsequent photon collection we use the same objective. The illumination and detection volume have to be carefully aligned to make up the confocal volume. The PSF is used to describe the confocal volume and thus the resolution of the microscope. One can think of it as the signal from a single point-like emitter with linear

[1] Diffraction is mainly caused by the objective that collects only part of the light of a single emitter and therefore acts as an aperture.

response that is scanned through the confocal volume. Hence, it is a 3d function. The PSF of a confocal microscope is the square of a comparable wide-field microscope and therefore features a higher resolution apart from the increased SNR. The lateral and axial resolution ($\Delta r,\ \Delta z$) of a confocal microscope[2] are given by

$$\Delta r = \frac{0.44\lambda}{\mathrm{NA}} \tag{B.1}$$

$$\Delta z = \frac{1.5n\lambda}{\mathrm{NA}^2} \tag{B.2}$$

$$\mathrm{NA} = n \cdot \sin(\theta) \tag{B.3}$$

where NA is the numerical aperture of the microscope objective (NA=1.35), θ is the half angle of the focused light cone and n is the refractive index of the immersion oil used in our microscope ($n = 1.517$). Thus, the immersion oil increases the resolution on the one hand. On the other hand it reduces the refractive index mismatch with respect to diamond. Therefore, more illumination light can enter and less fluorescence light is lost due to total internal reflection. Nevertheless, the usual objectives for confocal microscopy are optimized for standard microscopy glass cover slides with the same refractive index as the oil. Hence, their performance decreases for increasing imaging depth in the diamond sample. Summarizing, the lateral resolution of the used confocal microscope is $\approx 170\,\mathrm{nm}$ and the axial resolution is $\approx 660\,\mathrm{nm}$ according to the Rayleigh criterion and eqs. (B.1) and (B.2).

Apart from bare photon counting also the spectral distribution of the light originating from a single emitter can be analyzed using a spectrometer as displayed in figure 2.7a. The spectrum can be used to unambiguously identify an NV center. However, the samples we used are often so clean that only NV center defects could be found and these can be easily identified by their amount of fluorescence response and their ODMR response.

The illumination laser light is switched on and off by an AOM. In the AOM a traveling sound wave in a TeO_2 crystal is used for diffraction of the laser beam. If the first diffraction order is used for illumination of the sample, switching on and off the sound wave also switches on and off the illumination. This can be achieved on a timescale of $\approx 10\,\mathrm{ns}$. This is sufficient for the majority of experiments where pulse lengths down to 200 ns are used. If however, the fluorescence lifetime should be measured much shorter pulses are needed. Therefore, a pulsed Ti:Sapphire laser is used. Its infrared fs pulses are coupled into a non-linear photonic crystal fiber for supercontinuum pulsed white light generation with a pulse width of $\sim 100\,\mathrm{fs}$. A bandpass is used to cut out light in the green spectral range.

The confocal microscope is able to resolve NV centers with lateral distances down to $\approx 170\,\mathrm{nm}$ which is given by the diffraction limit. If the NV centers of interest are

[2] According to the Rayleigh criterion two identical point-like emitters are resolvable if their confocal scan image exhibits a signal dip of 26% between the two maxima.

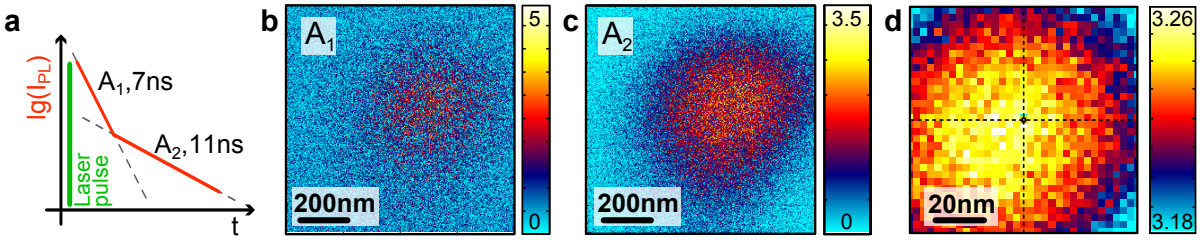

Figure B.1.: Fluorescence lifetime imaging with NV centers. **a,** Illustration of the fluorescence response (red) of two NV centers upon simultaneous excitation with a ps laser pulse (green). The decay shows a bi-exponential behavior where each exponential belongs to one NV and is described by its amplitude A_i and its lifetime. **b, c** Scan images showing the amplitudes A_1 and A_2 respectively for each position during a scan of the laser across the NV pair. **d,** The 2d cross-correlation of the images A_1 and A_2 yields the most likely lateral displacement of the two NV centers.

closer together than that other microscopy techniques have to be used. This can be a non-linear imaging technique where the fluorescence response depends non-linear on the excitation power like STED or GSD. Another possibility is to find a "tricky" way to distinguish photons from simultaneously illuminated emitters within a confocal spot (like FLIM). FLIM and GSD are explained in the following.

B.1.1. Fluorescence lifetime imaging — FLIM

Fluorescence lifetime imaging is used to take microscopy images where the signal relies on the fluorescence decay rate rather than on the fluorescence intensity. In our case we want to image several NV centers that might be closer to each other than the confocal resolution limit. As all NV centers are usually equal with respect to their emitted spectrum, their intensity and their fluorescence lifetime, resolution below the diffraction limit is surely challenging. However, here we are able to make the fluorescence lifetime of two closely spaced NV centers distinguishable and can therefore apply FLIM. Compared to methods like STED and GSD a standard Gaussian beam is sufficient for illumination which, however, has to be pulsed shorter than ns.

In our case a strong magnetic field of 70 mT is applied along the symmetry axis of one NV center and is therefore misaligned with the second NV center which is pointing along a different crystallographic [111] direction. This leads to a reduced fluorescence of the misaligned NV [28] due to a new set of eigenstates in which $m_S = 0$ is superposed with other m_S levels (see appendix C.1). Hence, $m_S = 0$ is not constant in time and on average we find a mixing of spin levels m_S (compare figures B.1b and c). As different m_S levels exhibit different fluorescence lifetimes [126] the misaligned center will eventually have a shorter lifetime than the aligned one which will reside in its $m_S = 0$ level. For the pair under study these lifetimes are ≈ 11 ns and ≈ 7 ns (see figure B.1a).

In the actual experiment a pulsed laser scans a lateral array containing the center of the confocal volume containing the two emitters. At every location an average fluorescence

decay time trace is acquired (see figure B.1a). As we expect the fluorescence to show a decay composed of two different exponential decays we fit the data accordingly. More precisely we use the above mentioned lifetimes as fixed parameters and fit the amplitude which is the actual signal. Hence, for every location (x, y) of the scanned array this yields two amplitudes $A_1(x, y)$ and $A_2(x, y)$ which results in two figures, one for each center (see figure B.1b,c). As these figures show diffraction limited spots of the respective NV emitter it is not possible in the first place to measure their displacement. However, each of the images is made up of a lot of photons which eventually lead to an uncertainty of their center positions which is below the lateral displacement of the two centers.

An elegant way to extract the displacement is a 2d cross-correlation of the two images. This yields an array

$$M(\Delta x, \Delta y) = \mathcal{F}_{2d}\left[\mathcal{A}_1^*(k_x, k_y) \cdot \mathcal{A}_2(k_x, k_y)\right] \text{ with} \tag{B.4}$$

$$\mathcal{A}_i(k_x, k_y) = \mathcal{F}_{2d}\left[A_i(x, y)\right] \tag{B.5}$$

where each entry resembles a probability for the corresponding displacement $(\Delta x, \Delta y)$ of the two images. Here, $\mathcal{A}_1$ and $\mathcal{A}_2$ are the 2d Fourier transforms of the two arrays A_1 and A_2. The resulting cross-correlated image $M(\Delta x, \Delta y)$ is displayed in figure B.1d. Indeed a small displacement of the two NV centers of about 10 nm is visible from this image.

B.1.2. Ground state depletion microscopy — GSD

GSD is a non-linear imaging technique that is able to achieve sub-diffraction limited microscopy images. Its application to NV centers in diamond has been shown to yield resolutions down to ≈ 8 nm [45]. We have done our experiments similar to the technique described therein. The idea behind GSD as well as behind STED is the creation of a spatially narrow region in which the fluorescence of the NV center is switched from the "on" to the "off" state. The smaller this region is the higher is the resolution. In GSD this is achieved by exploiting the metastable singlet state.

The presence of the metastable singlet state gives a higher bound $I_{PL,max}$ on the fluorescence intensity I_{PL} that sets in at laser intensity P_{sat}. This is due to an increasing amount of population that is pumped into the metastable state. Thus, a steep laser intensity gradient creates a steep fluorescence intensity gradient but keeps a maximum fluorescence intensity of $I_{PL,max}$. In turn, I_{PL} can be switched from zero to $I_{PL,max}$ on a very small length scale.

We use a single intense doughnut shaped illumination profile for imaging (compare figure 6.4a). The high gradient we are going to use occurs close to the center of the doughnut. Any emitter in the center of the spot does not fluoresce and any emitter in the illuminated ring of the doughnut fluoresces. The higher the power of the laser the higher is the intensity gradient when going from the center ("off" state) to the rim ("on" state). In turn the "on" state is reached on a smaller length scale and the "off" state is

confined to a shrinking spot in the center. The laser intensity profile $P(x)$ near the very center can be approximated by a parabola

$$P(x) = p_0 \cdot x^2 \ . \tag{B.6}$$

In the case of a single emitter and in a range where no saturation occurs but linear response this is proportional to the fluorescence profile. Therefore, the diameter d of the center circle of the fluorescence profile that is just below $I_{PL,max}$ can be approximated by

$$d \approx 2\sqrt{\frac{P_{max}}{p_0}} \ . \tag{B.7}$$

Hence, by increasing the laser intensity also p_0 increases and the diameter of the low fluorescent spot decreases. If, however, two or more emitters (say n) are within the confocal spot one has to note that I_{PL} exactly at the position of each emitter is not zero but the sum of the fluorescence intensities of all remaining emitters $[\approx (n-1) \cdot I_{PL,max}]$. In turn, the contrast between low fluorescent spots (i.e. the sites of the single emitters) and the high fluorescent plateau $(n \cdot I_{PL,max})$ decreases as $1/n$ and therefore also the signal to noise ratio.

In our experiment we have used laser light from a dye-laser with wavelength of $\approx$ 560 nm and a power of up to $\approx$ 100 mW. For the creation of the doughnut mode we have send the linearly polarized laser beam through a $\lambda/4$-plate to produce circularly polarized light. This light is then send through a helical phase plate, i.e. the phase shift ϕ that is exerted by the plate on the beam increases with the angle α with respect to the center of the plate ($\phi(\alpha) = \alpha$ in our case). Therefore, the resulting beam has zero intensity in its center. The detection volume of the confocal setup has to be aligned with the center of the doughnut mode. Figure 6.4a in chapter 6.2 shows the resulting fluorescence image. However, the two NV centers are in the middle of a common low fluorescent spot and are therefore unresolved. This may be attributed to mainly two things. On the one hand a drift of the sample during measurement was observed and on the other the NV centers are located $\approx$ 6 µm below the diamond surface where the doughnut mode might be severely distorted to prevent the resolution of the two centers.

B.2. The magnetic field

The magnetic field is used to tailor the energy levels of electron and nuclear spins associated with the NV center. As these possess long coherence times any spin dynamics produced by the magnetic field have to be controlled with a correspondingly high precision and stability. However, this field does not necessarily have to be homogeneous because we are observing single spins with an extension of spin density of less than 1 nm. The largest fixed term in the spin Hamiltonian is the ZFS which corresponds to a field strength of 100 mT. Therefore, the magnetic field should be as strong as or stronger than

100 mT and its direction should be well adjustable.

To account for the former requirements we have installed an electromagnet which produces an inhomogeneous field of up to ≈ 250 mT with an accuracy of up to the ppm level (see figure 2.7a). Due to its inhomogeneity proper positioning and alignment of the magnetic field can point into any direction at the position of the NV center. Here the positioning accuracy is in the sub-µm range. For even higher magnetic fields the electromagnet is replaced by a permanent magnet which can exert a field of up to ≈ 600 mT on the NV spin (see figure 5.14a).

B.3. Microwave and radiofrequency equipment

In this work we use separate signal generators for the generation of mw and rf radiation for the manipulation of electron and nuclear spins respectively. These signal generators are capable of switching between desired frequencies in about 1 ms which limits the sweep time when recording ODMR spectra. Their output power is on the order of +10 dBm. Therefore, we need to amplify these signals using separate rf and mw amplifiers in order to drive fast Rabi oscillations on the spins. These amplifiers can deliver peak powers on the order of 100 W.

Microwave and rf pulses are realized by fast switching of the relative signal before it is send to the respective amplifier. The used switches have rise and fall times of down to below 1 ns. Hence, we use rectangular pulses within good approximation. The mw and rf switches as well as the AOM for the laser are controlled by a pulse generator device (PG) which coordinates the whole experimental sequence. The PG also triggers other detection devices. It has a timing resolution of up to ≈ 300 ps.

We use phase shifters, splitters and combiners to generate phase shifted copies of mw and rf radiation. Different mw and rf frequencies that are used in the same experiment have to be delivered by separate signal generators due to the fast switching time. Finally, all mw and rf fields combined and guided through appropriate coaxial cables to the sample holder with a strip-line structure for further guidance. This strip-line is designed as transmission line and consequently the transmitted mw and rf fields are terminated or sent to analyzer devices for further characterization and experiment surveillance.

The sample holder has to be adjusted according to the frequency range of the oscillation fields. For fields of up to several GHz simple printed circuit boards (PCBs) are used with etched strip-lines as a guide to and from the sample and a copper wire (ø ≈ 20 µm) is used to connect them and guide the radiation across the sample. The oscillating magnetic field around the current carrying wire is used for spin manipulation. A higher magnetic field leads to a larger spin level splitting and therefore requires higher mw frequencies and more careful design of the sample holder to avoid too much loss. In that case the simple strip-line is replaced by an impedance matched coplanar waveguide on the PCB. The copper wire is replaced by a coplanar waveguide on a microscopy cover slide where the diamond is finally placed.

B.4. Optically detected magnetic resonance — ODMR

Optically detected magnetic resonance (ODMR) is the main tool to investigate single NV centers and their spins. In this work we use mainly two different ODMR techniques for the NV center. On the one hand there is an interleaved scheme that separates unitary spin manipulation (e.g. Rabi oscillations or entanglement sequences) and spin readout by laser pulses and the detection of subsequent fluorescence. We refer to this technique as pulsed ODMR and it is explained in chapter 2.2.6. On the other hand there is the so called cw-ODMR technique that uses simultaneous continuous laser illumination and mw radiation that leads to an incoherent spin manipulation. In chapter 2.3 a cw-ODMR spectrum is presented and the cw-ODMR technique is shortly explained.

CW-ODMR spectra A cw ODMR spectrum in this work is taken by shining a continuous laser beam onto the NV center and simultaneously applying mw radiation. Although, the mw alone might lead to a unitary evolution of the spin states the probabilistic excitation and emission processes caused by the laser make the overall process incoherent (except for special settings [26]). If the mw frequency is swept the fluorescence drops from its maximum value for off resonant mw to a $\approx 30\%$ reduced level for resonant mw radiation. The maximum fluorescence level corresponds to a polarized electron spin and the lowest level corresponds to a saturation of the EPR transition (i.e. the corresponding spin states are equally populated). This technique is particularly easy as it does not require any capabilities to pulse either laser or mw.

The mentioned contrast for cw-ODMR, however, is usually only achieved for high laser and mw intensities. For instance for roughly saturation laser intensity and electron spin Rabi frequencies on the order of 10 MHz. In this case the ODMR lines are usually power broadened either by laser or mw radiation.[3] Increasing laser intensity effectively reduces the ground state lifetime and increases the repolarization rate and therefore increases the linewidth. The repolarization rate, however, has an upper bound due to the lifetime of the metastable singlet state (≈ 250 ns). As in conventional EPR mw radiation that induces Rabi frequencies higher than the inhomogeneous linewidth also leads to power broadening. The stronger of the two broadening mechanisms determines the linewidth of the cw-ODMR spectrum.

In general, to achieve a high contrast in cw-ODMR spectra laser intensity and mw power have to be carefully adjusted. If on the one hand the laser induced repolarization rate is much higher than the electron spin Rabi frequency the mw is not capable of transferring population from the $m_S = 0$ level into other spin levels ($m_S = \pm 1$). In turn, the NV center spin will stay polarized and the ODMR contrast vanishes. On the other hand a Rabi frequency that exceeds the laser excitation rate by far is more than enough to achieve equal spin state population which leads to highest contrast but also

[3] For the samples used in this work the inhomogeneous linewidth is usually ~ 1 MHz or smaller.

leads to an unnecessarily high line broadening. Summing up, laser repolarization rate and electron spin state Rabi frequency should be comparable.

Eventually, when ODMR spectra should be measured with a spectral resolution of $\sim 1\,\mathrm{MHz}$ or better (e.g. to resolve the coupling to the nitrogen nucleus) both laser and mw radiation have to be reduced to achieve a suitable power broadening. Experimentally it turns out that for similar average fluorescence count rates, the cw-ODMR spectra show a much smaller contrast than spectra taken with pulsed ODMR (see below). Therefore, the SNR for cw-ODMR spectra is smaller than for pulsed ODMR spectra and in turn the acquisition time is longer.

Pulsed ODMR spectra It is technically more demanding to acquire a pulsed ODMR spectrum because laser and mw radiation have to be pulsed on a sub-µs timescale. More precisely, the readout laser has to have length of $\approx 300\,\mathrm{ns}$ (for optimal SNR, see section 5.2) followed by a waiting time of $\approx 1\,\mu\mathrm{s}$ and finally the unitary spin manipulation takes place (e.g. an electron spin π-pulse). This sequence is repeated continuously while the corresponding frequency is swept on a much larger timescale ($\sim$ ms). If the corresponding devices are available, however, it is preferable to use pulsed ODMR especially for high spectral resolution ODMR spectra and also for ENDOR spectra. Pulsed ODMR spectra on the electron spin using a π-pulse as unitary transformation are shown in figure 5.5c and ODMR spectra on the nitrogen nuclear spin using a π-pulse on the nuclear spin and a correlation with the electron spin are shown in figures 5.6b,c. This technique is superior mainly due to two things. At first, the full laser power can be used for readout without causing power broadening and second, a unitary manipulation of spin states is possible.

Using the full laser power leads to a high fluorescence count rate during readout and thus to fast repolarization and short readout times. As in all pulsed experiments the contrast between signals for electron spin state $m_S = 0$ and for $m_S = \pm 1$ is $\approx 30\%$ (see figure 5.5c). In our case the readout time of $\approx 300\,\mathrm{ns}$ is chosen such that the SNR is maximized (see figure 5.8c gray curve). If we would sub-select only those photons that arrive during these $\approx 300\,\mathrm{ns}$ we could afford a little bit longer laser pulses in order to repolarize the electron spin to a higher degree. However, the repolarization after $\approx 300\,\mathrm{ns}$ is already substantial.

The use of unitary spin manipulation is already sketched with the first two figure references (i.e. figures 5.5c and 5.6b,c). Not only simple EPR spectra can be recorded but also ENDOR spectra on distinct nuclei. In addition we are not restricted to square pulses. Using shaped pulses allows tailoring of the spectral response function (the upper part of figure 5.5c shows the spectral response of a square pulse).

In addition to its versatility pulsed ODMR spectra are also faster acquired because of a larger SNR. Therefore, we have to compare electron spin pulsed ODMR spectra (e.g. figure 5.1b and 5.5c). The former was taken by cw-ODMR and exhibits a contrast of $\approx 10\%$ and the latter was taken by pulsed ODMR and exhibits a contrast of $\approx 30\%$.

Both spectra have an equal spectral resolution and both were taken for similar average fluorescence count rates of $\approx 30 \cdot 10^3$ photons per second. Thus, the pulsed ODMR has roughly a 3 times larger SNR and is therefore about 10 times faster in data acquisition. As an example we are able to record a nice hyperfine resolved spectrum similar to the one in 5.5c within $\approx 20\,\mathrm{s}$ which would take several minutes using cw-ODMR. This makes it particularly easy to track magnetic field changes that occur for the experimental settings in chapter 5.3 where a permanent magnet is placed close to the NV and any slight position or temperature change leads to a field drift. Here, once in a while an electron spin ODMR spectrum as shown in 5.9 is acquired to track individual hyperfine lines.

C. Concerning spins

In chapter 2.2.4 the properties of the electron spin of the NV center are explained and in chapter 3.1 its interaction with proximal nuclear spins is highlighted. Although, many aspects of the spin properties are presented there, some peculiarities of chapters 3, 4, 5 and 6 will be further analyzed in this part. First, the Hamiltonian is analyzed more deeply for some special experimental settings, and then the spin manipulation is discussed followed by a deeper analysis of spin coherence time measurements. After that, some entanglement measures that were used in this work are summarized. Finally, the results of this work are reviewed with respect to magnetic field sensing with the electron spin.

C.1. Spin Hamiltonian

Electric field effects on the NV electron spin In eq. (2.2) the NV spin Hamiltonian is given which includes an a priori not axially symmetric ZFS tensor and an arbitrary magnetic field. Here we recall this Hamiltonian but we include the electric field explicitly which was formerly just mentioned to be able to lead to a not axially symmetric ZFS tensor. According to [137] an electric field $\underline{\mathcal{E}}$ yields the following energy level shifts

$$\hat{H}_{F\perp} = f_\perp \cdot \left[\mathcal{E}_y \cdot \left(\hat{S}_y^2 - \hat{S}_x^2\right) - \mathcal{E}_x \cdot \left(\hat{S}_x\hat{S}_y + \hat{S}_y\hat{S}_x\right)\right] \tag{C.1a}$$

$$\hat{H}_{F\parallel} = f_\parallel \cdot \mathcal{E}_z \cdot \hat{S}_z^2 \tag{C.1b}$$

$$F_{x,y} = f_\perp \cdot \mathcal{E}_{x,y}, \quad F_z = f_\parallel \cdot \mathcal{E}_z \tag{C.1c}$$

with $f_\perp = 170\,\mathrm{kHz\,\mu m\,V^{-1}}$ and $f_\parallel = 3.5\,\mathrm{kHz\,\mu m\,V^{-1}}$.[1] For the total electron spin Hamiltonian of the NV center this yields

$$\begin{aligned}\hat{H} &= D\hat{S}_z^2 + E\left(\hat{S}_x^2 - \hat{S}_y^2\right) - \underbrace{\tilde{\gamma}_e \underline{B}}_{\underline{b}} \cdot \underline{\hat{S}} + \hat{H}_{F\perp} + \hat{H}_{F\parallel} \\ &= \begin{pmatrix} D + F_z + b_z & b_x - ib_y/\sqrt{2} & E - F_y - iF_x \\ b_x + ib_y/\sqrt{2} & 0 & b_x - ib_y/\sqrt{2} \\ E - F_y + iF_x & b_x + ib_y/\sqrt{2} & D + F_z - b_z \end{pmatrix} .\end{aligned} \tag{C.2}$$

Obviously, an electric field along the NV axis is capable of shifting $m_S = 0$ and $m_S = \pm 1$ with respect to each other. Thus, it changes the D parameter of the ZFS to $D' = D + F_z$.

[1] Another term from [137] was neglected because its influence on the NV level positions is highly suppressed for magnetic fields $\ll D$ and Stark shifts in the kHz regime.

In contrast, transverse fields mix spin states $m_S = +1$ and -1. More precisely, transverse fields affect the E parameter of the ZFS ($E' = E - F_y - iF_x$). In chapter 2.2.4 the coordinate system is defined such that E is a real number. If we now keep the coordinate system fixed E' can be complex.

As the electric field of an elementary charge with distance d to the NV center is

$$|\underline{\mathcal{E}}| = \frac{1}{4\pi\epsilon_0\epsilon_r}\frac{e}{d^2} = \frac{262\ \mathrm{V\,\mu m^{-1}}}{d^2\ \mathrm{nm^{-2}}} \tag{C.3}$$

already several nm of separation lead to observable changes in E' and D'. Largest changes are achieved for fields perpendicular to the NV axis (i.e. if a charge is on the plane perpendicular to the NV) because $f_\perp \gg f_\parallel$. In this case an NV center with a coherence time of 1 ms is able to sense a charge at a distance of ≈ 300 nm. Actually, if the charge is placed along the NV axis the effect of the electric field is $\approx 50\times$ smaller. The effects of D' and E' on the energy levels, however, also depend on the magnetic field setting. For instance, the effects of transverse electric fields can be easily suppressed by a magnetic field parallel to the NV axis with $|b_z| \gg |E'|$ because $[E', b_z] \neq 0$. The effect of D' on the energy levels remains unaltered is this case ($[D', b_z] = 0$). Conversely, the effect of small magnetic fields can be easily suppressed by transverse electric fields if $|b_z| \ll |E'|$ (see eqs. (C.2), (C.5)).

Because the NV center can possess a charge (usually we use the negatively charged NV center) two NVs of a pair influence each other also by their electric field. The pair presented in chapter 6 has a separation of ≈ 10 nm and therefore the electric field they exert onto each other is 2.7 $\mathrm{V\,\mu m^{-1}}$. Thus the maximum expected $|E'|$ value caused by this electric field is ≈ 0.45 MHz (see eqs. (C.1) and (C.3)). From section 6.5 we know the exact position of the two NV centers with respect to each other and we can therefore calculate the exact value of $|E'|$. For NV A the field generated by the charge of NV B has an angle of 26° with its symmetry axis and NV B senses a field with an angle of 67° with its symmetry axis. Therefore, the expected values of $|E'|$ are 0.2 MHz and 0.4 MHz respectively. The actual $|E'|$ parameters, however are much larger (see section 6.3) and are therefore either generated by other charges or local strain fields.

Misaligned magnetic fields In most of the presented experiments the magnetic field is aligned along the NV center axis. Here we discuss the effect of a misaligned magnetic field. For small field strengths D is still the dominating term in the spin Hamiltonian (C.2). Therefore, at least the $m_S = 0$ state is hardly affected. Spin states $m_S = \pm 1$, however, easily mix. To demonstrate this we write the matrix representation of the Hamiltonian in the basis $(|T_X\rangle, |T_Y\rangle, |T_Z\rangle)$ instead of the usual $(|+1\rangle, |0\rangle, |-1\rangle)$ basis

[133].

$$|T_X\rangle = \frac{1}{\sqrt{2}}\left(|-1\rangle - |+1\rangle\right) \tag{C.4a}$$

$$|T_Y\rangle = \frac{i}{\sqrt{2}}\left(|-1\rangle + |+1\rangle\right) \tag{C.4b}$$

$$|T_X\rangle = |0\rangle \tag{C.4c}$$

where the new basis states are eigenstates with magnetic spin quantum number zero for the operators $\hat{S}_x$, $\hat{S}_y$ and $\hat{S}_z$. In this basis the Hamiltonian is expressed as

$$\tilde{H} = \begin{pmatrix} D + F_y + F_z & -ib_z - F_x & ib_y \\ ib_z - F_x & D - F_y + F_z & -ib_x \\ -ib_y & ib_x & 0 \end{pmatrix}. \tag{C.5}$$

Here, we have omitted strain splitting as it can be represented by electric fields as well. Due to the degeneracy of $m_S = \pm 1$ or $|T_X\rangle$, $|T_Y\rangle$ in the absence of magnetic and electric fields both bases are eigenbases. For a small magnetic field in x-direction both bases are no eigenbases anymore. However, we can see that $|T_X\rangle$ remains an eigenstate and $|T_Z\rangle$ and $|T_Y\rangle$ mix a little bit and therefore repel (see figure 2.4d). For a large magnetic field in x-direction new eigenstates form, which have eigenvalues $m_S = -1$, 0 and $+1$ with respect to $\hat{S}_x$.

Another interesting feature apparent from eq. (C.5) is that a linearly polarized mw field along x only induces a spin transition between $|T_Z\rangle$ and $|T_Y\rangle$ whereas a mw field along y induces a transition between $|T_Z\rangle$ and $|T_X\rangle$. Interestingly, also a field along z induces a transition, namely the one between $|T_X\rangle$ and $|T_Y\rangle$. Although our mw fields always have also a z component we usually don't see these transitions because they are in a frequency range of up to several 10 MHz whereas we use frequencies around 2.87 GHz. Eventually, by choosing the right linear polarization of the mw some transitions can be suppressed and others can be enhanced. Because our mw fields are indeed linearly polarized we occasionally see very different transition strength for the two main EPR transitions which depend on the angle between static magnetic field and mw field. This behavior is summarized in figure C.1. Finally, we can see from eq. (C.5) that a suitable transverse magnetic field (e.g. b_x) can suppress parts of transverse strain or electric fields (e.g. a b_x induced splitting of $|T_X\rangle$ and $|T_Y\rangle$ by ≈ 1 MHz would suppress $F_x \approx 0.1$ MHz but not $F_y \approx 0.1$ MHz). This effect has been used to reconstruct an applied electric field in [75].

In chapter 6 a pair of coupled NV centers is investigated. Their crystallographic orientation is different and therefore an aligned magnetic field for one NV is misaligned for the other. This has some consequences for the magnetic dipole moment of the individual eigenstates of the misaligned NV as sketched in figure 6.10. While the eigenstates of the aligned NV have magnetic dipole moments according to their magnetic quantum number $m_S = -1, 0, +1$ the eigenstates of the misaligned NV which we will still label "-1", "0"

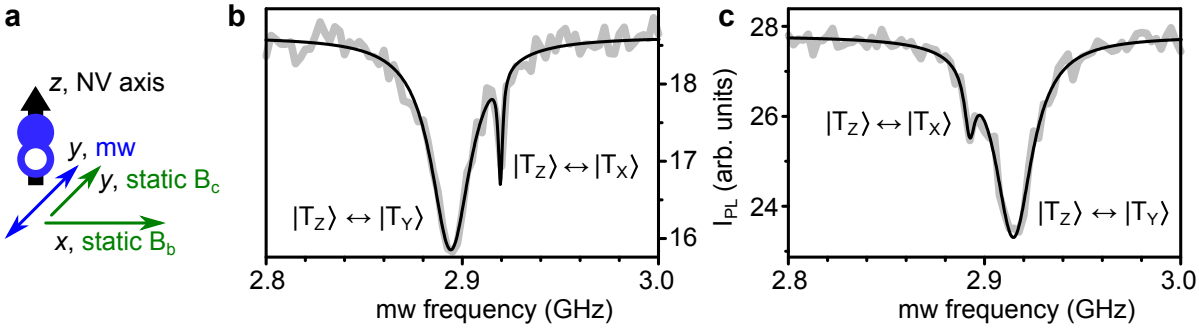

Figure C.1.: ODMR spectrum for perpendicular magnetic field. a, Sketch of the experimental setting. A magnetic field of 6.7 mT is applied perpendicular to the NV (z) axis, first along x (panel b), then along y (panel c). The linearly polarized mw field in the plane perpendicular to the NV axis points along y. **b,c,** ODMR spectra for the experimental settings explained above. The eigenstates are similar to $|T_X\rangle, |T_Y\rangle, |T_Z\rangle$ and the corresponding transitions are marked. Due to the special field setting the transition $|T_Z\rangle \leftrightarrow |T_X\rangle$ is suppressed showing a mw power-broadened linewidth of ≈ 2 MHz whereas transition $|T_Z\rangle \leftrightarrow |T_Y\rangle$ shows a mw power-broadened linewidth of ≈ 25 MHz. Please note, that the hyperfine splitting is not visible because hyperfine interaction is decreased due to the decreased magnetic moment of the eigenstates. The different orientations of the static magnetic field shift either $|T_X\rangle$ or $|T_Y\rangle$ to higher energies.

and "+1" have different magnetic moments than their names suggest. In figure C.2 the corresponding expectation values $\langle \hat{S}_x \rangle$ $\langle \hat{S}_y \rangle$ and $\langle \hat{S}_z \rangle$ for the magnetic dipoles in x, y and z direction are shown for all three eigenstates.

Magnetic field sweeps and ODMR In the previous paragraphs the spin Hamiltonian for misaligned magnetic fields has been discussed. However, for too strong transverse magnetic fields the mixing of the $m_S = 0$ level with other level becomes significant in ground and excited state such that the ODMR effect of the NV center breaks down [28]. More specifically, during the optical polarization of the electron spin the NV center relaxes from the metastable singlet state into the $m_S = 0$ state in 250 ns on average. But because $m_S = 0$ is not an eigenstate it evolves to a great extend into other states on a much faster timescale (~ 1 ns, depends on energy level spacing). Hence, the optical pumping process no longer creates a pure spin state but an incoherent mixture of all m_S states. Similar things happen when the NV center is promoted to the excited state where the spin eigenstates might look different. Effectively, optical spin polarization and readout, which is the prerequisite for ODMR of the NV center, spin is prohibited.

The evolution of the $m_S = 0$ state into other states is similar to the evolution which leads to nuclear spin polarization as explained in section 5.1. But as this happens in the excited state it is also not easily probed. However, with the right experimental settings this whole behavior can be simulated using the NV center spin close to the gsLAC. Therefore, first of all a magnetic field parallel to the NV center axis with a strength

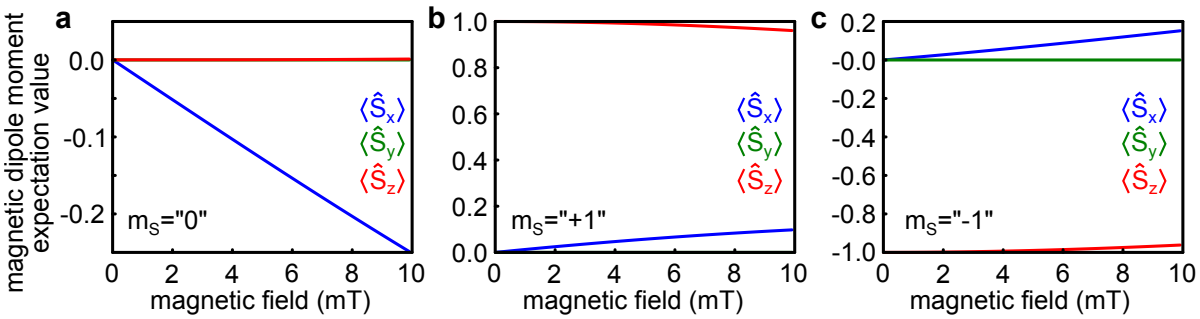

Figure C.2.: Expectation values of magnetic dipole moment. **a–c,** Expectation values of the magnetic moment in all three dimensions ($\langle\hat{S}_x\rangle$, $\langle\hat{S}_y\rangle$ and $\langle\hat{S}_z\rangle$) for the three eigenstates $m_S =$"-1", "0" and "$+1$" of the NV center spin dependent on the magnetic field strength. The field vector is lying in the x-z-plane and has an angle of 109.5° (70.5°) with the z-axis (pointing towards positive x half-plane of the x-z-plane).

corresponding to D_{gs} is applied ($\approx 102\,\mathrm{mT}$, see figure 2.4a and C.3a,c[2]). Hence, the spin levels $m_S = 0$ and -1 are degenerate. However, this is exactly only true for those levels that really cross (include nuclear spin states, compare section 5.1 and figure 5.2). Other levels will anti-cross due to hyperfine induced mixing. As these hyperfine terms are on the order of several MHz they lead to dynamics faster than the repolarization rate and are therefore hardly visible. The crossing levels, however, do really cross only for perfectly aligned magnetic fields and no transverse fields. Hence, their anti-crossing can be slowly turned on by increasing a transverse field $\varepsilon B_\perp$ (see figure 2.4c and figure C.3a). In this case after a repolarization laser pulse the NV spin will start oscillating slow enough between $m_S = 0$ and $m_S = -1$ to be tracked. The experimental measurement scheme and the results are shown in figure C.3b,d. The upper trace of figure C.3d oscillates with a frequency of 0.23 MHz which corresponds to a transverse magnetic field of 0.01 mT. Hence, the magnetic field is misaligned by $0.006° = 23''$.

Having the coherent evolution of figure C.3d in mind we can explain the fluorescence trace while the magnetic field strength is swept (see figure C.3c). Away from the gsLAC the laser polarizes the NV center spin into $m_S = 0$, the spin remains in that state and therefore the fluorescence is high. Around the gsLAC the spin evolves from $m_S = 0$ into -1 while laser illumination and eventually ends up in the metastable singlet state accompanied with a reduced fluorescence. Similar to figure 5.2a the highest probability to flip the electron spin and thus to pass into the metastable state is achieved exactly at the anti-crossing. For lower transverse fields the oscillation frequency decreases and therefore it takes some time to evolve from $m_S = 0$ into -1. If the laser excitation rate is too high compared to this oscillation frequency the spin has not enough time to

[2]The given magnetic field values are assumed to be proportional to the electrical current in the applied electromagnet and the drop in fluorescence occurs at the field calculated by eq. (2.4) and $D_{gs} = 2870\,\mathrm{MHz}$.

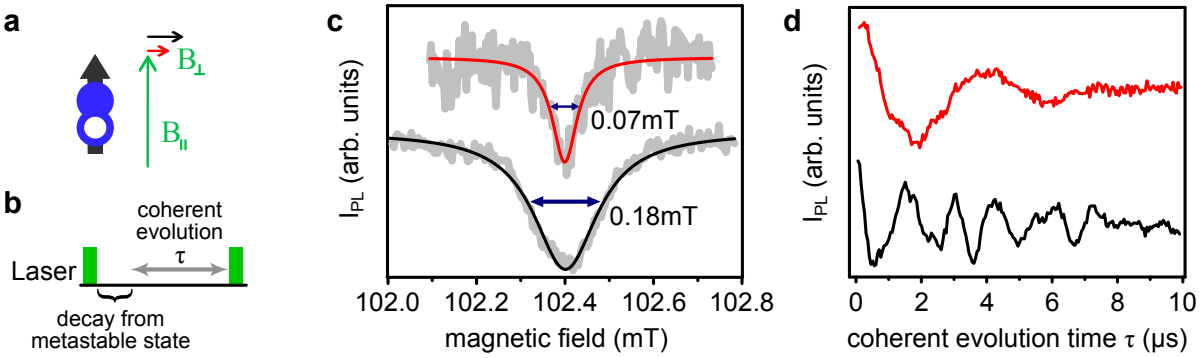

Figure C.3.: Coherent evolution at the gsLAC. a, A magnetic field of $B_{\parallel} \approx 102\,\mathrm{mT}$ parallel to the NV axis is applied to make $m_S = 0$ and -1 degenerate. A tiny transverse field $B_{\perp}$ will lead to a level anti-crossing (compare figure 2.4c). We have applied two different transverse field strengths (color-coding black and red). **b,** Pulse sequence for results in panel d. A green laser pulse repolarizes the electron spin. After the laser pulse it takes $\approx 250\,\mathrm{ns}$ for the NV centers to relax to the ground state. Then the coherent evolution of the spin state starts. Finally, the spin state is read out by another laser pulse. **c,** Magnetic field sweep while monitoring the fluorescence intensity I_{PL}. At around 102 mT the above mentioned level anti-crossing occurs accompanied by a drop in fluorescence. The upper curve has a slightly smaller transverse magnetic field than the lower one. **d,** Coherent oscillation between spin states $m_S = 0$ and -1. The decay is due to inhomogeneous broadening. For a higher transverse magnetic field (lower curve) the oscillation is faster.

evolve into $m_S = -1$ therefore no dip would be visible in figure C.3c. Actually, the laser intensity has been reduced from saturation intensity in order to see the dips presented here. For larger misalignment angles a dip occurs even for saturation intensity.

Similar dips as in C.3c occur around the esLAC [28] (i.e. $B_{\parallel} \approx 51\,\mathrm{mT}$, see figure C.4a). There, however, the rate that depopulates the excited state spin levels is fixed at $\approx 100\,\mathrm{MHz}$. As shown in 5.1 at the esLAC the nuclear spin is polarized and thus only those levels that would cross for perfectly aligned field have to be considered. If the field is aligned such that the oscillation frequency between $m_S = 0$ and -1 in the excited state is smaller than the decay rate, the fluorescence dip also vanishes. Because the decay rate is so large the dip in fluorescence only appears for comparatively large misalignment angles of $\sim 1°$.

A straight forward calculation can model the fluorescence intensity dependence $I_{PL}(B, \theta)$ on magnetic field strength B and orientation θ. The fluorescence intensity monotonically rises for increasing $m_S = 0$ ($|0\rangle$) spin state population in the excited state. Thus by estimating $\mathrm{Tr}(|0\rangle\langle 0|\ \rho_{es})$ we can approximate $I_{PL}(B, \theta)$ where ρ_{es} is the spin density matrix in the excited state. The estimation is done in two steps. First, $|0\rangle$ is projected onto the eigenstates $|e_{i\ gs}\rangle$ of the ground state spin Hamiltonian. And these projections build up the ground state density matrix $\rho_{gs} = \sum_{i=1}^{3} \langle 0|e_{i\ gs}\rangle\langle e_{i\ gs}|0\rangle\ |e_{i\ gs}\rangle\langle e_{i\ gs}|$. In the second and last step a similar projection is performed with ρ_{gs} onto the eigenstates of the excited state $|e_{i\ es}\rangle$ which yields $\rho_{es} = \sum_{i=1}^{3} \langle e_{i\ es}|\ \rho_{gs}\ |e_{i\ es}\rangle\ |e_{i\ es}\rangle\langle e_{i\ es}|$. The corre-

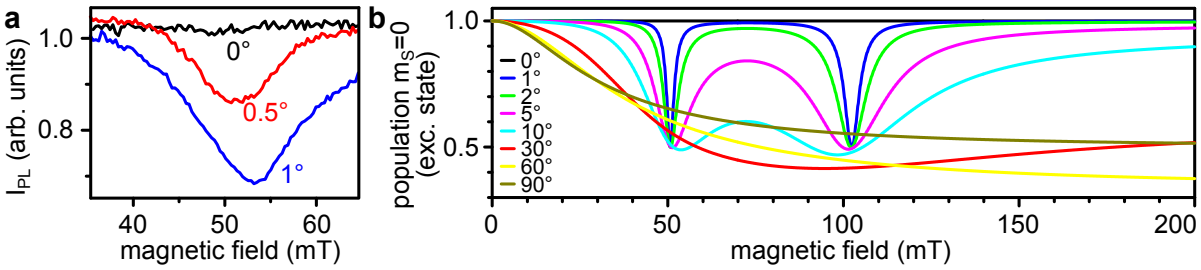

Figure C.4.: Magnetic field sweep around esLAC and simulation. a, A magnetic field parallel to the NV axis is swept around the esLAC and the laser induced fluorescence is recorded (black curve). For slightly misaligned field directions (red and blue curve, $0.5°$ and $1.0°$) a fluorescence dip at the esLAC occurs due to spin state mixing in the ground and excited state. **b,** Theoretical modeling of the part of the excited state population that is in the $m_S = 0$ state during optical pumping. This calculation is performed for a large magnetic field range and several angles between magnetic field and NV axis. The shown population resembles the experimentally measured fluorescence response (compare panel a, figure C.3 and [28]).

sponding result of $\mathrm{Tr}(|0\rangle\langle 0|\ \rho_{es})$ is displayed in figure C.4b and resembles the measured I_{PL} data (see figures C.4a, C.3c and [28]).

Two ^{13}C Hamiltonian Here, the spin Hamiltonian for the study of section 3.3 is presented in more detail. The quantum register of that section consists of the NV electron spin and the nuclear spins of two ^{13}C nuclei in the first coordination shell.

Naively, when thinking of an electron spin coupled to two identical nuclear spins one would expect an ODMR spectrum similar to the one observed in C.5a but with the two central lines of each m_S manifold falling on top of each other yielding a doubled contrast for these degenerate lines. However, this is only true for cases where the hyperfine interaction is much smaller than the energy splitting of the electron spin levels [133]. As this requirement is not fulfilled in our case ($a_{iso} = 150\,\mathrm{MHz}$ vs. $2.64\,\mathrm{GHz}$) we see deviations from this simple picture (i.e. the central lines of each m_S transition in figure C.5a do split). These splittings mark the breakdown of the secular approximation and is accounted for by calculating higher order (starting from second order) perturbation theory contributions [133]. For this calculation it is convenient to change the nuclear spin basis states to $|\mathcal{I}, \mathcal{M}\rangle_{\mathcal{I}\mathcal{M}}$ where $\mathcal{I}$ is the total nuclear spin that can be achieved by vectorial addition of the single nuclear spins (i.e. $\mathcal{I} \in \{0, 1\}$ for two nuclear spins with $I = 1/2$) and $\mathcal{M}$ the corresponding total nuclear spin projection (i.e. $\mathcal{M} \in \{-1, 0, +1\}$ for $\mathcal{I} = 1$ and $\mathcal{M} = 0$ for $\mathcal{I} = 0$). In addition we take the hyperfine interaction to be isotropic for this approximation. In the nuclear spin product basis $|m_{I1}\rangle_{n1} \otimes |m_{I2}\rangle_{n2}$ the

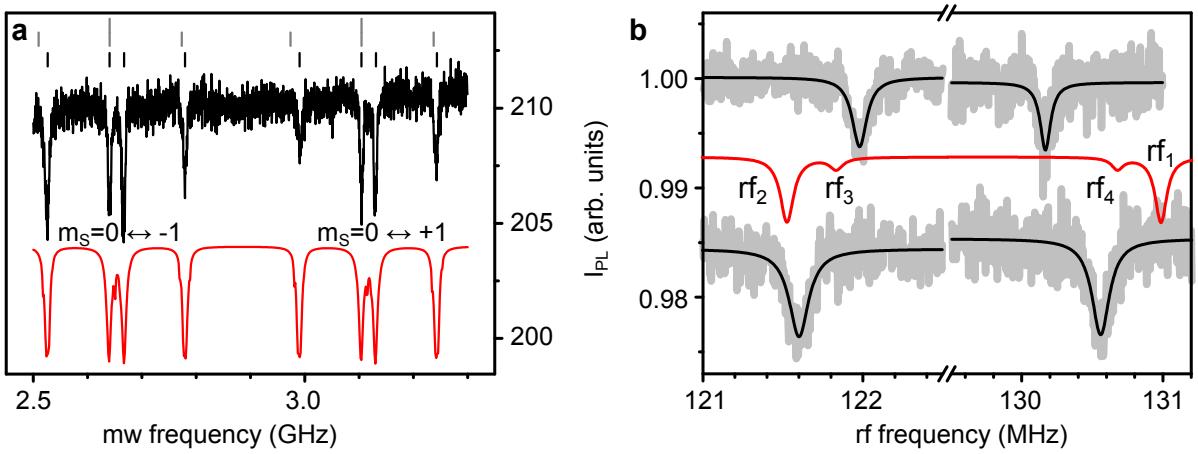

Figure C.5.: EPR and NMR spectra for the NV spin and two ^{13}C spins. a, EPR spectrum of a NV center with two ^{13}C nuclear spins in its first coordination shell and a magnetic field of $8.32\,\mathrm{mT}$ aligned along the NV axis. The upper curve is the measurement and the lower curve is a simulation for the given magnetic field. The black stick spectrum in the upper part shows the shifted lines according to second order perturbation theory and the gray lines show the corresponding spectrum for secular approximation. **b,** ENDOR spectra as in figure 3.11c with additional simulated spectrum (red curve).

new basis states are

$$|0,0\rangle_{\mathcal{IM}} = {}^1/\sqrt{2}\,(|{\downarrow}\rangle_{n1} \otimes |{\uparrow}\rangle_{n2} - |{\uparrow}\rangle_{n1} \otimes |{\downarrow}\rangle_{n2}) \tag{C.6a}$$
$$|1,+1\rangle_{\mathcal{IM}} = |{\uparrow}\rangle_{n1} \otimes |{\uparrow}\rangle_{n2} \tag{C.6b}$$
$$|1,0\rangle_{\mathcal{IM}} = {}^1/\sqrt{2}\,(|{\downarrow}\rangle_{n1} \otimes |{\uparrow}\rangle_{n2} + |{\uparrow}\rangle_{n1} \otimes |{\downarrow}\rangle_{n2}) \tag{C.6c}$$
$$|1,-1\rangle_{\mathcal{IM}} = |{\downarrow}\rangle_{n1} \otimes |{\downarrow}\rangle_{n2} \tag{C.6d}$$

For an isotropic hyperfine interaction the quantum states $|m_S\rangle_e \otimes |0,0\rangle_{\mathcal{IM}}$, $|-1\rangle_e \otimes |1,-1\rangle_{\mathcal{IM}}$ and $|+1\rangle_e \otimes |1,+1\rangle_{\mathcal{IM}}$ will not shift because they do not mixed with other states by off-diagonal hyperfine terms. But the remaining states in the $m_S \neq 0$ levels shift upwards by $A_\perp^2/\nu$, states $|0\rangle_e \otimes |1,\pm1\rangle_{\mathcal{IM}}$ are shifted down by $A_\perp^2/\nu$ and state $|0\rangle_e \otimes |1,0\rangle_{\mathcal{IM}}$ is shifted down by $2A_\perp^2/\nu$. Here, ν is the original EPR transition frequency. Consequently, the EPR transition frequencies shift like

$$(m_S = 0 \leftrightarrow \pm1): \Delta\nu_{|0,0\rangle_{\mathcal{IM}}} = 0 \tag{C.7a}$$
$$\Delta\nu_{|1,0\rangle_{\mathcal{IM}}} = 3A_\perp^2/\nu \approx 26\ \mathrm{MHz} \tag{C.7b}$$
$$(m_S = 0 \leftrightarrow -1): \Delta\nu_{|1,+1\rangle_{\mathcal{IM}}} = 2A_\perp^2/\nu \approx 17\ \mathrm{MHz} \tag{C.7c}$$
$$\Delta\nu_{|1,-1\rangle_{\mathcal{IM}}} = A_\perp^2/\nu \approx 9\ \mathrm{MHz} \tag{C.7d}$$
$$(m_S = 0 \leftrightarrow +1): \Delta\nu_{|1,+1\rangle_{\mathcal{IM}}} = A_\perp^2/\nu \approx 9\ \mathrm{MHz} \tag{C.7e}$$
$$\Delta\nu_{|1,-1\rangle_{\mathcal{IM}}} = 2A_\perp^2/\nu \approx 17\ \mathrm{MHz} \tag{C.7f}$$

according to second order corrections (i.e. the EPR lines are shifted towards higher frequencies). Hence, the splitting of the two central lines of 26 MHz is nicely approximated (see figure C.5a). In addition, no shift of the EPR transitions for nuclear spin states $|0,0\rangle_{\mathcal{IM}}$ is well demonstrated in figure 3.10c. However, the hyperfine tensor is not isotropic and it is therefore not identical for the two nuclei with respect to the lab frame. Here, we have only estimated the EPR line shifts due to higher order perturbation theory. Please note, however, that the used hyperfine interaction constant of 150 MHz does not reproduce the EPR spectrum itself. In addition for in the present case higher order perturbation corrections become important [133]. Therefore, the real eigenstates and eigenvalues should be calculated by diagonalizing the full spin Hamiltonian (see below).

According to [107] the axial hyperfine tensor for the interaction of a ^{13}C nuclear spin with the NV center electron spin is tilted against the NV axis by 105.9° (i.e. 3.5° less than the C-C-bond angle) in the direction of that ^{13}C atom and its values are $A_{\parallel} = 205\,\text{MHz}$ ($68.3 \times 10^{-4}\,\text{cm}^{-1}$) and $A_{\perp} = 123\,\text{MHz}$ ($41.1 \times 10^{-4}\,\text{cm}^{-1}$). Using these values we can compute the eigenvectors and eigenvalues of the Hamiltonian eq. (3.14). As a result we can simulate the ODMR and the ENDOR spectra of figures (3.10c and 3.11c). These spectra accompanied by the respective simulated spectra are shown in figure C.5. Apparently, the ODMR spectrum for the electron spin is well reproduced by the simulation. However, the ENDOR spectrum does not fit that well. The reasons for this can be caused by the uncertainties of the hyperfine tensor orientation and strength given in [107]. The different strength of the simulated ENDOR lines respect the different transition strengths of the respective transitions. As already mentioned in section 3.3 the nuclear spin state $|01\rangle_{nn}$ has strong singlet character and $|10\rangle_{nn}$ has triplet character. This causes smaller transition strengths for rf_3 and rf_4 as compared to rf_1 and rf_2. However, according to the non-vanishing ENDOR lines rf_3 and rf_4 the eigenstate $|01\rangle_{nn}$ cannot be a perfect nuclear spin singlet state.

C.2. Spin manipulation and quantum gates

Spin manipulation and Bloch sphere In this work coherent spin manipulation is often realized by appropriate rf or mw radiation as shortly explained in 2.2.4 and 2.3. Although, the NV electron spin or the ^{14}N nuclear spin are spin triplets and therefore qutrits, most of the time all three spin projections are non-degenerate with unequal energy spacing. Hence, two of the three levels can be used as effective qubit levels. Equations (2.6) and (C.5) illustrate how mw radiation can induce spin transitions among two levels and these mw fields can be visualized on the Bloch sphere.

Usually the Bloch sphere illustrates the spin dynamics in the rotating frame (i.e. the mw radiation or the B_1 field with amplitude Ω are static, figure C.6a). The eigenstates in the absence of the mw field (e.g. $|-1\rangle$ and $|0\rangle$) coincide with North and South Pole of the sphere and any other pure state can be associated with a point on the sphere.

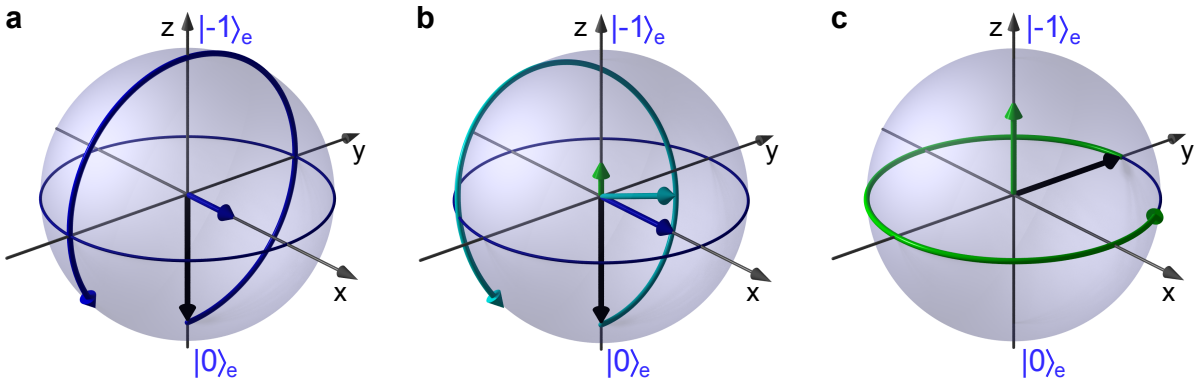

Figure C.6.: Bloch sphere representation of spin manipulation. a, Resonant Rabi oscillation around B_1 field with strength Ω along x (blue arrow). The initial spin state $|0\rangle_e$ is represented by the black arrow. The blue circular arrow shows the path of the quantum state during Rabi oscillation. **b,** For off-resonant Rabi oscillation there is a detuning field in z-direction (green arrow). Here the Rabi oscillation is a Larmor precession (cyan circular arrow) around the resulting field vector (cyan arrow). **c,** Free evolution of a coherent superposition state due to a detuning field. The mw is switched off.

Especially, the superposition states

$$\Psi = \frac{1}{\sqrt{2}}\left(|-1\rangle + e^{i\varphi}\,|0\rangle\right) \tag{C.8}$$

lie on the equator where phase $\varphi = 0$ is associated with the x-direction and $\varphi = \pi/2$ with the y-direction. Mixed states (usually are expressed by a density matrix ρ) are represented by a point inside the sphere, where the totally mixed state or unity is the center. As the Bloch sphere draws a picture in the rotating frame any offset or detuning of the two eigenstates' energy difference from the mw frequency results in a magnetic field in z-direction and the mw field itself usually points in x-direction if no specific other phase on the equator is given. Thus, the Hamiltonian is time-independent (or at least quasi static). Any spin dynamics can therefore be thought of as Larmor precession around the resulting magnetic field vector (i.e. vectorial sum of mw field Ω and detuning Δ, figure C.6b). In this case, where the driving field is not resonant, the visible Rabi frequency is an effective one

$$\Omega_{\text{eff}} = \sqrt{\Omega^2 + \Delta^2} \tag{C.9}$$

and apparently the amplitude in z-direction decreases as

$$A = \frac{A_0}{1 + \left(\frac{\Delta}{\Omega}\right)^2} \tag{C.10}$$

where A_0 is the full amplitude. Please note, that the amplitude A of the oscillation in z-direction is proportional to the contrast of the fluorescence light I_{PL}.

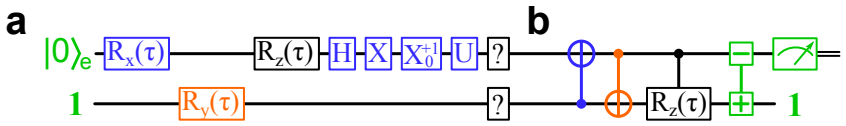

Figure C.7.: Single qubit and controlled quantum gates. **a,** Quantum circuit comprised of NV electron spin (top line) and nuclear spin (bottom line). Single qubit gates as they appear in this work from left to right. The NV electron spin it is initialized by green laser illumination ($|0_e\rangle$) and the nuclear spin is usually scrambled into a totally mixed state ("**1**"). Unselective electron spin rotations around x (mw, blue), nuclear spin rotations around y (rf, orange) and phase rotation (e.g. detuning, black) are displayed by $R_{x,y,z}(\tau)$. We illustrate unselective $\pi/2$ and π-pulses by Hadamard (H) and Pauli X gates. If necessary, in a qutrit the used transition is given by the corresponding m_S values (here for an X gate). U stands for an arbitrary unitary operation and "?" symbolizes an unknown influence by the environment for example. **b,** Controlled two qubits gates. Selective electron and nuclear spin π-pulses are shown as the proper CNOT gates. Electron spin state dependent phase rotation on the nuclear spin. Laser induced Electron-nuclear spin flip-flop lowering m_S and raising m_I. Finally, a laser pulse performs an electron spin measurement and a classical communication (double) line carries the result. The nuclear spin is scrambled.

In this work, we mainly use rectangular mw pulses which indeed lead to a static B_1 field on the Bloch sphere. In the case of rectangular pulses the only time-dependence arises when the mw field is switched on or off which we approximate to be infinitely fast. However, one can also think of shaped or chirped pulses where the field amplitude or the frequency or the phase changes which lead to a time-dependent Hamiltonian.

Figure C.6 illustrates some typical dynamics on the Bloch sphere like a resonant and off-resonant Rabi oscillation and a free Larmor precession due to detuning. Single qubit gates and controlled multi-qubit gates can be realized by these methods.

Quantum wire diagrams It is convenient to display measurement sequences comprised of single qubit or controlled multi-qubit gates in a quantum wire diagram (see figure C.7, [197]). The most abundant single qubit gates in this work are rotations around x and y axes of the Bloch sphere facilitated by oscillating magnetic fields and rotations around z induced by a detuning of the driving field. They are symbolized by

$$R_{x,y,z}(\theta) = e^{i\,(\mathrm{X,Y,Z})\,\theta/2} \tag{C.11}$$

where θ is the rotation angle and X, Y and Z are the Pauli matrices (see appendix A). In our case the rotation angle θ often depends on the time τ which is why $\theta(\tau)$ is often replaced by τ. Rotations by an angle of $\pi/2$ or π are special because they can create an equal superposition state or perform a spin flip respectively. For these operations there are special symbols, namely the Hadamard (H) and the Pauli X, Y and Z gates. Although H and X do not properly match an x rotation around $\pi/2$ or π we use these

symbols for convenience and brevity in the quantum wire diagrams.

$$\text{bitflip}: \quad \mathrm{X} = \begin{pmatrix} 0 & 1 \\ 1 & 0 \end{pmatrix} \qquad R_x(\pi) = \begin{pmatrix} 0 & i \\ i & 0 \end{pmatrix} \tag{C.12a}$$

$$\text{Hadamard}: \quad \mathrm{H} = \frac{1}{\sqrt{2}} \begin{pmatrix} 1 & 1 \\ 1 & -1 \end{pmatrix} \qquad R_x(\pi/2) = \frac{1}{\sqrt{2}} \begin{pmatrix} 1 & i \\ i & 1 \end{pmatrix} \tag{C.12b}$$

In quantum circuit diagrams each single line represents a qubit. As we are often encoding a qubit in a three level system (e.g. $S = 1$ for the NV electron spin and $I = 1$ for the ^{14}N nuclear spin) we have to specify the qubit levels in advance. In some occasions, however, we change the qubit levels during one run but we never use a superposition of more that two eigenstates at the same time. In that case it might be necessary to specify for example on which transition in a 3-level system an X gate is performed (see figure C.7). In addition in this work conditional gates like z rotations are used (see for example figure 6.7) where the condition can be one of three states. From the context and the information given in the diagram the operation should be conceivable. As in the case of the Hadamard and the X gate also the CNOT gate is not quite the same as a selective π-pulse which we perform in our experiments.

A special flip-flop gate is displayed in figure C.7b (with green "+" and "-") which is used to explain the enhanced readout mechanism of section 5.2. This gate is similar to a SWAP gate but it is applied here to a qubit and a qutrit and in addition this gate is not fully unitary. Although, when applied to two qubits its unitary part is a SWAP (see eq. (5.3)) its non-unitary part gives a preferential direction (i.e. the electron spin flips down and the nuclear spin flips up).

C.3. Coherence properties

In the case of the NV center spins the longitudinal relaxation time T_1 is on the order of several milliseconds and is therefore much longer than usual transverse relaxation times T_2 and T_2^*. Therefore decoherence of quantum states happens mainly due to the loss of phase information of a superposition state as compared to spin flips. In section 3.1.5 the main reason for NV center electron spin decoherence was found to be the nuclear spin bath consisting of ^{13}C nuclei in the diamond lattice. The coherence time was measured using Ramsey interferometry and ESEEM or Hahn echo measurements (see section 2.3). Here, the latter measurement techniques are explained in more detail.

C.3.1. Ramsey interferometry

In Ramsey experiments usually first a coherent superposition state is generated using a $\pi/2$-pulse either around x or y. If a detuning of the energy level spacing from the driving B_1 field is present the quantum state will evolve as shown in figure C.6c. After

this evolution time a final $\pi/2$-pulse around an arbitrary axis in the equator plane will convert the phase into a population difference which can be finally read out. A resulting fluorescence response for such a Ramsey experiment is shown in figure 2.7e where decoherence manifests as the damping of the oscillation. The free evolution time after which the oscillation amplitude has decayed to $1/e$ is called T_2^* and usually leads to an inhomogeneous linewidth of the corresponding EPR resonance line.

The decay origins from the averaging over many measurement runs compared to an ensemble average for measurements on ensembles of quantum systems. As this averaging process takes usually several minutes any change of the energy levels (e.g. due to a changed magnetic field at the position of the NV center) will lead to a different free oscillation frequencies. Consequently a larger spread of different frequencies leads to a faster decay. Summarizing, a Ramsey experiment on the NV electron spin is sensitive to changes of the splitting of the corresponding energy levels on a timescale up to the total measurement time and therefore for almost all noise frequencies (except those changes that are much faster than the inverse free evolution time).

As it turns out for the NV electron spin slow level and field fluctuations affect the spin coherence much stronger than faster fluctuations. Therefore, the T_2^* time is usually much shorter than the T_2 time which is explained next and is less sensitive to slow fluctuations.

C.3.2. Electron spin echo envelope modulation — ESEEM

As seen above a Ramsey measurement is sensitive to slow field fluctuations and therefore quantum coherences decay very fast. Here, first of all a Hahn echo measurement is explained in more detail which effectively suppresses decoherence effects of slow fluctuations.

Basically, a Hahn echo measurement is a Ramsey measurement where a π-pulse is inserted right in the middle of the free evolution time. The full sequence in Bloch sphere representation is depicted in figure C.8. Obviously, the final state will be reached regardless of the current detuning during one run of the Hahn echo sequence. In conventional EPR and NMR the duration of the second waiting time is varied. In this case the signal depending on the second waiting time resembles an FID when first and second waiting times are similar. When the second waiting time approaches the length of the first waiting time the measured signal increases like a time inversed FID and for further increasing times the signal decays again. This is actually the echo.

In this work usually first and second waiting times are constant as shown in figure C.8 and we increase the total free evolution time τ. Hence, the signal I_{PL} should be the maximum of the echo. This maximum depending on time τ is called the electron spin echo envelope modulation (ESEEM). As the name suggests the echo maximum will not stay maximum for all times τ but can either decay as in figure 3.6c or it can exhibit a modulation as in figure 3.6b. We will call the time when the ESEEM has decayed T_2.

In section 3.1.5 the occurrence of the modulation is explained by the influence of the

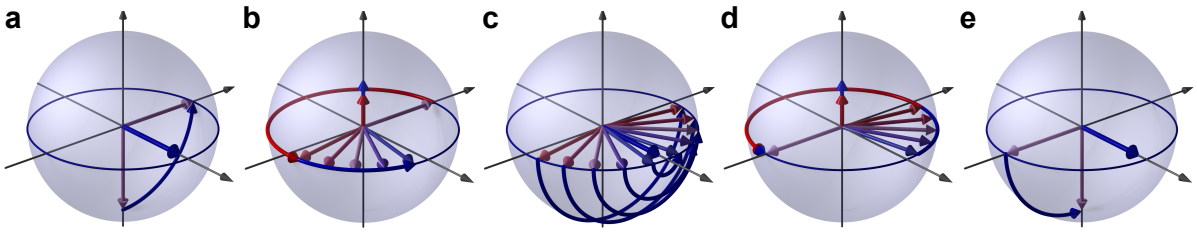

Figure C.8.: Hahn echo sequence on Bloch sphere. **a,** The initial state $|0\rangle_e$ is converted into $1/\sqrt{2}\,(|-1\rangle + i\,|0\rangle)$ by a mw $\pi/2$-pulse. **b,** In the first free evolution time $\tau/2$ a precession depending on the current detuning occurs (different colors of final quantum states for different detunings). This leads to a dephasing when averaging over subsequent runs. The free precession can contain many revolutions; the shown part can be understood as modulo 2π. **c,** A mw π-pulse rotates the electron spin states around the x-axis by 180°. This acts similar to a time inversion as the quantum states will now start to refocus. **d,** In the second waiting time $\tau/2$ every quantum state will evolve into $1/\sqrt{2}\,(|-1\rangle - i\,|0\rangle)$ *as long as the detuning has not changed during complete* τ. Hence, the quantum states are refocused and a distinct quantum state is achieved. **e,** Finally, the phase of the refocused quantum state is converted into population difference and can then be readout.

nuclear spin bath. The decay happens when the detuning changes during τ such that the phase of the first free precession is on average more than π different from the phase of the second free precession. If the detuning is changed slowly due to slow field fluctuations on a time scale much larger than τ the echo does not decay but faster fluctuations cannot be corrected. Hence, the Hahn echo sequence is robust against fluctuations with zero to very small frequencies (i.e. it decouples the spin dynamics from these influences). However, there are more advanced decoupling sequences that are able to cope with varying field fluctuations of much higher frequency. By decoupling the spin dynamics from an increasing part of the noise spectrum the quantum coherence can be preserved much longer. Depending on the noise spectrum different decoupling schemes can be effective. The common feature of all these decoupling sequences is the application of much more than one π-pulse during the free evolution time. The sequences differ, however, in spacing and the phase of the applied pulses. As an example, for the NV center electron spin the so called Carr-Purcell-Meiboom-Gill (CPMG) sequence performs better than a pure Hahn echo [157] and better than for instance the Uhrig dynamical decoupling sequences (UDD) [198]. In addition spin locking sequences can be applied [157]. However, these dynamical decoupling sequences can only be applied in their designed form in which they excite the coherence they want to preserve on their own. Hence, they are designed to protect a known phase only and that is indeed what they do [199] (i.e. a $\pi/2$ phase shifted quantum state is not protected). To protect an arbitrary superposition quantum state the so called KDD sequence performs much better [199]. Nevertheless, using a known phase the coherence time of the spin state can be tested. In addition, for instance the CPMG sequence has been shown to extend the magnetic field sensing time in metrology applications using the NV center compared to a Hahn echo sequence [157].

C.4. Entanglement measures

In section 3.3 of this work entangled states in a quantum register comprised of one electron spin and two nuclear spins are generated. Their amount of entanglement is estimated by three measures. These are the fidelity $\mathcal{F}$ of the entangled state compared to the desired target entangled state, the concurrence $\mathcal{C}$ and the partial transpose $\mathcal{T}_p$. The fidelity can be applied to arbitrary quantum states whereas concurrence and partial transpose can only be applied to two qubits. In the following all three entanglement measures are explained.

Fidelity The fidelity is the overlap of two quantum states $|\Psi_1\rangle$ and $|\Psi_2\rangle$ and is defined as

$$\mathcal{F} = \langle\Psi_1|\Psi_2\rangle\langle\Psi_2|\Psi_1\rangle \tag{C.13}$$

for pure states. For mixed states with density matrices σ and ρ the fidelity is

$$\mathcal{F} = \left[\mathrm{Tr}\left(\sqrt{\sqrt{\rho}\sigma\sqrt{\rho}}\right)\right]^2 \tag{C.14a}$$

$$\mathcal{F} = \mathrm{Tr}(\sigma\rho) \tag{C.14b}$$

where the latter equation only holds if at least one state is a pure state. Obviously, the fidelity is 1 if both state vectors or density matrices are identical and it is 0 if they are orthogonal. We use the fidelity to calculate the overlap of the measured density matrix with the desired density matrix. As the latter is a pure state we can apply equation C.14b. For example, the matrix representation of the W is state is

$$\mathrm{W} = \sigma = \frac{1}{3}\begin{pmatrix} 0 & 0 & 0 & 0 & 0 & 0 & 0 & 0 \\ 0 & 1 & 1 & 0 & 1 & 0 & 0 & 0 \\ 0 & 1 & 1 & 0 & 1 & 0 & 0 & 0 \\ 0 & 0 & 0 & 0 & 0 & 0 & 0 & 0 \\ 0 & 1 & 1 & 0 & 1 & 0 & 0 & 0 \\ 0 & 0 & 0 & 0 & 0 & 0 & 0 & 0 \\ 0 & 0 & 0 & 0 & 0 & 0 & 0 & 0 \\ 0 & 0 & 0 & 0 & 0 & 0 & 0 & 0 \end{pmatrix} \tag{C.15}$$

and obviously to calculate the fidelity according to eq. (C.14b) only those density matrix entries of the experimentally entangled state need to be measured that correspond to the nonzero elements of eq. (C.15). These are three populations and three coherences that are shown in figure 3.19b,d.

Partial Transpose To estimate the amount of entanglement of the experimentally generated Bell states we additionally use the partial transpose and the concurrence. The

partial transpose method [172] relies on the fact that entangled states are inseparable. For a system comprised of two qubits the density matrix ρ has to fulfill

$$\rho = \sum_A w_A \rho'_A \otimes \rho''_A \tag{C.16}$$

in order to be separable. Here, w_A are the positive weights with $\sum_A w_A = 1$ for the individual density matrices ρ'_A and ρ''_A of the two qubits. The density matrix entries of ρ can be indexed like

$$\rho_{m\mu,n\nu} = \sum_A w_A (\rho'_A)_{m,n} \otimes (\rho''_A)_{\mu,\nu} \tag{C.17}$$

where m, n index the entries of ρ'_A and μ, ν index the entries of ρ''_A. A. Peres has shown that the partially transposed matrix

$$\begin{aligned} \sigma_{m\mu,n\nu} &= \rho_{n\mu,m\nu} \\ (\sigma &= \sum_A w_A (\rho'_A)^T \otimes \rho''_A \text{ if eq. (C.16) is valid}) \end{aligned} \tag{C.18}$$

has to have only positive eigenvalues for the density matrix ρ to be separable (i.e. for eq. (C.16) to hold). Thus the positivity of all eigenvalues of σ is a necessary condition for eq. (C.16). In addition in [173] it was shown that for a system comprised of two qubits or of one qubit and one qutrit the condition is even sufficient. Eventually, we use $\mathcal{T}_p$ which is the smallest eigenvalue of the partially transposed density matrix ρ to verify entanglement or inseparability. If $\mathcal{T}_p$ is negative the two quantum systems are inseparable or entangled.

Concurrence In contrast to the partial transpose method the concurrence not only proves entanglement but it also is a measure of the amount of entanglement [174, 175]. It ranges monotonically from 0 for no entanglement to 1 for full entanglement like in a Bell state. Its advantage over other entanglement measures is its analytic expression rather than being the result of a search for a minimum over many possible decompositions of the density matrix ρ [174, 175]. For a mixed state with density matrix ρ the concurrence is defined as

$$\mathcal{C} = \max(0, \lambda_1 - \lambda_2 - \lambda_3 - \lambda_4) \tag{C.19}$$

where the λ_i are the eigenvalues in decreasing order of

$$R = \sqrt{\sqrt{\rho}\tilde{\rho}\sqrt{\rho}} \tag{C.20}$$

with the spin flipped density matrix

$$\tilde{\rho} = (\sigma_y \otimes \sigma_y)\rho^*(\sigma_y \otimes \sigma_y) \ . \tag{C.21}$$

In eq. (C.21) the density matrices are given in the basis $|11\rangle$, $|10\rangle$, $|01\rangle$, $|00\rangle$ and ρ^* is the complex conjugate of ρ.

C.5. Quantum metrology

This work demonstrates the applicability of a single NV center as a qubit and as part of a quantum register comprised of other single NV centers and proximal nuclear spins for quantum metrology. All this can be achieved at room temperature because of the unique features of diamond, due to the optical addressability of single centers and due to the possibility to initialize, manipulate and readout a single qubit. As this qubit is an electron spin, however, it is susceptible to external magnetic fields. Thus the NV can act as a single, highly confined and well controllable magnetic field sensor [66, 65, 200] with the potential ability to sense even single nuclear spins within a few nanometers under ambient conditions. In essence, the qubit turns into a quantum sensor.

Basically, magnetic fields lead to a spin energy level splitting that can be monitored. Due to the build in magnetic field of $D_{gs} = 2.87\,\mathrm{GHz}$ because of the ZFS the NV center is even a vector magnetometer. The NV center spin comprises of two electron spins with effective spin $S = 1$, which leads to a g-factor of 4 instead of 2 that can be used for sensing. There are two main ways to sense magnetic fields. On the one hand there is the Ramsey method (see section C.3.1) which is sensitive to the total magnetic field at the position of the NV center [200, 56]. Hence, any change of the external field will be monitored but also will lead to decoherence and thus a shortening of the available field sensing time T_2^*. Please note, that the pulsed ODMR measurement scheme explained in section B.4 is comparable to the Ramsey method with regard to field sensitivity. On the other hand there are echo based field sensing methods (see section C.3.2) which are intrinsically insensitive to constant or slowly varying fields. Thus, they exhibit the longer field sensing time T_2 which is one of their advantages. A second advantage or feature is the possibility to selectively sense the fields of interest by switching these fields [66, 65]. Thus, this technique can be made sensitive to specific sub-ensembles of magnetic field sources (e.g. ac fields or electron and specific nuclear spins) or even electric field sources (e.g. elementary charges or ac fields). To achieve this selectivity, the respective sub-ensembles are switched in the appropriate phase with the echo sequence. Therefore, ac-fields have to have the right phase and frequency [66, 65, 56, 157, 75], spins have to be flipped at the right point in time (see section 6.4) or the source of interest is approximated and retracted from the NV with the right frequency and phase (e.g. in an AFM [65]). In addition to the selectivity regarding a specific species a magnetic field gradient can be used to achieve further increased spatial resolution [200].

The magnetic field sensitivity δB of these measurement methods is limited mainly by the photon shot noise and the signal contrast of the spin readout and by the limited sensing or coherence times [200]

$$\delta B \approx \frac{\pi\hbar}{g\mu_B C\sqrt{T}} \,. \tag{C.22}$$

Here, the g-factor depends on the used EPR transition (see above), $0 < C \leq 1$ accounts for the limited readout fidelity and T is the effective sensing time. For our current

measurement techniques this formula can be rewritten into

$$\delta B = \frac{2}{c\,\gamma\,T}\sqrt{\frac{T+T_{rp}}{N}} \tag{C.23}$$

where c is the signal contrast (usually $c \approx 0.3$), γ is the appropriate gyromagnetic ratio (e.g. $\gamma = 350.8\,\mathrm{GHz/T}$ for sensing transition $m_S = -1 \leftrightarrow +1$), T_{rp} is the time for readout and preparation and N is the number of photons per readout step.[3] If we set $N = 0.24$,[4] $\gamma = 350.8\,\mathrm{GHz/T}$ and $T_{rp} = 2\,\mu\mathrm{s}$ for optimum measurement conditions this yields a sensitivity of $\delta B_{T_2^*} = 5.1\ {}^{\mathrm{nT}}/\sqrt{\mathrm{Hz}}$ for $T = T_2^* = 60\,\mu\mathrm{s}$ [37] in the case of a Ramsey measurement and $\delta B_{T_2} = 0.91\ {}^{\mathrm{nT}}/\sqrt{\mathrm{Hz}}$ for $T = T_2 = 1.8\,\mathrm{ms}$ [56] in the case of an echo measurement.[5] For the measurement conditions in [56] an experimental value of $4\ {}^{\mathrm{nT}}/\sqrt{\mathrm{Hz}}$ has been achieved where formula (C.23) predicts $3.7\ {}^{\mathrm{nT}}/\sqrt{\mathrm{Hz}}$.

In this work we have demonstrated two methods to increase the signal to noise ratio of single spin readout (see section 5.2 and 5.3). Both methods correlate the final electron spin state with that of nuclear spin states (see figures 5.7b and 5.16). This would happen right after a unitary operation period (i.e. field sensing) and just before the readout part (i.e. also the nuclear spin contains information about the sensed field). Finally, information on the electron and on the nuclear spin can be extracted which increases the SNR and finally the sensitivity. If these new readout methods are applied to the field measurement protocols described above the values for N and T_{rp} are changed. For the technique described in section 5.2 the number of photons N is roughly tripled whereas T_{rp} rises from $\approx 2\,\mu\mathrm{s}$ to $\approx 20\,\mu\mathrm{s}$ in our experiment.[6] This yields sensitivities $\delta B_{T_2^*} = 3.3\ {}^{\mathrm{nT}}/\sqrt{\mathrm{Hz}}$ and $\delta B_{T_2} = 0.53\ {}^{\mathrm{nT}}/\sqrt{\mathrm{Hz}}$ for the above mentioned optimal conditions. The single shot readout sequence described in section 5.3 can improve the sensitivity much more because a much larger amount of photons is read out per phase accumulation step (e.g. $N = 150$ photons are read out in 5 ms). For the typical readout conditions in section 5.3 the spin lifetime is up to $T_1 = 80\,\mathrm{ms}$. If, however, the repetitive readout (compare [53]) is performed for $t \sim T_1$ one has to keep in mind that the overall contrast will reduce due to increasing nuclear spin flip probability according to

$$c(t) = c_0 \cdot T_1/t(1 - e^{-t/T_1}) \tag{C.24}$$

where usually $c_0 \approx 0.3$ (e.g. $c = 0.19$ for $t = 80\,\mathrm{ms}$). This leads to an optimum repetitive readout time t which together with the time to correlate the electron with the

[3] The number N includes all photons that are accumulated during the readout phase of the laser pulse (i.e. in the phase before the system is reset, compare section 2.2.6).

[4] This corresponds to a count rate of $8 \cdot 10^5$ photons/s and a readout interval of 300 ns.

[5] In the echo measurement the field is assumed to constant during the phase accumulation times and the sign is inverted at the EPR π-pulse. The sensitivity is related to the amplitude and not to the peak-to-peak field change.

[6] Stronger rf driving fields for the nuclear spin manipulation should be able to reduce T_{rp} down to $\approx 5\,\mu\mathrm{s}$.

nuclear spin state ($\approx 160\,\mu s$, compare sections 5.3.4 and 5.2) delivers T_{rp}. Finally, for the above mentioned optimal conditions we calculate the sensitivities $\delta B_{T_2} = 43\,\mathrm{pT}/\sqrt{\mathrm{Hz}}$ for $t = 12\,\mathrm{ms}$ and $\delta B_{T_2^*} = 1.2\ \mathrm{nT}/\sqrt{\mathrm{Hz}}$ for $t = 4\,\mathrm{ms}$. Especially, in the case of the long echo measurement time the repetitive readout pays off. By decreasing δB by a factor of ≈ 20 the measurement time can be reduced ≈ 400 times for the same accuracy. A measurement time of 1 s would yield a noise floor comparable to the field of a single ^{13}C nuclear spin with a separation of 25 nm (see appendix A).

The readout enhancement techniques which utilize the nitrogen nuclear spin can also be employed to ensemble based NV magnetic field sensors because the ^{14}N nuclear spin is present in almost every NV center which is not the case for ^{13}C nuclei. In the ensemble case, however, the nuclear spins cannot be initialized by a projective measurement but they need to be initialized by methods mentioned in section 3.2.

The previous techniques improve the magnetic field sensitivity of a single NV center. In some cases where high spatial resolution is required it might be inevitable to use a single one. If, however, the spatial resolution can be slightly lower one can use multiple NV centers close to each other. In that case entanglement of these centers can again boost the sensitivity in that the effective g-factor of the entangled state increases. However, a much faster dephasing of the entangled state could spoil the sensitivity.

All afore mentioned techniques for enhanced readout also apply for electric field sensing [75].

D. Hidden Markov Model

A Hidden Markov Model analysis allows gaining insight into the hidden intrinsic states of a system by analyzing the system response to an external stimulus. While the response of the system depends on the system state it is not sufficient to determine the system state from a single response because different states can have identical responses. In that sense the intrinsic states are hidden. However, with statistics of the responses individual states can be discriminated and in addition transition rates from one state into others can be deduced.

One example for this model assumes two dices where one is fair and the other has some unequal probabilities to show the results $1 \ldots 6$ [184]. A player is given one of these dices but he cannot distinguish it from the other. By throwing the dice once he cannot tell if it is the fair or unfair one. But he can accomplish this by analyzing its responses to many throws. This yields the probability distribution of results or the emission function of that dice. In the terminology of [184] each state (dice) can emit a number of symbols $(1 \ldots 6)$ and the probability distribution of that state to emit the specific symbols is the emission function. If the dice of the player is exchanged unnoticed it should be still possible for him to notice the change of the corresponding emission functions and therefore to determine the dice. This, however, is only possible if enough responses (i.e. throws of the dice) can be acquired before the dice is exchanged again.

With the HMM one can analyze a sequence $y(t)$ of responses or symbols k and will try to find the emission function $b_i(k)$ of each state i, the transition rates A_{ij} between the states i and j and finally the most likely sequence $s(t)$ of states according to the sequence of responses $y(t)$. The HMM makes two basic assumptions. First, the emission function of each state depends only on that present state. Second, the transition probability from one state to another depends only on the former one and not on the past. The algorithm needs the number of states i as an input. In addition, a proper initialization of the emission functions $b_i(k)$ and the transition matrix A_{ij} will allow the algorithm to converge faster.

In [183] it was shown how HMM can be applied to distinguish hidden states of a biological protein in action by analyzing its fluorescence response to laser excitation via fluorescence resonance energy transfer (FRET). A HMM analysis can deliver more reliable information on the protein state than conventional strategies which are the investigation of a time trace like D.1b "by eye" or using a threshold algorithm [201]. Especially, in the "by eye" method in particular short dwell times in one state are missed and the result usually differs from one researcher to another. The threshold method is of course more reproducible but for very noise data it can also yield wrong

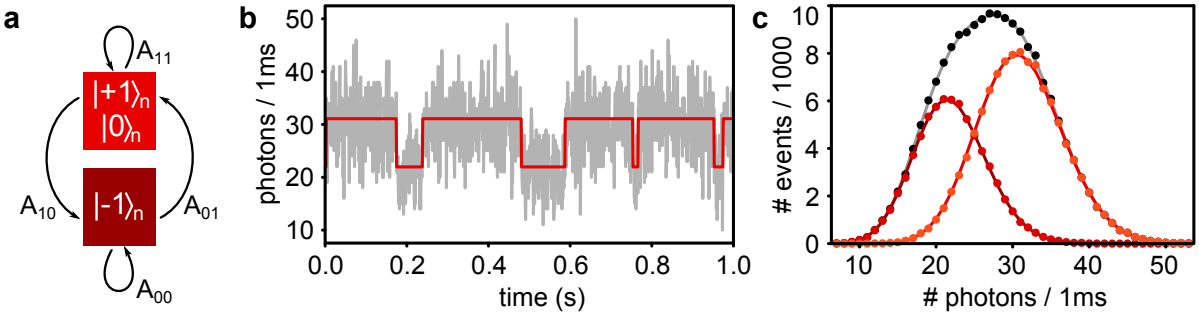

Figure D.1.: Hidden Markov Model. **a,** Illustration of the two state system as input for the HMM. The transition rates are symbolized as arrows and the color coded emission functions are plotted in panel c. **b,** Partial fluorescence time trace or sequence of responses of the system (gray curve). It shows the number of fluorescence photons per millisecond for a period of 1 s. The red curve is the most likely sequence of states according to the HMM analysis. **c,** The black dots represent the fluorescence photon counting histogram of the time trace and the red lines are fits of two Poisson distributions to that histogram (the gray curve is the sum of the two red curves). The left Poissonian is proportional to initial $b_0(k)$ whereas the right one is proportional to initial $b_1(k)$. The red dots represent the two final emission functions $b_i(k)$ for the two states of the system as retrieved by the HMM analysis (i.e. the red curves are no fits to the red dots but initial guesses).

results. Especially, in biology researchers are interested in the transition rates between the states of the system. As the HMM method directly adjusts these transition rates to model the data it is particularly useful in these cases. For example, this allows revealing a rotation direction of a rotating biological molecule with a high confidence level [183] and by adjusting the number of participating states the most likely number can be found. The HMM applied in this work is based on [184, 183].

Here, we have applied HMM analysis to tell apart nuclear spin states of the ^{14}N isotope (see section 5.3) and to find the transition rates between these states. More precisely we distinguish the state $i = 0$ associated with nuclear spin projection $m_I = -1$ from the state $i = 1$ which comprises of $m_I = 0$ and $+1$ (i.e. the number of states for the HMM is 2, see figure D.1a). The two different states are associated with different average fluorescence levels. However, one response to an external stimulus (i.e. one nuclear spin state readout step) delivers only several tens of photons (k, number of photons) and shot noise in this case is comparable to the signal (i.e. the difference of the average fluorescence levels). Thus, the photon counting histograms of each spin state (i.e. the emission functions) greatly overlap (see figure D.1c). As the fluorescence level depends indeed only on the present state of the nuclear spin and the transition between states usually also depends only on the present state the HMM seems to be an ideal analysis tool.

In the following, we show an example evaluation of a fluorescence time trace $y(t)$ with a time bin of 1 ms (i.e. a sequence of responses where each response corresponds to the number of fluorescence photons within 1 ms, see figure D.1b). To estimate the initial

emission functions $b_i(k)$ of the two spin states we fit the histogram of the complete time trace with two Poisson distributions (see figure D.1c). Apparently the fits (red curves) in figure D.1c are not normalized. The initial $b_i(k)$ are the normalized fit functions (i.e. $\sum_k b_i(k) = 1$). The transition matrix A_{ij} contains the transition probability of the spin from state i to state j during one step (see figure D.1a). If the duration Δt of one step is much shorter than the average life time T_1^i of state i ($\Delta t = 1\text{ms} \ll T_1^0 \approx 80\text{ms}$ in our case) the values A_{ii} can be calculated as

$$A_{ii} = e^{-\Delta t/T_1^i} \tag{D.1}$$

while all entries have to suffice condition $\sum_j A_{ij} = 1$. Now that we have obtained the number of states, the initial emission functions of each state and the initial transition matrix we calculate the probability $P_i(t)$ (eq. (D.2)) for the spin to be in state i at time t given the *whole* data set $y(t)$ [184].

$$P_i(t) = \frac{\alpha_i(t)\beta_i(t)}{\mathcal{L}(t)} \tag{D.2}$$

$$\mathcal{L}(t) = \sum_i \alpha_i(t)\beta_i(t) \tag{D.3}$$

$$\alpha_j(t + \Delta t) = \sum_i \alpha_i(t) A_{ij} b_j(y(t + \Delta t)) \tag{D.4}$$

$$\beta_i(t - \Delta t) = \sum_j A_{ij} b_j(y(t)) \beta_j(t) \tag{D.5}$$

The probability $P_i(t)$ is calculated from the so called forward and backward estimates $\alpha_i(t)$ and $\beta_i(t)$ respectively which are obtained recursively (eqs. (D.4), (D.5)). Forward and backward means that $\alpha_i(t)$ and $\beta_i(t)$ yield the unnormalized probabilities of the part of the data before and after time t if the state at t is i. The value $\mathcal{L}$ is the Likelihood of the data given the parameters which we have provided.[1] Finally, to recursively calculate $\alpha_i(t)$ and $\beta_i(t)$ we need to know their initial values which are

$$\alpha_i(0) = b_i(y(0)) \tag{D.6}$$

$$\beta_i(t_{\text{end}}) = 1\ . \tag{D.7}$$

Eventually, the initially provided parameters for the transition matrix A_{ij} and the emission functions $b_i(k)$ can be re-estimated using the so called Baum-Welch algorithm which increases the Likelihood $\mathcal{L}$ [184],

$$A_{ij}^{\text{new}} = \frac{\sum_t \alpha_i(t) A_{ij} b_j(y(t + \Delta t)) \beta_j(t + \Delta t)}{\sum_t \alpha_i(t)\beta_i(t)} \tag{D.8}$$

$$b_i^{\text{new}}(k) = \frac{\sum_t \delta(y(t), k)\alpha_i(t)\beta_i(t)}{\sum_t \alpha_i(t)\beta_i(t)} \tag{D.9}$$

[1] It can be shown that $\mathcal{L}(t)$ is in fact time independent. Therefore, we omit (t).

where $\delta(y, k)$ is the Kronecker-delta. It can be shown that repeated applications of the HMM analysis with subsequent re-estimation of the parameters A_{ij} and $b_i(k)$ increases the overall Likelihood $\mathcal{L}$ [184]. In fact, any not to strange initialization of the parameters for the HMM will eventually lead to the same result. The trajectory of the most likely states $s(t)$ is simply the sequence of the most likely states at each time t. Hence, $P_{s(t)}(t) = \max\{P_i(t)\}$. The red curve in figure D.1b shows the average fluorescence level of the corresponding most likely state according to the emission function.

For peculiarities in programming the HMM we would like to refer to [184].

Acknowledgements

At this stage it is time to thank all the people who made my work possible in the first place and contributed to it in one way or the other.

First of all, I would like to thank Prof. Jörg Wrachtrup for giving me the opportunity of doing my PhD thesis at his institute together with all the positive experiences I gained and for the overall support. My special thanks go to my supervisor and mentor Prof. Fedor Jelezko for all the time he spend giving useful and encouraging advice, helping set up experiments of any kind and giving inspiring ideas. Furthermore, I would like to thank Prof. Dr. Tilman Pfau for taking the time to give the second referee report about my thesis and Prof. Dr. Hans-Rainer Trebin for chairing the final exam.

In addition, I would like to thank Torsten Gaebel for sharing all his knowledge about diamond, color centers in it and the NV center in particular as well as for explaining and teaching every detail of his experimental setup which I finally "inherited". I also want to thank Prof. Philippe Tamarat for explaining me the peculiarities of NV centers at cryogenic temperatures and how they are investigated. Furthermore, I would like to thank Prof. Lilian Childress for sharing her experimental and theoretical knowledge about NV centers and their interaction with nuclear spins. Thanks a lot also to Prof. Phil Hemmer — a frequent and very welcome guest in our institute — because of his great experimental and technical expertise and his great ideas.

All experiments and findings of this work are the result of collaborations with many partners; and I want to thank all of them very much for their support. First of all there is Prof. Norikazu Mizuochi with whom we conducted all the experiments with ^{13}C nuclear spins which finally lead to two wonderful publications. Next, there is Florian Rempp who also participated in the former work and who contributed theoretical insight into many other projects of this thesis. Thanks also to Gopi Balasubramanian for his collaboration in many experiments like the excited state studies and for his insight in magnetometry. The same goes to Roman Kolesov who could give useful advice in every situation and who is always enthusiastic in supporting experiments and who was helping us many times to set up new devices. Specifically, Roman was able to locate a nicely coupled pair of NV centers which appeared to be much less likely than we initially expected. My thanks go also to Boris Naydenov for sharing his expertise in EPR and NMR and for supporting our experiments by providing the proper implanted NV diamonds. At the same time I want to thank Jan Meijer who helped us to implant thousands of NV centers by providing access to the RUBION ion beam facility and planning and performing the implantation. I also want to thank Vincent Jacques for kicking our asses to not let good measurement results rot in the lab books but to write nice papers in "decent"

journals. With Vincent we had a fruitful collaboration regarding the excited state of the NV center at cryogenic and ambient conditions as well as with the dynamic nuclear spin polarization (DNP) experiments. In addition, I want to thank Petr Siyushev for his expertise on low temperature NV studies especially regarding the NV level structure and the NV pair. Thanks go also to Bernhard Grotz for our collaboration regarding the sensing of diamond surface spins. Finally, I would like to introduce a very successful lab-combo which includes Johannes Beck and Matthias Steiner. Together we were in a kind of gold rush period of NV experiments which still has some legacy today. We have performed the experiments that utilize the nitrogen nuclear spin (e.g. for enhanced readout and QND measurement) and the coupling of two NV centers just to name a few. I am very grateful for this collaboration. Last but not least all experiments are conducted in diamond whose quality and quantity has grown over the years which is the merit of Daniel Twitchen and Matthew Markham from the company element six and as well of Prof. Junichi Isoya. Their diamond samples made many of the experiments possible in the first place which is why we are particularly grateful for their contribution.

Eventually, I have had many inspiring discussions with many experts in the field of diamond and NV centers as well as other important topics. I want to thank Prof. Neil Manson — one of the pioneers regarding NV centers in diamond — for fruitful discussions. The same goes to Lachlan Rogers who gave us insight in the excited and metastable state level structure. In addition, I am thankful to Adam Gali for sharing his expertise on the *ab initio* calculation of the NV electronic and spin configuration. Furthermore, I would like to thank Nawid Zarrabi for adapting his software for the HMM analysis to our nuclear spin data and for introducing us to the theory of HMM. My thanks go also to Florian Dolde for the design and fabrication of microwave coplanar waveguide structures, to Gerald Waldherr and Friedemann Reinhard for fruitful discussions, to Helmut Fedder for his expertise in FPGA programming, to Prof. Gerd Denninger for providing us with a lot of useful microwave equipment and to Robert Fisher and Thomas Schulte-Herbrüggen for teaching us the concept of robust pulses and its application in our spin system. Additionally, I want to thank Stephan Hirschmann for support regarding IT and chemistry related issues, Andrea Zappe for her expertise in biochemistry and Ms. Schettler, Ms. Unger and Ms. Faletar for their support when it comes to organizing non-scientific issues. Finally, the greatest part of our experimental setup might just fall apart without the experience of Mr. Kamella and his crew from the mechanical workshop whose expertise we appreciate very much.

After all, life at the institute would have been less amusing without all the current and less current members of the institute who participated — in addition to science — in lively discussions at the coffee corner, who taught me lessons at the kicker table and on the soccer ground or with whom we had beautiful extra-university events. Summarizing, at this stage I want to thank Carsten Tietz, Michael Börsch, Sebastian Schuler, Andrew Aird, Christoffer Wittman, Nawid Zarrabi, Monika Düser, Felix Neugart, Steffen Steinert, Aurélien Nicolet, Julia Tisler, Rolf Reuter, Karin Seyfert, Thomas Wolf,

Merle Becker, Torsten Rendler and all members of the institute.[2]

At this stage my thanks go to those that have proof-read my thesis or at least parts of it. Therefore, I want to thank Prof. Fedor Jelezko, Johannes Beck, Boris Naydenov and Nawid Zarrabi.

In the very end I would like to thank my family. My special thanks go to my beloved wife Antje Tönnies for her support and her patience during my thesis and also for one or the other sacrifice. Next I want to thank my son Nils for the most beautiful distraction from writing my thesis. I also want to thank my parents and grandparents for their emotional as well as financial support of my whole academic career so far. Last but not least I am very thankful for the kind support of my parents in law who have given me a second home and who provide my wife and me with some extra time by being loving grandparents for our son.

[2] This includes of course many of the already mentioned persons above.

Bibliography

[1] R. P. Feynman. *Simulating physics with computers*. International Journal of Theoretical Physics **21**, 467 (1981).
URL http://dx.doi.org/10.1007/BF02650179

[2] D. Deutsch. *Quantum Theory, the Church-Turing Principle and the Universal Quantum Computer*. Proceedings of the Royal Society A: Mathematical, Physical and Engineering Science **400**(1818), 97–117 (1985).
URL http://dx.doi.org/10.1098/rspa.1985.0070

[3] D. Deutsch and R. Jozsa. *Rapid Solution of Problems by Quantum Computation*. Proceedings of the Royal Society A: Mathematical, Physical and Engineering Science **439**(1907), 553–558 (1992).
URL http://dx.doi.org/10.1098/rspa.1992.0167

[4] P. W. Shor. *Polynomial-Time Algorithms for Prime Factorization and Discrete Logarithms on a Quantum Computer*. arXiv:quant-ph/9508027v2 (January 1996).
URL http://arxiv.org/abs/quant-ph/9508027v2

[5] L. K. Grover. *A fast quantum mechanical algorithm for database search*. arXiv:quant-ph/9605043v3 (November 1996).
URL http://arxiv.org/abs/quant-ph/9605043v3

[6] C. H. Bennet and G. Brassard. *Quantum Cryptography: Public key distribution and coin tossing*. Proceedings of the IEEE International Conference on Computers, Systems, and Signal Processing page 175 (December 1984).
URL http://www.research.ibm.com/people/b/bennetc/bennettc198469790513.pdf

[7] I. L. Chuang and Y. Yamamoto. *Simple Quantum Computer*. Physical Review A **52**(5), 3489–3496 (1995).
URL http://dx.doi.org/10.1103/PhysRevA.52.3489

[8] L. M. K. Vandersypen, M. Steffen, G. Breyta, C. S. Yannoni, M. H. Sherwood, and I. L. Chuang. *Experimental realization of Shor's quantum factoring algorithm using nuclear magnetic resonance*. Nature **414**(6866), 883–887 (2001).
URL http://dx.doi.org/10.1038/414883a

[9] W. S. Warren. *The Usefulness of NMR Quantum Computing*. Science **277**(5332), 1688–1690 (1997).
URL http://dx.doi.org/10.1126/science.277.5332.1688

[10] E. Knill, R. Laflamme, and G. J. Milburn. *A scheme for efficient quantum computation with linear optics*. Nature **409**(6816), 46–52 (January 2001). ISSN 0028-0836.
URL http://dx.doi.org/10.1038/35051009

[11] J. L. O'Brien. *Optical quantum computing*. Science **318**(5856), 1567–1570 (2007).
URL http://dx.doi.org/10.1126/science.1142892

[12] R. Blatt and D. Wineland. *Entangled states of trapped atomic ions*. Nature **453**(7198), 1008–1015 (June 2008). ISSN 0028-0836.
URL http://dx.doi.org/10.1038/nature07125

[13] I. Bloch. *Quantum coherence and entanglement with ultracold atoms in optical lattices*. Nature **453**(7198), 1016–1022 (June 2008). ISSN 0028-0836.
URL http://dx.doi.org/10.1038/nature07126

[14] J. Wrachtrup, C. von Borczyskowski, J. Bernard, M. Orritt, and R. Brown. *Optical detection of magnetic resonance in a single molecule*. Nature **363**(6426), 244–245 (May 1993).
URL http://dx.doi.org/10.1038/363244a0

[15] R. Hanson and D. D. Awschalom. *Coherent manipulation of single spins in semiconductors*. Nature **453**(7198), 1043–1049 (June 2008). ISSN 0028-0836.
URL http://dx.doi.org/10.1038/nature07129

[16] J. Clarke and F. K. Wilhelm. *Superconducting quantum bits*. Nature **453**(7198), 1031–1042 (June 2008). ISSN 0028-0836.
URL http://dx.doi.org/10.1038/nature07128

[17] T. J. Kippenberg and K. J. Vahala. *Cavity Optomechanics: Back-Action at the Mesoscale*. Science **321**(5893), 1172–1176 (2008).
URL http://dx.doi.org/10.1126/science.1156032

[18] R. Kolesov, B. Grotz, G. Balasubramanian, R. J. Stöhr, A. A. L. Nicolet, P. R. Hemmer, F. Jelezko, and J. Wrachtrup. *Wave-particle duality of single surface plasmon polaritons*. Nature Physics **5**(7), 470–474 (July 2009). ISSN 1745-2473.
URL http://dx.doi.org/10.1038/nphys1278

[19] G. Davies and M. F. Hamer. *Optical studies of the 1.945 eV Vibronic Band in Diamond*. Proceedings of the Royal Society A: Mathematical, Physical and Engineering Science **348**(1653), 285–298 (February 1976).
URL http://dx.doi.org/10.1098/rspa.1976.0039

[20] A. Gruber, A. Dräbenstedt, C. Tietz, L. Fleury, J. Wrachtrup, and C. vonBorczyskowski. *Scanning confocal optical microscopy and magnetic resonance on single defect centers*. Science **276**(5321), 2012–2014 (1997).
URL http://dx.doi.org/10.1126/science.276.5321.2012

[21] C. Kurtsiefer, S. Mayer, P. Zarda, and H. Weinfurter. *Stable solid-state source of single photons*. Physical Review Letters **85**(2), 290–293 (2000).
URL http://dx.doi.org/10.1103/PhysRevLett.85.290

[22] A. Beveratos, R. Brouri, T. Gacoin, J.-P. Poizat, and P. Grangier. *Nonclassical radiation from diamond nanocrystals*. Physical Review A **64**, 061802 (Nov 2001).
URL http://dx.doi.org/10.1103/PhysRevA.64.061802

[23] A. Beveratos, R. Brouri, J.-P. Poizat, and P. Grangier. *Bunching and Antibunching from Single NV Color Centers in Diamond*. In *Quantum Communication, Computing, and Measurement 3*, pages 261–267. Springer US (2002). ISBN 978-0-306-47114-8.
URL http://dx.doi.org/10.1007/0-306-47114-0_42

[24] A. Beveratos, R. Brouri, T. Gacoin, A. Villing, J.-P. Poizat, and P. Grangier. *Single Photon Quantum Cryptography*. Physical Review Letters **89**, 187901 (Oct 2002).
URL http://dx.doi.org/10.1103/PhysRevLett.89.187901

[25] F. Jelezko, I. Popa, A. Gruber, C. Tietz, J. Wrachtrup, A. Nizovtsev, and S. Kilin. *Single spin states in a defect center resolved by optical spectroscopy*. Applied Physics Letters **81**(12), 2160–2162 (2002).
URL http://dx.doi.org/10.1063/1.1507838

[26] F. Jelezko, T. Gaebel, I. Popa, A. Gruber, and J. Wrachtrup. *Observation of coherent oscillations in a single electron spin*. Physical Review Letters **92**(7), 076401 (2004).
URL http://dx.doi.org/10.1103/PhysRevLett.92.076401

[27] F. Jelezko, T. Gaebel, I. Popa, M. Domhan, A. Gruber, and J. Wrachtrup. *Observation of coherent oscillation of a single nuclear spin and realization of a two-qubit conditional quantum gate*. Physical Review Letters **93**(13), 130501 (2004).
URL http://dx.doi.org/10.1103/PhysRevLett.93.130501

[28] R. J. Epstein, F. M. Mendoza, Y. K. Kato, and D. D. Awschalom. *Anisotropic interactions of a single spin and dark-spin spectroscopy in diamond*. Nature Physics **1**(2), 94–98 (2005).
URL http://dx.doi.org/10.1038/nphys141

[29] T. Gaebel, M. Domhan, I. Popa, C. Wittmann, P. Neumann, F. Jelezko, J. R. Rabeau, N. Stavrias, A. D. Greentree, S. Prawer, J. Meijer, J. Twamley, P. R. Hemmer, and J. Wrachtrup. *Room-temperature coherent coupling of single spins in diamond*. Nature Physics **2**(6), 408–413 (2006).
URL http://dx.doi.org/10.1038/nphys318

[30] R. Hanson, F. M. Mendoza, R. J. Epstein, and D. D. Awschalom. *Polarization and readout of coupled single spins in diamond*. Physical Review Letters **97**(8), 087601 (2006).
URL http://dx.doi.org/10.1103/PhysRevLett.97.087601

[31] L. Childress, M. V. G. Dutt, J. M. Taylor, A. S. Zibrov, F. Jelezko, J. Wrachtrup, P. R. Hemmer, and M. D. Lukin. *Coherent dynamics of coupled electron and nuclear spin qubits in diamond*. Science **314**(5797), 281–285 (2006).
URL http://dx.doi.org/10.1126/science.1131871

[32] M. V. G. Dutt, L. Childress, L. Jiang, E. Togan, J. Maze, F. Jelezko, A. S. Zibrov, P. R. Hemmer, and M. D. Lukin. *Quantum register based on individual electronic and nuclear spin qubits in diamond*. Science **316**(5829), 1312–1316 (2007).
URL http://dx.doi.org/10.1126/science.1139831

[33] L. Jiang, M. V. G. Dutt, E. Togan, L. Childress, P. Cappellaro, J. M. Taylor, and M. D. Lukin. *Coherence of an Optically Illuminated Single Nuclear Spin Qubit*. Physical Review Letters **100**(7), 073001 (Feb 2008).
URL http://dx.doi.org/10.1103/PhysRevLett.100.073001

[34] J. Meijer, B. Burchard, M. Domhan, C. Wittmann, T. Gaebel, I. Popa, F. Jelezko, and J. Wrachtrup. *Generation of single color centers by focused nitrogen implantation*. Applied Physics Letters **87**(26), 261909 (dec 2005). ISSN 0003-6951.
URL http://dx.doi.org/10.1063/1.2103389

[35] J. R. Rabeau, P. Reichart, G. Tamanyan, D. N. Jamieson, S. Prawer, F. Jelezko, T. Gaebel, I. Popa, M. Domhan, and J. Wrachtrup. *Implantation of labelled single nitrogen vacancy centers in diamond using N-15*. Applied Physics Letters **88**(2), 023113 (2006).
URL http://dx.doi.org/10.1063/1.2158700

[36] P. Neumann, N. Mizuochi, F. Rempp, P. Hemmer, H. Watanabe, S. Yamasaki, V. Jacques, T. Gaebel, F. Jelezko, and J. Wrachtrup. *Multipartite entanglement among single spins in diamond*. Science **320**(5881), 1326–1329 (2008).
URL http://dx.doi.org/10.1126/science.1157233

[37] J. Beck. *Quantenregister in Diamant: Experimentelle Realisierung von Mehrspinverschränkung*. diploma thesis, Universität Stuttgart; 3. Physikalisches Institut

(March 2009). Language = English, English title = "Quantum registers in diamond", Call number [SIG] at library of Universität Stuttgart: Y 3487.
URL http://swb.bsz-bw.de/DB=2.201/PPNSET?PPN=330107909&INDEXSET=1

[38] P. Cappellaro, L. Jiang, J. S. Hodges, and M. D. Lukin. *Coherence and Control of Quantum Registers Based on Electronic Spin in a Nuclear Spin Bath*. Physical Review Letters **102**(21), 210502 (2009).
URL http://dx.doi.org/10.1103/PhysRevLett.102.210502

[39] H. Bluhm, S. Foletti, I. Neder, M. Rudner, D. Mahalu, V. Umansky, and A. Yacoby. *Dephasing time of GaAs electron-spin qubits coupled to a nuclear bath exceeding 200 μs*. Nature Physics **7**(2), 109–113 (February 2011). ISSN 1745-2473.
URL http://dx.doi.org/10.1038/nphys1856

[40] R. Hanson, V. V. Dobrovitski, A. E. Feiguin, O. Gywat, and D. D. Awschalom. *Coherent dynamics of a single spin interacting with an adjustable spin bath*. Science **320**(5874), 352–355 (2008).
URL http://dx.doi.org/10.1126/science.1155400

[41] S. Takahashi, R. Hanson, J. van Tol, M. S. Sherwin, and D. D. Awschalom. *Quenching Spin Decoherence in Diamond through Spin Bath Polarization*. Physical Review Letters **101**(4), 047601 (Jul 2008).
URL http://dx.doi.org/10.1103/PhysRevLett.101.047601

[42] N. Mizuochi, P. Neumann, F. Rempp, J. Beck, V. Jacques, P. Siyushev, K. Nakamura, D. J. Twitchen, H. Watanabe, S. Yamasaki, F. Jelezko, and J. Wrachtrup. *Coherence of single spins coupled to a nuclear spin bath of varying density*. Physical Review B **80**(4), 041201 (2009).
URL http://dx.doi.org/10.1103/PhysRevB.80.041201

[43] P. Neumann, R. Kolesov, B. Naydenov, J. Beck, F. Rempp, M. Steiner, V. Jacques, G. Balasubramanian, M. L. Markham, D. J. Twitchen, S. Pezzagna, J. Meijer, J. Twamley, F. Jelezko, and J. Wrachtrup. *Quantum register based on coupled electron spins in a room-temperature solid*. Nature Physics **6**(4), 249–253 (April 2010). ISSN 1745-2473.
URL http://dx.doi.org/10.1038/nphys1536

[44] E. Rittweger, K. Y. Han, S. E. Irvine, C. Eggeling, and S. W. Hell. *STED microscopy reveals crystal colour centres with nanometric resolution*. Nature Photonics **3**(3), 144–147 (2009).
URL http://dx.doi.org/10.1038/nphoton.2009.2

[45] E. Rittweger, D. Wildanger, and S. W. Hell. *Far-field fluorescence nanoscopy of diamond color centers by ground state depletion*. Europhysics Letters **86**(1), 14001

(2009).
URL http://dx.doi.org/10.1209/0295-5075/86/14001

[46] P. Neumann, R. Kolesov, V. Jacques, J. Beck, J. Tisler, A. Batalov, L. Rogers, N. B. Manson, G. Balasubramanian, F. Jelezko, and J. Wrachtrup. *Excited-state spectroscopy of single NV defects in diamond using optically detected magnetic resonance*. New Journal of Physics **11**, 013017 (2009).
URL http://dx.doi.org/10.1088/1367-2630/11/1/013017

[47] A. Batalov, V. Jacques, F. Kaiser, P. Siyushev, P. Neumann, L. J. Rogers, R. L. McMurtrie, N. B. Manson, F. Jelezko, and J. Wrachtrup. *Low Temperature Studies of the Excited-State Structure of Negatively Charged Nitrogen-Vacancy Color Centers in Diamond*. Physical Review Letters **102**(19), 195506 (2009).
URL http://dx.doi.org/10.1103/PhysRevLett.102.195506

[48] G. D. Fuchs, V. V. Dobrovitski, R. Hanson, A. Batra, C. D. Weis, T. Schenkel, and D. D. Awschalom. *Excited-state spectroscopy using single spin manipulation in diamond*. Physical Review Letters **101**(11), 117601 (2008).
URL http://dx.doi.org/10.1103/PhysRevLett.101.117601

[49] K.-M. C. Fu, C. Santori, P. E. Barclay, L. J. Rogers, N. B. Manson, and R. G. Beausoleil. *Observation of the Dynamic Jahn-Teller Effect in the Excited States of Nitrogen-Vacancy Centers in Diamond*. Physical Review Letters **103**(25), 256404 (Dec 2009).
URL http://dx.doi.org/10.1103/PhysRevLett.103.256404

[50] V. Jacques, P. Neumann, J. Beck, M. Markham, D. Twitchen, J. Meijer, F. Kaiser, G. Balasubramanian, F. Jelezko, and J. Wrachtrup. *Dynamic Polarization of Single Nuclear Spins by Optical Pumping of Nitrogen-Vacancy Color Centers in Diamond at Room Temperature*. Physical Review Letters **102**(5), 057403 (2009).
URL http://dx.doi.org/10.1103/PhysRevLett.102.057403

[51] M. Steiner, P. Neumann, J. Beck, F. Jelezko, and J. Wrachtrup. *Universal enhancement of the optical readout fidelity of single electron spins at nitrogen-vacancy centers in diamond*. Physical Review B **81**(3), 035205 (2010).
URL http://dx.doi.org/10.1103/PhysRevB.81.035205

[52] B. Smeltzer, J. McIntyre, and L. Childress. *Robust control of individual nuclear spins in diamond*. Physical Review A **80**, 050302 (Nov 2009).
URL http://dx.doi.org/10.1103/PhysRevA.80.050302

[53] L. Jiang, J. S. Hodges, J. R. Maze, P. Maurer, J. M. Taylor, D. G. Cory, P. R. Hemmer, R. L. Walsworth, A. Yacoby, A. S. Zibrov, and M. D. Lukin. *Repetitive Readout of a Single Electronic Spin via Quantum Logic with Nuclear Spin Ancillae*.

Science **326**, 267–271 (2009).
URL http://dx.doi.org/10.1126/science.1176496

[54] P. Neumann, J. Beck, M. Steiner, F. Rempp, H. Fedder, P. R. Hemmer, J. Wrachtrup, and F. Jelezko. *Single-Shot Readout of a Single Nuclear Spin*. Science **329**(5991), 542–544 (2010).
URL http://dx.doi.org/10.1126/science.1189075

[55] M. Steiner. *Towards Diamond-Based Quantum Computers*. diploma thesis, Universität Stuttgart, 3. Physikalisches Institut (October 2009). Call number [SIG] at library of Universität Stuttgart: Y 3522.
URL http://swb.bsz-bw.de/DB=2.201/PPNSET?PPN=329968653&INDEXSET=1

[56] G. Balasubramanian, P. Neumann, D. Twitchen, M. Markham, R. Kolesov, N. Mizuochi, J. Isoya, J. Achard, J. Beck, J. Tissler, V. Jacques, P. R. Hemmer, F. Jelezko, and J. Wrachtrup. *Ultralong spin coherence time in isotopically engineered diamond*. Nature Materials **8**(5), 383–387 (2009).
URL http://dx.doi.org/10.1038/nmat2420

[57] N. Zhao, J.-L. Hu, S.-W. Ho, J. T. K. Wan, and R. B. Liu. *Atomic-scale magnetometry of distant nuclear spin clusters via nitrogen-vacancy spin in diamond*. Nature Nanotechnology **6**(4), 242–246 (April 2011). ISSN 1748-3387.
URL http://dx.doi.org/10.1038/nnano.2011.22

[58] J. Meijer, S. Pezzagna, T. Vogel, B. Burchard, H. Bukow, I. Rangelow, Y. Sarov, H. Wiggers, I. Plümel, F. Jelezko, J. Wrachtrup, F. Schmidt-Kaler, W. Schnitzler, and K. Singer. *Towards the implanting of ions and positioning of nanoparticles with nm spatial resolution*. Applied Physics A: Materials Science & Processing **91**, 567–571 (2008). ISSN 0947-8396. 10.1007/s00339-008-4515-1.
URL http://dx.doi.org/10.1007/s00339-008-4515-1

[59] B. Naydenov, V. Richter, J. Beck, M. Steiner, P. Neumann, G. Balasubramanian, J. Achard, F. Jelezko, J. Wrachtrup, and R. Kalish. *Enhanced generation of single optically active spins in diamond by ion implantation*. Applied Physics Letters **96**(16), 163108 (2010). ISSN 00036951.
URL http://dx.doi.org/10.1063/1.3409221

[60] D. M. Toyli, C. D. Weis, G. D. Fuchs, T. Schenkel, and D. D. Awschalom. *Chip-scale nanofabrication of single spins and spin arrays in diamond*. Nano Letters **10**(8), 3168–3172 (Aug 2010).
URL http://dx.doi.org/10.1021/nl102066q

[61] W. Schnitzler, N. M. Linke, R. Fickler, J. Meijer, F. Schmidt-Kaler, and K. Singer. *Deterministic Ultracold Ion Source Targeting the Heisenberg Limit*. Physical Re-

view Letters **102**(7), 070501 (2009).
URL http://dx.doi.org/10.1103/PhysRevLett.102.070501

[62] M. S. Grinolds, P. Maletinsky, S. Hong, M. D. Lukin, R. L. Walsworth, and A. Yacoby. *Quantum control of proximal spins using nanoscale magnetic resonance imaging*. Nature Physics **7**(9), 687–692 (September 2011). ISSN 1745-2473.
URL http://dx.doi.org/10.1038/nphys1999

[63] K. Y. Han, S. K. Kim, C. Eggeling, and S. W. Hell. *Metastable Dark States Enable Ground State Depletion Microscopy of Nitrogen Vacancy Centers in Diamond with Diffraction-Unlimited Resolution*. Nano Letters **10**(8), 3199–3203 (2010).
URL http://dx.doi.org/10.1021/nl102156m

[64] P. C. Maurer, J. R. Maze, P. L. Stanwix, L. Jiang, A. V. Gorshkov, A. A. Zibrov, B. Harke, J. S. Hodges, A. S. Zibrov, A. Yacoby, D. Twitchen, S. W. Hell, R. L. Walsworth, and M. D. Lukin. *Far-field optical imaging and manipulation of individual spins with nanoscale resolution*. Nature Physics **6**(11), 912–918 (November 2010). ISSN 1745-2473.
URL http://dx.doi.org/10.1038/nphys1774

[65] G. Balasubramanian, I. Y. Chan, R. Kolesov, M. Al-Hmoud, J. Tisler, C. Shin, C. Kim, A. Wojcik, P. R. Hemmer, A. Krueger, T. Hanke, A. Leitenstorfer, R. Bratschitsch, F. Jelezko, and J. Wrachtrup. *Nanoscale imaging magnetometry with diamond spins under ambient conditions*. Nature **455**(7213), 648–651 (2008).
URL http://dx.doi.org/10.1038/nature07278

[66] J. R. Maze, P. L. Stanwix, J. S. Hodges, S. Hong, J. M. Taylor, P. Cappellaro, L. Jiang, M. V. G. Dutt, E. Togan, A. S. Zibrov, A. Yacoby, R. L. Walsworth, and M. D. Lukin. *Nanoscale magnetic sensing with an individual electronic spin in diamond*. Nature **455**(7213), 644–647 (2008).
URL http://dx.doi.org/10.1038/nature07279

[67] S. Steinert, F. Dolde, P. Neumann, A. Aird, B. Naydenov, G. Balasubramanian, F. Jelezko, and J. Wrachtrup. *High sensitivity magnetic imaging using an array of spins in diamond*. Review of Scientific Instruments **81**(4) (APR 2010). ISSN 0034-6748.
URL http://dx.doi.org/10.1063/1.3385689

[68] L. Childress, J. M. Taylor, A. S. Sorensen, and M. D. Lukin. *Fault-tolerant quantum communication based on solid-state photon emitters*. Physical Review Letters **96**(7), 070504 (2006).
URL http://dx.doi.org/10.1103/PhysRevLett.96.070504

[69] E. Togan, Y. Chu, A. S. Trifonov, L. Jiang, J. Maze, L. Childress, M. V. G. Dutt, A. S. Sorensen, P. R. Hemmer, A. S. Zibrov, and M. D. Lukin. *Quantum entanglement between an optical photon and a solid-state spin qubit*. Nature **466**(7307), 730–734 (August 2010). ISSN 0028-0836.
URL http://dx.doi.org/10.1038/nature09256

[70] Y. Kubo, F. R. Ong, P. Bertet, D. Vion, V. Jacques, D. Zheng, A. Dréau, J.-F. Roch, A. Auffeves, F. Jelezko, J. Wrachtrup, M. F. Barthe, P. Bergonzo, and D. Esteve. *Strong Coupling of a Spin Ensemble to a Superconducting Resonator*. Physical Review Letters **105**, 140502 (Sep 2010).
URL http://dx.doi.org/10.1103/PhysRevLett.105.140502

[71] R. Amsüss, C. Koller, T. Nöbauer, S. Putz, S. Rotter, K. Sandner, S. Schneider, M. Schramböck, G. Steinhauser, H. Ritsch, J. Schmiedmayer, and J. Majer. *Cavity QED with Magnetically Coupled Collective Spin States*. Physical Review Letters **107**, 060502 (Aug 2011).
URL http://dx.doi.org/10.1103/PhysRevLett.107.060502

[72] P. Rabl, S. J. Kolkowitz, F. H. L. Koppens, J. G. E. Harris, P. Zoller, and M. D. Lukin. *A quantum spin transducer based on nanoelectromechanical resonator arrays*. Nature Physics **6**(8), 602–608 (August 2010). ISSN 1745-2473.
URL http://dx.doi.org/10.1038/nphys1679

[73] V. M. Acosta, E. Bauch, M. P. Ledbetter, C. Santori, K.-M. C. Fu, P. E. Barclay, R. G. Beausoleil, H. Linget, J. F. Roch, F. Treussart, S. Chemerisov, W. Gawlik, and D. Budker. *Diamonds with a high density of nitrogen-vacancy centers for magnetometry applications*. Physical Review B **80**(11), 115202 (Sep 2009).
URL http://dx.doi.org/10.1103/PhysRevB.80.115202

[74] V. M. Acosta, A. Jarmola, E. Bauch, and D. Budker. *Optical properties of the nitrogen-vacancy singlet levels in diamond*. Physical Review B **82**(20), 201202 (Nov 2010).
URL http://dx.doi.org/10.1103/PhysRevB.82.201202

[75] F. Dolde, H. Fedder, M. W. Doherty, T. Nobauer, F. Rempp, G. Balasubramanian, T. Wolf, F. Reinhard, L. C. L. Hollenberg, F. Jelezko, and J. Wrachtrup. *Electric-field sensing using single diamond spins*. Nature Physics **7**(6), 459–463 (June 2011). ISSN 1745-2473.
URL http://dx.doi.org/10.1038/nphys1969

[76] T. D. Ladd, F. Jelezko, R. Laflamme, Y. Nakamura, C. Monroe, and J. L. O'Brien. *Quantum computers*. Nature **464**(7285), 45–53 (March 2010). ISSN 0028-0836.
URL http://dx.doi.org/10.1038/nature08812

[77] P. Hemmer and J. Wrachtrup. *Where Is My Quantum Computer?* Science **324**(5926), 473–474 (2009).
URL http://dx.doi.org/10.1126/science.1170912

[78] M. Stoneham. *Is a room-temperature, solid-state quantum computer mere fantasy?* Physics **2**, 34 (2009).
URL http://dx.doi.org/10.1103/Physics.2.34

[79] J. A. Jones, M. Mosca, and R. H. Hansen. *Implementation of a quantum search algorithm on a quantum computer.* Nature **393**(6683), 344–346 (May 1998). ISSN 0028-0836.
URL http://dx.doi.org/10.1038/30687

[80] I. L. Chuang, N. Gershenfeld, and M. Kubinec. *Experimental Implementation of Fast Quantum Searching.* Physical Review Letters **80**, 3408–3411 (Apr 1998).
URL http://dx.doi.org/10.1103/PhysRevLett.80.3408

[81] K.-A. Brickman, P. C. Haljan, P. J. Lee, M. Acton, L. Deslauriers, and C. Monroe. *Implementation of Grover's quantum search algorithm in a scalable system.* Physical Review A **72**, 050306 (Nov 2005).
URL http://dx.doi.org/10.1103/PhysRevA.72.050306

[82] D. P. DiVincenzo. *The Physical Implementation of Quantum Computation.* arXiv:quant-ph/0002077v3 (April 2000).
URL http://arxiv.org/abs/quant-ph/0002077v3

[83] R. Ursin, F. Tiefenbacher, T. Schmitt-Manderbach, H. Weier, T. Scheidl, M. Lindenthal, B. Blauensteiner, T. Jennewein, J. Perdigues, P. Trojek, B. Omer, M. Furst, M. Meyenburg, J. Rarity, Z. Sodnik, C. Barbieri, H. Weinfurter, and A. Zeilinger. *Entanglement-based quantum communication over 144 km.* Nature Physics **3**(7), 481–486 (July 2007). ISSN 1745-2473.
URL http://dx.doi.org/10.1038/nphys629

[84] D. Elser, T. Bartley, B. Heim, C. Wittmann, D. Sych, and G. Leuchs. *Feasibility of free space quantum key distribution with coherent polarization states.* New Journal of Physics **11**(4), 045014 (2009).
URL http://dx.doi.org/10.1088/1367-2630/11/4/045014

[85] O. Morsch and M. Oberthaler. *Dynamics of Bose-Einstein condensates in optical lattices.* Reviews of Modern Physics **78**, 179–215 (Feb 2006).
URL http://dx.doi.org/10.1103/RevModPhys.78.179

[86] E. Urban, T. A. Johnson, T. Henage, L. Isenhower, D. D. Yavuz, T. G. Walker, and M. Saffman. *Observation of Rydberg blockade between two atoms.* Nature

Physics **5**(2), 110–114 (February 2009). ISSN 1745-2473.
URL http://dx.doi.org/10.1038/nphys1178

[87] M. Mehring, J. Mende, and W. Scherer. *Entanglement between an electron and a nuclear spin 1/2*. Physical Review Letters **90**(15), 153001 (2003).
URL http://dx.doi.org/10.1103/PhysRevLett.90.153001

[88] R. Hanson, L. P. Kouwenhoven, J. R. Petta, S. Tarucha, and L. M. K. Vandersypen. *Spins in few-electron quantum dots*. Reviews of Modern Physics **79**, 1217–1265 (Oct 2007).
URL http://dx.doi.org/10.1103/RevModPhys.79.1217

[89] C. B. Simmons, M. Thalakulam, B. M. Rosemeyer, B. J. Van Bael, E. K. Sackmann, D. E. Savage, M. G. Lagally, R. Joynt, M. Friesen, S. N. Coppersmith, and M. A. Eriksson. *Charge Sensing and Controllable Tunnel Coupling in a Si/SiGe Double Quantum Dot*. Nano Letters **9**(9), 3234–3238 (2009).
URL http://dx.doi.org/10.1021/nl9014974

[90] B. E. Kane. *A silicon-based nuclear spin quantum computer*. Nature **393**(6681), 133–137 (May 1998). ISSN 0028-0836.
URL http://dx.doi.org/10.1038/30156

[91] A. Wallraff, D. I. Schuster, A. Blais, L. Frunzio, R.-S. Huang, J. Majer, S. Kumar, S. M. Girvin, and R. J. Schoelkopf. *Strong coupling of a single photon to a superconducting qubit using circuit quantum electrodynamics*. Nature **431**(7005), 162–167 (September 2004). ISSN 0028-0836.
URL http://dx.doi.org/10.1038/nature02851

[92] P. Tamarat, T. Gaebel, J. R. Rabeau, M. Khan, A. D. Greentree, H. Wilson, L. C. L. Hollenberg, S. Prawer, P. Hemmer, F. Jelezko, and J. Wrachtrup. *Stark Shift Control of Single Optical Centers in Diamond*. Physical Review Letters **97**(8), 083002 (Aug 2006).
URL http://dx.doi.org/10.1103/PhysRevLett.97.083002

[93] B. L. Higgins, D. W. Berry, S. D. Bartlett, H. M. Wiseman, and G. J. Pryde. *Entanglement-free heisenberg-limited phase estimation*. Nature **450**(7168), 393 (2007).
URL http://dx.doi.org/10.1038/nature06257

[94] R. S. Said, D. W. Berry, and J. Twamley. *Nanoscale magnetometry using a single-spin system in diamond*. Physical Review B **83**, 125410 (Mar 2011).
URL http://dx.doi.org/10.1103/PhysRevB.83.125410

[95] F. Shi, X. Rong, N. Xu, Y. Wang, J. Wu, B. Chong, X. Peng, J. Kniepert, R.-S. Schoenfeld, W. Harneit, M. Feng, and J. Du. *Room-Temperature Implementation*

of the Deutsch-Jozsa Algorithm with a Single Electronic Spin in Diamond. Physical Review Letters **105**, 040504 (Jul 2010).
URL http://dx.doi.org/10.1103/PhysRevLett.105.040504

[96] L. Childress and J. McIntyre. *Multifrequency spin resonance in diamond*. Physical Review A **82**(3), 033839 (Sep 2010).
URL http://dx.doi.org/10.1103/PhysRevA.82.033839

[97] J. Wrachtrup. *Quantum physics: Schrödinger's cat is still alive*. Nature Physics **5**(4), 248–249 (April 2009).
URL http://dx.doi.org/10.1038/nphys1245

[98] J. Isberg, J. Hammersberg, E. Johansson, T. Wikström, D. J. Twitchen, A. J. Whitehead, S. E. Coe, and G. A. Scarsbrook. *High Carrier Mobility in Single-Crystal Plasma-Deposited Diamond*. Science **297**(5587), 1670–1672 (2002).
URL http://dx.doi.org/10.1126/science.1074374

[99] N. Mizuochi, J. Isoya, J. Niitsuma, T. Sekiguchi, H. Watanabe, H. Kato, T. Makino, H. Okushi, and S. Yamasaki. *Isotope effects between hydrogen and deuterium microwave plasmas on chemical vapor deposition homoepitaxial diamond growth*. Journal of Applied Physics **101**(10), 103501 (2007).
URL http://dx.doi.org/10.1063/1.2727380

[100] D. Twitchen. Private communication.

[101] J. Isoya. Private communication.

[102] M. Markham. Private communication.

[103] J. Isoya, H. Kanda, Y. Uchida, S. C. Lawson, S. Yamasaki, H. Itoh, and Y. Morita. *EPR identification of the negatively charged vacancy in diamond*. Physical Review B **45**, 1436–1439 (Jan 1992).
URL http://dx.doi.org/10.1103/PhysRevB.45.1436

[104] H. B. Dyer, F. A. Raal, L. Du Preez, and J. H. N. Loubser. *Optical absorption features associated with paramagnetic nitrogen in diamond*. Philosophical Magazine **11**(112), 763–774 (1965).
URL http://dx.doi.org/10.1080/14786436508230081

[105] J. Walker. *Optical absorption and luminescence in diamond*. Reports on Progress in Physics **42**(10), 1605 (1979).
URL http://dx.doi.org/10.1088/0034-4885/42/10/001

[106] J. H. N. Loubser and J. A. van Wyk. *Optical spin-polarization in a triplet state in irradiated and annealed Typ Ib diamonds*. Diamond Research **11**, 4–8 (1977).

[107] J. H. N. Loubser and J. A. van Wyk. *Electron spin resonance in the study of diamond*. Reports on Progress in Physics **41**(8), 1201 (1978).
URL http://dx.doi.org/10.1088/0034-4885/41/8/002

[108] N. Reddy, N. Manson, and E. Krausz. *Two-laser spectral hole burning in a colour centre in diamond*. Journal of Luminescence **38**(1-6), 46–47 (1987). ISSN 0022-2313.
URL http://dx.doi.org/10.1016/0022-2313(87)90057-3

[109] J.-P. Boudou, P. A. Curmi, F. Jelezko, J. Wrachtrup, P. Aubert, M. Sennour, G. Balasubramanian, R. Reuter, A. Thorel, and E. Gaffet. *High yield fabrication of fluorescent nanodiamonds*. Nanotechnology **20**(23), 235602 (2009).
URL http://dx.doi.org/10.1088/0957-4484/20/23/235602

[110] A. Lenef and S. C. Rand. *Electronic structure of the N-V center in diamond: Theory*. Physical Review B **53**(20), 13441–13455 (May 1996).
URL http://dx.doi.org/10.1103/PhysRevB.53.13441

[111] A. Gali, M. Fyta, and E. Kaxiras. *Ab initio supercell calculations on nitrogen-vacancy center in diamond: Electronic structure and hyperfine tensors*. Physical Review B **77**(15), 155206 (Apr 2008).
URL http://dx.doi.org/10.1103/PhysRevB.77.155206

[112] M. V. Hauf, B. Grotz, B. Naydenov, M. Dankerl, S. Pezzagna, J. Meijer, F. Jelezko, J. Wrachtrup, M. Stutzmann, F. Reinhard, and J. A. Garrido. *Chemical control of the charge state of nitrogen-vacancy centers in diamond*. Physical Review B **83**(8), 081304 (Feb 2011).
URL http://dx.doi.org/10.1103/PhysRevB.83.081304

[113] L. Rondin, G. Dantelle, A. Slablab, F. Grosshans, F. Treussart, P. Bergonzo, S. Perruchas, T. Gacoin, M. Chaigneau, H.-C. Chang, V. Jacques, and J.-F. Roch. *Surface-induced charge state conversion of nitrogen-vacancy defects in nanodiamonds*. Physical Review B **82**(11), 115449 (Sep 2010).
URL http://dx.doi.org/10.1103/PhysRevB.82.115449

[114] N. B. Manson and J. Harrison. *Photo-ionization of the nitrogen-vacancy center in diamond*. Diamond and Related Materials **14**, 1705–1710 (2005).
URL http://dx.doi.org/10.1016/j.diamond.2005.06.027

[115] T. Gaebel, M. Domhan, C. Wittmann, I. Popa, F. Jelezko, J. R. Rabeau, A. D. Greentree, S. Prawer, E. Trajkov, P. Hemmer, and J. Wrachtrup. *Photochromism in single nitrogen-vacancy defect in diamond*. Applied Physics B **82**, 243–246 (2006).
URL http://dx.doi.org/10.1007/s00340-005-2056-2

[116] J. P. Goss, R. Jones, P. R. Briddon, G. Davies, A. T. Collins, A. Mainwood, J. A. van Wyk, J. M. Baker, M. E. Newton, A. M. Stoneham, and S. C. Lawson. *Comment on "Electronic structure of the N-V center in diamond: Theory"*. Physical Review B **56**(24), 16031–16032 (Dec 1997).
URL http://dx.doi.org/10.1103/PhysRevB.56.16031

[117] A. Lenef and S. C. Rand. *Reply to "Comment on 'Electronic structure of the N-V center in diamond: Theory' "*. Physical Review B **56**(24), 16033–16034 (Dec 1997).
URL http://dx.doi.org/10.1103/PhysRevB.56.16033

[118] J. R. Maze, A. Gali, E. Togan, Y. Chu, A. Trifonov, E. Kaxiras, and M. D. Lukin. *Properties of nitrogen-vacancy centers in diamond: the group theoretic approach*. New Journal of Physics **13**(2), 025025 (2011).
URL http://dx.doi.org/10.1088/1367-2630/13/2/025025

[119] J. P. Goss, R. Jones, S. J. Breuer, P. R. Briddon, and S. Öberg. *The Twelve-Line 1.682 eV Luminescence Center in Diamond and the Vacancy-Silicon Complex*. Physical Review Letters **77**(14), 3041–3044 (Sep 1996).
URL http://dx.doi.org/10.1103/PhysRevLett.77.3041

[120] L. J. Rogers, S. Armstrong, M. J. Sellars, and N. B. Manson. *Infrared emission of the NV centre in diamond: Zeeman and uniaxial stress studies*. New Journal of Physics **10**(10), 103024 (2008).
URL http://dx.doi.org/10.1088/1367-2630/10/10/103024

[121] N. B. Manson, L. Rogers, M. Doherty, and L. Hollenberg. *Optically induced spin polarisation of the NV centre in diamond: role of electron-vibration interaction*. arXiv:1011.2840v1 (2010).
URL http://arxiv.org/abs/1011.2840v1

[122] N. B. Manson, J. P. Harrison, and M. J. Sellars. *Nitrogen-vacancy center in diamond: Model of the electronic structure and associated dynamics*. Physical Review B **74**(10), 104303 (Sep 2006).
URL http://dx.doi.org/10.1103/PhysRevB.74.104303

[123] N. Manson and R. McMurtrie. *Issues concerning the nitrogen-vacancy center in diamond*. Journal of Luminescence **127**(1), 98–103 (2007). ISSN 0022-2313. Proceedings of the Ninth International Meeting on Hole Burning, Single Molecule, and Related Spectroscopies: Science and Applications, Hole Burning, Single Molecule, and Related Spectroscopies: Science and Applications.
URL http://dx.doi.org/10.1016/j.jlumin.2007.02.013

[124] A. Gali. *Identification of individual C 13 isotopes of nitrogen-vacancy center in diamond by combining the polarization studies of nuclear spins and first-principles*

calculations. Physical Review B **80**(24), 241204 (2009).
URL http://dx.doi.org/10.1103/PhysRevB.80.241204

[125] S. Felton, A. M. Edmonds, M. E. Newton, P. M. Martineau, D. Fisher, D. J. Twitchen, and J. M. Baker. *Hyperfine interaction in the ground state of the negatively charged nitrogen vacancy center in diamond*. Physical Review B **79**(7), 075203 (Feb 2009).
URL http://dx.doi.org/10.1103/PhysRevB.79.075203

[126] A. Batalov, C. Zierl, T. Gaebel, P. Neumann, I. Y. Chan, G. Balasubramanian, P. R. Hemmer, F. Jelezko, and J. Wrachtrup. *Temporal coherence of photons emitted by single nitrogen-vacancy defect centers in diamond using optical Rabi-oscillations*. Physical Review Letters **100**(7), 077401 (2008).
URL http://dx.doi.org/10.1103/PhysRevLett.100.077401

[127] P. Tamarat, N. B. Manson, J. P. Harrison, R. L. McMurtrie, A. Nizovtsev, C. Santori, R. G. Beausoleil, P. Neumann, T. Gaebel, F. Jelezko, P. Hemmer, and J. Wrachtrup. *Spin-flip and spin-conserving optical transitions of the nitrogen-vacancy centre in diamond*. New Journal of Physics **10**(4), 045004 (2008).
URL http://dx.doi.org/10.1088/1367-2630/10/4/045004

[128] C. Santori, P. Tamarat, P. Neumann, J. Wrachtrup, D. Fattal, R. G. Beausoleil, J. Rabeau, P. Olivero, A. D. Greentree, S. Prawer, F. Jelezko, and P. Hemmer. *Coherent Population Trapping of Single Spins in Diamond under Optical Excitation*. Physical Review Letters **97**(24), 247401 (Dec 2006).
URL http://dx.doi.org/10.1103/PhysRevLett.97.247401

[129] J. Harrison, M. J. Sellars, and N. B. Manson. *Optical spin polarisation of the N-V centre in diamond*. Journal of Luminescence **107**(1-4), 245–248 (2004).
URL http://dx.doi.org/10.1016/j.jlumin.2003.12.020

[130] J. Harrison, M. J. Sellars, and N. B. Manson. *Measurement of the optically induced spin polarisation of N-V centres in diamond*. Diamond and Related Materials **15**(4-8), 586–588 (2006).
URL http://dx.doi.org/10.1016/j.diamond.2005.12.027

[131] E. van Oort, N. B. Manson, and M. Glasbeek. *Optically detected spin coherence of the diamond N-V centre in its triplet ground state*. Journal of Physics C: Solid State Physics **21**(23), 4385–4391 (1988).
URL http://dx.doi.org/10.1088/0022-3719/21/23/020

[132] G. Waldherr, J. Beck, M. Steiner, P. Neumann, A. Gali, T. Frauenheim, F. Jelezko, and J. Wrachtrup. *Dark States of Single Nitrogen-Vacancy Centers in Diamond Unraveled by Single Shot NMR*. Physical Review Letters **106**(15), 157601 (Apr

2011).
URL http://dx.doi.org/10.1103/PhysRevLett.106.157601

[133] J. A. Weil, J. R. Bolton, and J. E. Wertz. *Electron paramagnetic resonance: elementary theory and practical applications*. John Wiley & Sons, Inc. (1994). ISBN 0-471-57234-9.

[134] A. Schweiger and G. Jeschke. *Principles of Pulse Electron Paramagnetic Resonance*. Oxford University Press (2001). ISBN 0-19-850634-1.

[135] J. H. N. Loubser. *ESR Studies of Diamond Powders*. Solid State Communications **22**(12), 767–770 (1977).
URL http://dx.doi.org/10.1016/0038-1098(77)90064-3

[136] H. Haken and H. C. Wolf. *Molekülphysik und Quantenchemie*. Springer, 3rd edition edition (1998). ISBN 3-540-63786-9.

[137] E. van Oort and M. Glasbeek. *Electric-Field-Induced Modulation of Spin Echoes of N-V Centers in Diamond*. Chemical Physics Letters **168**(6), 529–532 (1990).
URL http://dx.doi.org/10.1016/0009-2614(90)85665-Y

[138] E. van Oort, B. van der Kamp, R. Sitter, and M. Glasbeek. *Microwave-induced line-narrowing of the N-V defect absorption in diamond*. Journal of Luminescence **48-49**(Part 2), 803–806 (1991). ISSN 0022-2313.
URL http://dx.doi.org/10.1016/0022-2313(91)90245-Q

[139] A. C. Victor. *Heat Capacity of Diamond at High Temperatures*. Journal of Chemical Physics **36**(7), 1903 (1962).
URL http://dx.doi.org/10.1063/1.1701288

[140] A. Gali, T. Simon, and J. E. Lowther. *An ab initio study of local vibration modes of the nitrogen-vacancy center in diamond*. New Journal of Physics **13**(2), 025016 (2011).
URL http://dx.doi.org/10.1088/1367-2630/13/2/025016

[141] A. M. Zaitsev. *Vibronic spectra of impurity-related optical centers in diamond*. Physical Review B **61**, 12909–12922 (May 2000).
URL http://dx.doi.org/10.1103/PhysRevB.61.12909

[142] T. Gaebel, I. Popa, A. Gruber, M. Domhan, F. Jelezko, and J. Wrachtrup. *Stable single-photon source in the near infrared*. New Journal of Physics **6**(1), 98 (2004).
URL http://dx.doi.org/10.1088/1367-2630/6/1/098

[143] M. Mehring and J. Mende. *Spin-bus concept of spin quantum computing*. Physical Review A **73**, 052303 (May 2006).
URL http://dx.doi.org/10.1103/PhysRevA.73.052303

[144] L. Jiang, J. M. Taylor, A. S. Sørensen, and M. D. Lukin. *Distributed quantum computation based on small quantum registers*. Physical Review A **76**(6), 062323 (2007).
URL http://dx.doi.org/10.1103/PhysRevA.76.062323

[145] B. Grotz, J. Beck, P. Neumann, B. Naydenov, R. Reuter, F. Reinhard, F. Jelezko, J. Wrachtrup, D. Schweinfurth, B. Sarkar, and P. Hemmer. *Sensing external spins with nitrogen-vacancy diamond*. New Journal of Physics **13**(5), 055004 (2011).
URL http://dx.doi.org/10.1088/1367-2630/13/5/055004

[146] J. R. Weber, W. F. Koehl, J. B. Varley, A. Janotti, B. B. Buckley, C. G. Van de Walle, and D. D. Awschalom. *Quantum computing with defects*. Proceedings of the National Academy of Sciences **107**(19), 8513–8518 (2010).
URL http://dx.doi.org/10.1073/pnas.1003052107

[147] J. R. Weber, W. F. Koehl, J. B. Varley, A. Janotti, B. B. Buckley, C. G. V. de Walle, and D. D. Awschalom. *Defects in SiC for quantum computing*. Applied Physics Letters **109**(10), 102417 (2011). ISSN 00218979.
URL http://dx.doi.org/10.1063/1.3578264

[148] U. F. S. D'Haenens-Johansson. *EPR of silicon related defects in CVD diamond*. In *Gordon Research Conference: Defects in Semiconductors*. Colby-Sawyer College, New Hampshire, United States of America (August 2010).

[149] M. Orrit and J. Bernard. *Single pentacene molecules detected by fluorescence excitation in a p-terphenyl crystal*. Physical Review Letters **65**, 2716–2719 (Nov 1990).
URL http://dx.doi.org/10.1103/PhysRevLett.65.2716

[150] M. Orrit and J. Bernard. *Single molecule spectroscopy in a solid*. Journal of Luminescence **53**(1-6), 165–169 (1992). ISSN 0022-2313.
URL http://dx.doi.org/10.1016/0022-2313(92)90130-2

[151] J. Wrachtrup, C. von Borczyskowski, J. Bernard, M. Orrit, and R. Brown. *Optically detected spin coherence of single molecules*. Physical Review Letters **71**, 3565–3568 (Nov 1993).
URL http://dx.doi.org/10.1103/PhysRevLett.71.3565

[152] R. M. Dickson, D. J. Norris, Y.-L. Tzeng, and W. E. Moerner. *Three-Dimensional Imaging of Single Molecules Solvated in Pores of Poly(acrylamide) Gels*. Science **274**(5289), 966–968 (1996).
URL http://dx.doi.org/10.1126/science.274.5289.966

[153] R. M. Dickson, A. B. Cubitt, R. Y. Tsien, and W. E. Moerner. *On/off blinking and switching behaviour of single molecules of green fluorescent protein*. Nature

388(6640), 355–358 (July 1997). ISSN 0028-0836.
URL http://dx.doi.org/10.1038/41048

[154] A. Dräbenstedt, L. Fleury, C. Tietz, F. Jelezko, S. Kilin, A. Nizovtzev, and J. Wrachtrup. *Low-temperature microscopy and spectroscopy on single defect centers in diamond*. Physical Review B **60**(16), 11503–11508 (1999).
URL http://dx.doi.org/10.1103/PhysRevB.60.11503

[155] F. Jelezko, C. Tietz, A. Gruber, I. Popa, A. Nizovtsev, S. Kilin, and J. Wrachtrup. *Spectroscopy of Single N-V Centers in Diamond*. Single Molecules **2**(4), 255–260 (2001). ISSN 1438-5171.
URL http://dx.doi.org/10.1002/1438-5171(200112)2:4<255::AID-SIMO255>3.0.CO;2-D

[156] R. H. Webb. *Confocal optical microscopy*. Reports on Progress in Physics **59**(3), 427 (1996).
URL http://dx.doi.org/10.1088/0034-4885/59/3/003

[157] B. Naydenov, F. Dolde, L. T. Hall, C. Shin, H. Fedder, L. C. L. Hollenberg, F. Jelezko, and J. Wrachtrup. *Dynamical decoupling of a single-electron spin at room temperature*. Physical Review B **83**(8), 081201 (Feb 2011).
URL http://dx.doi.org/10.1103/PhysRevB.83.081201

[158] A. Morello, J. J. Pla, F. A. Zwanenburg, K. W. Chan, K. Y. Tan, H. Huebl, M. Mottonen, C. D. Nugroho, C. Yang, J. A. van Donkelaar, A. D. C. Alves, D. N. Jamieson, C. C. Escott, L. C. L. Hollenberg, R. G. Clark, and A. S. Dzurak. *Single-shot readout of an electron spin in silicon*. Nature **467**(7316), 687–691 (October 2010). ISSN 0028-0836.
URL http://dx.doi.org/10.1038/nature09392

[159] T. D. Ladd, J. R. Goldman, F. Yamaguchi, Y. Yamamoto, E. Abe, and K. M. Itoh. *All-Silicon Quantum Computer*. Physical Review Letters **89**, 017901 (Jun 2002).
URL http://dx.doi.org/10.1103/PhysRevLett.89.017901

[160] W. Harneit. *Fullerene-based electron-spin quantum computer*. Physical Review A **65**, 032322 (Feb 2002).
URL http://dx.doi.org/10.1103/PhysRevA.65.032322

[161] A. Gali. Private communication.

[162] B. Smeltzer, L. Childress, and A. Gali. *13 C hyperfine interactions in the nitrogen-vacancy centre in diamond*. New Journal of Physics **13**(2), 025021 (2011).
URL http://dx.doi.org/10.1088/1367-2630/13/2/025021

[163] E. van Oort and M. Glasbeek. *Optically detected low field electron spin echo envelope modulations of fluorescent N-V centers in diamond*. Chemical Physics **143**, 131–140 (1990).
URL http://dx.doi.org/10.1016/0301-0104(90)85013-M

[164] W. M. Witzel, R. de Sousa, and S. Das Sarma. *Quantum theory of spectral-diffusion-induced electron spin decoherence*. Physical Review B **72**(16), 161306 (2005).
URL http://dx.doi.org/10.1103/PhysRevB.72.161306

[165] J. R. Maze, J. M. Taylor, and M. D. Lukin. *Electron spin decoherence of single nitrogen-vacancy defects in diamond*. Physical Review B **78**(9), 094303 (Sep 2008).
URL http://dx.doi.org/10.1103/PhysRevB.78.094303

[166] V. V. Dobrovitski, A. E. Feiguin, D. D. Awschalom, and R. Hanson. *Decoherence dynamics of a single spin versus spin ensemble*. Physical Review B **77**, 245212 (Jun 2008).
URL http://dx.doi.org/10.1103/PhysRevB.77.245212

[167] W. Kohn. *Solid State Physics*, volume 5. Academic Press, New York (1957).

[168] E. Abe, A. M. Tyryshkin, S. Tojo, J. J. L. Morton, W. M. Witzel, A. Fujimoto, J. W. Ager, E. E. Haller, J. Isoya, S. A. Lyon, M. L. W. Thewalt, and K. M. Itoh. *Electron spin coherence of phosphorus donors in silicon: Effect of environmental nuclei*. Physical Review B **82**(12), 121201 (Sep 2010).
URL http://dx.doi.org/10.1103/PhysRevB.82.121201

[169] J. Zhou, L. Li, H. Hu, B. Yang, Z. Dan, J. Qiu, J. Guo, F. Chen, and C. Ye. *Study of natural diamonds by dynamic nuclear polarization-enhanced 13C nuclear magnetic resonance spectroscopy*. Solid State Nuclear Magnetic Resonance **3**(6), 339–351 (1994). ISSN 0926-2040.
URL http://dx.doi.org/10.1016/0926-2040(94)90018-3

[170] B. W. Lovett and S. C. Benjamin. *Comment on "Multipartite Entanglement Among Single Spins in Diamond"*. Science **323**(5918), 1169 (2009).
URL http://dx.doi.org/10.1126/science.1168458

[171] P. Neumann, N. Mizuochi, F. Rempp, P. Hemmer, H. Watanabe, S. Yamasaki, V. Jacques, T. Gaebel, F. Jelezko, and J. Wrachtrup. *Response to Comment on "Multipartite Entanglement Among Single Spins in Diamond"*. Science **323**(5918), 1169 (2009).
URL http://dx.doi.org/10.1126/science.1168459

[172] A. Peres. *Separability criterion for density matrices.* Physical Review Letters **77**(8), 1413–1415 (1996).
URL http://dx.doi.org/10.1103/PhysRevLett.77.1413

[173] M. Horodecki, P. Horodecki, and R. Horodecki. *Separability of mixed states: Necessary and sufficient conditions.* Physics Letters A **223**(1-2), 1–8 (1996).
URL http://dx.doi.org/10.1016/S0375-9601(96)00706-2

[174] S. Hill and W. K. Wootters. *Entanglement of a Pair of Quantum Bits.* Physical Review Letters **78**(26), 5022–5025 (Jun 1997).
URL http://dx.doi.org/10.1103/PhysRevLett.78.5022

[175] W. K. Wootters. *Entanglement of Formation of an Arbitrary State of Two Qubits.* Physical Review Letters **80**(10), 2245–2248 (Mar 1998).
URL http://dx.doi.org/10.1103/PhysRevLett.80.2245

[176] R. Fisher. *Optimal Control of Multi-Level Quantum Systems.* Ph.D. thesis, Technische Universität München – Department Chemie – Fachgebiet Organische Chemie (October 2010).
URL http://nbn-resolving.de/urn/resolver.pl?urn:nbn:de:bvb:91-diss-00101213-1002028-1-6

[177] V. Giovannetti, S. Lloyd, and L. Maccone. *Quantum-enhanced measurements: Beating the standard quantum limit.* Science **306**(5700), 1330–1336 (2004).
URL http://dx.doi.org/10.1126/science.1104149

[178] P. G. Kwiat, A. J. Berglund, J. B. Altepeter, and A. G. White. *Experimental verification of decoherence-free subspaces.* Science **290**(5491), 498–501 (2000).
URL http://dx.doi.org/10.1126/science.290.5491.498

[179] D. Kielpinski, V. Meyer, M. A. Rowe, C. A. Sackett, W. M. Itano, C. Monroe, and D. J. Wineland. *A decoherence-free quantum memory using trapped ions.* Science **291**(5506), 1013–1015 (2001).
URL http://dx.doi.org/10.1126/science.1057357

[180] L. J. Rogers, R. L. McMurtrie, M. J. Sellars, and N. B. Manson. *Time-averaging within the excited state of the nitrogen-vacancy centre in diamond.* New Journal of Physics **11**(6), 063007 (2009).
URL http://dx.doi.org/10.1088/1367-2630/11/6/063007

[181] F. Jelezko. Private communication.

[182] V. B. Braginsky and F. Y. Khalili. *Quantum nondemolition measurements: The route from toys to tools.* Reviews of Modern Physics **68**(1), 1–11 (1996).
URL http://dx.doi.org/10.1103/RevModPhys.68.1

[183] N. Zarrabi. *Hidden Markov Modelle für Einzelmolekül̈daten*. Ph.D. thesis, Universität Stuttgart, 3. Phsikalisches Institut (2010). Language = German.
URL http://nbn-resolving.de/urn:nbn:de:bsz:93-opus-56913

[184] W. H. Press, S. A. Teukolsky, W. T. Vetterling, and B. P. Flannery. *Numerical Recipes*. Cambridge University Press, third edition (2007). ISBN 978-0-521-88407-5.

[185] X.-F. He, N. B. Manson, and P. T. H. Fisk. *Paramagnetic resonance of photoexcited N-V defects in diamond. I. Level anticrossing in the 3A ground state*. Physical Review B **47**(14), 8809–8815 (Apr 1993).
URL http://dx.doi.org/10.1103/PhysRevB.47.8809

[186] A. V. Gorshkov, A. M. Rey, A. J. Daley, M. M. Boyd, J. Ye, P. Zoller, and M. D. Lukin. *Alkaline-Earth-Metal Atoms as Few-Qubit Quantum Registers*. Physical Review Letters **102**(11), 110503 (2009).
URL http://dx.doi.org/10.1103/PhysRevLett.102.110503

[187] I. Reichenbach and I. H. Deutsch. *Sideband cooling while preserving coherences in the nuclear spin state in Group-II-like atoms*. Physical Review Letters **99**(12), 123001 (2007).
URL http://dx.doi.org/10.1103/PhysRevLett.99.123001

[188] N. Imoto, H. A. Haus, and Y. Yamamoto. *Quantum Nondemolition Measurement of the Photon Number Via the Optical Kerr Effect*. Physical Review A **32**(4), 2287–2292 (1985).
URL http://dx.doi.org/10.1103/PhysRevA.32.2287

[189] T. C. Ralph, S. D. Bartlett, J. L. O'Brien, G. J. Pryde, and H. M. Wiseman. *Quantum nondemolition measurements for quantum information*. Physical Review A **73**(1), 012113 (2006).
URL http://dx.doi.org/10.1103/PhysRevA.73.012113

[190] T. M. Babinec, H. J. M., M. Khan, Y. Zhang, J. R. Maze, P. R. Hemmer, and M. Loncar. *A diamond nanowire single-photon source*. Nature Nanotechnology **5**(3), 195–199 (March 2010). ISSN 1748-3387.
URL http://dx.doi.org/10.1038/nnano.2010.6

[191] D. Englund, B. Shields, K. Rivoire, F. Hatami, J. Vuckovic, H. Park, and M. D. Lukin. *Deterministic Coupling of a Single Nitrogen Vacancy Center to a Photonic Crystal Cavity*. Nano Letters **10**(10), 3922–3926 (2010).
URL http://dx.doi.org/10.1021/nl101662v

[192] R. Prevedel, P. Walther, F. Tiefenbacher, P. Bohi, R. Kaltenbaek, T. Jennewein, and A. Zeilinger. *High-speed linear optics quantum computing using active feed-forward*. Nature **445**(7123), 65–69 (January 2007). ISSN 0028-0836.
URL http://dx.doi.org/10.1038/nature05346

[193] *SRIM ® – Stopping and Range of Ions in Matter*. software.
URL http://www.srim.org

[194] J. Tisler, G. Balasubramanian, B. Naydenov, R. Kolesov, B. Grotz, R. Reuter, J.-P. Boudou, P. A. Curmi, M. Sennour, A. Thorel, M. Börsch, K. Aulenbacher, R. Erdmann, P. R. Hemmer, F. Jelezko, and J. Wrachtrup. *Fluorescence and Spin Properties of Defects in Single Digit Nanodiamonds*. ACS Nano **3**(7), 1959–1965 (2009).
URL http://dx.doi.org/10.1021/nn9003617

[195] B. Naydenov, F. Reinhard, A. Lämmle, V. Richter, R. Kalish, U. F. S. D'Haenens-Johansson, M. Newton, F. Jelezko, and J. Wrachtrup. *Increasing the coherence time of single electron spins in diamond by high temperature annealing*. Applied Physics Letters **97**(24), 242511 (2010). ISSN 00036951.
URL http://dx.doi.org/10.1063/1.3527975

[196] G. Jeschke. *Distance Measurements in the Nanometer Range by Pulse EPR*. Chemphyschem: a European journal of chemical physics and physical chemistry **3**(11), 927–932 (2002). ISSN 1439-7641.
URL http://dx.doi.org/10.1002/1439-7641(20021115)3:11<927::AID-CPHC927>3.0.CO;2-Q

[197] M. A. Nielsen and I. L. Chuang. *Quantum Computation and Quantum Information*. Cambridge University Press (2000). ISBN 0-521-63503-9.
URL http://www.cambridge.org/9780521635035

[198] G. de Lange, Z. H. Wang, D. Ristè, V. V. Dobrovitski, and R. Hanson. *Universal dynamical decoupling of a single solid-state spin from a spin bath*. Science **330**(6000), 60–63 (Oct 2010).
URL http://dx.doi.org/10.1126/science.1192739

[199] A. M. Souza, G. A. Álvarez, and D. Suter. *Robust Dynamical Decoupling for Quantum Computing and Quantum Memory*. Physical Review Letters **106**, 240501 (Jun 2011).
URL http://dx.doi.org/10.1103/PhysRevLett.106.240501

[200] J. M. Taylor, P. Cappellaro, L. Childress, L. Jiang, D. Budker, P. R. Hemmer, A. Yacoby, R. Walsworth, and M. D. Lukin. *High-sensitivity diamond magnetometer with nanoscale resolution*. Nature Physics **4**(10), 810–816 (October 2008).

ISSN 1745-2473.
URL http://dx.doi.org/10.1038/nphys1075

[201] S. A. McKinney, C. Joo, and T. Ha. *Analysis of Single-Molecule FRET Trajectories Using Hidden Markov Modeling.* Biophysical Journal **91**(5), 1941–1951 (2006). ISSN 0006-3495.
URL http://dx.doi.org/10.1529/biophysj.106.082487